Mémoires de Géologie (Lausanne) No. 31, 1999

Intracontinental alkaline magmatism: Geology, Petrography, Mineralogy and Geochemistry of the Jebel Hayim Massif (Central High Atlas - Morocco)

Giovanni Armando

IMPRIMERIE TIPOLITO SUBALPINA, Rivoli (TO), Italie ISSN 1015-3578

Mémoires de Géologie (Lausanne)

Section des Sciences de la Terre
Université de Lausanne
BFSH-2, 1015 Lausanne, Suisse

31

Mémoires de Géologie (Lausanne)

Mémoires de Géologie (Lausanne)
Section des Sciences de la Terre
Institut de Géologie et Paléontologie
Université de Lausanne
BFSH-2, CH 1015 Lausanne

ARMANDO, Giovanni
Title: Intracontinental alkaline magmatism: Geology, Petrography, Mineralogy and Geochemistry of the Jebel Hayim Massif (Central High Atlas - Morocco)
Mém. Géol. (Lausanne), n° 31, 1999, 109 pp., 51 figs., 23 tables, 1 map.
ISSN: 1015-3578
Imprimeur: Tipolito Subalpina S.r.l., Rivoli (TO), Italie

Cover figure: Jebel Issoual (High Atlas, Morocco)

Author's present address: *P.zza Costantino il G. 168, 10134 Torino (I)*

Material request: *jean.hernandez@imp.unil.ch*

Intracontinental alkaline magmatism: Geology, Petrography, Mineralogy and Geochemistry of the Jebel Hayim Massif (Central High Atlas - Morocco)

Giovanni Armando

Mémoires de Géologie (Lausanne) No. 31, 1999

Questo lavoro é dedicato
ai pochi che avranno
la voglia e la forza
di leggere questo libro.

Table of Contents

Appendixes

Abstract

Jebel Hayim Massif belongs to a suite of alkaline to transitional intrusive massifs scattered in the axial zone of the Moroccan Central High Atlas and formed during a Middle to Upper Jurassic transtensional phase. Country rock is locally strongly deformed and the style of deformation is consistent with a sinistral strike-slip regime contemporaneous to magma emplacement. During the Oxfordian, magma ascended to the upper crust where it solidified in Triassic to Early Jurassic sedimentary sequences at the base of the High Atlas sedimentary cover. Present position of magmatic rocks is within Bajocian to Bathonian sediments and is the result of a post-magmatic tectonic extrusion.

Jebel Hayim Massif is made of two gabbroic layered complexes (JH1 and JH2) overlain by pneumatolytic gabbros and cross-cut by monzonitic to syenitic dikes. Both complexes consist of a lower troctolite series and of an upper oxide-rich gabbros and ol-gabbros series, respectively. The contacts between lower and upper series are horizontal and have a primary magmatic origin. Troctolites and ol-gabbros are cumulates with olivine, plagioclase and augite as early cumulus phases, and ilmenite, biotite and kaersutite as late interstitial phases. Both cumulates display modal and cryptic layering with a decrease of the olivine content and of the MgO content of all mineral phases from bottom to top. Oxide-rich gabbros are characterized by abundant magnetite (10%), scarce olivine, low MgO content, and flow texture, and they do not display modal or cryptic layering.

Liquid compositions were calculated for representative rock types using the trace element content in olivine, plagioclase and clinopyroxene, and selected sets of partition coefficients. On the basis of the calculations, it is clear that the evolution of the gabbros was not continuous nor linear, and that different parental magmas were responsible for the different series. Different degrees of partial melting are invoked to explain the variations of incompatible elements (Hf, Ta, REE and Th) abundances. A early differentiation stage, at depth, is invoked to explain the relatively low MgO calculated contents (<9%) and the large variations of Ni and Cr abundances. Oxide-rich gabbros are depleted in both compatible elements and incompatible elements which is attributed to a larger degree of partial melting (2.5%) and to more fractionation of olivine and chromite at depth (11% of crystal fractionation) than for generating troctolites and ol-gabbros melts (<7%). Troctolites and ol-gabbros parental magmas resulted from a degree of partial melting ranging from 0.8% for JH2 troctolites to 1.8% for JH2 ol-gabbros to 3% for JH1 troctolites.

Résumé

Le massif de Jebel Hayim appartient à une série de massifs intrusifs à affinité alcaline à transitionnelle affleurant dans la zone axiale du Haut Atlas central. Ces massifs se sont formés lors d'une phase transtensive d'âge Jurassique moyen à Jurassique supérieur. Les séries sédimentaires du Jurassique Moyen, qui forment les roches encaissantes du massif sont localement fortement déformées dans un régime tectonique décrochant sénestre, contemporain de la mise en place des magmas. La position actuelle du massif, dans les sédiments du Bajocien-Bathonien, est liée à une extrusion tectonique post-magmatique.

Le massif de Jebel Hayim est constitué de deux complexes gabbroiques stratifiés (JH1 et JH2) recouverts par des gabbros pneumatolitiques et recoupés par des filons de monzonite et syénite. Ces deux complexes sont composés d'une série inférieure à troctolites et d'une série supérieure à gabbros riches en oxydes et gabbros à olivine. Les contacts entre les deux séries sont d'origine magmatique primaire et horizontaux. Les troctolites et les gabbros à olivine sont des cumulats à olivine, plagioclase et augite comme phases cumulatives primaires et ilménite, biotite et kaersutite comme phases interstitielles tardives. Les deux types de roches montrent une stratification modale et minérale avec une décroissance de la proportion d'olivine ainsi qu'une diminution de la teneur en MgO de toutes les phases minérales de la base au sommet. Les gabbros riches en oxyde sont caractérisés par l'abondance de la magnétite (10%), la quasi absence d'olivine, des teneurs faibles en MgO, des textures de flux et ne montrent pas de stratification minérale ou modale.

La composition des liquides a été calculé pour une série des roches types, en utilisant les coefficients de partage des éléments traces contenus dans l'olivine, le plagioclase et le clinopyroxène. Les calculs indiquent que l'évolution des gabbros n'est pas continue et linéaire et que différents magmas parents en sont l'origine. Des degrés croissants de fusion partielle permettent d'expliquer les variations des teneurs en éléments incompatibles (Hf, Ta, REE and Th). Un stade précoce de différenciation par cristallisation fractionnée, en profondeur, permet d'expliquer les teneurs relativement basses en MgO (<9%), Ni (<100 ppm) et Cr. Les gabbros riches en oxydes sont appauvris en éléments compatibles et incompatibles qui est attribué à un plus fort degré de fusion partielle de leurs liquides (5.7%) par rapport à ceux générant les troctolites et les gabbros à olivine, mais aussi à un plus fort fractionnement d'olivine et chromite en profondeur (11% de cristallisation

fractionnée). Les magmas à l'origine des troctolites et des gabbros à olivine résultent d'un degré de fusion partielle de 0.8%, pour les troctolites JH2, 1.8% pour les gabbros à olivine et 3% pour les troctolites JH1.

Riassunto

Il Massiccio di Jebel Hayim appartiene a una serie di massicci intrusivi ad affinità da alcalina a transizionale affioranti nella zona assiale dell'Alto Atlante centrale. Questi massicci si sono formati durante una fase transtensiva di età Giurassico medio a Giurassico superiore. Le serie sedimentarie del Giurassico medio, che formano la roccia incassante del massiccio, sono localmente fortemente deformate in un regime tettonico trascorrente sinistro, contemporaneo alla messa in posto dei magmi. La posizione attuale del massiccio, all'interno dei sedimenti del Baiociano-Batoniano, é legata a un'estrusione tettonica post-magmatica.

Il Massiccio di Jebel Hayim à costituito da due complessi gabbroici stratificati (JH1 e JH2) ricoperti da gabbri pneumatolitici e attraversati da filoni di sieniti e monzoniti. I due complessi sono entrambi composti da una serie inferiore a trottoliti e da una serie superiore a gabbri ricchi in ossidi (magnetite) e a gabbri a olivina. I contatti tra le due serie sono di origine magmatica primaria e orizzontali. Le trottoliti e i gabbri a olivina sono cumulati a olivina, plagioclasio e augite come fasi di cumulus, e ilmenite, biotite e kaersutite come fasi interstiziali tardive. I due litotipi mostrano una stratificazione modale e minerale con diminuzione della quantità di olivina e del tenore in MgO di tutte le fasi minerali dal basso verso l'alto. I gabbri ricchi in ossidi sono caratterizzati dall'abbondanza di magnetite (10%), dalla quasi assenza di olivina, da deboli tenori in MgO, da tessiture di flusso e non mostrano stratificazione modale o minerale.

La composizione dei liquidi é stata calcolata per una serie di rocce tipo utilizzando i coefficienti di distribuzione degli elementi in tracce contenuti nell'olivina, nel plagioclasio e nel clinopirosseno. I calcoli indicano che l'evoluzione dei gabbri non é continua e lineare e che diversi magmi parentali ne sono all'origine. Dei gradi sempre piu alti di fusione parziale permettono di spiegare le variazioni dei tenori in elementi incompatibili (Hf, Ta, REE and Th). Uno stadio precoce di differenziazione per cristallizzazione frazionata in profondità permette altresi' di spiegare i tenori relativamente bassi in MgO (< 9%), Ni (² 100 ppm) e Cr. I gabbri ricchi in ossidi sono impoveriti sia negli elementi incompatibili che negli elementi compatibili; l'apparente contraddizione é attribuita a un piu' forte grado di fusione parziale (5.7%) in rapporto a quello che ha generato le trottoliti e i gabbri a olivina, ed a un piu' forte frazionamento di olivina e cromite in profondità (11%). I magmi all'origine delle trottoliti e dei gabbri a olivina risultano da un grado di fusione parziale di 0.8% per le trottoliti di JH2, 1.8% per i gabbri a olivina e 3.0% per le trottoliti di JH1.

- CHAPTER 1 -

Introduction

This study was conceived with the intention of 1) understanding the mechanism of formation, emplacement and evolution of an alkaline magma in an intracontinental domain, and 2) contributing to our knowledge of the High Atlas geology. A geological, petrographic, mineralogical and geochemical study was performed on the Jebel Hayim Massif (JHM) in order to:

- determine the geometric relationships between the different groups of igneous rocks forming JHM;

- determine the geometric relationships between JHM and the sedimentary sequences forming the country rock;

- determine the deformation phases related to JHM history;

- determine the petrographic, mineralogical and geochemical character of the magmatic association;

- determine the physical conditions of magma emplacement and cooling;

- determine the differentiation process(es) which guided magma evolution;

- determine the liquid line(s) of descent.

This manuscript aims to present, discuss and interpret field and analytical data, and to propose a global model which is consistent with all collected data. In Chapter 2 the investigated area is presented together with our current knowledge of the Central High Atlas. Chapters 3 to 6 are assigned to the presentation, discussion and interpretation of field, petrographic, geochemical and mineralogical data, respectively. In Chapter 7 the physical conditions of magma cooling are established and the liquid lines of descent of JHM magmas are modeled through calculated liquid compositions. Chapter 8 contains the global model with some implications for the Central High Atlas history during Jurassic times and for the present geophysical structure of the chain.

Sampling and analytical techniques

Almost 300 samples of magmatic and sedimentary rocks were collected during 5 field trips (1993-1995) in the Central High Atlas and investigated by optical microscopy. Paragenes are listed in Appendix 1 and location of most representative samples is shown in the outcrop map (Appendix 6).

X-ray fluorescence analysis (XRF) of 98 magmatic rocks was performed at the "Centre d'Analyse Minérale" (CAM) of the University of Lausanne (CH), in order to measure major and trace element bulk compositions. FeO was measured by colorimetry and CO_2 by coulometric titration. Detection limits are found in Appendix 2 and complete analyses are listed in Appendix 3.

REE compositions were measured by **inducted coupled plasma-mass spectrometry** (ICP-MS) analysis on 35 samples at XRAL Laboratory (Toronto, Canada). Detection limits are found in Appendix 3 and complete analyses in Appendix 4. Isotopic ratios ($^{87}Sr/^{86}Sr$ and $^{143}Nd/^{144}Nd$) were measured on 3 gabbros, 1 monzonite and 1 syenite by chromatographic separation and mass spectometry at the Department of Mineralogy of the University of Geneva.

Electron microprobe analysis was performed on olivine, plagioclase, clinopyroxene, amphibole, biotite and Fe-Ti oxides from 12 gabbros, on feldspar, clinopyroxene, biotite and amphibole from 4 «metagabbros», 2 monzonites and 2 syenites at the "Laboratoire de Microscopie Electronique" (LAME) of the University of Lausanne, using a CAMECA SX50. Standard operating conditions consisted of a focused electron beam, an accelerating potential of 15 kV and a sample current of 15 to 20 nA. Standards were both natural silicates and synthetic oxides (Appendix 2). Mineral formulae calculation was based on Spear's (1993) method and personally carried out by

Microsoft Excel Macros. The number of cations per formula unit in olivine, plagioclase and biotite was calculated by normalisation of microprobe data on the basis of the negative charge (number of oxygens). In pyroxene, amphibole and Fe-Ti oxide, cation distribution was firstly calculated on the basis of the number of cations required by the mineral structure and then the eventual negative charge excess was balanced by transformation of suitable amount of Fe^{2+} in Fe^{3+} (ilmenite resulted Fe^{3+}-free). The four tests proposed by Cameron & Papike (1981) were used to consider pyroxene analysis as "superior": 1) the sum ($Si+{}^{IV}Al$) must be equals to 2.00+/-0.02; 2) the octahedral cations (Mn, Fe^{2+}, Fe^{3+}, Mg, Ti, Cr, ${}^{VI}Al$) sum must exceed 0.98 atoms; 3) the M2 site cations sum must be equals to 1.00 ± 0.02; 4) the charge balance equation (${}^{VI}Al + Fe^{3+} + Cr + 2Ti = {}^{IV}Al + Na$) must be balanced to 0.03 of a charge. Microprobe data tables could not be listed as appendix because of space limitations; consequently, they are stored in computer data bases. You can acquire a copy to the Institute of Mineralogy and Petrography of the University of Lausanne (jean.hernandez@imp.unil.ch).

Instrumental neutronic activation (INA) analysis was performed on olivine, plagioclase and clinopyroxene from 8 gabbros at the LGCS (University P. et M. Curie, Paris VI) and at the LPS (CE, Saclay: CEA/CNRS) in order to measure trace element composition of mineral phases. Standard deviations are found together with complete data in Tables 6.2, 6.4 and 6.7 of Chapter 6. Selected elements were: scandium, cobalt, nickel, strontium, hafnium, tantalum, lanthanum, europium, terbium and thorium, for which analytical precision is estimated better than 5%. Chromium was measured, but results were rejected because of the presence of Cr-spinel inclusions in olivine from troctolites and ol-gabbros. Nickel in olivine was measured both by electron microprobe and INA, and results are in good agreement. Mineral separation was made using heavy liquids, magnetic separator and hand-picking techniques, and analysis was carried out according to Chayla (1973).

Finally, **X-ray diffractometry** analysis was performed on 7 samples of " white breccias " in order to investigate high-temperature phases in sedimentary rocks (pelites, marls and carbonates) suspected of contact metamorphism.

Aknowledgements

The realization of this research was possible thanks to the "Fond national suisse de la recherche scientifique" (FNRS) which funded the project, to the « Direction de la Géologie - Division de la Géologie Générale » of the « Ministère de l'Energie et des Mines » of Morocco (Mr.M.Dahmani, Director of Geology), and to Jean Hernandez which was a patient, helpful and friendly tutor, and knew how to direct me through the maze of geology.

I am also grateful to all the people who taught me the analytical techniques and helped me in the laboratory work: Mr.F.Bussy (Laboratoire de Microanalyse Electronique, Université de Lausanne) for microprobe analysis, Mr.B.Villemant (Laboratoire de Géochimie Comparée et Systematique, Université P. et M. Curie de Paris) for INA analysis, Mr.J.-C.Lavanchy (Centre d'Analyse Minérale, Université de Lausanne) for XRF analysis, Mr.J.Hunziker and Mr.M.Cosca (Laboratoire de Géochimie Isotopique, Université de Lausanne) for ${}^{39}Ar/{}^{40}Ar$ analyses, Mr.P.Thelin and Mrs.L.Dufresne (Laboratoire RX, Université de Lausanne) for X-ray analysis. Thanks also to Philippe Favre, Jean-Claude Vannay and Jean-Luc Epard who helped me with the structural interpretation, to Alice, my nice officemate, and to François, Franco and Pierre-Yves who accompanied me during my unforgettable stays in the High Atlas. Reviews by R. Arculus, M.P. Semet, and D. Kirschner greatly improved Chapter 6.

Thanks to my family and to all the people who made my stay in Lausanne exceptionally nice, at work as well as at home: Mizzi, Andrea, Guido, Michelle, Antonio, Laurent, Luigi, Annachiara, Filomena, Sabrina, Elena. And thanks to my faithful friends in Turin: Gigi, Edward & Elena, Valeria, Sergio, Silvia, Luca, Angelo, Paolino, Alex, Rocco, Carmelo, Santina... and Paolo to whom I dedicate my work. And thanks to Nicola and Kara, who corrected my poor english, thanks to «I Ticinesi», thanks to Assou, «le gardien du Poste» and his family, thanks to Philippe and to all the people that I forgot to thank you.

List of abbreviations used in the text

ANR = anorthosite; DOL = dolerite; JHM = Jebel Hayim Massif; LCG = leucogabbro; LS = Lower Series; MCG = microgabbro; MG = metagabbro; MNZ = monzonite; OLG = ol-gabbro; OXG = oxide-rich gabbro; PNG = pneumatolytic gabbro; SB = small body; SYE = syenite; TRC = troctolite; US = Upper Series.

- CHAPTER 2 -

An Overview of the Jebel Hayim Massif and the Central High Atlas

Jebel Hayim is a 2755 m high mountain, 25 km north-east of the village of Imilchil, in the heart of the Moroccan High Atlas. Imilchil is considered by local people to be located at the boundary between the Central and the Eastern High Atlas, and by geologists as lying in the middle of the Central High Atlas. The discrepancy is due to the different geographical and geological subdivisions of the range in Eastern, Central and Western High Atlas. The latter subdivision, in which Jebel Hayim belongs to the Central High Atlas, will be used in this work. The western boundary of the Eastern High Atlas is delimited by the Ziz Valley, which connects Midelt to Errachidia (Figs.2.1 and 2.2).

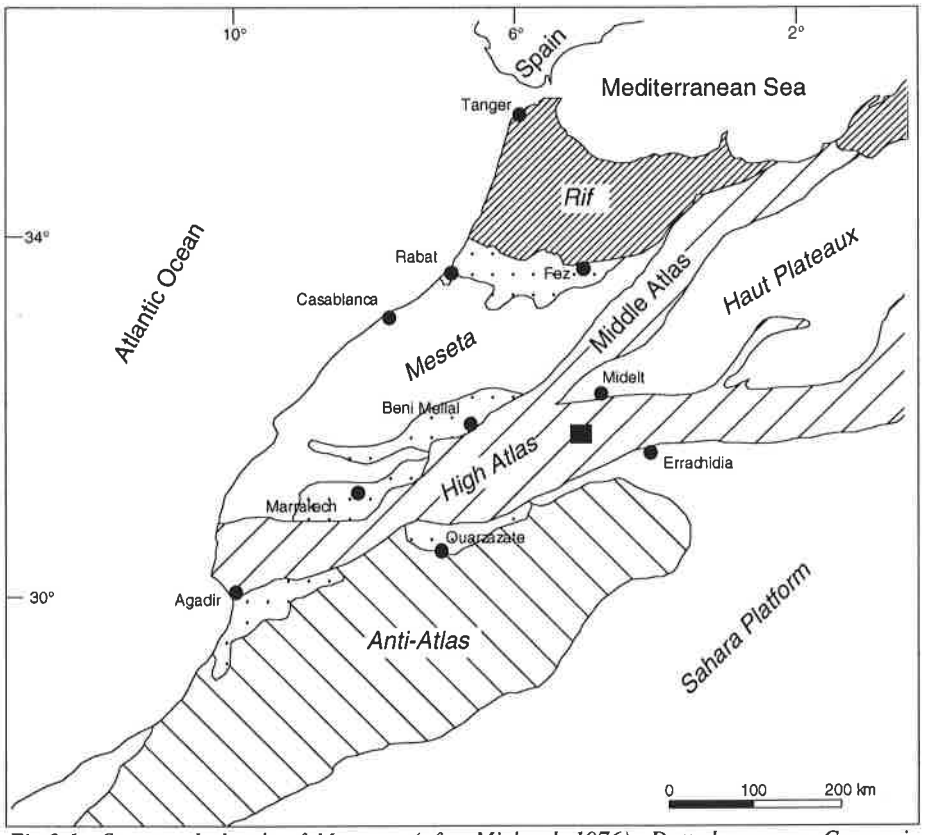

Fig.2.1 - Structural sketch of Morocco (after Michard, 1976). Dotted areas are Cenozoic basins. The black square is the investigated area.

The Jebel Hayim Massif is approximately 30 km^2 and polygonal in shape. Its boundary is constituted by two parallel SSW-NNE trending boundaries, a E-W trending boundary and a WNW-ESE trending boundary. JHM forms a morphological depression, surrounded by the Tameskourt Valley to the north, the Tardagal Valley to the east, Jebel Issoual (2922 m) to the south, and Afoud n'Aoujil (2754 m) to the west. Jebel Hayim is a E-W trending ridge, lying in the middle of the massif (Fig.2.3).

From the north, a 70 km long track links Tounfite to Anefgou and Tirrhist, two small villages at the NE and SE extremities of JHM, respectively. This is the shortest route, but track conditions are very bad and one must allow 4 to 8 hours with a solid four-wheel drive car (even better, with a Renault 4) to cover the distance. Alternative routes

are from Rich, Beni Mellal and Tinerhir. These routes are longer, but safer and more practical. Coming from Tounfite, Jebel Hayim appears a few kilometres before arriving at Anefgou. Its sharp-peaked profile contrasting with the surrounding landscape, which is largely composed of long and monotonous "cuestas", allows it to be easily identified.

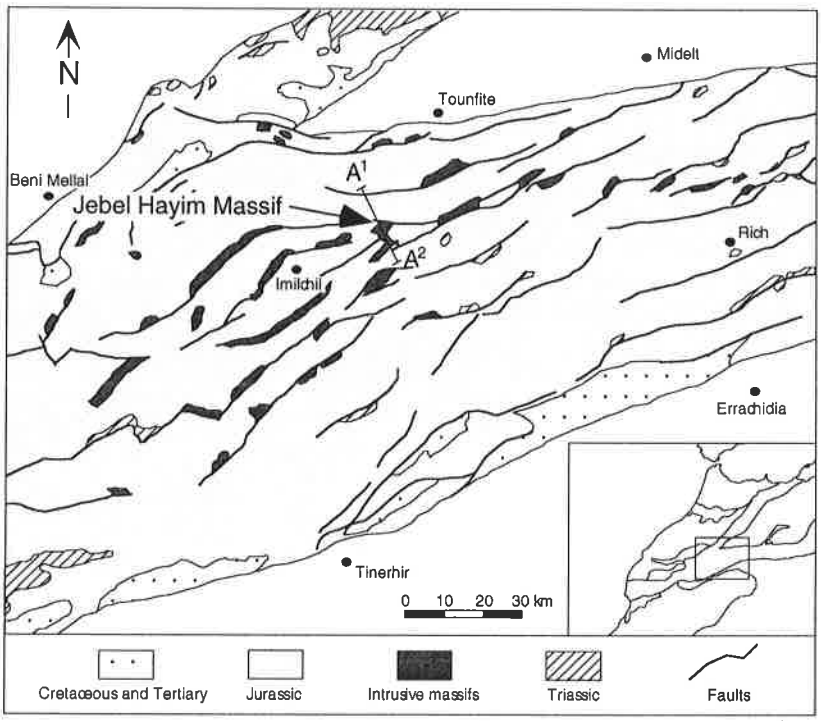

Fig.2.2 - Geological map of the Central High Atlas (after Brede, 1992). A^1-A^2 is the cross-section in Fig.2.3.

Approximately midway between Anefgou and Tirrhist, at the foot of Jebel Hayim, two french-style "chalets" and a perpetual spring of drinking water mark the old site of a French garnison and the present site of a check-point, called "le Poste" or "la Maison Forestière" by native Berbers. Today, a couple of forest rangers living at the Poste protect the area from hunters, smuggler and illegal wood-cutters. The Poste also represents the best starting point for hiking around Jebel Hayim.

2.1 - The Central High Atlas and its history since the Triassic

The Central High Atlas is part of an intracontinental Cenozoic fold belt, the High Atlas, ranging from western Morocco to Tunisia. Its geology is extensively described and illustrated in the works of Choubert & Faure-Muret (1960-62) and Michard (1976).

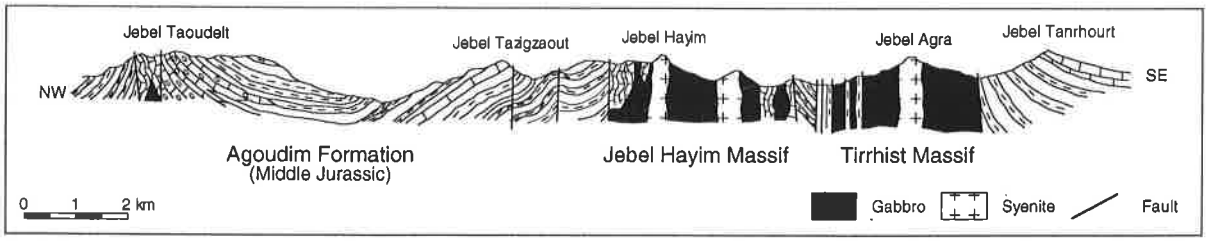

Fig.2.3 - NW-SE cross-section in the Tounfite-Tirrhist region (after Studer, 1987). Agoudim Formation stratigraphy is found in Fig.2.4.

Today, the Central High Atlas appears to geologists as a thick and deformed Mesozoic sedimentary cover (Fig.2.4), widely intruded by a variety of igneous rocks. Its basement is poorly exposed, but, if the same basement is assumed for the whole High Atlas range, it would be a Precambrian to Paleozoic basement, belonging to the African plate (Mattauer *et al.*, 1977). According to geophysical data, the basement of the Central High Atlas is only slightly thicker than the basement of surrounding domains (Meseta, Haut Plateaux and Anti-Atlas), it does not exceed 40 km in thickness and is not characterized by any gravimetric anomaly (Makris *et al.*, 1985; Wigger *et al.*, 1992).

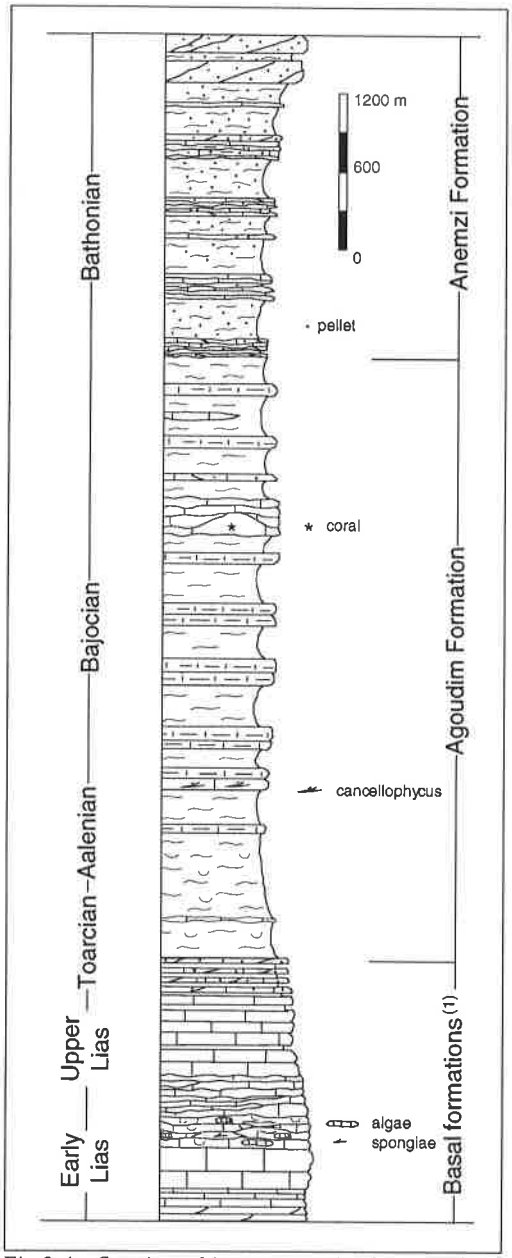

Fig.2.4 - Stratigraphic sequence in the Tounfite-Tirrhist region (after Studer, 1987). (1) = Idikel + Aberdouz + Ouchbis + Tagoudite Formations.

Where relationships between basement and cover are visible, the Mesozoic series are decoupled from their basement (Michard, 1976; Laville *et al.*, 1977). To the south the Central High Atlas is delimited by the South Atlas Fault system, separating the Atlas from the Anti-Atlas range, and whose existence and tectonic role is strongly debated (Laville *et al.*, 1977; Proust *et al.*, 1977; Jacobshagen, 1992). To the north, the Central High Atlas is intersected by the Middle Atlas.

The Central High Atlas originated as a continental subsident basin in response to the early stage of the Central Atlantic rifting during Permo-Triassic times. From the Triassic to the Quaternary, its sedimentary and structural evolution was mainly governed by the interaction of sea-level changes and plate tectonic (Africa and Iberia drift), and by the repeated reactivation of a pre-existing late-Hercynian fault pattern (Mattauer *et al.*, 1977; Proust *et al.* 1977; Laville, 1981; Jenny, 1983; Laville & Petit, 1984; Jacobshagen, 1992; Brede *et al.*, 1992; Laville & Piqué, 1992). The fault pattern is constituted by three main structural trends: the first being E-W, the second SW-NE and the third WNW-ESE (Laville, 1981; Brede, 1992). The E-W and the SW-NE trends are the most developed and form an "en échelon" pattern (Fig.2.2).

During Early and Middle Jurassic the Central High Atlas was still a subsident basin characterized by high sedimentation rate and tholeiitic to alkaline magmatism (Bertrand *et al.*, 1982; Beraâouz *et al.*, 1994). Radiometric ages measured on whole rocks and relative ages indicate that tholeiitic magmatism occured during the Early Jurassic (Hailwood & Mitchell, 1971; Westphal *et al.*, 1979; Sebai *et al.*, 1991), while alkaline magmatism occured later and lasted from the Middle Jurassic to the Early Cretaceous (Hailwood & Mitchell, 1971; Westphal *et al.*, 1979; Monbaron, 1980; Seufert, 1988).

The post-Triassic evolution

Given that the Mesozoic cover is exceptionally well exposed and post-Jurassic outcrops are rare, most evolutive models of the Central High Atlas are based on structural and stratigraphic investigations of the Jurassic sediments. According to Monbaron (1988) and Jacobshagen *et al.* (1988), the post-Triassic evolution of the Central High Atlas can be subdivised in two main tectonic phases (Fig.2.5): the first one occuring during the Early-Middle Jurassic and culminating during the Bajocian-Bathonian (the Jurassic phase); the second one starting during the Late Oligocene-Early Miocene (the Tertiary phase).

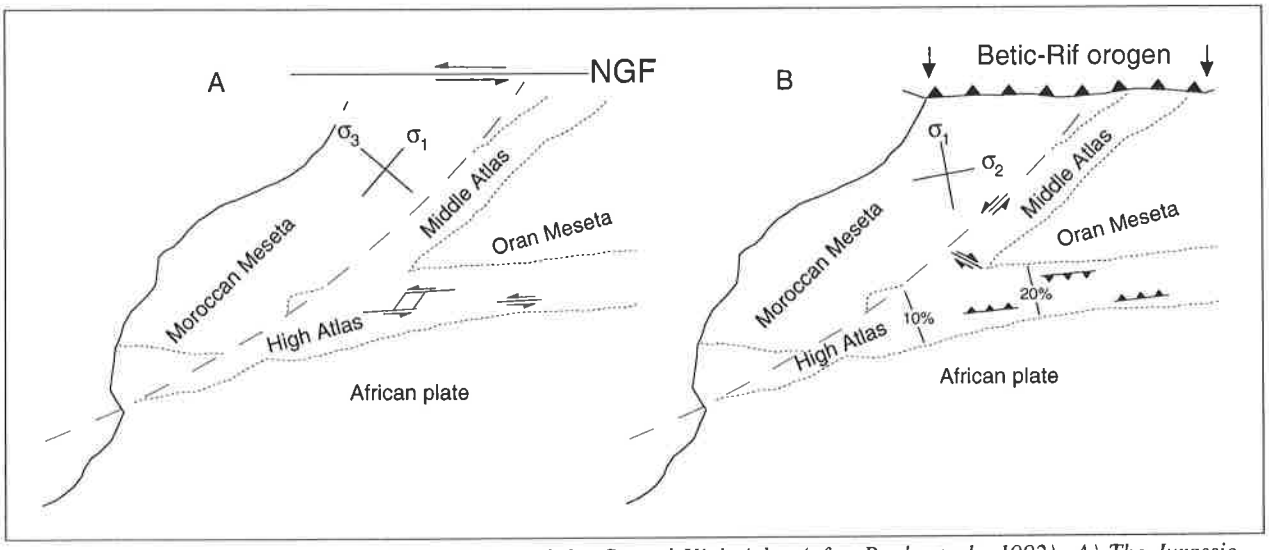

Fig.2.5 - The post-Triassic tectonic evolution of the Central High Atlas (after Brede et al., 1992). A) The Jurassic phase: from Middle Jurassic to Early Cretaceous the eastward drift of Africa caused sinistral wrenching along the Newfoundland-Gibraltar Fault (NGF) and a sinistral strike-slip system in the Central High Atlas. B) The Tertiary phase: from Late Eocene to Recent the convergence of Iberia and Africa plates (Betic-Rif orogen) caused the uplift of the belt and the shortening of the Mesozoic cover in the Central High Atlas. Eastward increasing shortening rates (10 to 20%) reflects a clockwise rotation of the Moroccan Meseta.

1) *The Jurassic phase* was dominated by a sinistral transtensional regime, originating block-faulting, horst-and-graben structures, and pull-apart basins (Michard *et al.*, 1975; Mattauer *et al.*, 1977; Laville, 1981; Seufert, 1988). Also the widespread formation of the "en échelon" anticlinal ridges intruded by magmatic rocks is attributed by most authors to this phase. Jurassic tectonic instability is evidenced by a variety of synsedimentary deformations (Studer & Du Dresnay, 1980; Monbaron, 1981; Jenny, 1984; Seufert, 1988; Ibouh *et al.*, 1996) and by a large number of stratigraphic discontinuities (Sadki, 1992). Mattauer *et al.* (1977), Laville (1978), Studer (1980) and Laville & Piqué (1992) pointed out that since the Late Jurassic-Early Cretaceous a transpressive régime progressively replaced the transtensional one. During the Early and Middle Jurassic sedimentation was essentially calcareous with dominant Toarcian to Bathonian marly limestones to marls deposition (Fig.2.4). During the Bajocian a coral-reef horizon discontinuously developed throughout the basin in response to the synsedimentary formation of ridges (Stanley, 1981; Studer, 1987). In the investigated area this thick and spectacular horizon, also known as the "Calcaire-Corniche", is widely exposed and forms the top of the highest mountains surrounding Jebel.

2) *The Tertiary phase* started during the Oligocene and was essentially characterized by a compressive regime in response to the Africa-Iberia collision (Froitzheim *et al.*, 1988, Jacobshagen *et al.*, 1988, Laville & Piqué, 1992; Giese & Jacobshagen, 1992). This phase is commonly associated to the uplift and shortening of the Central High Atlas (tectonic inversion). According to Jacobshagen (1988), the shortening of the sedimentary cover of the Central High Atlas does not exceed 20% and increases from west to east. Although main deformations are attributed to this phase, the scarcity of Cretaceous and Tertiary outcrops makes the post-Jurassic evolution of the Central High Atlas still largely unknown.

The Jurassic magmatism in the Central High Atlas

One of the most striking features of the Central High Atlas is the widespread presence of magmatic rocks intruding the Mesozoic sedimentary series. These massifs have elongated to polygonal to S-shapes (Figs.2.2 and 2.6), crop out in the core of E-W and SW-NE trending anticlinal ridges, and all have a similar internal organisation with leucocratic rocks, mostly syenites, associated with dominant gabbros. Some authors recognize a ring-shaped structure with gabbros surrouding syenites.

The Tassent, Tasraft, Tirrhist and Anemzi massifs have already been the object of some petrographic, mineralogical, geochemical and structural studies, all indicating a mildly alkalic to transitional nature of magmatic associations (Chèvremont, 1975; Brechbühler, 1984; Studer, 1987; Lhachmi, 1992; Zayane, 1992; Beraâouz &

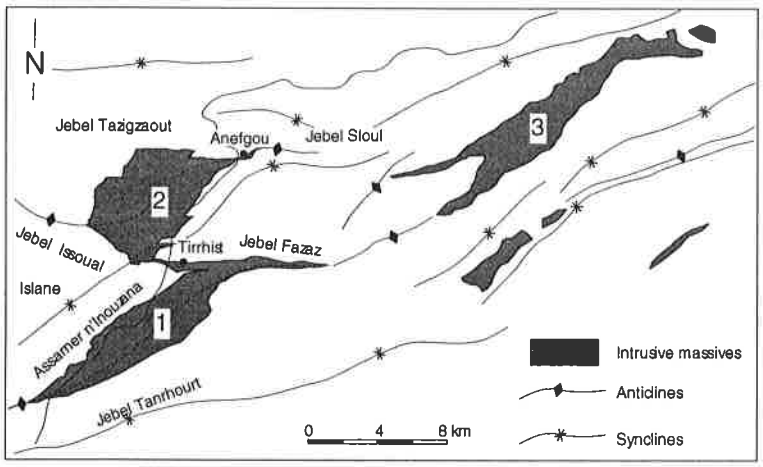

Fig.2.6 - Schematic map of the Tounfite-Tirrhist region (after Studer, 1987). Intrusive massifs crop out in the middle of Jurassic anticlines. 1 = Tirrhist Massif; 2 = Jebel Hayim Massif; 3 = Anemzi Massif.

Bonin, 1993; Beraâouz *et al.*, 1994). The Tirrhist Massif consists of two distinct parts: the northern one corresponds to the Jebel Hayim Massif (JHM is the Anefgou Massif in Studer's work; in this work, the name "Tirrhist Massif" is used only for the southern part).

The Jebel Hayim Massif (JHM) was firstly investigated by Caïa (1968) within a study concerning relationships between magmatic rocks and Pb-Zn-Sr mineralizations. Studer (1987) describes complete magmatic series ranging from olivine gabbros to quartz-bearing syenites in the intrusive massifs of the Tounfite-Tirrhist region (Jebel Hayim, Tirrhist and Anemzi Massifs). He also suggests the presence of a metasomatic event transforming many gabbros into "epidiorites" and interprets the scarcity of contact metamorphism around the massifs as the consequence of post-magmatic, vertical tectonic movements.

Lhachmi (1992) and Zayane (1992) put some constraints to the physical conditions of magma emplacement for some of the intrusive massifs. According to the former, magma differentiation occurred at low pressure (0.1 ± 0.05 GPa) from a slightly undersatured liquid of dioritic composition which evolved under rising P_{H_2O} and low f_{O_2} conditions. He suggests the occurrence of a early fractionation stage in a deeper magma chamber and a slightly enriched upper mantle origin. According to Zayane, magma chambers were situated at a depth of 10-15 km (0.3-0.4 GPa) and parental magmas were affected by crustal contamination.

More recently, Beraâouz & Bonin (1993) argue that, despite a continuous fractional crystallisation process, basic cumulates were not in equilibrium with an intermediate liquid, but with a less evolved melt. Finally, Beraâouz *et al.* (1994) attribute the origin of the mid-Jurassic alkaline magmatism to a small degree of partial melting of a LILE-enriched mantle, triggered by deep-seated fluids.

In conclusion, the basic petrographical and geochemical features of the Jurassic magmatism in the Central High Atlas are known, but many essential points still remain unsolved. In particular, we poorly know the mechanism and age of magma emplacement, the origin and evolution of magma, and the structural relationships between magmatism and deformation of the sedimentary cover.

- CHAPTER 3 -

Geological Setting and Field Relationships

The aim of this chapter is to present and discuss field data with special attention to structural and petrographic relationships between different families of magmatic rocks and between magmatic and sedimentary rocks. Geochronological data are also presented and a preliminary evolutive model of the investigated area will conclude the chapter (§ 3.5). A detailed outcrop map (scale 1:10.000, Appendix 6) of the intrusive massif was completed and a structural study was performed in order to investigate and interpret the structural evolution of the sedimentary sequences before, during and after magma emplacement. In the text, numbers and letters in brackets indicate outcrops coordinates on the map.

3.1 - Essential features of the Jebel Hayim Massif

As shown by the geological map and the cross-section (Figs.3.1 and 3.2), JHM is characterized by the following essential features:

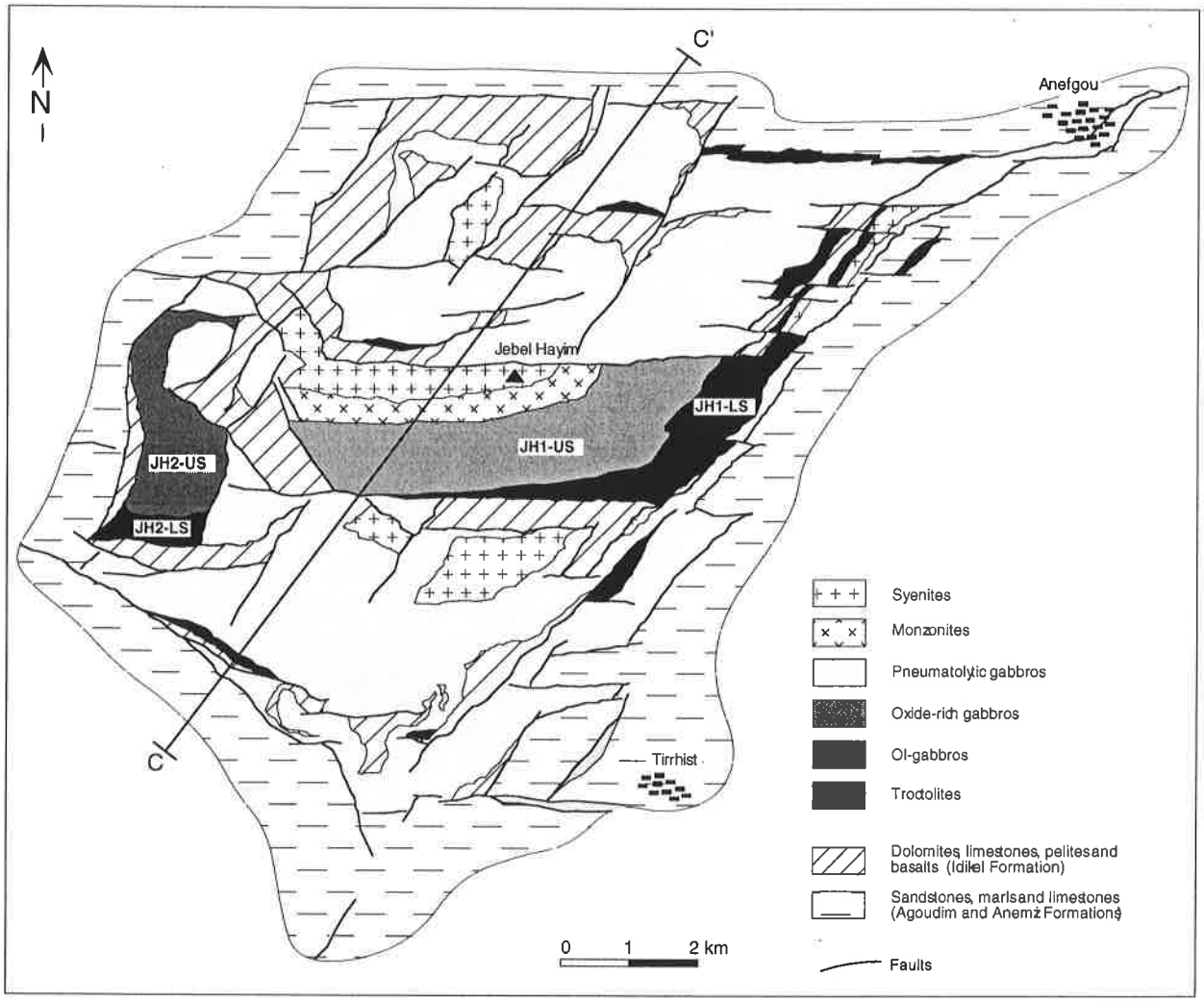

Fig.3.1 - Geological map of the Jebel Hayim Massif. C-C' is the cross-section in Fig.3.2

- JHM is polygonal in shape and delimited by tectonic contacts with country rock. Its eastern and western boundaries coincide with two SW-NE trending faults, the northern one with an E-W fault, and the southern one with a WNW-ESE fault. All faults are subvertical (>70°).

- JHM consists mostly of a variety of olivine gabbros and "metagabbros". All gabbros are intruded by monzonitic to syenitic dikes and megadikes, few decimetres to hundreds of metres thick. Basic dikes have also been observed intruding both gabbros and syenites.

- JHM is pervasively affected by the same fault pattern which defines its boundaries. Faults fragmented the original intrusion into several minor blocks, partially hiding primary relationships.

- large and deformed volcano-sedimentary bodies are scattered throughout JHM within gabbros. They approximately form a sixth of the whole massif surface and comprise limestones and dolomites discontinuously associated with red pelites and basalts. Their size ranges from few metres to few kilometres.

- the country rock consists mostly of a deformed sedimentary sequence comprising mid-Jurassic marls, marly limestones and limestones. The Bajocian coral-reef horizon (§ 2.1) is widely exposed and is an excellent marker horizon.

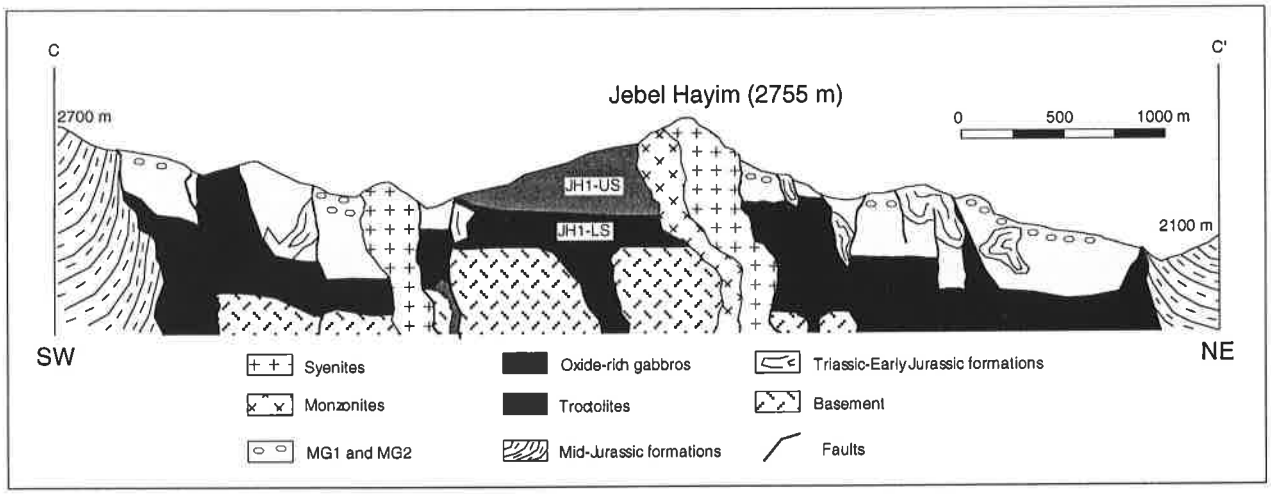

Fig.3.2 - SW-NE cross-section through the Jebel Hayim Massif.

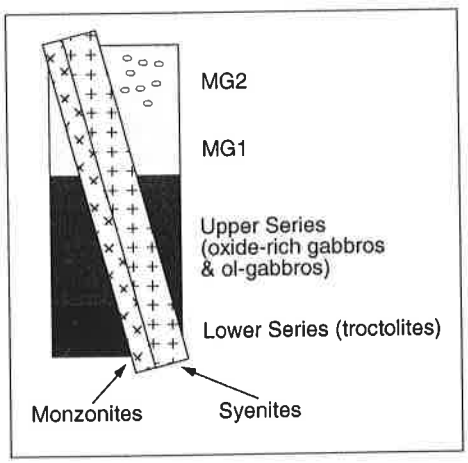

Fig.3.3 - Schematic primary relationships between different magmatic rocks forming JHM. The figure is dimensionless.

3.2 - The magmatic rocks

Five main groups of magmatic rocks have been found in JHM: 1) olivine gabbros, 2) "metagabbros", 3) monzonites, 4) syenites and 5) dolerites. Metagabbros is, for the moment, only a descriptive term with no genetic implication.

Olivine gabbros

Six kinds of olivine gabbros have been distinguished in the field on the basis of their modal composition:

- **troctolites** (olivine > 30% and pyroxene < 10% of the mode);

- **oxide-rich gabbros** (olivine <10%, Fe-Ti oxides> 5%);

- **ol-gabbros** (olivine < 30%, pyroxene > 10%);

- **leucogabbros** (plagioclase > 65%, olivine < 15%);

- **anorthosites** (plagioclase > 80%, olivine < 5%);

- **microgabbros** (plagioclase ± olivine ± pyroxene, fine to very fine grain-size)

Olivine gabbros are all biotite-bearing, unaltered (except those close to fractures and faults) and form two main complexes (JH1 and JH2), and several small scattered bodies.

JH1

JH1 is exposed in the southern and eastern side of Jebel Hayim, forming a 2 km long and 350 m thick continuous body mostly constituted of troctolites and oxide-rich gabbros. To the north, a composite syeno-monzonitic subvertical megadike cuts JH1, forming the sharp ridge of Jebel Hayim.

JH1 comprises a 100-150 m thick lower series (JH1-LS) made up of troctolites and overlain by a 200-250 m thick upper series (JH1-US), which is entirely made up of oxide-rich gabbros. Troctolites and oxide-rich gabbros are separated by a 3-5 m thick leucocratic layer (leucogabbros). JH1-LS is layered, and layering is due to the upward decrease in olivine content (modal layering); no layering has been macroscopically observed within JH1-US. Both troctolites and oxide-rich gabbros are medium to coarse-grained, dark and strongly affected by "onion-like" exfoliation processes, transforming outcrops into rounded isolated blocks. JH1-US gabbros are characterized by the presence of flow textures and of reddish alteration surfaces throughout the series.

Where visible, the contact between JH1-LS and JH1-US is sub-horizontal and sharp. No evidence of tectonic movement has been observed at the contact and, as a consequence, the contact is assumed as being primary and magmatic in origin. The lower contact of JH1-LS and the contact between JH1-US and Jebel Hayim megadike are not exposed. The contact between JH1 and the volcano-sedimentary bodies is characterized by a 2 to 10 metres thick level of white to violet tectonic breccias (§ 3.3) and by a rapid and gradual transformation from medium-grained troctolites to very fine-grained, doleritic, olivine-free gabbros (microgabbros) in the last metres moving toward the contact. This textural change allows us to consider microgabbros as representing the chilled margin which formed at the contact with the volcano-sedimentary body.

JH2

JH2 crops out at the SW extremity of the massif and it is mostly constituted by troctolites, ol-gabbros and anorthosites. As in the case of JH1, JH2 comprises two superposed series: a 30-50 m thick lower series (JH2-LS) and a 80-120 m thick upper series (JH2-US). The lower contact of JH2-LS is not exposed and the contact between lower and upper series is sharp, sub-horizontal and magmatic in origin. Troctolites form JH2-LS, ol-gabbros form JH2-US and anorthosites form interstratified, plastically deformed centimetric layers within ol-gabbros. No modal layering has been observed in troctolites, also because of the scarcity of outcrops and the limited thickness of the

exposed series. On the contrary, the upper series is characterized by modal layering with a steady decrease of the olivine content from the lowermost to the uppermost ol-gabbros.

The contact between JH2 and surrounding sedimentary rocks is clearly tectonic and it is characterized by the presence of the same white to violet tectonic breccias as in JH1. Only to the north (D/E-1/2), ol-gabbros and metagabbros have a primary contact, with metagabbros overlying JH2-US. Troctolites and ol-gabbros are medium to coarse-grained and they gradually pass to fine and very fine-grained olivine-free gabbros (microgabbros) moving toward the contact with sedimentary rocks (chilled margin).

Olivine gabbros age

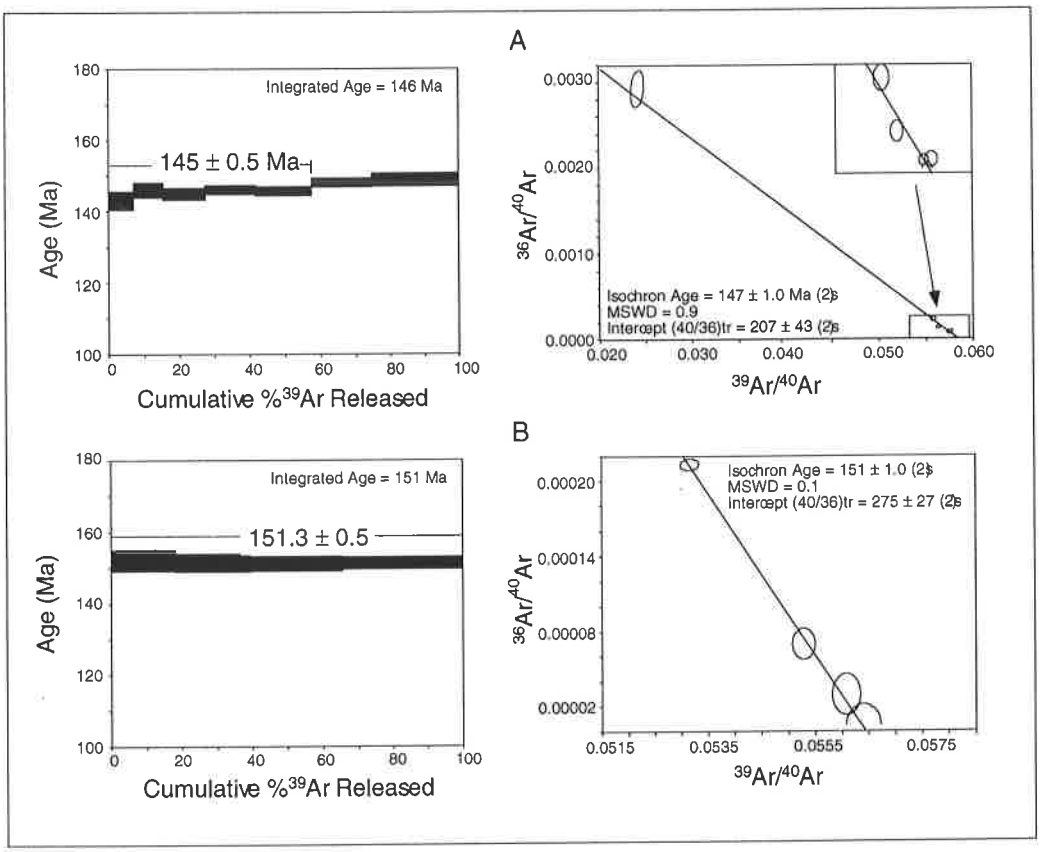

Fig.3.4 - $^{39}Ar/^{40}Ar$ plateaux and isochrones for A) JH1 troctolites, and B) JH2 ol-gabbros. Analyses were carried out on separated biotites.

Two $^{40}Ar/^{39}Ar$ age determinations were carried out on separated biotite from JH1-LS troctolites and from JH2-US ol-gabbros. Isochrons and plateaux are presented in Fig.3.4. Ol-gabbros forming JH2-US are 151 Ma old and troctolites forming JH1-LS are 145 Ma (Oxfordian, Upper Jurassic). Then, on the basis of these new results, JHM magmatism is younger than the country rock (the Agoudim Formation), which is Toarcian to Bajocian in age, and a synsedimentary emplacement of the intrusion within the Agoudim Formation must be excluded.

Small bodies

Troctolites also form several small bodies scattered throughout the massif, overlain by metagabbros or in tectonic contact with volcano-sedimentary bodies and country rock. Their thickness does not exceed 30 m, but their lateral extension can reach hundreds of metres. The most extended ones have been observed close and parallel to JHM boundary, suggesting the presence of a troctolitic marginal zone following JHM boundary. Troctolites forming small bodies have the same textural and modal features as troctolites forming JH1 and JH2 and, as well as in the two main complexes, grain-size gradually decreases moving toward the contact with sedimentary rocks.

"Metagabbros"

The largest portion of the JHM surface consists of light green, medium to coarse-grained to pegmatitic rocks characterized by the presence of non-magmatic parageneses and texture partially or totally replacing the original ones. As already written, metagabbros is only a descriptive term and has no genetic implication; their origin will be discussed in the next chapter (§ 4.4). Similar rocks are widespread in other intrusive massifs of the Central High Atlas and are named "diorites vertes" (Caïa, 1968), "diorites à amphiboles" and "diorites albitisées" (Chevremont, 1975), "épidiorites" (Studer, 1987; Zayane, 1992, Lhachmi, 1992), "monzodiorites" (Zayane, 1992; Lhachmi, 1992). According to these authors, they are interpreted as the result of hydrothermal transformations, of metasomatic reactions triggered by the emplacement of syenitic dikes or of pneumatolytic processes. In JHM two main groups of metagabbros have been distinguished (MG1 and MG2), on the basis of the amount of the non-magmatic phases.

MG1 metagabbros
They form thick bodies (up to 200 m) and are exposed along the Tardagal left tributary stream flowing down from Jebel Hayim, at the NE extremity of the massif, on the E-W ridge immediately at the north of Jebel Hayim and on the eastern side of Jebel Ouakloum. MG1 metagabbros are represented by olivine gabbros with well preserved primary texture and paragenesis. Non-magmatic paragenesis mostly consists of green amphibole, epidote, chlorite, and prehnite. In the field these rocks look very similar to olivine gabbros, except for their lighter colour and the scattered presence of green to yellow centimetric clusters made up of green amphibole and epidote.

MG2 metagabbros
They form discontinuous bodies not exceeding a few dozen of metres in thickness and exposed mostly in the northern part of the massif, in the upper part of Taouarrhist Valley and in the SE side of Jebel Ouakloum. MG2 gathers all metagabbros whose primary textures and paragenesis have been widely overprinted by secondary transformations. In the most extreme cases magmatic texture is completely absent and only the gradual and continuous passage from MG1 allows identification. MG2 metagabbros are easily distinguishable in the field thanks to their light green colour and the widespread presence of leucocratic pegmatitic ocelli, a few centimetres to a few decimetres in diameter, essentially made up of alkali-feldspar. Secondary phases are the same as those of MG1 metagabbros with dominant green amphibole and epidote.

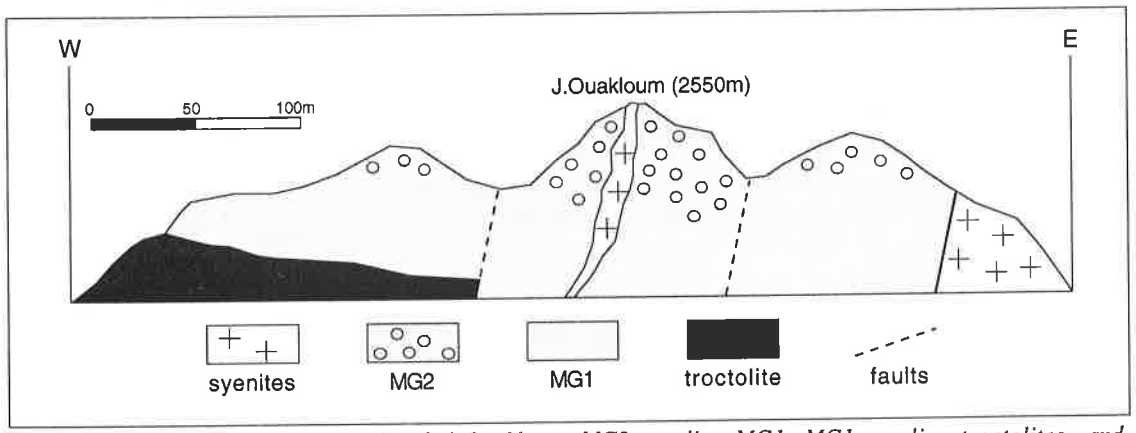

Fig.3.5 - W-E cross-section through Jebel Ouakloum. MG2 overlies MG1, MG1 overlies troctolites, and syenites cut MG1 and MG2.

Although MG1 and MG2 are widespread throughout the massif, field relationships between them and olivine gabbros are often lacking or ambiguous, due to the large presence of faults. In the north-eastern part of the massif (B/C-10/11) and at the north of Jebel Hayim (D/E-4/5) small bodies made up of troctolites are overlain by a thick (200 and 50 metres, respectively) and homogeneous bodies formed by MG1 metagabbros which are similar to JH2-US ol-gabbros. In the western extremity of the Jebel Ouakloum ridge (G/H-2/3), troctolites are overlain by metagabbros belonging to MG1 and having textural and modal features similar to those observed in leucogabbros and oxide-rich gabbros. MG1 metagabbros are in turn overlain by light coloured pegmatitic metagabbros belonging to MG2 and forming the top of the ridge (Fig.3.5).

Along the track linking Anefgou to Tirrhist, 400m south of "le Poste" (G/H-6/7), a 150 m long continuous outcrop is made up of weakly transformed oxide-rich gabbros (MG1) gradually changing into very coarse-grained MG2 metagabbros with abundant feldspatic ocelli (10 cm to 1 m in diameter). MG2 metagabbros disappear in the last ten metres of the outcrop where grain-size gradually and rapidly decreases and a very fine-grained, vesicular and strongly altered doleritic gabbro appears. North of JH2 (D/E-1/2), MG1 overlies JH2-US. The transition from ol-gabbros to metagabbros occurs in 2-3 m. Moving upwards, the extent of transformation increases. Finally, to the north (B/C-7/8) a small body made up of troctolites is overlain by MG2.

In conclusion, everywhere clear primary relationships were observed, it was found that MG2 overlies MG1 and MG1 overlies olivine gabbros; in a few cases MG2 directly overlies olivine gabbros.

Syenites and monzonites

Syenites and monzonites form vertical to subvertical megadikes intruding olivine gabbros and metagabbros, and building most main ridges rising within JHM. Megadikes distribution follows E-W, SSW-NNE and WNW-ESE distinct trends, paralleling JHM's boundary and faults. Megadikes thickness ranges from 30 m to 1 km. Minor dikes thickness does not exceed 3 metres.

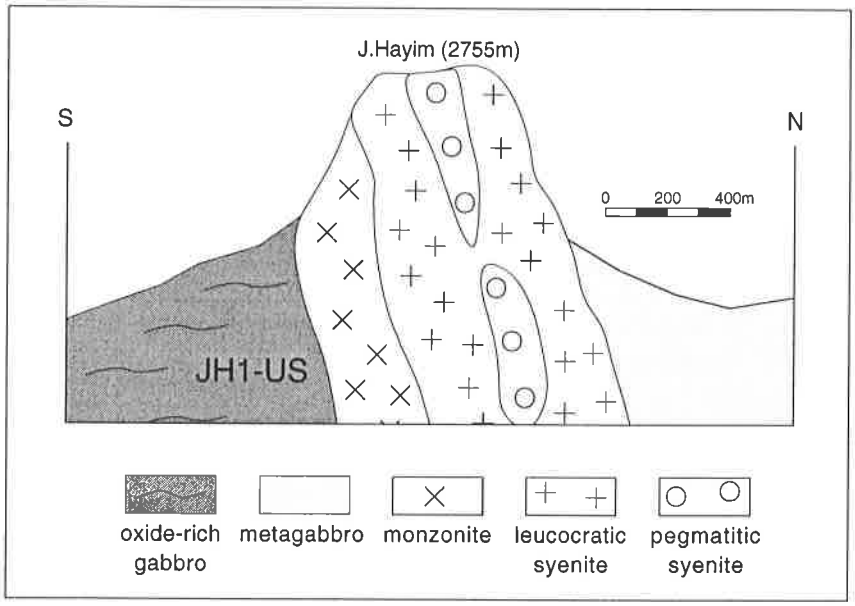

Fig.3.6 - S-N cross-section through Jebel Hayim.

Two adjacent megadikes make up the Jebel Hayim ridge (Fig.3.6). Moving southward, the first one consists of leucocratic and pegmatitic syenites and the second one of monzonites. Leucocratic syenites also form other megadikes while mesocratic amphibole-bearing syenites have been found at the western extremity of Jebel Hayim.

When syenites are in contact with volcano-sedimentary bodies, contacts are tectonic. When syenites are in contact with gabbros, contacts are either tectonic or intrusive. The contact between the Jebel Ouakloum megadike and metagabbros is perfectly exposed in the Oued Taouarrhist gorge, close to the track linking Anefgou and Tirrhist, approximately 150 m south of the Poste (F/G-6/7). Here, the contact is between syenites and MG2, it is sharp, subvertical (N40/70), and accompanied by a complex system of leucocratic dikes, 2-3 metres thick, crossing the gabbros. The presence of thin dikes characterises all contacts between megadikes and gabbros, and also most contacts between megadikes and volcano-sedimentary bodies. The contact between syenites and monzonites can be observed at the easternmost and close to the westernmost extremities of the Jebel Hayim megadike (D/E-6/7 and D/E-3/4). In the first case (Fig.3.6) the contact is sharp and straight, and is characterized by the abrupt grain-size decrease and by appearance of flow texture and lamination in syenites. In the second one the contact is lobate and there is a transitional zone in which syenites penetrate monzonites, forming 20-60 cm large ocelli within monzonites. The former is interpreted as being a « cold contact » with syenites intruding monzonites while the latter is interpreted as a « hot contact » with simultaneous emplacement of syenites and monzonites.

Dolerites and basalts

Dolerites and basalts form sills and dikes and have been found scattered throughout JHM along contacts between olivine gabbros and metagabbros, between gabbros and volcano-sedimentary bodies, between gabbros and syenites,

between syenites and volcano-sedimentary bodies, and between these lasts and the country rock. Some others cut syenites. Texture ranges from doleritic to porphyric to mylonitic.

Close to the upper exit of Oued Taouarrhist gorge (F/G-6/7), a strongly altered basic dike marks the boundary between the Jebel Ouakloum syenitic megadike and a sedimentary body. The contact is irregular and lobate, and the basalt pervasively penetrates the syenite forming isolated bubbles. The outermost part of the dike and of the bubbles are characterized by decreasing grain-size (fine to very-fine) and by the appearance of large scattered feldspar phenocrysts. A 30 m thick basic dike formed by metagabbros crops out at the west of Tirrhist (I/J-6/7), outside JHM and it is surrounded by a 3 m thick contact aureole. Along the western part of the northern JHM boundary (A/B-4/5/6/7) a dikes having mylonitic texture follows the contact and extends eastward out of the massif.

3.3 - The volcano-sedimentary bodies

One of the most striking features of JHM is the widespread presence throughout the massif of large deformed volcano-sedimentary bodies mostly made up of carbonates (white to yellow dolomites and grey to black limestones) and pink to violet pelites. Strongly altered basalts are discontinuously associated to pelites.

Their age

No fossils and other age markers have been found in volcano-sedimentary bodies and the only way to determine their age was to compare their lithology and stratigraphy to those of other similar sequences already described and dated elsewhere in the Central High Atlas. According to Studer (1987), the age of volcano-sedimentary bodies ranges from Late Triassic to Early Liassic, mostly belonging to the "Dolomies et calcaires massifs d'Idikel" Formation, i.e. the basal formation of the Central High Atlas Mesozoic cover (Fig.2.4). Studer (1987) describes these formation as consisting of continental violet pelites strictly associated to strongly altered basalts, and overlain by more and more massive dolomites which are, in turn, replaced by biodetrital limestones.

Throughout the Central High Atlas similar lithological associations have been recognized and dated, and always they have been referred to the Late Triassic and Early Jurassic (Mattis, 1977; Evans et al., 1977; Burgess & Lee, 1978; Manspeizer *et al.*, 1978; Heitzmann, 1987; Seufert, 1988). In JHM the same facies association described by Studer (1987) was found; as a consequence, volcano-sedimentary bodies are assumed to be Late Triassic to Early Liassic. Though one must be aware of the limits of this kind of age determination, which bases itself on facies similarity rather than on paleontological data, this age determination is strongly believed to be consistent.

Their relationships with magmatic rocks: the white breccias

Volcano-sedimentary bodies are strongly deformed and in tectonic contact with the magmatic rocks (gabbros and syenites). Contacts are always characterized by the presence of levels of tectonic breccias, named « white breccias » in this work, ranging from 50 cm to 10 m in thickness and up to 2 km in length. Faults are mostly vertical, but horizontal contacts have also been observed. White breccias are unconsolidated, polygenic, very poorly sorted and matrix supported. Matrix is loose, fine to very fine-grained and mainly composed either by carbonate (white/yellow breccias) or by pelitic (pink/violet breccias) material. Clasts are angular, 1 to 50 cm in diameter, and their nature is strictly related to the nature of wall rocks (on one hand gabbros, on the other one carbonates and pelites). White breccias can be easily observed along the path going from the Poste to Tizi Bouroujdemt (F/G-5/6), where the path skirts a group of shepherds' houses. Here, JH1 troctolites are in contact with a volcano-sedimentary body, and a 5-10 m thick level of white breccias containing clasts of troctolites, microgabbros, basalts, pelites, dolomites and limestones follows the contact. The outcrop belongs to one of the most important and continuous fault, which crosses JHM from east to west.

The loose nature of the white breccias is a peculiar feature of almost every contact between gabbros and volcano-sedimentary bodies. On the contrary, white breccias are only sporadically present along the tectonic contacts between gabbros and country rock. For instance, the gabbros/marls contact which is magnificently exposed along Oued Tardagal Valley (E/F-9/10), approximately midway between the Poste and Anefgou, has a 5 m thick level of consolidated breccias with clasts of gabbros and marls, and no loose matrix of sedimentary origin has been observed.

Tectonics within the magma chamber

Walking through JHM, it is easy to remark that most shepherds' houses are aligned along faults and that their roofs are covered by the same loose material forming white breccias. Berbers explain that, when water is added, this material consolidates and sets, becoming efficiently waterproof. Consequently, it constitutes an excellent material for roof covering. Inspired by shepherds' wisdom, the process originating these peculiar material was found comparable to the process commonly used to form synthetic hydraulic lime (Hermann, 1995). In fact, hydraulic lime is made from calcareous marl (65-75% of limestone) which is firstly crushed to obtain a 30-50 mm grain size and then "cooked" at 900-1000°C. The result of this double operation is called "clinker". In the next step water is added to the clinker in order to slake free lime favouring the transformation of CaO into $Ca(OH)_2$. A further powdering ends the process and makes the hydraulic lime ready to be used. Finally, when water is added again, lime consolidates and cement forms.

A similar but natural and incomplete process can be supposed to be at the origin of the white breccias. In JHM matter is supplied by limestones, dolomites and pelites forming volcano-sedimentary bodies, whereas heating and crushing are supplied respectively by the emplacement of the hot magma (temperatures of 900-1000°C are consistent with a cooling basaltic magma), and by repeated tectonic movements along contacts. Water contained in volcano-sedimentary bodies and circulating along fractures allowed free lime to slake. The final powdering is the result of later tectonic movements. If this comparison is valid it can be assumed as evidence for tectonic movements within the magma chamber. In particular, since the first crushing must be made before heating, tectonic movements already occurred before magma emplacement and cooling. The presence of gabbros clasts indicates that tectonic movements were still active after gabbros solidification.

Since the same loose breccias have also been discontinuously found at the contact between gabbros and country rock, the same kind of process is believed to have been active along JHM boundary. On the contrary, volcano-sedimentary bodies/country rock contacts are not characerized by th presence of white breccias. This different feature indicates a different genetic process; in particular, it is likely that neither country rock marls nor limestones reached a sufficiently high temperature. It follows that Mid-Jurassic sequences were not directly affected by magma intrusion and that crushing was not followed by heating.

3.4 - The country rock

JHM country rock is essentially represented by marls and marly limestones which, according to Studer (1987), belong to the "Marnes et Marno-calcaires d'Agoudim" Formation of Toarcian to Bajocian age (Fig.2.4). The Agoudim Formation is mainly characterized by monotonous stratification where a marly lower part and a calcareous upper part can be roughly distinguished. Age determination of the Agoudim Formation is based on ammonite zonation (Dubar & Mouterde, 1978; Studer, 1987; Sadki *et al.*, 1986; Sadki *et al.*, 1989; Sadki, 1992). The Agoudim Formation is supposed to be part of the Mesozoic cover representing the filling of the Central High Atlas trough, which formed during Permo-Triassic times (§ 2.1).

A discontinuous level of massif coralliferous oolithic limestones constitutes the ridges of the highest mountains surrounding JHM (Jebel Fazaz, 3023 m; Jebel Issoual, 2922 m; Afoud n'Aoujil, 2754 m; Assamer n'Inouzana, 2914 m). It belongs to the upper part of the Agoudim Formation and represents a coral-reef horizon; it is known as the "Calcaires-Corniche" horizon in the literature. It is easily recognisable due to its yellowish colour and to its remarkable thickness (up to 400 m) contrasting with the thinness of over- and underlying marls and marly limestones strata. Its thickness is strongly variable around JHM and it is the largest at Jebel Fazaz.

Red and green calcareous sandstones and marls, belonging to the "Formation detritique rouge et verte d'Anemzi" (Studer, 1987; Fig.2.4) crop out discontinuously along the external contacts of JHM. The Anemzi Formation contains the youngest Jurassic sediments (Bathonian) exposed in the Tounfite-Tirrhist region (Studer, 1987) and is characterized by a rhythmical marl-sandstone thin stratification. These sediments are typical of intertidal to supratidal deposition environments and mark the end of the subsidence. The largest outcrop of Bathonian sediments has been found at west of JHM where strongly deformed marls are associated to a vertical disconnected block of the « Calcaire-Corniche » horizon (Afoud n'Aoujil).

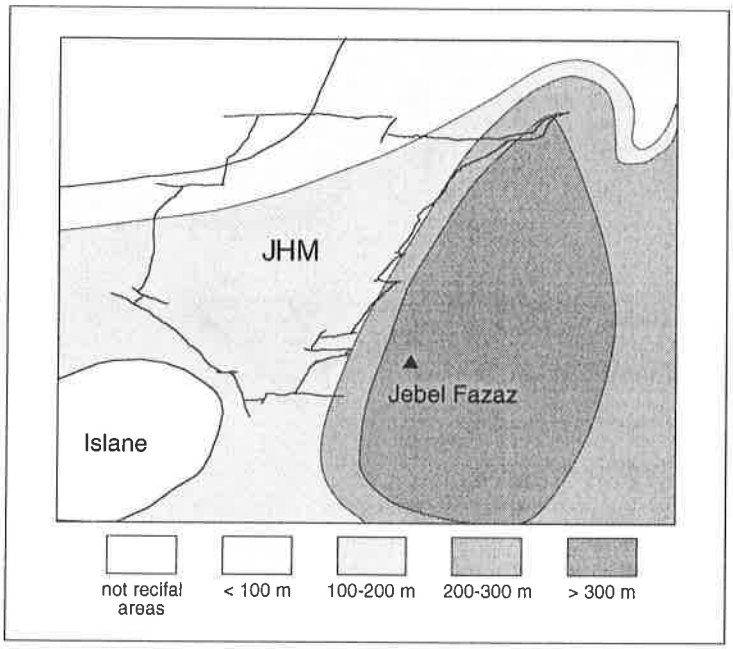

Fig.3.7 - Isopachous map of the coral-reef horizon around JHM (after Suder, 1987). The coral-reef horizon is the thickest around Jebel Fazaz where the Anefgou and the Tirrhist anticlines intercept, and the thinnest at Islane, where the two anticlines are separated by the Islane syncline.

Anticlinal ridges

JHM is located in the core of an E-W trending anticlinal ridge, the Anefgou anticline, close to the intersection with a SW-NE anticlinal ridge, the Tirrhist Anticline (Fig.2.6). Like the Anefgou anticline, the Tirrhist anticline is characterized by the presence of magmatic rocks in its core (the Tirrhist Massif). A wide and flat syncline separates the two ridges (the Islane Syncline).

According to previous structural and stratigraphic works (§ 2.1), ridges are interpreted as the result of local compressional regimes formed within a regional transtensional regime. The formation of anticlinal ridges created topographic highs, on the top of the "Calcaire-Corniches" horizon formed in response to sea-level changes. To the east of JHM (Jebel Fazaz), where Anefgou and Tirrhist anticline intersect, the "Calcaires-Corniches" horizon has its largest thickness (Fig. 3.7).

Although ridges were affected by post-Bajocian deformations, evidence of anticlinal structure is all around JHM: Jebel Tazigzaout is characterized by north-verging strata and it forms the northern limb of the Anefgou anticline; Jebel Issoual is characterized by south-western-verging strata and it forms the southern limb of the Anefgou anticline; Islane Plateau is characterized by roughly horizontal strata and it forms the Islane Syncline; Assamer n'Inouzana is characterized by north-eastern-verging strata and it forms the north-western limb of the Tirrhist anticline; finally, Jebel Tanrhourt is characterized by south-eastern-verging strata and it forms the south-eastern limb of the Tirrhist anticline.

The anticline-syncline system is strongly deformed around the Tizi Islane area (Fig.3.7), but moving away from the investigated area it extends undeformed. This clearly indicates that ridges were already formed when magmatic rocks intruded the Mesozoic cover and that the deformation of the anticline-syncline sytsem was limited to the volume intruded by magmatic rocks.

Folds and faults

Folds and faults strongly affect the Anefgou and Tirrhist anticlinal system, and deformations are mostly concentrated in a narrow zone comprised within the eastern end of Jebel Issoual, the north-eastern side of Assamer n'Inouzana and the western side of Jebel Fazaz (the Tizi Islane area), that is to say where the two convergent anticlines get close (Figs.3.7 and 3.8) and where the "Calcaire-Corniche" horizon is the thickest. Since post-anticlines deformation also affected the Calcaire-Corniche horizon and overlying sediments, folds are attributed to a post-Bathonian phase.

Here, deformations are strictly associated to four convergent vertical faults: the first fault (α) being E-W trending; the second one (β) WNW-ESE trending; the third and the forth ones (χ and δ) SW-NE trending. α coincides with the northern boundary of Tirrhist Massif and, in part, with the southern border of JHM; β coincides with the SW boundary of JHM and it extends to the west, besides JHM; χ coincides with the eastern boundary of JHM; δ cross the NW limb of the Tirrhist anticline and parallels the western boundary of the Tirrhist Massif. The four above-mentioned faults fragment the investigated area in four main blocks (Fig. 3.8), two of them (the north-western one

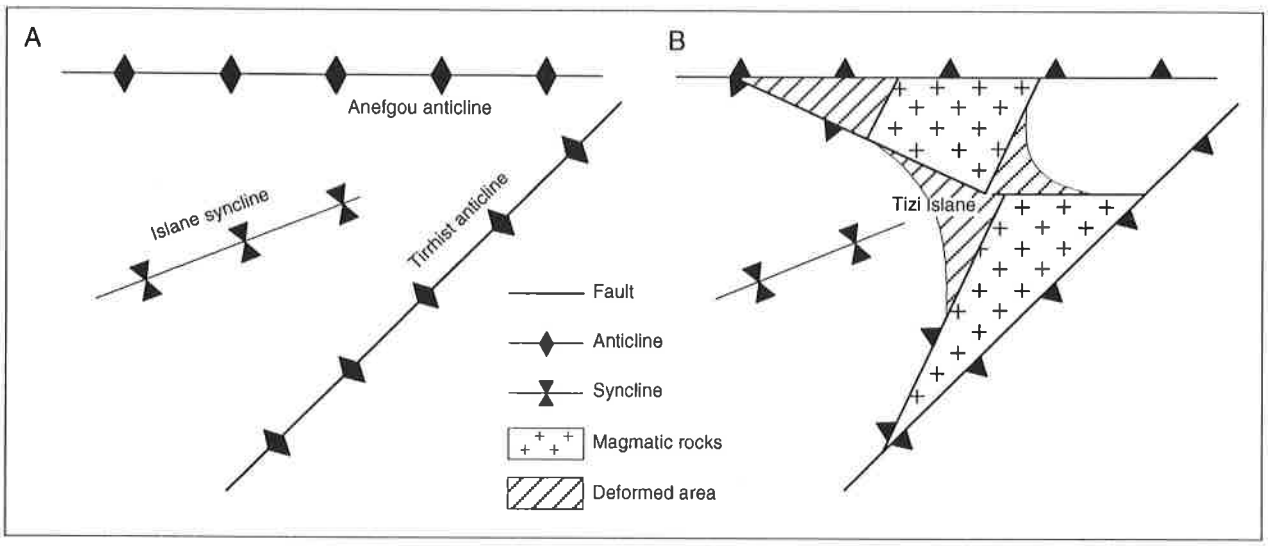

Fig.3.8 - Anticline, syncline and fault distribution around JHM in the Upper Jurassic: A) before magma emplacement and B) after magma emplacement. The magmatic rocks and the deformed area are situated at the intersection of two anticlines.

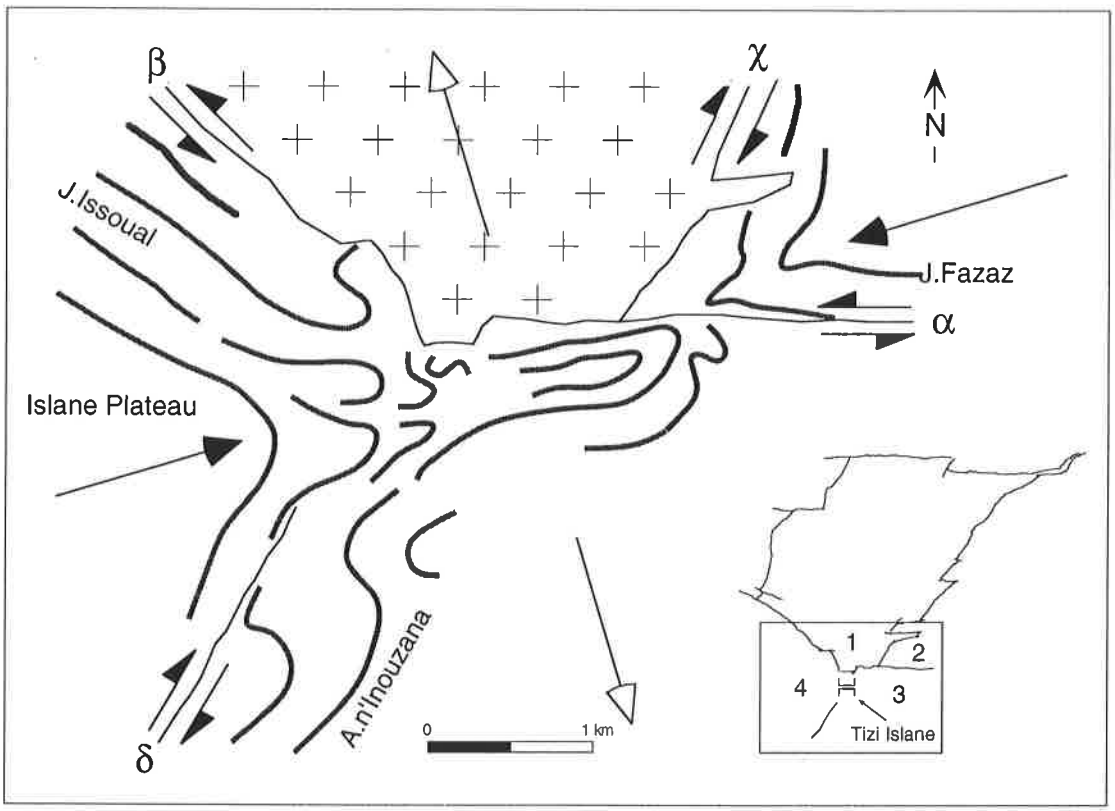

Fig.3.9 - Country rock deformation around Tizi Islane. In this simplified map the axial planes of drag folds are shown as thick grey lines and related folds as black lines. Movement along α and β was sinistral, while movement along χ and δ was dextral. Numbers in the little square indicate the four blocks formed by the four vertical faults. Compression affected blocks 2 and 4, while extension affected blocks 1 and 3.

and the south-eastern one) characterized by the presence of magmatic rocks, and the other two by the presence of deformed sedimentary sequences.

Deformations are mostly represented by asymmetrical folds, metric to kilometric in size, and having deformed and steeply inclined axial planes discordant to associated faults. Deformations associated to δ tend to be reduced and disappear at the same time than fault 2 km SW from Tizi Islane, indicating that folding was the consequence of faulting. As well, deformation associated to the other faults tend to be reduced, moving away from Tizi Islane. Then, on the basis of folds geometry and their relationships with α, β, χ and δ, deformations are interpreted as being the results of the horizontal movement of α, β, χ and δ (drag folds).

Assamer n'Inouzana represents the best exposed drag fold. Here, the Calcaire-Corniche horizon is repeatedly folded and the axial plane rotates from NE to EW (Fig.3.9) moving from SW to NE. At 200 m south to the confluence of Oued Tardagal and Oued Tirrhist (J-6/7), the core of a synform drag fold is exposed, and the synform widens westward and disappears eastward. Movement was sinistral along α and dextral along δ. Deformation is attributed to a contemporaneous movement along α and δ. At a few dozen of meters east of Tizi Islane, deformation is pervasive and mostly characterized by disconnected, randomly arranged, metric to decametric folds, which are interpreted as the result of a vigorous stretching of the hinge zone of the Islane syncline. In particular, stretching was caused by the contemporaneous horizontal movement of α, β and χ. Movement was sinistral along α and β, and dextral along χ. Jebel Fazaz also is a drag fold. It is constituted by a vertical limb paralleling α and by a roughly S-N trending limb discordant to χ. The fold hinge is south-westward stretched, supporting a contemporaneous movement along α and χ. Movement was sinistral for α and dextral for χ. Same folding and same hinge stretching has been observed to a smaller scale at the foot of Jebel Fazaz, west of Tirrhist. A further evidence of drag fold is observed at the south-eastern side of Jebel Issoual; here deformation is attributed to a sinistral movement along β. Also, the strongly deformed red marls belonging to the Anemzi Formation and cropping out at the west of JHM indicate horizontal movement, but outcrop conditions do not allow us to reconstruct fault movements in the zone.

3.5 - Conclusions

JHM consists mainly of two distinct gabbroic layered complexes (JH1 and JH2) cross-cut by syenitic and monzonitic dikes, and includes a large number of roof pendants (a few meters to kilometres in dimension), consisting of limestones, dolomites, red pelites and basalts. According to facies similarities with other volcano-sedimentary sequences of the Central High Atlas, pendants are attributed to Late Triassic to Early Jurassic and belong to the basal formation of the Central High Atlas Mesozoic cover. New $^{39}Ar/^{40}Ar$ radiogenic data on biotite allow us to fix the cooling age of JHM gabbros between 145 and 151 Ma (Oxfordian). In both JH1 and JH2, a lower series (JH1-LS and JH2-LS) consisting of troctolites and an upper series (JH1-US and JH2-US) consisting of oxide-rich gabbros and ol-gabbros may be distinguished. The two complexes are overlain by gabbros having medium-grained to pegmatitic textures, widespread leucocratic ocelli, and low-temperature paragenesis partially replacing primary mineral assemblages. These rocks are interpreted as the result of pneumatolytic processes occurring in the uppermost part of the magma chamber during late-stage crystallisation.

The country-rock is a deformed Middle Jurassic (Bajocian to Bathonian) carbonate sequence which is in tectonic contact with JHM gabbros. No metamorphism has been observed in the contact zone. Folds deform two pre-existing E-W and SW-NE trending anticlines and are strictly associated with a complex system of faults which are interpreted as conjugate Riedel shears in a E-W trending sinistral strike-slip régime. Three tectonic phases can be distinguished from Middle to Upper Jurassic

Anticline formation
As previously indicated (§ 3.4), JHM is located in the core of a E-W trending anticlinal ridge (the Anefgou anticline) which is separated by a wide and flat syncline (the Islane syncline) from a SW-NE trending anticline (the Tirrhist anticline). These anticlines are interpreted as the result of a mild synsedimentary tectonic phase occurring during the Middle Jurassic (§ 2.1), culminating in the Bajocian with the formation of the coral-reef horizon.

As shown by field investigation, anticlines are faulted and deformed, and limbs diverge where magmatic rocks are exposed within the sedimentary cover (anticline break). On the contrary, where magmatic rocks disappear, limbs

converge, anticlines reconstitute and extend undeformed until other magmatic rocks crop out. This evidence, when considered together with the supposed anticline formation age (Dogger) and the measured gabbros age (Malm), clearly indicates that anticlinal formed before magma emplacement. The coincidence between the axial trace of anticlines and vertical faults which caused anticline break indicates that pre-existing faults are also at the origin of the anticline formation.

Magma emplacement

Drag folds pervasively deform JHM country rock in the Tizi Islane area, but rapidly disappear moving away from the intrusive massif (Fig.3.8). By consequence, horizontal movements originating drag folds (§ 3.4) are considered as being intimately associated to magma emplacement.

According to kinematics laws, a variety of shear fractures and faults are often found associated with strike-slip zones (Fig.3.10). In particular, subsidiary shear fractures, known as Riedel shears (R shears), develop at a small angle (<20°) to the main fault with an "echelon" distribution. R shears are synthetic to the main fault. Along with R shears, R1 and P shears may develop. R1 are anthitetic shear fractures that are oriented at high angles (>70°) to the main fault whereas P shears, as well as R shears, are synthetic and symmetrically oriented with respect to the main fault from the orientation of the R shears. In a sinistral strike-slip zone, R and P are sinistral, and R1 is dextral.

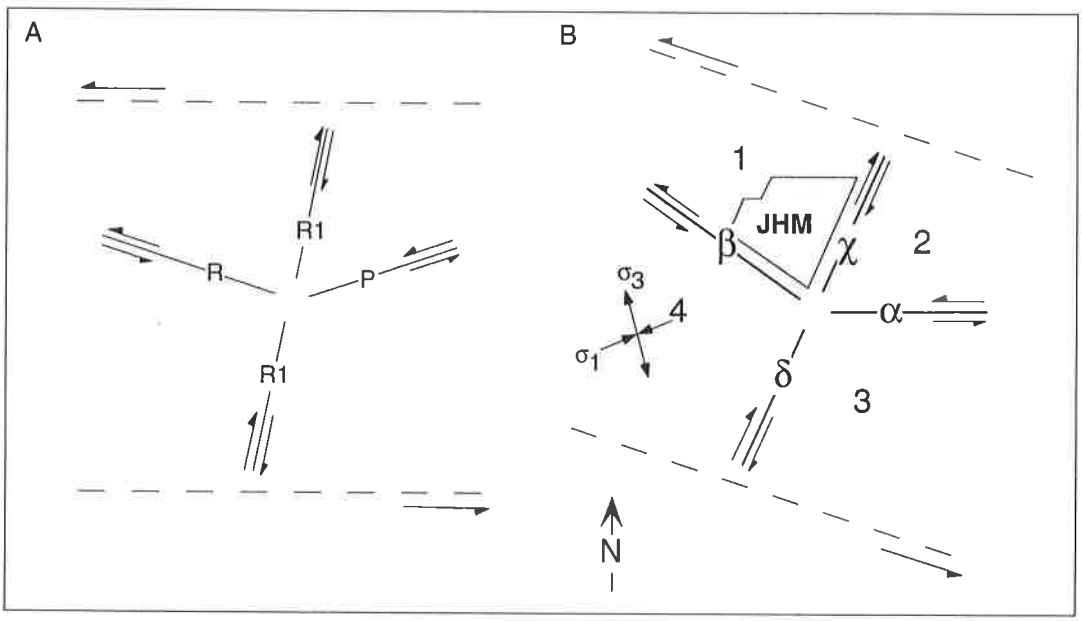

Fig.3.10 - Shear fracture distribution in A) a sinistral strike-slip zone and B) in JHM. A N110° sinistral transtensional régime can explain distribution and senses of shear of α, β, χ and δ.

The four faults observed in the Tizi Islane area draw a similar pattern (Fig.3.10). The E-W and the WNW-ESE trending faults (α and β) have both a sinistral sense of shear and the angle formed by their prolongation is roughly 30°, so they respectively correspond to R and P shear fractures. On the contrary, the two SW-NE trending faults (χ and δ) are dextral anthitetic faults and correspond to R1 shear fractures. As a consequence, horizontal movements in JHM were due to a sinistral, N15° trending transtensional regime.

The transtensional regime in the presence of a pre-existing fault pattern drove blocks movement, leading to identification of both extensional zones and compressional zones (Fig.3.8) according to the senses of shear of α, β, χ and δ. Extension affected the north-western and the south-eastern blocks (1 and 3 in Fig.3.9), while compression affected the south-western and the north-eastern blocks (2 and 4). Where extension occurred, magma rose up along pre-existing and reactivated faults, and filled the new-created empty space. Where compression occurred, sedimentary sequences were strongly deformed and stretched (drag folds). The main stress σ1 was WSW-ENE oriented. If magma emplacement and horizontal movements are assumed as being contemporaneous, then the transtensional phase occured in the Oxfordian.

Magma emplacement was essentially characterized by two different episodes, the first one coinciding with olivine gabbros and metagabbros formation, the second one with monzonites and syenites intrusion. The age of syenites emplacement is unknown.

Magma chamber extrusion

The presence of microgabbros (chilled margins) at the contacts between olivine gabbros and volcano-sedimentary bodies allows us to constrain the original position of JHM magma chamber which is not at its original place, as supposed on the basis of the presence of tectonic contacts between magmatic rocks and country rock. In fact, the presence of chilled margin indicates that volcano-sedimentary bodies were in contact with a hot and still liquid magma. Then, they are interpreted as slabs of volcano-sedimentary sequences collapsed into the magma chamber (roof pendants). Since no younger sediments have been found in pendants, and since the collapsed volcano-sedimentary sequences represent the bottom of the Mesozoic cover (Studer, 1987), it follows that magma rose up and cooled within the lowermost part of the Jurassic sedimentary series. Also, since the present position of magmatic rocks is within mid-Jurassic sequences, it must be concluded that JHM magma chamber was affected by post-magmatic vertical movements. As the thickness of the Triassic to mid-Jurassic sediments does not exceed 4000 m (Wigger *et al.*, 1992), a 3-4 km uplift is estimated as being broadly correct. The widespread presence of post-magmatic faults (white breccias) within the intrusive massif and the strong fragmentation of the original magma chamber also indicate post-magmatic tectonic movements.

Among the four main faulting systems (α, β, χ and δ) only δ does not coincide with a JHM boundary, but parallels the western boundary of Tirrhist Massif. It follows that the same fault pattern driving the transtensional phase was reactivated during magma chamber extrusion. Movements along faults were horizontal during the transtensional phase and vertical during the extrusion phase. The observed straightening up of stratification close to JHM boundary is interpreted as the result of two different tectonic phases: the first one being the anticline formation; the second one the magma chamber extrusion.

In conclusion, magma emplacement occurred during the Oxfordian and was favoured by the contemporaneous horizontal activation of four vertical faults, which support an Upper Jurassic sinistral transtensional regime and which affected a pre-existing anticlinal system. The magma chamber formed within the lowermost series of the Mesozoic cover and was later fragmented and tectonically extruded toward the mid-Jurassic sedimentary sequences. Essential condition necessary to make this model realistic and consistent with field data is that the same fault pattern was repeatedly reactivated and that faults were not limited to the sedimentary cover, but reached and affected the basement, allowing magma uplift and fragmentation of the crust into disconnected blocks. This is perfectly consistent with main structural models proposed for the Central High Atlas (§ 2.1).

- CHAPTER 4 -

Petrography

A petrographic study was carried out on JHM rocks in order to define mineral associations and textural features in olivine gabbros, metagabbros, monzonites, syenites, basic dikes and associated sedimentary sequences. In this chapter modal associations and textures are presented and interpreted in order to investigate and discuss the mechanical processes controlling gabbros emplacement (cooling rate, layering, convection, pneumatolysis), the magmatic sequence and the contact metamorphism in roof pendants and country rock.

4.1 - The magmatic rocks

Troctolites, ol-gabbros, oxide-rich gabbros, leucogabbros and anorthosites form two main complexes (JH1 and JH2) and smaller scattered bodies. Both JH1 and JH2 are layered and both consist of two superimposed series (Fig.4.1.) The transition from the lower series (LS) to the upper series (US) is horizontal, sharp and of magmatic origin in both complexes (§ 3.2).

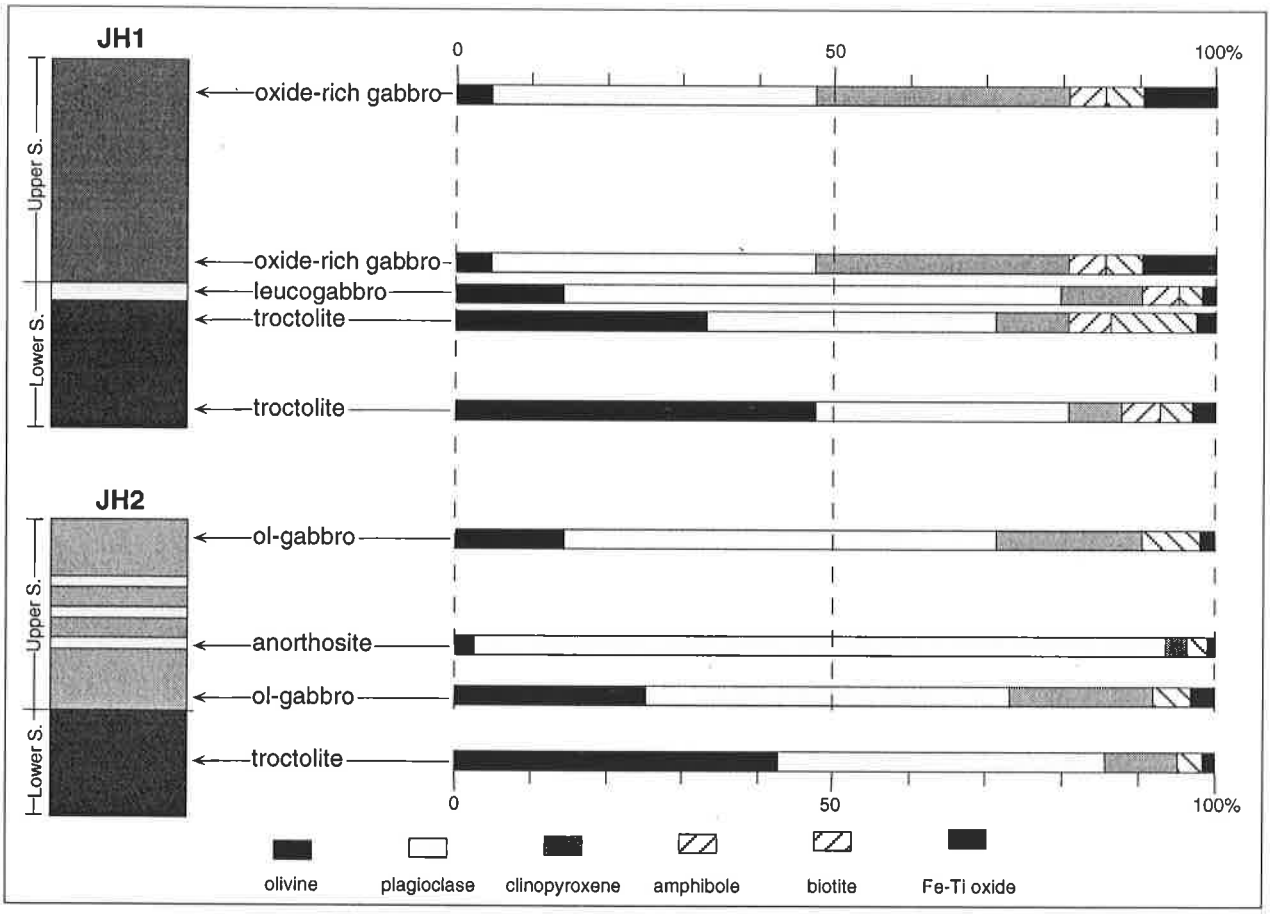

Fig.4.1 - Graphical representation of modal associations in JH1 and JH2 olivine gabbros. Fe-Ti oxide in oxide-rich gabbros is magnetite, in other rock types is ilmenite. The figure is dimensionless.

JH1-LS and JH2-LS are composed of troctolites and overlain by oxide-rich gabbros and ol-gabbros, forming JH1-US and JH2-US, respectively. A leucogabbro layer has been observed at the transition between JH1-LS and JH1-US, and anorthosites have been found interstratified within JH2-US. Ol-gabbros and troctolites rapidly grade to very fine-grained gabbros (microgabbros) getting closer to their contact with pendants (chilled margins). SSB also consist of troctolites and microgabbros.

Troctolites

Troctolites are characterized by abundant olivine, rare poikilitic megacrysts of pyroxene and by ophitic to subhedral-granular texture. Troctolite modal composition (Fig.3.1) is as follows:

olivine (35-50%)

plagioclase (35-40%)

clinopyroxene (7-10%)

biotite (3-12%)

brown amphibole (0-4%)

ilmenite (1-2%)

Cr-spinel (<1%)

From the bottom of JH1-LS upwards, troctolites are affected by modal layering, with gradual decrease in olivine content and parallel increase in biotite and, to minor extent, pyroxene content (Fig.4.1). Plagioclase and ilmenite contents remain almost constant. Amphibole is absent in JH2-LS. Secondary paragenesis is absent or insignificant.

Like mode, texture also has an upward trend variation from the bottom to the top of JH1-LS: the ophitic texture, which characterizes troctolites from the lowermost part of the series, is gradually replaced upwards by the subhedral-granular texture. While the ophitic texture is characterized by rare poikilitic megacrysts of pyroxene (2-3 cm large), enclosing abundant olivine grains and plagioclase laths, the subhedral-granular texture is formed by interstitial, rarely poikilitic crystals of pyroxene (<1 cm large), enclosing rare olivine and plagioclase. Ilmenite, brown amphibole and biotite are always interstitial phases.

Amphibole and biotite rim pyroxene and ilmenite. In both ophitic and subhedral-granular troctolites olivine grains are fine to coarse grained, sub-idiomorphic to idiomorphic, sometimes rounded and contain tiny inclusions of Cr-spinel. The layered distribution of olivine within the series, its largely variable grain-size and the scarcity of triple joints between grains are all evidence for crystal settling and accumulation of olivine in the magma chamber. As a consequence, troctolites can be classified as cumulates.

Plagioclase from ophitic troctolites is characterized by a marked bimodal grain-size distribution with small idiomorphic laths (<1 mm) enclosed by pyroxene poikilocrysts and large subidiomorphic laths (>2 mm) not enclosed. This is evidence for the simultaneous crystallization of plagioclase and pyroxene, with pyroxene growing more rapidly than plagioclase. The scarcity and the very fine grain-size of olivine inclusions in plagioclase and of plagioclase inclusions in olivine indicate that plagioclase and olivine crystallization was also almost contemporaneous. According to previous observations, four crystallization stages and the following crystallization order (Fig. 4.2) can be established for troctolites:

Cr-spinel > (olivine + plagioclase + clinopyroxene) > ilmenite > (brown amphibole + biotite).

Oxide-rich gabbros

Oxide-rich gabbros form JH1-US and, unlike troctolites, they are not characterized by modal layering. Mineral association varies slightly and randomly from bottom to top. Texture is markedly laminated throughout the series (flow texture); lamination is magmatic and defined by the preferential orientation of plagioclase laths. Modal composition of oxide-rich gabbros (Fig.4.1) is:

plagioclase (40-45%)

clinopyroxene (35-40%)

magnetite (8-10%)

olivine (5-7%)

brown amphibole (4-5%)

biotite (1-2%)

sulphides (<1%)

Unlike troctolites, oxide-rich gabbros do not contain neither poikilitic megacrysts of pyroxene nor two different plagioclase families. Cr-spinel and ilmenite are lacking, and sulphides (pyrite and chalcopyrite) are present, but randomly distributed. Olivine, plagioclase and pyroxene have the same medium grain-size (isogranular texture), reciprocal inclusions are absent, contacts between grains are usually sharp and straight, and triple junctions are common (polygonal texture), indicating the cotectic crystallisation of the three phases and the absence of processes of accumulation processes. Magnetite, amphibole and biotite are interstitial, with the two lasts surrounding

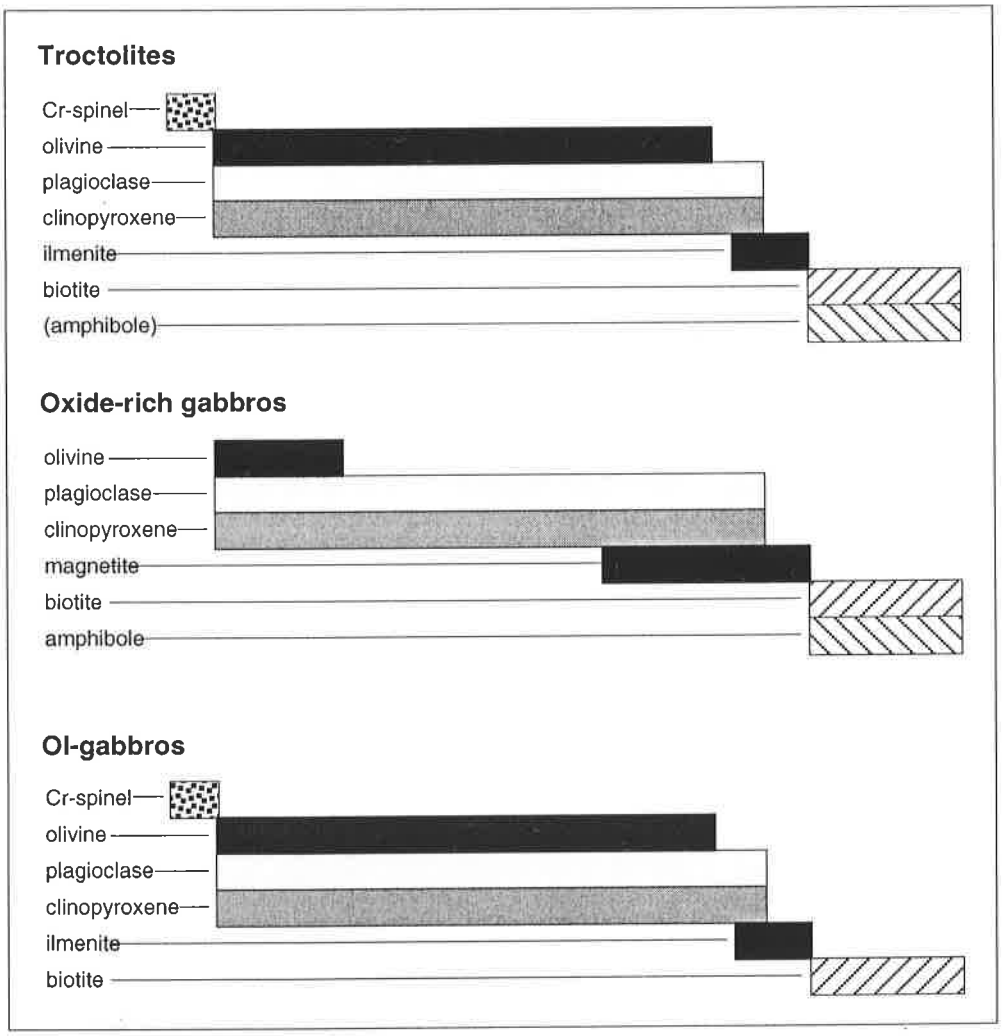

Fig.4.2 - Crystallization order in JHM olivine gabbros. Amphibole is present in JH1 troctolites but not in JH2 troctolites. Olivine, plagioclase and clinopyroxene are cumulus phases; Fe-Ti oxide, biotite and amphibole are intercumulus phases.

pyroxene and magnetite. Brown amphibole largely replaces pyroxene by both penetrating into pyroxene from the outside and by forming blobs within pyroxene. Sulphides are usually found strictly associated with magnetite. Their crystallization order (Fig. 4.2) is:

(olivine + plagioclase + clinopyroxene) > (magnetite + sulphides) > (brown amphibole + biotite)

Ol-gabbros

Ol-gabbros form JH2-US and small scattered bodies. They have subhedral-granular texture and, as in the case of JH1-LS troctolites, are characterized by a marked modal layering, with olivine decreasing from bottom to top in JH2-US. Modal association in ol-gabbros (Fig.4.1) is:

plagioclase (40-60%)

clinopyroxene (15-25%)

olivine (15-25%)

biotite (2-7%)

ilmenite (1-2%)

Cr-spinel (<1%)

Modal content of all mineral phases, but ilmenite, changes within the series with decreasing olivine and pyroxene, and increasing plagioclase and biotite from bottom to top. Throughout JH2-US olivine contains inclusions of Cr-spinel, and pyroxene is only weakly and marginally transformed into biotite. Amphibole is lacking in JH2-US ol-gabbros. Like troctolites, ol-gabbros are cumulates and their crystallisation order (Fig.4.2) is:

Cr-spinel > (olivine + plagioclase + clinopyroxene) > ilmenite > biotite

Leucogabbros

Leucogabbros have been found at the top of JH1-LS and have subhedral-granular flow texture. Like in oxide-rich gabbros, magmatic lamination is determined by the preferential orientation of plagioclase laths. If compared to underlying troctolites, leucogabbros are (Fig.4.1) richer in plagioclase (60-70%) and poorer in olivine (15-20%). Pyroxene content is steady (10%), brown amphibole abundant (5-6%), biotite rare (2-3%), and ilmenite is the unique Fe-Ti oxide. Brown amphibole mildly replaces pyroxene rims. Crystallisation order is the same than in JH1-LS troctolites.

Anorthosites

Anorthosites are interstratified within ol-gabbros in JH2-US and display magmatic lamination. Amphibole and magnetite are lacking (Fig.4.1), and olivine and pyroxene are rare (<10%), the former forming small sub-idiomorphic to rounded grains, the latter forming interstitial to poikilitic crystals. Grain-size is smaller than in ol-gabbros.

Microgabbros

Microgabbros have been found at the contact between troctolites and pendants, troctolites and country rock, and between ol-gabbros and pendants in JH1, in JH2, and in most small scattered bodies. They are fine to very fine-grained, with grain-size rapidly decreasing moving to the contacts, and have ophitic to porphyritic to doleritic to intersertal texture. While the fine-grained microgabbros are constituted by the same mineral phase than troctolites and ol-gabbros (olivine, plagioclase, clinopyroxene, biotite, brown amphibole, Fe-Ti oxides) the very fine-grained microgabbros are olivine- and pyroxene-free, and mainly characterized by idiomorphic small plagioclase laths, and interstitial brown-greenish amphibole. Most of them are also characterized by low-temperature secondary transformation, mainly represented by plagioclase saussuritisation, oxide exsolutions, green amphibole and epidote appearance.

« Metagabbros »

MG1 and MG2 overlie olivine gabbros and are characterized by the presence of both relics of primary assemblage and widespread secondary mineral association comprising green amphibole, epidote, chlorite, prehnite, albite, titanite, apatite and calcite (Fig.4.3). From MG1 to MG2, mineral assemblage does not change, but secondary paragenesis is more and more abundant.

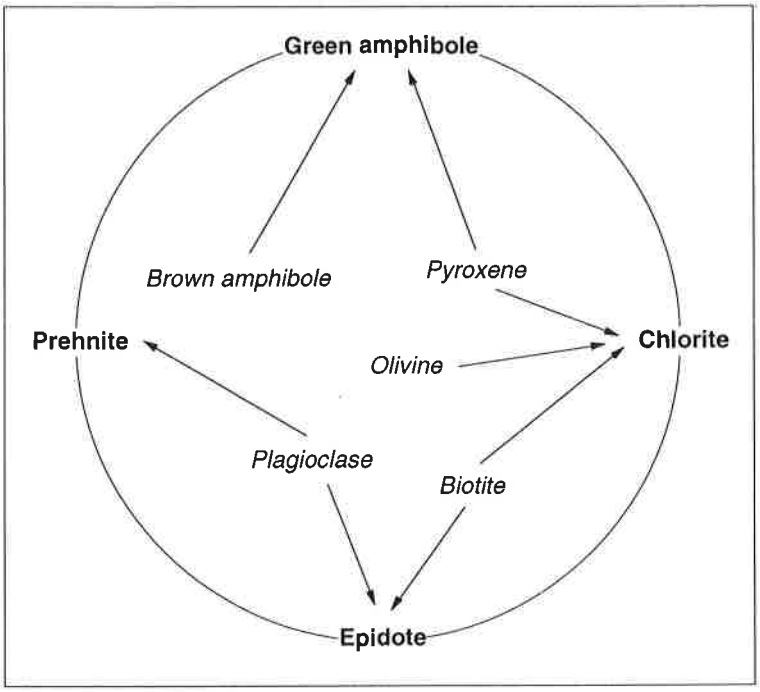

Fig.4.3 - Secondary transformations affecting JHM magmatic paragenesis. Primaty phases are in italic; secondary phases are in bold.

Green amphibole (actinolite) is always present and it is the most common secondary phase in almost all samples (up to 40%). It has been observed replacing pyroxene and brown amphibole as fibrous and acicular crystals forming round aggregates and as large interstitial crystals. It is often associated to small amounts of both blue-greenish and colourless amphiboles, and the appearance order of different secondary amphiboles randomly changes from one sample to another.

Chlorite is light-green coloured, weakly pleochroic and it commonly forms fine-grained aggregates replacing olivine and biotite and in saussuritizated plagioclases.

Epidote is yellow, develops after biotite and plagioclase, and forms isolated spherical aggregates. When aggregates are large enough, typical yellow-greenish spots appear on the rock surface.

Prehnite replaces plagioclase and forms large aggregates. When prehnite is absent, plagioclase is usually strongly saussuritizated and characterized by sub-solidus transformation, like formation of albitic rim and perthites.

Titanite and apatite are widespread, but their abundance largely even inside the same outcrop. Calcite is confined in veins crossing metagabbros close to contacts with pendants, in saussuritizated plagioclase and in interstitial spaces.

In most metagabbros ophitic, subhedral-granular and fluidal textures which characterize olivine gabbros are still preserved, and this allows identification of the original lithotype. MG1 and MG2 differ in the presence of late-magmatic interstitial green amphibole and of leucocratic ocelli in MG2. Leucocratic ocelli are mostly constituted by large laths (up to 1 cm) of sodic plagioclase and by minor green amphibole and epidote. Among all olivine gabbros, troctolites are the less affected by secondary transformation, while ol-gabbros and oxide-rich gabbros are the most

commonly and strongly affected by secondary transformation. Since troctolites form the lower series in JH1 and JH2, and ol-gabbros and oxide-rich gabbros form the upper series, it follows that the extent of transformation increases upwards.

Monzonites

Monzonites are rare and they form the outer zone of the Jebel Hayim megadike. All monzonites are quartz-free and biotite-bearing, and have abundant pyroxene and amphibole (up to 30%); agpaitic texture is rare. Both pyroxene and amphibole display strong and discontinuous optical zoning: pyroxene has colourless core and greenish rim, while amphibole has brown core and blue-greenish rim. Brown amphibole commonly rims pyroxene. Feldspar laths are altered and surrounded by perthitic alkali-feldspar. Sphene and apatite are abundant, but randomly distributed accessory phases and epidote is the most common secondary phase together with saussurite and calcite.

Syenites

Syenites form most dikes and megadikes, and are characterized by a marked bimodal composition. Two main groups have been distinguished:

- leucocratic syenites, when albite and quartz constitute more than the 95% of the modal association. They are the most widespread ones in JHM, and form the easternmost part of Jebel Ouakloum, the top of Jebel Hayim and others topographic culminations. Texture is commonly subhedral-granular, with idiomorphic laths of feldspar and interstitial quartz. Perthites, granophyres and pegmatites are frequent with pegmatites mostly forming the inner part of dikes. Titanite, Fe-Ti oxides, allanite and melanite are the most common accessory phase.

- mesocratic syenites, when amphibole is present and quartz is lacking. They form the western part of the Jebel Hayim megadike. Amphibole is blue-greenish, interstitial (agpaitic texture) and, in a few cases, crystals of altered fayalite have been observed. Epidote and green amphibole are the main and often unique secondary products.

Dolerites and basalts

Rocks forming basic dikes are very similar to microgabbros observed at the contacts between gabbros and sedimentary rocks. Basic dikes have doleritic, intersertal, or porphyritic textures and mineral association is mostly represented by microlites of saussuritizated plagioclase and by interstitial brown-greenish amphibole, ilmenite and rare poikilitic pyroxene. Olivine and plagioclase altered phenocrysts are present when rock is porphyritic. Chlorite is the most abundant phase in the mylonitic dike at the north-western extremity of JHM.

4.2 - The pendants

Limestones, dolomites and pelites forming pendants are characterized by very pronounced and pervasive recrystallization of carbonates and quartz, and the same low-temperature secondary phases observed in metagabbros are widespread in both sedimentary and volcanic rocks. In particular, amphiboles, chlorite and sphene are typical secondary phases in all carbonate and pelitic facies, whereas albite, epidote and prehnite presence is limited to basalts. High-temperature minerals (olivine) have only been found in one outcrop from a pendant at the SE extremity of JHM (I/J-5/6).

White breccias mainly are made up of magmatic and sedimentary angular clasts enclosed by a loose matrix, which is either formed by carbonate or pelitic material. As evidenced by X-ray diffractometry (Table 4.1), only low-temperature minerals have been detected in white breccias. No significant difference has been pointed out between pelitic and white carbonate matrices at the contact between pendants and pneumatolytic gabbros. Paragenesis is as follows: Kf + Qtz + Cal + Chl + Bio ± Ab ± Tal ± Amp ± Dol. White breccias matrices at the contact between pendants and troctolites display different paragenesis, characterized by the lack of K-Feldspar, quartz and biotite, and by the presence of abundant talc.

Sample	95.G	95.H	95.I	95.J	95.M	95.N	94.112
Analysis	1	2	3	4	5	6	7
K-feldspar	X	X	X	X	X	X	
Quartz	X	X	X	X	X	X	
Calcite	X	X	X	X	X	X	X
Dolomite				X			
Chlorite	X	X	X	X	X	X	X
Biotite	X	X		X	X	X	
Albite		X	X		X	X	X
Talc		X	X				X
Amphibole			X		X	X	

Table 3.1 - Mineral associations in white breccias. Samples 95.G, 95.J and 95.N were collected at the contact between pneumatolytic gabbros and pelites; samples 95.H, 95.I and 95.M at the contact between pneumatolytic gabbros and carbonates; sample 94.112 at the contact between JH1 troctolites and carbonates.

4.3 - The country rock

Unlike pendants, country rock are characterized, at most, by recrystallization of quartz and carbonates, and no evidence of low- or high-temperature metamorphic phases has been found. At the west of Tirrhist (I/J-6/7), a 1 meter thick contact aureole has been observed around a 30 metres thick dikes. Here, the presence of fine-grained aggregates of chlorite and green biotite replacing garnet is evidence for contact metamorphism. However, this outcrop cannot be considered as representative of the JHM contact aureole, but rather of the contact aureole formed during the intrusion of the dike, which is not part of JHM, but rather of the country rock.

4.4 - Discussion

About cooling rate in troctolites and ol-gabbros

Troctolites have ophitic texture, which is characterized by the presence of cumulative olivine and of poikilitic megacrysts of pyroxene, enclosing small laths of plagioclase. The ophitic texture is commonly interpreted as the result of the rapid cooling of a basaltic liquid (Carmichael *et al.*, 1974; Coish & Taylor, 1979; Mathison, 1987; Hort & Spohn, 1991; Cashman, 1993). According to most authors, ophitic texture reflects the "in situ" crystallisation of plagioclase and pyroxene, with the two phases nucleating and growing at different rates. At high cooling rates (supercooling) pyroxene has low nucleation rate (= few nucleii) and high growth rate (= large crystals), whereas plagioclase has high nucleation rate (= many nucleii) and low growth rate (= small crystals). Consequently, the resulting rock comprises few but large pyroxene crystals, and many but small plagioclase laths. Only plagioclases which were not enclosed by pyroxene megacrysts have large grain-size.

The transition from ophitic to subhedral-granular texture, along with the smaller and smaller grain-size of pyroxene, reflect the decreasing cooling rate from the floor and the walls to the middle of the magma chamber. The widespread presence of the ophitic texture in JHM is supported by the abundance of pendants, representing cold bodies in contact with a hot melt.

About layering in JH1 and JH2

Three kinds of layering have been recognised in the two complexes:

- the **large-scale layering**; it is characterized by the sudden modal and textural change (olivine decrease and ophitic texture disappearance) from the lower to the upper series in both complexes;

- the **modal layering**; it is characterized by the gradual and continuous variation in the modal content of one or more mineral phases from the bottom to the top of the series. JH1 and JH2 modal layering is essentially given

by the upward decrease of olivine modal content, which is classically related to fractional crystallization processes. The lack of modal layering in JH1-US questions the presence of fractional crystallization controlling oxide-rich gabbros solidification.

- the **textural layering**; it has been observed in both complexes, moving closer to magma chambers walls. It is characterized by the gradual and continuous textural change (grain-size decrease), and by olivine and pyroxene disappearance.

Magmatic layering is commonly due either to variation in physical and chemical conditions of crystallization or to new magma injection above or below an already solidified magma. In JHM the textural layering affecting olivine gabbros is attributable to the increasing cooling rate toward the magma chamber walls (Coish & Taylor, 1979; Cashman, 1993), the modal layering reflects crystal accumulation of olivine, and the large-scale layering is ambiguous, being both attributable to new magma injection and to abrupt variations in physical and chemical conditions. The origin of the large-scale layering will be discussed in the next chapters.

About convection in JH1-US

According to Sparks *et al.* (1993), convective regime can maintain a homogeneous distribution of particles and prevent crystal settling, modal layering and cumulate formation, provided that: a) particle fall velocities are small if compared with turbulent fluid velocities, and b) critical concentrations of particles are not exceeded. Fall velocity and critical concentration are strictly dependent on mineral and liquid density. For common basaltic melts, the critical concentrations of precipitating phases (olivine, pyroxene, plagioclase, oxides) are very small and in most cases only the least dense phase (e.g. plagioclase in basaltic systems) remain suspended, whereas dense phases (e.g. oxides, olivine, pyroxene) settle down. Only vigorous and turbulent convective regimes enable suspension of dense phases, preventing crystal accumulation.

The ubiquitous presence of magmatic flow texture, the lack of modal layering and of cumulative character are typical features of JH1-US oxide-rich gabbros. As a consequence, oxide-rich gabbros texture is interpreted as the result of a long-lived turbulent convective regime, which was active throughout the solidification of the series.

About metagabbros origin

Rocks very similar to MG2 were interpreted by Elsdon (1982) as the result of an autometasomatic process: in particular, gabbros reacted with a volatile-rich phase which separated during the magmatic stage and remained trapped within the walls of the intrusion. More recently, Larsen & Brooks (1994) interpreted gabbroic pegmatites found associated to cumulates in the Skaergaard intrusion as the result of the crystallisation of the intercumulus liquid which were derived from the Skaergaard parental melts and which were buoyant owing to their small density, if compared to cumulates density.

In JHM pegmatitic metagabbros are characterized by low-temperature mineral assemblages, by an upward increasing extent of transformation and by the presence of leucocratic ocelli in the uppermost part of the magma chamber. The observed secondary paragenesis indicates a post- to late-magmatic stage occurring under greenschist facies conditions (Fig.4.4) at a temperature of 350-400°C (Liou, 1971; Liou, 1973, Liou *et al.*, 1974; Moody *et al.*, 1983; Spear, 1993), if low-pressure conditions are assumed (Fig.4.5). Textural variation from MG1 to MG2, appears with interstitial green amphibole appearance.

Leucocratic ocelli associated to basic rocks are relatively common in many shallow intrusions (Carman, 1994) and are usually considered either as a form of segregation vesicles (Smith, 1967, MacKenzie & White, 1970; Carman *et al.*, 1975; Sato, 1978, Cooper, 1979, Anderson *et al.*, 1984) or as the result of liquid immiscibility (Philpotts & Hodgson, 1968; Ferguson & Currie, 1971). According to Burnham (1979) and Carman (1994), which described and interpreted similar leucocratic ocelli in similar basic rocks, the preferred mechanism for the formation of ocelli is the filling of vesicles by drops of residual liquid. Vesicles form in a highly viscous and partially crystallized basic magma during a second boiling episode caused by the early crystallization of anhydrous minerals from a hydrous melt, by the concentration of volatiles in the residual liquid and by an abrupt temperature fall (pneumatolysis).

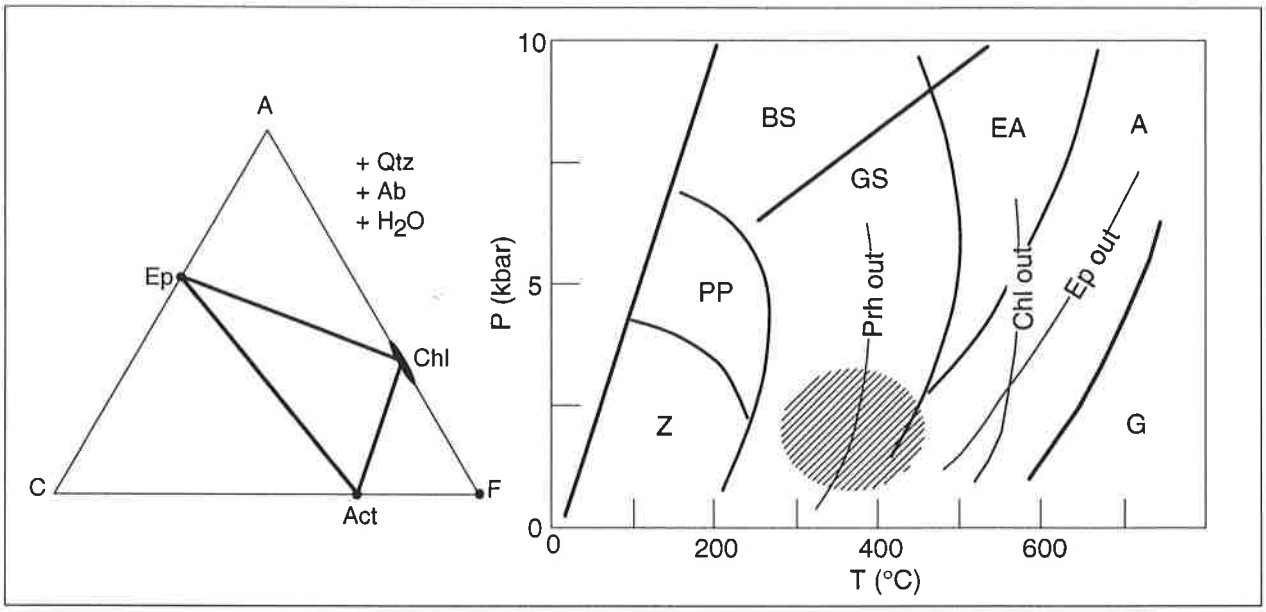

Fig.4.4 - A) ACF diagram for the greenschist facies (after Spear, 1993). Thick lines indicate mineral association of JHM pneumatolytic gabbros. Ab = albite; Act = actinolite; Chl = chlorite; Ep = epidote; Qtz = quartz. B) P-T diagram showing metamorphic facies and stability domains for prehnite (Prh), chlorite (Chl) and epidote (Ep). A = amphibolite facies; BS = blueschist facies; EA = epidote amphibolite facies; G = granulite facies; GS = greenschist facies; PP = pumpellyte-prehnite facies; Z = zeolite facies.

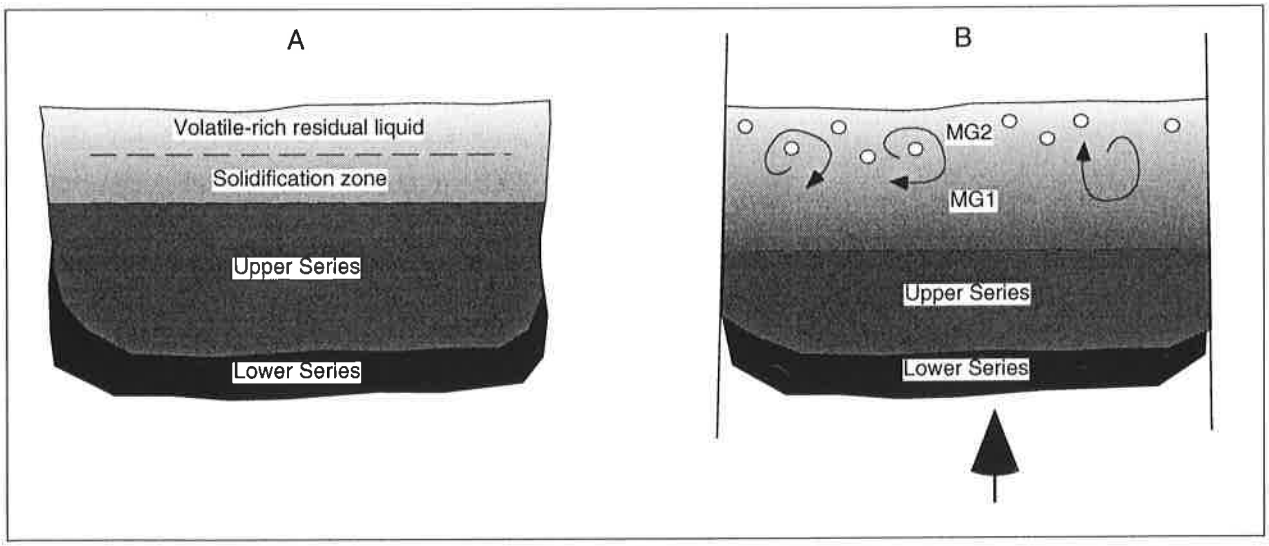

Fig.4.5 - A) The magma chamber stratification after lower and upper series formation and before the pneumatolytic event, and B) after the pneumatolytic event. Arrows indicate the vertical movement of the magma chamber.

In JHM, the required conditions for pneumatolysis were present. Early crystallization of anhydrous minerals (olivine, plagioclase and pyroxene) from a hydrous melt along with fractional crystallization originated a volatile-rich residual liquid. Vertical movements occurring during solidification destroyed the original magma chamber stratification, put in contact the solidifying gabbros with the residual volatile-rich liquid, and caused the temperature fall from magmatic to greenschist conditions (Fig. 4.6). MG1 resulted from low-temperature transformations of solidified ol-gabbros and oxide-rich gabbros forming the upper series in JH1 and JH2, respectively. Troctolites forming the lower seris of both complexes were not in contact with the residual volatile-rich liquid and they were not affected by pneumatolysis. MG2 resulted from the solidification, under pneumatolytic conditions, of still partially

liquid gabbroic rocks in contact with a volatile-rich residual liquid. Given that pneumatolysis was the main process originating MG1 and MG2, JHM metagabbros will be from this moment forth named "pneumatolytic gabbros".

About contact metamorphism and post-magmatic reequilibration

The rarity of high-temperature phases and the widespread presence of low-temperature phases in pendants and white breccias can be interpreted in two different ways:

1) High-temperature phases developed in pendants, but they were replaced by low-temperature minerals during post-magmatic reequilibrations, as in the case of the outcrop of § 3.2. This is perfectly consistent with vertical movements affecting the whole massif during and after gabbros cooling (§ 2.3);

2) Pendants were in contact with a relatively cold (≈300-400°C) melt and low-temperature phases were the result of a low-temperature contact metamorphism. This possibility is consistent with the presence of pneumatolytic processes, occurring in the last stage of gabbros solidification (§ 3.4). In this case, it must be assumed that pendants collapsed into the magma chamber at the time of pneumatolysis.

As pendants are in contact with both troctolites and pneumatolytic gabbros, 2) is not sufficient to explain all observed paragenesis. As a consequence, we argue that low-temperature paragenesis found at the contacts between troctolites and pendants are the result of post-magmatic reequilibration, while low-temperature paragenesis found at the contacts between pneumatolytic gabbros and pendants are the result of either post-magmatic reequilibration or low-temperature contact metamorphism, which occurred at the same time than pneumatolysis. In contrast with pendants, JHM country rock has no trace of high-temperature phase. Since a contact aureole is present around a dike (§ 3.3), it must be concluded that magma emplacement caused contact metamorphism, but, because of vertical post-magmatic movement of the massif, is today not exposed, but buried at depth. Also the mylonitic texture observed in the basic dikes cropping out along the country rock-JHM contact at the NW extremity of the investigated area is evidence for post-magmatic movements.

4.5 - Conclusions

Three distinct magmatic episodes can be distinguished during JHM history on the basis of field releationships and petrographical features.

Olivine gabbros formation
This first episode was characterized by the formation of troctolites, ol-gabbros, oxide-rich gabbros, leucogabbros and anorthosites. High cooling rate, crystal settling and accumulation, and, locally, vigorous convection were dominant processes during JH1 and JH2 crystallization. A chilled margin formed all around troctolites and ol-gabbros and a discontinuous marginal zone developed along the external boundary of the massif. The presence of two distinct complexes differing significantly in paragenesis and texture reflects the presence of two main magma chambers. Also, the sudden change of texture and paragenesis from the lower to the upper series in JH1 reflects at least two distinct episodes of crystallization due to an abrupt variation of crystallization conditions or to different mechanisms of magma chamber replenishment.

Pneumatolysis
Olivine gabbros solidification was interrupted by a pneumatolytic episode which was the second main magmatic episode in JHM history. Pneumatolysis was triggered by the a volatile-rich residual phase and by vertical movement of the magma chambers. Pneumatolysis mainly occurred in the uppermost, still partially liquid portion of the magma chamber, while the already solidified underlying olivine gabbros were affected by low-temperature transformation. Resulting rocks (pneumatolytic gabbros) are characterized by green-schist paragenesis and pegmatitic texture.

Syenites and monzonites intrusion
The third magmatic episode was charcaterized by syenite and monzonite emplacement. Both syenites and monzonites form dikes intruding olivine gabbros and metagabbros. The transition from quartz-free monzonite to quartz-free

syenite to quartz-bearing syenites within the same megadike (the Jebel Hayim megadike) reflects the presence of a differentiation process, at depth, generating more and more evolved saturated liquid. Assuming that the basic magma generating JHM gabbros and the more differentiated liquid generating monzonites and syenites have a common parental magma, it can be argued that monzonites and syenites formed by differentiation of JHM gabbros. The differentiated liquid was partially expulsed and stored within the continental crust, and partially trapped in the uppermost part of JHM magma chambers. The trapped portion interacted with the solidifying basic magma generating pneumatolytic gabbros, while the expulsed portion evolved by differentiation generating intermediate and acidic liquids. Differentiation was followed by a multistage emplacement of monzonites and syenites within gabbros.

- CHAPTER 5 -

Whole-Rock Chemistry

In this chapter whole-rock analyses of JHM magmatic rocks are presented and discussed. The interpretation of XRF data is essentially based on binary variation diagrams (Harker diagrams) where the concentration of major and trace elements is plotted against a differentiation index. A first set of Harker diagrams (Figs.5.2 and 5.3) regards only olivine gabbros and have the MgO number (MgO# = 100*MgO/MgO+Fe_2O_{3tot}, where Fe_2O_{3tot} is equal to total iron measured as ferrous iron) as the differentiation index. Since most syenites and monzonites have very small MgO# values, a second set of Harker diagrams having SiO_2 as differentiation index and including all JHM magmatic rocks, is also presented (Figs.5.4. and 5.5). REE data are classically presented on multi-elements diagrams, using McDonough *et al.* (1991) primitive mantle-normalised values (Fig.4.7). Complete analyses of most representative samples are found in Tables 5.1 to 5.6.

5.1. Essential geochemical features of JHM magmatic rocks

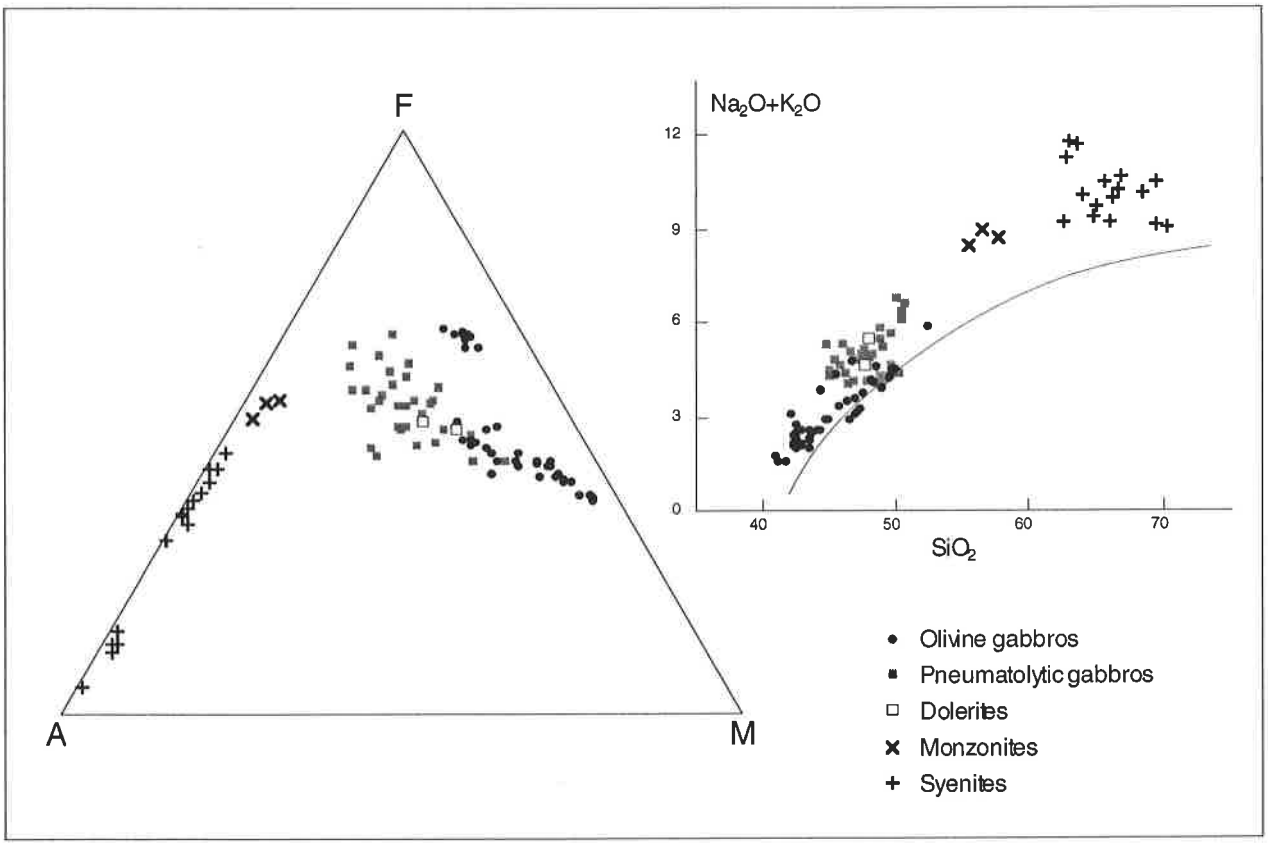

Fig.5.1 - AFM and TAS diagrams of JHM magmatic rocks.

Some general, but basic observations about the whole family of JHM magmatic rocks can be made from two commonly used diagrams (Fig.5.1): the TAS (Total Alkali vs SiO_2) and the AFM (Alkali-Fe_2O_{3tot}-MgO). In particular:

- JHM magmatic rocks form a transitional to mildly alkaline suite with SiO_2 ranging from 40 to 70% and Total Alkali from 1.5 to 12%.

- two main compositional gaps exist, the former between gabbros and monzonites, the latter between monzonites and syenites;

- olivine gabbros form two distinct families, the first one being Mg-rich (troctolites and ol-gabbros), the other one being Fe-rich (oxide-rich gabbros);

- syenites form two distinct families, one being alkali-rich and Fe_2O_3-poor, the other being alkali-poor and Fe_2O_3-rich.

5.2. Bulk compositions

Troctolites

Troctolites form regular and continuous compositional trends. Their MgO number decreases from 62 to 50 and the highest values belong to the troctolites forming JH1-LS bottom (samples 93.14, C and 93.12). MgO, Cr, Co and Ni decrease with decreasing MgO#, while SiO_2, TiO_2, Al_2O_3, CaO, Na_2O, K_2O, V, Rb, Sr, Y, Zr and Ba increase with decreasing MgO#. Fe_2O_{3tot} roughly parallels MgO. Finally, Cu and S are lower in JH2-LS than in JH1-LS troctolites. REE content is almost constant and low in all samples, and patterns are characterized by mild slope from LREE to HREE. JH1-LS troctolites are mildly enriched in middle REE due to the presence of amphibole and JH2-LS troctolites have values which are slightly higher than the most differentiated JH1-LS troctolites. No positive Eu-anomaly indicating plagioclase accumulation is present.

Oxide-rich gabbros

Oxide-rich gabbros form a family which is compositionally clearly distinct and in most cases not in line with the main whole-rock trend drawn by troctolites. They display small and random variations of MgO# from the bottom to the top of the series (28-32) and differ from troctolites in the abundance of MgO, Cr, Co and Ni, which is strongly lower in oxide-rich gabbros than in troctolites, and in the abundance of TiO_2, Fe_2O_{3tot}, CaO, V and Sr, which are higher in oxide-rich gabbros than in troctolites. Cu and S have either very high and very low values reflecting the discontinuous presence of sulphides. Other elements do not display significant variations, if compared to troctolites. REE content is low and approximately the same than in JH1-LS lowermost troctolites and REE pattern differs only for slightly lower LREE content. No Eu-anomaly is present.

Ol-gabbros

The major and trace element trend of ol-gabbros is the prolongation of the troctolite trend, with lower MgO# and higher SiO_2. Their MgO# decreases from 55 to 42 from the bottom to the top of JH2-US, and MgO, Cr, Co and Ni decrease with decreasing MgO#. Only Ni trend is characterized by a small compositional gap (300-500 ppm) between troctolites and ol-gabbros. SiO_2,TiO_2, Al_2O_3, Na_2O, K_2O, V, Rb, Y, Zr and Ba increase with decreasing MgO. Fe_2O_{3tot}, CaO and Sr randomly vary, Cu and S are almost constant and, as in the case of JH2-LS troctolites, lower than in JH1-LS troctolites. REE patterns of ol-gabbros parallel those of troctolites and REE contents are higher than in troctolites, continuously increasing from the less differentiated to the most differentiated ol-gabbro. No Eu-anomaly is present.

Leucogabbros

In comparison with underlying troctolites, leucogabbros are depleted in TiO_2 (0.7%), Fe_2O_{3tot}, MnO, MgO, V, Cr, Co, Ni, and enriched in SiO_2, Al_2O_3, CaO, Na_2O and Sr. Leucogabbro REE pattern parallels those of troctolites and has a mild positive Eu-anomaly reflecting plagioclase accumulation.

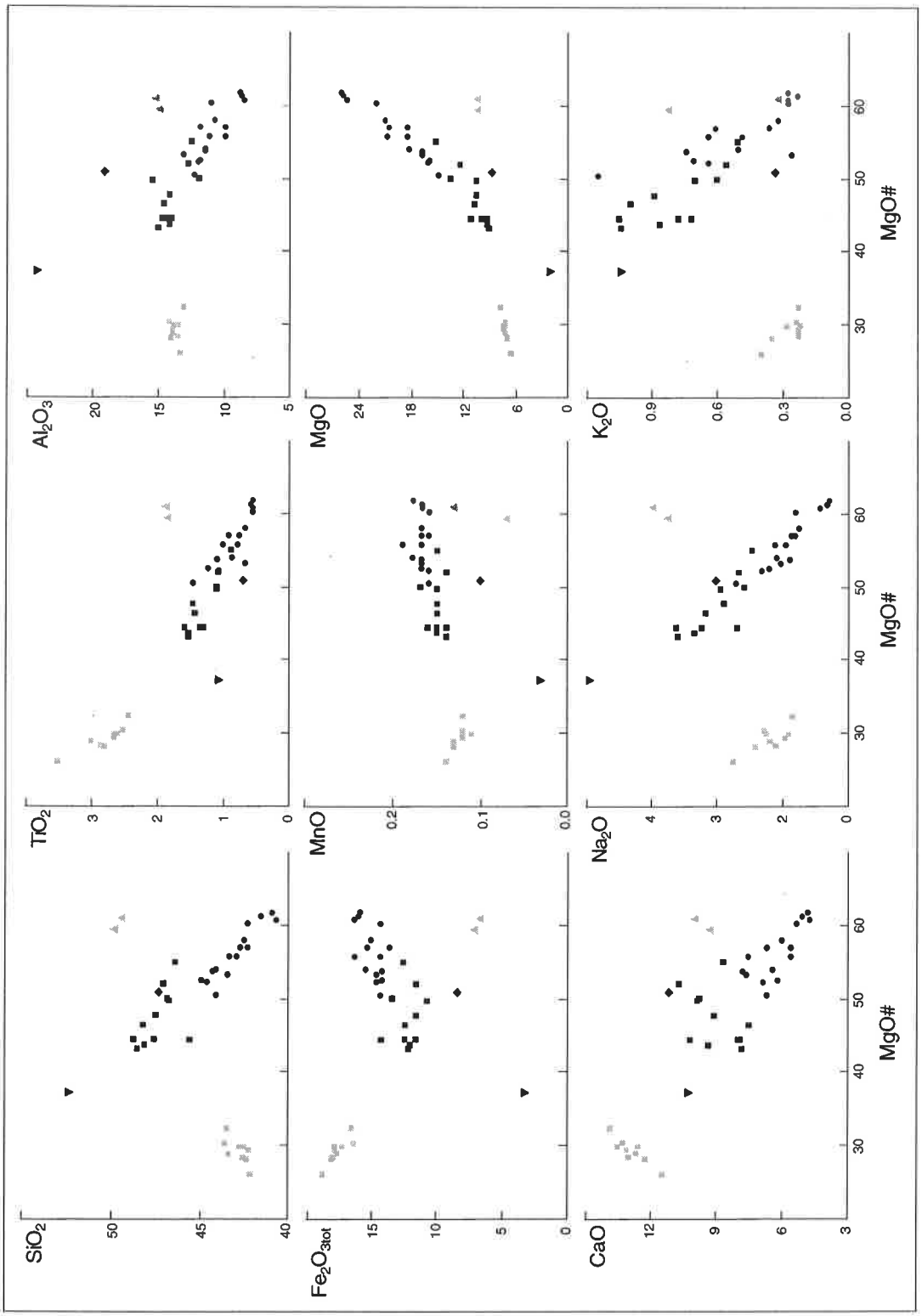

Fig.5.2 - Major element composition of olivine gabbros. Black circles = troctolites; black square =ol-gabbro; grey square = oxide-rich gabbro; black diamond = leucogabbro; black triangle = anorthosite; grey triangle = microgabbro; MgO# = 100MgO/(MgO+Fe2O3tot). Concentrations are expressed as wt%.

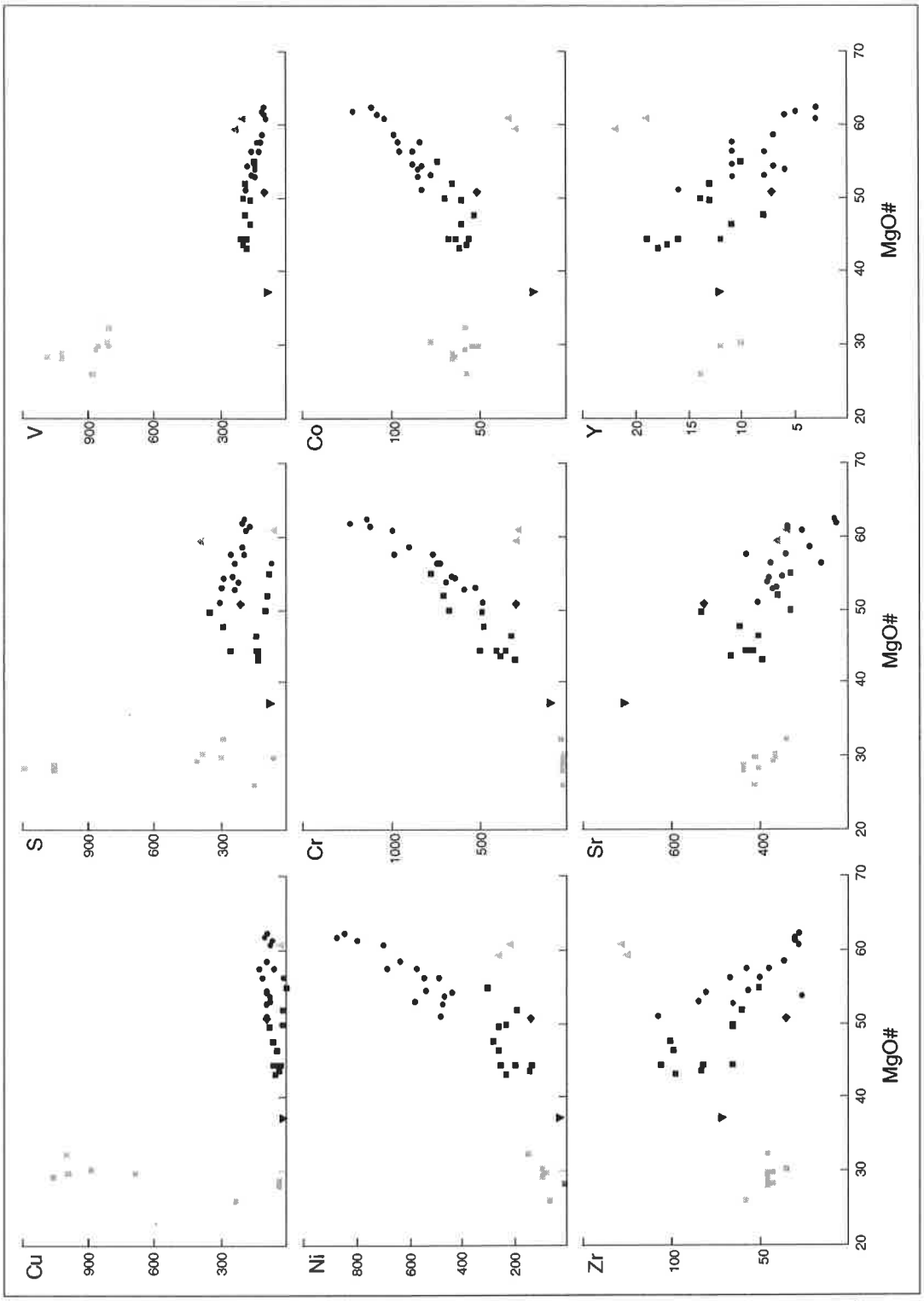

Fig.5.3 - Trace element composition of olivine gabbros. Same legend as Fig.5.2. Concentrations are expressed as ppm.

Sample	93.14	93.12	94.10	94.53	94.29	93.61	93.60	94.121
Series	JH1-LS	JH1-LS	SB	JH1-LS	JH2-LS	JH1-LS	JH1-LS	SB
Analysis	1	2	3	4	5	6	7	8
SiO_2	40.76	41.58	42.31	42.49	43.37	44.08	44.68	44.92
TiO_2	0.56	0.60	0.92	0.68	0.79	0.88	1.06	1.25
Al_2O_3	8.49	8.71	9.94	10.80	9.88	11.50	12.07	11.87
Fe_2O_3	3.75	4.48	n.m.	n.m.	2.99	4.86	2.29	6.43
FeO	11.29	10.40	n.m.	n.m.	12.01	9.53	11.16	7.06
Fe_2O_{3tot}	16.30	16.04	15.34	15.02	16.34	15.45	14.69	14.28
MnO	0.17	0.17	0.17	0.17	0.19	0.18	0.16	0.17
MgO	25.67	25.94	20.66	21.11	20.87	18.41	16.34	16.13
CaO	4.75	5.12	5.58	6.07	5.61	6.48	6.85	6.22
Na_2O	1.46	1.35	1.81	1.75	2.12	2.09	2.32	2.21
K_2O	0.28	0.24	0.61	0.32	0.49	0.51	0.64	0.71
P_2O_5	0.12	0.10	0.14	0.11	0.10	0.12	0.13	0.16
H_2O	1.63	0.61	n.m.	n.m.	0.53	1.10	1.74	n.m.
CO_2	0.27	0.63	n.m.	n.m.	0.09	0.21	0.22	n.m.
LOI	n.m.	n.m.	1.45	0.69	n.m.	n.m.	n.m.	2.87
Total	99.20	99.93	98.93	99.21	99.04	99.95	99.66	100.00
MgO#	61.2	61.8	57.4	58.4	56.1	54.4	52.7	53.0
S	168	199	252	202	71	242	236	292
V	102	110	136	111	129	140	146	162
Cr	1133	1250	988	909	732	671	596	527
Co	109	123	97	99	96	89	86	78
Ni	806	878	689	640	547	545	481	583
Cu	66	98	123	90	15	97	91	76
Rb	4	4	11	5	9	9	10	14
Sr	340	231	432	289	263	352	374	366
Y	6	5	11	7	8	11	11	8
Zr	31	31	58	37	51	57	65	86
Ba	n.d.	n.d.	101	53	21	53	49	73
La	n.m.	3.5	7.3	n.m.	5.4	5.1	n.m.	n.m.
Nd	n.m.	4.7	8.2	n.m.	6.2	6.4	n.m.	n.m.
Sm	n.m.	2.3	2.5	n.m.	2.0	2.2	n.m.	n.m.
Eu	n.m.	0.69	0.81	n.m.	0.74	0.76	n.m.	n.m.
Tb	n.m.	0.4	0.4	n.m.	0.3	0.3	n.m.	n.m.
Yb	n.m.	0.8	0.9	n.m.	0.8	0.9	n.m.	n.m.

Table 5.1 - Representative analyses of troctolites. Major element concentrations are expressed as wt%; trace element concentrations as ppm. MgO# = $100MgO/(MgO+Fe_2O_{3tot})$. n.m. = mot measured; n.d. = not detected.

Sample	93.20	94.71	94.77B	93.55	94.78	94.77	94.80	93.56
Series	JH1-US	JH1-US	JH1-US	JH1-US	JH1-US	JH1-US	JH1-US	JH1-US
Analysis	1	2	3	4	5	6	7	8
SiO_2	42.08	42.22	42.36	42.43	42.78	43.35	43.45	43.62
TiO_2	3.48	2.65	2.78	2.65	2.59	2.98	2.43	2.50
Al_2O_3	13.37	13.84	14.08	13.69	13.52	13.90	13.07	14.20
Fe_2O_3	9.12	11.26	9.32	8.78	10.46	9.11	8.65	9.28
FeO	8.68	5.80	7.86	8.06	6.10	7.67	7.06	6.38
Fe_2O_{3tot}	18.77	17.71	18.05	17.74	17.24	17.63	16.50	16.37
MnO	0.14	0.12	0.13	0.12	0.11	0.13	0.12	0.12
MgO	6.63	7.32	7.04	7.49	7.29	7.14	7.83	7.15
CaO	11.46	13.02	12.23	12.54	13.51	12.65	13.80	13.20
Na_2O	2.76	1.96	2.42	2.25	1.91	2.17	1.84	2.26
K_2O	0.40	0.23	0.35	0.28	0.22	0.23	0.23	0.24
P_2O_5	0.08	0.05	0.07	0.06	0.05	0.05	0.05	0.05
H_2O	0.70	n.m.	n.m.	0.65	n.m.	n.m.	n.m.	0.43
CO_2	0.29	n.m.	n.m.	0.10	n.m.	n.m.	n.m.	0.18
LOI	n.m.	0.56	0.71	n.m.	0.56	0.70	0.66	n.m.
Total	99.19	99.03	99.35	99.10	99.10	100.08	99.19	99.61
MgO#	26.1	29.3	28.1	29.7	29.7	28.8	32.2	30.4
S	147	406	1051	57	297	1051	286	384
V	881	865	1018	807	857	1018	802	815
Cr	17	19	21	19	19	21	34	16
Co	57	58	66	51	54	66	58	78
Ni	65	91	3	84	81	3	149	94
Cu	232	1055	36	683	989	36	1000	891
Rb	7	6	7	7	7	7	6	5
Sr	410	370	436	410	364	436	339	365
Y	14	n.d.	n.d.	12	n.d.	n.d.	n.d.	10
Zr	58	45	45	42	45	45	45	35
Ba	47	26	38	38	21	38	22	23
La	n.m.	3.1	n.m.	3.3	n.m.	3.0	n.m.	n.m.
Nd	n.m.	5.1	n.m.	5.0	n.m.	5.7	n.m.	n.m.
Sm	n.m.	2.1	n.m.	2.0	n.m.	2.3	n.m.	n.m.
Eu	n.m.	0.74	n.m.	0.74	n.m.	0.88	n.m.	n.m.
Tb	n.m.	0.3	n.m.	0.3	n.m.	0.4	n.m.	n.m.
Yb	n.m.	0.8	n.m.	0.7	n.m.	0.9	n.m.	n.m.

Table 5.2 - Representative analyses of oxide-rich gabbros. Major element concentrations is expressed as wt%; trace element concentrations as ppm. Same legend as Table 5.1.

Anorthosites

In comparison with surrounding ol-gabbros, anorthosites have lower MgO#, Fe_2O_{3tot}, MnO, MgO, V, Cr, Co, Ni, and higher SiO_2, Al_2O_3, Na_2O, K_2O and Sr. As in the case of leucogabbros, a positive Eu-anomaly reflecting plagioclase accumulation characterises anorthosite REE pattern.

Microgabbros

Microgabbros have bulk compositions which vary much from one sample to another, according to their grain-size (i.e. to their distance from the magma chamber border) and to the composition of adjacent olivine gabbros. However, the two very-fine grained olivine -free microgabbros collected from JH1-LS chilled margin are compositionally almost identical and have higher content of SiO_2, TiO_2, Al_2O_3, CaO, Na_2O, V, Zr and Y, and lower content of Fe_2O_{3tot}, MgO, Cr, Co and Ni than adjacent troctolites. REE content is higher than in troctolites, but their profiles parallel each other.

Pneumatolytic gabbros

As a whole, pneumatolytic gabbros are characterized by bulk compositions which are broadly similar to those of ol-gabbros, oxide-rich gabbros and leucogabbros, and by large variations in most major and trace elements. TiO_2, Na_2O, K_2O, P_2O_5, Rb, Sr, Y, Zr, Ba and S are higher in pneumatolytic gabbros than in olivine gabbros. In Harker diagrams pneumatolytic gabbros do not form linear trends, but rather scattered points lying between the troctolites-ol-gabbros trend and the oxide-rich gabbros trend. REE patterns of pneumatolytic gabbros parallel olivine gabbros s.l patterns, and their content is variable and higher than in ol-gabbros.

Monzonites

Bulk compositions of monzonites are broadly similar between each other. SiO_2 content is between 55 and 58% and MgO does not exceed 1%. If compared to the most differentiated ol-gabbros, they are depleted in TiO_2, Fe_2O_{3tot}, CaO, V, Cr, Co, and Ni, and enriched in Al_2O_3, Na_2O, K_2O, Zr, Y, Rb and Ba. REE content is higher than in olivine gabbros, profile is parallel (steady decrease from heavy to light REE), except for the positive Eu-anomaly, reflecting plagioclase accumulation.

Syenites

Syenites are characterized by SiO_2 content exceeding 62% and MgO content not exceeding 0.2%. If compared to monzonites, syenites are richer in Na_2O (5.9-10.2%) and poorer in TiO_2 (0.1-0.5%), Fe_2O_{3tot} (<8%), CaO (<2.8%), and Sr (38-178 ppm). K_2O, Zr, Y, Rb and Ba display large variations with values which are both lower and higher than in monzonites. Two families of syenites can be distinguished, according to the K_2O (and Rb) content:

- K-rich syenites ($K_2O > 3\%$).

- K-poor syenites ($K_2O < 2\%$)

According to the Fe_2O_{3tot} content, two further families of syenites can be also distinguished:

- Fe-rich syenites ($Fe_2O_{3tot} > 5\%$)

- Fe-poor syenites ($Fe_2O_{3tot} < 2\%$)

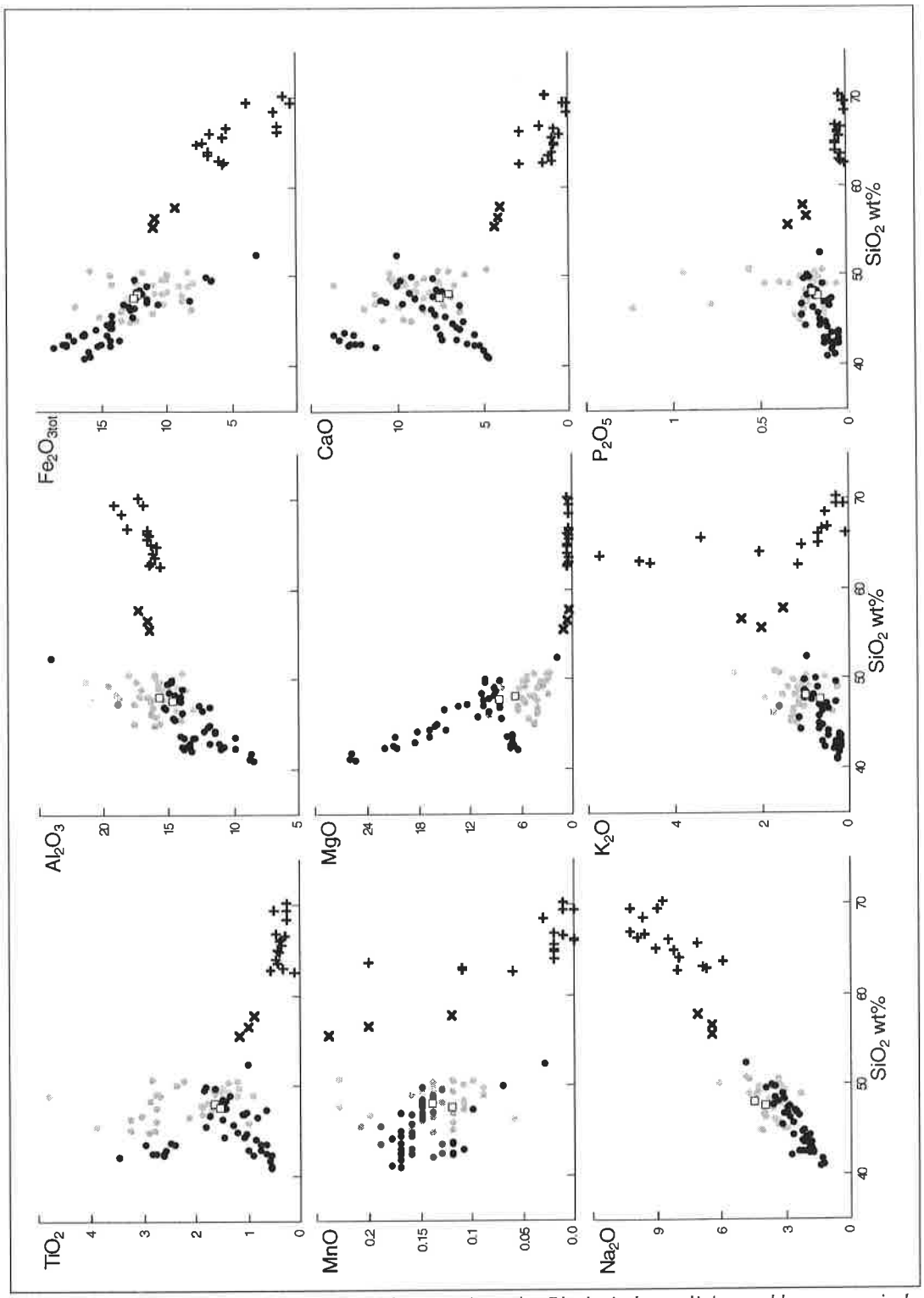

Fig.5.4 - Major element composition of JHM magmatic rocks. Black circle = olivine gabbro; grey circle =pneumatolytic gabbro; white square = dolerite; x = monzonite; + = syenite. Concentrations are expressed as wt%.

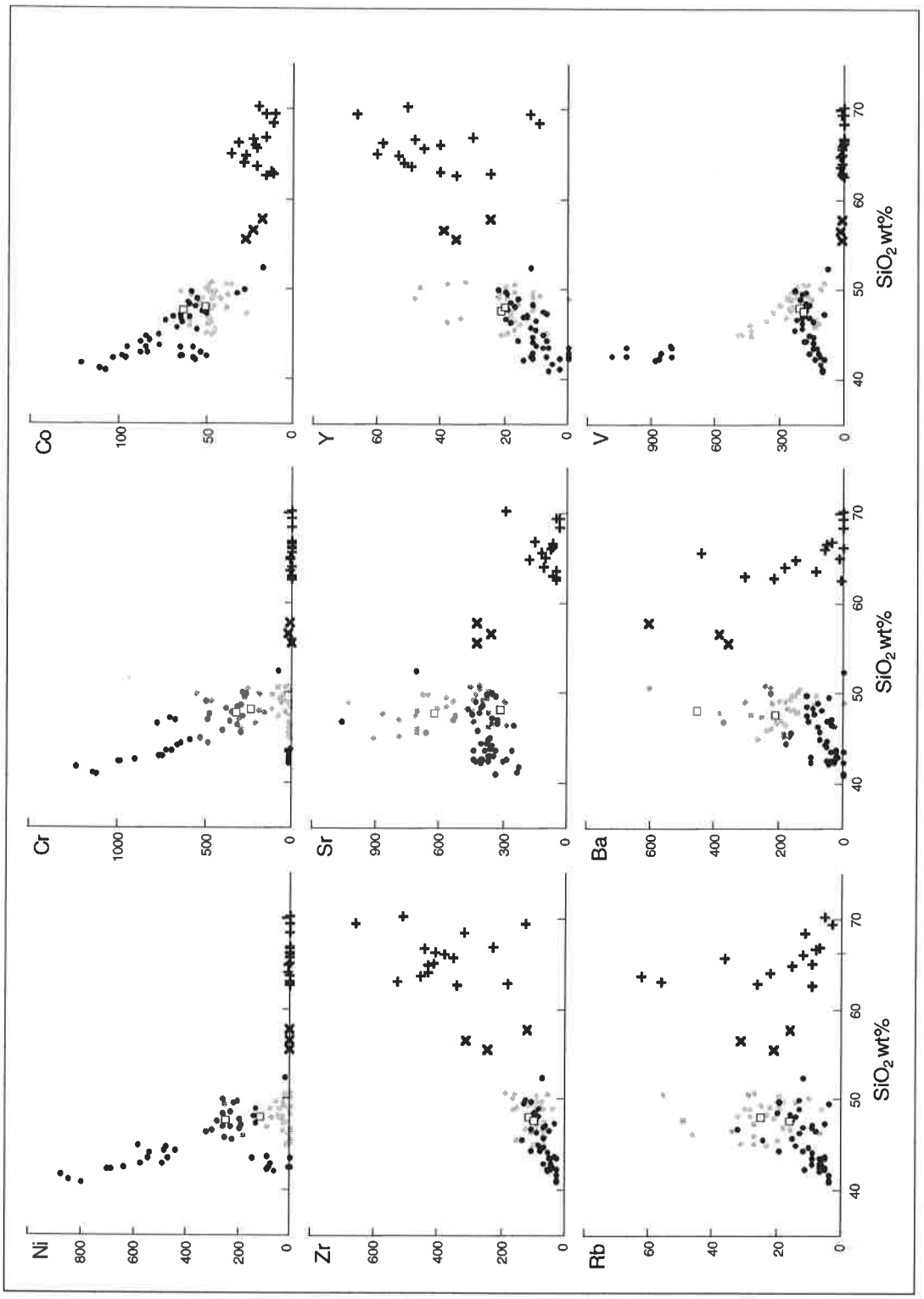

Fig.5.5 - Trace element composition of JHM magmatic rocks. Same legend as Fig.5.4. Concentrations are expressed as ppm.

Sample	94.28	94.24	94.25	94.97	94.17	94.19	94.10	94.21
Series	JH2-US	JH2-US	JH2-US	SSB	JH2-US	JH2-US	SSB	JH2-US
Analysis	1	2	3	4	5	6	7	8
SiO_2	46.46	46.87	47.09	47.45	47.59	48.13	48.24	48.79
TiO_2	0.86	1.11	1.06	1.46	1.58	1.53	1.44	1.36
Al_2O_3	12.41	11.84	12.80	14.13	14.38	14.19	14.60	13.99
Fe_2O_3	3.99	3.92	2.51	n.m.	2.54	3.28	5.10	2.64
FeO	7.66	8.57	8.10	n.m.	8.84	7.78	6.54	7.98
Fe_2O_{3tot}	12.50	13.44	11.51	11.49	12.36	11.93	12.37	11.51
MnO	0.15	0.17	0.14	0.15	0.15	0.15	0.15	0.14
MgO	15.26	13.46	12.42	10.48	9.88	9.27	10.73	9.22
CaO	8.67	9.78	10.73	9.11	8.01	9.37	7.46	10.17
Na_2O	2.46	2.57	2.66	2.90	3.63	3.35	3.16	3.22
K_2O	0.51	0.60	0.56	0.89	1.05	0.86	1.00	0.78
P_2O_5	0.11	0.14	0.11	0.19	0.23	0.18	0.20	0.15
H_2O	0.38	0.55	0.52	n.m.	1.02	0.85	n.m.	0.85
CO_2	0.10	0.08	0.24	n.m.	0.10	0.07	n.m.	0.09
LOI	n.m.	n.m.	n.m.	1.29	n.m.	n.m.	0.43	n.m.
Total	99.02	99.66	98.94	99.54	99.00	99.01	99.05	99.38
MgO#	55.0	50.0	51.9	47.7	44.4	43.7	46.5	44.5
S	80	89	88	289	131	124	139	136
V	145	193	189	182	179	192	160	201
Cr	785	678	710	479	344	376	317	495
Co	74	70	65	53	63	57	60	56
Ni	301	236	192	285	198	143	259	136
Cu	n.d.	18	15	56	37	34	40	26
Rb	8	9	9	16	15	14	16	13
Sr	332	330	359	446	417	467	403	434
Y	10	14	13	8	19	17	11	16
Zr	51	66	60	101	107	84	99	82
Ba	38	53	37	114	90	65	96	79
La	n.m.	n.m.	n.d.	n.m.	n.m.	n.m.	n.m.	n.d.
Nd	n.m.	n.m.	1.7	n.m.	n.m.	n.m.	n.m.	2.5
Sm	n.m.	n.m.	7.8	n.m.	n.m.	n.m.	n.m.	11.2
Eu	n.m.	n.m.	2.7	n.m.	n.m.	n.m.	n.m.	3.7
Tb	n.m.	n.m.	2.3	n.m.	n.m.	n.m.	n.m.	3.6
Yb	n.m.	n.m.	0.1	n.m.	n.m.	n.m.	n.m.	0.2

Table 5.3 - Representative analyses of ol-gabbros. Major element concentration is expressed as wt%; trace element concentration as ppm. Same legend as Table 5.1.

Sample	93/57	94/26	94/11	93/22	94/23	94/110	94/56	12A
Rock type	LCG	ANR	MCG	MCG	MCG	MCG	DOL	DOL
Analysis	1	2	3	4	5	6	7	8
SiO_2	47.32	52.37	46.76	49.45	49.73	49.80	47.74	48.02
TiO_2	0.67	1.03	1.75	1.85	1.66	1.82	1.55	1.64
Al_2O_3	18.94	24.02	15.23	15.09	14.93	14.89	14.74	15.69
Fe_2O_3	2.70	0.99	n.m.	n.m.	3.29	n.m.	n.m.	n.m.
FeO	5.06	1.85	n.m.	n.m.	8.35	n.m.	n.m.	n.m.
Fe_2O_{3tot}	8.32	3.05	12.91	6.65	12.57	7.05	12.47	12.31
MnO	0.10	0.03	0.16	0.13	0.15	0.07	0.12	0.14
MgO	8.65	1.82	8.66	10.34	8.64	10.35	8.58	6.83
CaO	11.09	10.17	6.44	9.89	8.00	9.27	7.61	7.06
Na_2O	3.00	4.92	3.16	3.95	3.51	3.73	3.94	4.47
K_2O	0.33	1.03	1.63	0.32	1.07	0.82	0.69	1.03
P_2O_5	0.10	0.16	0.26	0.25	0.22	0.23	0.17	0.20
H_2O	0.94	0.59	n.m.	n.m.	0.44	n.m.	n.m.	n.m.
CO_2	0.14	0.08	n.m.	n.m.	0.07	n.m.	n.m.	n.m.
LOI	n.m.	n.m.	2.79	1.79	n.m.	1.15	2.44	2.48
Total	99.04	99.06	99.75	99.71	100.06	99.18	100.05	99.87
MgO#	51.0	37.4	40.1	60.9	40.7	59.5	40.8	35.7
S	202	66	54	56	115	387	1091	225
V	91	78	220	197	176	231	186	207
Cr	289	80	361	270	261	283	317	231
Co	51	18	66	33	59	29	63	51
Ni	134	19	198	220	206	261	248	112
Cu	86	12	53	24	24	n.d.	30	n.d.
Rb	5	12	32	4	19	13	16	25
Sr	526	709	1054	339	379	359	616	311
Y	7	12	20	19	20	22	21	20
Zr	35	71	105	129	109	126	96	113
Ba	n.d.	1	370	48	115	225	209	450
La	3.8	n.d.	15.6	23.4	n.d.	n.m.	10.0	14.5
Nd	4.7	2.4	17.6	30.4	3.5	n.m.	12.7	16.7
Sm	1.6	10.4	5.3	7.1	15.8	n.m.	4.4	5.3
Eu	0.78	3.3	1.53	1.48	4.8	n.m.	1.38	1.40
Tb	0.3	2.9	0.7	0.8	4.5	n.m.	0.6	0.7
Yb	0.6	0.2	1.6	1.5	0.3	n.m.	1.6	1.9

Table 5.4 - Representative analyses of leucogabbros (LCG), anorthosites (ANR), microgabbros (MCG) and doerites (DOL). Major element concentration is expressed as wt%; trace element concentration as ppm. Same legend as Table 5.1.

Sample	3B	G	93.20	94.18	3A	93.46	94.30	94.13
Rock type	MG1	MG2	MG2	MG2	MG1	MG1	MG2	MG2
Analysis	1	2	3	4	5	6	7	8
SiO_2	44.90	46.12	47.77	49.68	49.76	50.20	50.50	50.65
TiO_2	2.91	2.78	1.93	1.71	1.19	1.41	2.26	2.85
Al_2O_3	16.19	16.35	16.43	17.49	21.29	16.10	16.13	14.00
Fe_2O_3	n.m.	11.78	n.m.	4.61	n.m.	n.m.	n.m.	5.49
FeO	n.m.	1.54	n.m.	5.03	n.m.	n.m.	n.m.	9.42
Fe_2O_{3tot}	12.89	13.49	11.88	10.20	6.54	9.95	11.94	15.96
MnO	0.14	0.15	0.15	0.13	0.09	0.14	0.10	0.23
MgO	4.71	4.30	6.06	3.76	3.26	5.52	3.16	2.77
CaO	9.37	8.64	9.43	8.68	10.50	10.70	7.22	5.00
Na_2O	4.13	3.51	2.98	4.30	3.61	3.37	4.72	4.90
K_2O	1.22	1.78	1.16	1.33	1.05	1.02	1.66	1.72
P_2O_5	0.27	0.25	0.21	0.27	0.17	0.19	0.57	0.57
H_2O	n.m.	1.99	n.m.	1.74	n.m.	n.m.	n.m.	n.m.
CO_2	n.m.	0.35	n.m.	0.50	n.m.	n.m.	n.m.	n.m.
LOI	2.48	n.m.	1.43	n.m.	1.67	0.95	1.53	1.96
Total	99.21	99.54	99.43	99.23	99.13	99.55	99.79	99.56
MgO#	26.8	24.2	33.8	26.9	33.3	35.7	20.9	14.8
S	350	408	116	56	209	177	67	50
V	431	443	256	207	248	220	170	96
Cr	15	20	190	49	118	249	45	23
Co	48	50	53	48	45	50	36	48
Ni	15	5	72	28	57	23	11	n.d.
Cu	20	14	47	43	26	74	19	n.d.
Rb	23	46	21	18	14	19	29	27
Sr	908	372	450	648	675	418	460	411
Y	21	15	19	21	11	20	38	32
Zr	104	68	92	109	76	90	156	184
Ba	264	218	139	153	117	137	228	243
La	13.5	n.m.	11.3	n.m.	n.m.	11.0	30.7	21.7
Ce	29.5	n.m.	23.8	n.m.	n.m.	23.5	61.9	45.6
Nd	17.7	n.m.	13.6	n.m.	n.m.	13.3	32.5	26.6
Sm	5.5	n.m.	4.4	n.m.	n.m.	4.4	9.6	8.5
Eu	1.68	n.m.	1.22	n.m.	n.m.	1.40	2.24	2.04
Tb	0.7	n.m.	0.6	n.m.	n.m.	0.7	1.3	1.2
Yb	1.8	n.m.	1.5	n.m.	n.m.	1.6	2.8	3.0

Table 5.5 - Representative analyses of pneumatolytic gabbros. Major element concentration is expressed as wt%; trace element concentration as ppm. Same legend as Table 5.1.

Sample	94.5	94.65	94.60	95.90	94.64	94.12	94.34	94.70
Rock type	MNZ	MNZ	MNZ	SYE	SYE	SYE	SYE	SYE
Analysis	1	2	3	4	5	6	7	8
SiO_2	55.44	56.50	57.68	62.47	63.61	64.66	66.00	69.30
TiO_2	1.17	0.99	0.88	0.12	0.42	0.39	0.39	0.48
Al_2O_3	16.37	16.54	17.28	15.58	15.99	15.82	16.47	19.06
Fe_2O_3	n.m.	8.34	n.m.	n.m.	3.24	5.60	n.m.	n.m.
FeO	n.m.	2.27	n.m.	n.m.	3.11	1.81	n.m.	n.m.
Fe_2O_{3tot}	11.01	10.86	9.33	5.66	6.70	7.61	6.64	0.48
MnO	0.24	0.20	0.12	0.06	0.20	0.02	0.00	0.01
MgO	1.00	0.65	0.51	0.13	0.03	0.20	0.00	0.00
CaO	4.33	4.16	3.99	2.81	1.14	0.83	0.53	0.15
Na_2O	6.46	6.45	7.14	8.04	5.92	8.23	8.47	10.23
K_2O	2.03	2.49	1.54	1.17	5.77	1.11	0.72	0.29
P_2O_5	0.34	0.23	0.25	0.01	0.03	0.06	0.05	0.01
H_2O	n.m.	n.m.	n.m.	n.m.	n.m.	n.m.	n.m.	n.m.
CO_2	n.m.	n.m.	n.m.	n.m.	n.m.	n.m.	n.m.	n.m.
LOI	0.72	1.05	1.21	3.07	0.64	0.40	0.76	0.36
Total	99.11	99.87	99.93	99.12	100.10	99.13	100.03	100.37
MgO#	8.3	5.7	5.2	2.3	0.5	2.6	0.0	0.0
S	47	53	79	n.d.	228	26	n.d.	n.d.
V	6	19	12	1	13	15	6	6
Cr	n.d.	18	7	1	7	6	3	n.d.
Co	28	23	18	16	21	28	22	11
Ni	n.d.	n.d.	n.d.	n.d.	n.d.	4	3	n.d.
Cu	17	n.d.	n.d.	n.d.	n.d.	28	n.d.	n.d.
Rb	21	31	16	9	62	15	12	3
Sr	422	354	424	51	55	178	75	54
Y	35	39	24	35	49	53	40	12
Zr	244	311	117	336	450	427	379	122
Ba	355	381	601	3	86	146	55	n.d.
La	n.m.	28.7	17.5	n.m.	43.9	40.8	25.2	n.m.
Ce	n.m.	59.2	37.1	n.m.	90.5	87.6	52.3	n.m.
Nd	n.m.	31.9	20.5	n.m.	42.2	42.5	31.1	n.m.
Sm	n.m.	9.7	6.2	n.m.	11.9	12.3	9.1	n.m.
Eu	n.m.	3.60	4.01	n.m.	1.66	2.12	1.58	n.m.
Tb	n.m.	1.5	0.8	n.m.	1.6	1.8	1.2	n.m.
Yb	n.m.	3.8	2.0	n.m.	5.6	5.3	4.3	n.m.

Table 5.6 - Representative analyses of monzonites (MNZ) and syenites (SYE). Major element concentration is expressed as wt%; trace element concentration as ppm. Same legend as Table 5.1.

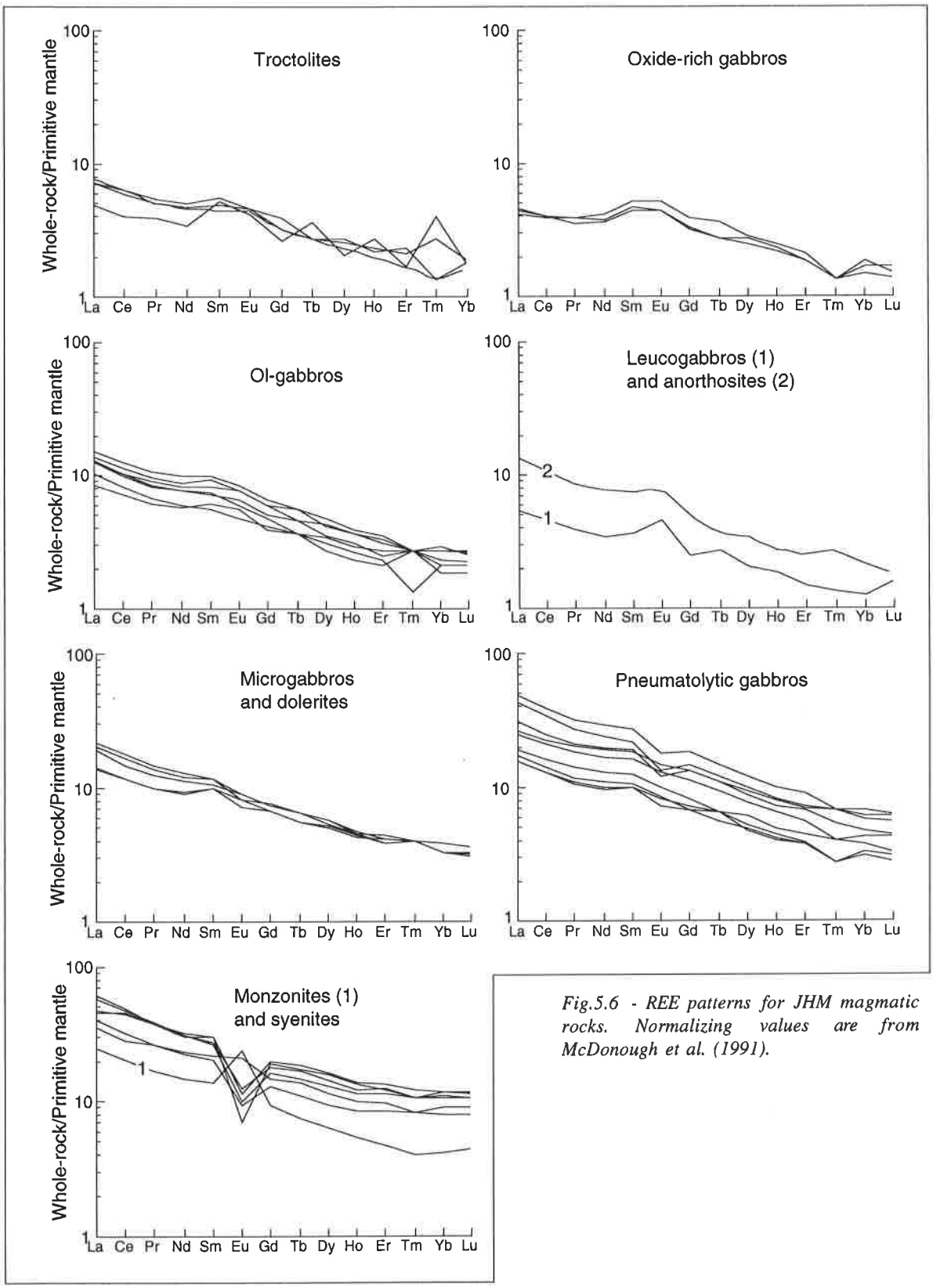

Fig.5.6 - REE patterns for JHM magmatic rocks. Normalizing values are from McDonough et al. (1991).

This subdivision follows the macroscopic and petrographic subdivision between mesocratic (Fe-rich syenites) and leucocratic syenites (Fe-poor syenites). REE contents are the highest among all JHM magmatic rocks, their patterns parallel each others and those of monzonites, except for the negative Eu-anomaly reflecting plagioclase early fractionation.

Dolerites and basalts

Dolerites and basalts are characterized by small compositional variations in most major elements from one dike to another. Trace elements, above all S, vary more. REE content and patterns do not display any significant variation between basic dikes and microgabbros.

The main compositional trend in JHM

Observing the main trend formed by troctolites, ol-gabbros, monzonites and syenites in Figs.5.3 and 5.4, we can conclude that:

- SiO_2 and Na_2O regularly increase from troctolites to syenites, but two compositional gaps exist, one between ol-gabbros, the other between monzonites and syenites (the high density of sampling and the large number of XRF analyses exclude the possibility that gaps are due to lack of representative samples);

- TiO_2 and CaO increase from troctolites to ol-gabbros and decrease from ol-gabbros to monzonites to syenites;

- Al_2O_3 increases from troctolites to monzonites and is roughly constant from monzonites to syenites;

- Fe_2O_{3tot} and MgO decrease from troctolites to syenites;

- K_2O increases from troctolites to monzonites and forms two distinct trends from monzonites to syenites: one is characterized by increasing K_2O, the other by decreasing K_2O;

- Trace elements parallel major elements. In particular, V, Ga and Sr parallels TiO_2 and CaO; Cr, Co, Ni parallel MgO; Rb, Y, Zr and Ba parallel K_2O;

- REE pattern broadly parallel each other and their content increases from troctolites to ol-gabbros to monzonites to syenites. The Eu positive anomaly is present in leucogabbros and anorthosites.

5.3 - Isotopic compositions

Nd and Sr isotopic data (Table 5.7, Fig.5.7) indicate that the mantle component in the primary magma of olivine gabbros was dominant and that crustal contamination during the ascent of the primary magma within the crust was insignificant. On the contrary, syenites display high values of $^{87}Sr/^{86}Sr$, reflecting a certain amount of crustal contamination. Pneumatolytic gabbros and monzonites have isotopic compositions characterized by a Sr-ratio which is only slightly higher than in olivine gabbros.

Sample	93.12	93.55	93.47	94.65	94.64
Rock type	TRC	OXG	PNG	MNZ	SYE
Analysis	1	2	3	4	5
87Sr/86Sr	0.703777	0.703345	0.704497	0.704147	0.713381
143Nd/144Nd	0.512779	0.512807	0.512695	n.m.	n.m.

Table 5.7 - Isotopic compositions of JHM magmatic rocks. TRC = troctolite; OXG = oxide-rich gabbro; PNG = pneumatolytic gabbro; MNZ = monzonite; SYE = syenite.

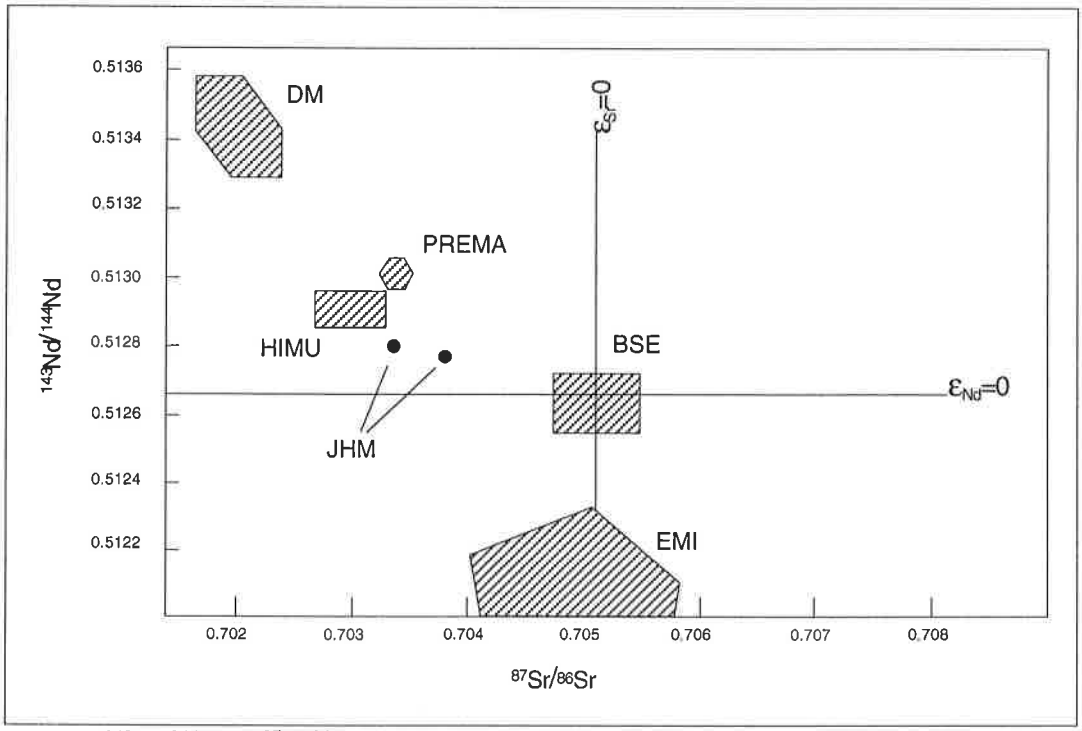

Fig.5.7 - $^{143}Nd/^{144}Nd$ vs $^{87}Sr/^{86}Sr$ isotope correlation diagram (after Zindler & Hart, 1986). DM=depleted mantle; PREMA=prevalent mantle; HIMU=mantle with high U/Pb ratio; BSE=bulk silicate Earth; EMI=enriched mantle; JHM=Jebel Hayim Massif.

5.4 - Discussion

About the significance of whole-rock trends in cumulates

As shown in the previous chapter (§ 4.1), troctolites and ol-gabbros are cumulates having been formed through crystal settling and accumulation of olivine (Fig.5.8). On the contrary, syenites and monzonites form dikes and they do not have evidence of crystal accumulation.

Because of crystal accumulation and residual liquid expulsion, modal association in cumulates never coincides with modal association expected when all rock-forming minerals have grown in equilibrium with the same coexisting liquid. Furthermore, when coexisting liquid is not completely expelled, but trapped, it is commonly affected by post-cumulus liquid-solid reactions. As a consequence, cumulus phases are not representative of the solid fraction, because of crystal accumulation, and interstitial phases are not representative of the liquid fraction, because of liquid expulsion and post-cumulus reactions. Only when evidence for equilibrium crystallisation is strong, one can assumed that the whole-rock composition is representative of the original liquid.

Then, the compositional trend of troctolites and ol-gabbros from JHM does not reflect their liquid evolution, but rather their modal layering which mask any possible observation of liquid evolution. So, the continuous decrease of MgO, Fe_2O_{3tot}, Cr, Co and Ni from troctolite to ol-gabbro must be firstly attributed to the decrease of the modal content of olivine. As well, the CaO-, TiO_2-, Al_2O_3-, Na_2O- and K_2O-enrichment trend from troctolites to ol-gabbros mainly reflects the modal increase of plagioclase, pyroxene and biotite.

About microgabbros and a theoretical parental liquid of troctolites

When dealing with intrusive rocks, geologists commonly assume that the unknown parental liquid of a magmatic series can be represented by its chilled margin.

Geochemical data indicate that microgabbros constituting the JH1-LS chilled margin have a broadly constant bulk composition (Table 5.4), except for Cu and S. Then, assuming that the bulk composition of a chilled margin reflects the composition of the parental magma, and that the parental magma is unique for all JH1-LS troctolites, a

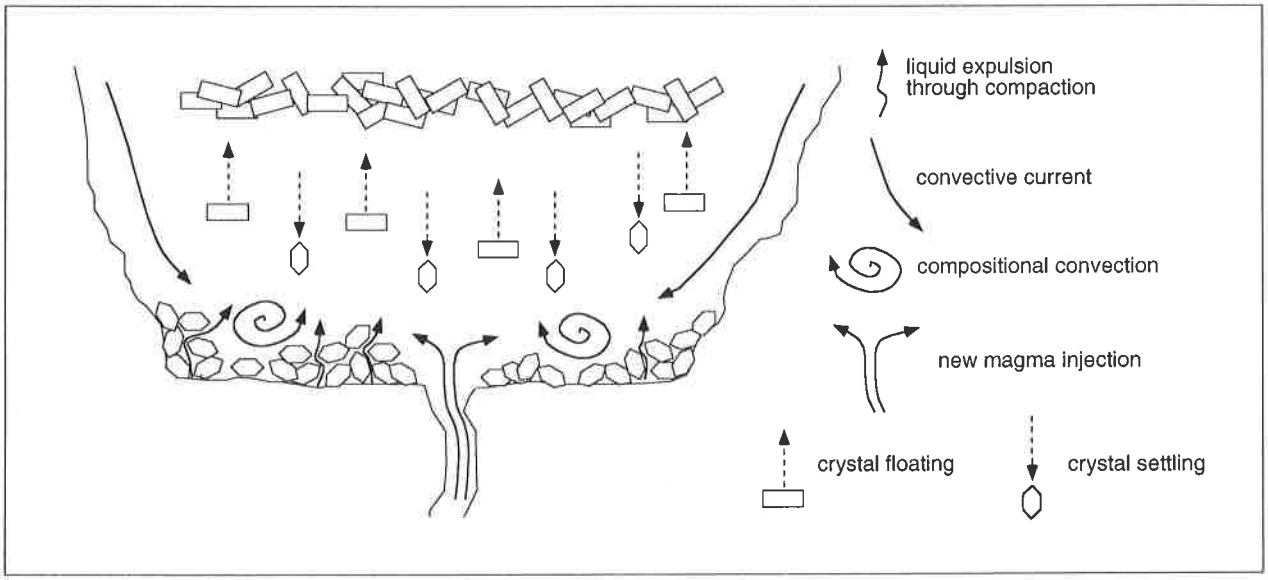

Fig.5.8 - Cumulate-forming mechanical processes in a magma chamber.

theoretical composition of JH1-LS parental magma can be obtained by the average composition of JH1-LS microgabbros. It is a basaltic (SiO_2 = 50%), slightly evolved (MgO# = 58), alkalic (Na_2O+K_2O = 4.4%) magma.

Troctolites are, if compared to this theoretical parental magma, strongly enriched in MgO, Fe_2O_{3tot}, Cr, Co and Ni indicating the large amount of olivine accumulation during troctolite solidification. The higher content of TiO_2, Al_2O_3 and CaO in the parental liquid than in troctolites indicates that plagioclase, pyroxene and Fe-Ti oxides did not accumulate together with olivine.

About oxide-rich gabbros and the liquid evolution in JH1

The compositional homogeneity of oxide-rich gabbros throughout JH1-US reflects the lack of modal layering in the series. If crystal accumulation did not occur and if transformations affecting the coexisting liquid are neglected, then we can assume that oxide-rich gabbros are not cumulates and that the average bulk composition of oxide-rich gabbros is broadly representative of that of JH1-US parental magma.

In comparison with the parental magma obtained for JH1-LS troctolites (§ 5.4), the calculated JH1-US parental magma is poorer in SiO_2, Al_2O_3, MgO, Na_2O, K_2O, Cr, Ni, Rb, Y, Zr, and Ba, and richer in TiO_2, Fe_2O_{3tot}, CaO, V, Cu and Zn (Table 5.8). This compositional discrepancy between the two liquids cannot be attributed to a process of fractional crystallisation linking troctolites to oxide-rich gabbros, because the depletion in compatible elements is not mirrored by the enrichment in incompatible elements. Then, assuming that both calculated liquids represent two parental magmas, it follows that JH1-LS troctolites and JH1-US oxide-rich gabbros originated from two different parental magmas and that the large-scale layering of JH1 is likely to be due to a new magma injection. If two different parental magmas are present within the same magma chamber, it follows that early differentiation processes occurred before magma emplacement.

The oxide-rich gabbros parental magma was, if compared to the troctolites parental magma, extremely depleted in Cr and Ni, and this can be intuitively explained by a early differentiation involving large precipitation of chromite and olivine. The high Fe_2O_3/FeO ratio measured in oxide-rich gabbros could then be the consequence of chromite

and olivine precipitation, which depleted the residual liquid in Fe^{2+} more than in Fe^{3+}. As a consequence, the appearance of magnetite in JH1-LS replacing ilmenite could reflect the higher Fe_2O_3/FeO ratio.

	A	B
SiO_2	42.8 ± 0.5	49.6 ± 0.2
TiO_2	2.8 ± 0.3	1.8 ± 0.0
Al_2O_3	13.7 ± 0.3	15.0 ± 0.1
Fe_2O_{3tot}	17.5 ± 0.7	6.9 ± 0.2
MnO	0.1 ± 0.0	0.1 ± 0.0
MgO	7.2 ± 0.3	10.4 ± 0.0
CaO	12.8 ± 0.7	9.6 ± 0.3
Na_2O	2.2 ± 0.3	3.8 ± 0.1
K_2O	0.3 ± 0.1	0.6 ± 0.3
P_2O_5	0.1 ± 0.0	0.2 ± 0.0
S	540 ± 407	221 ± 166
V	905 ± 100	214 ± 17
Cr	21 ± 5	276 ± 7
Co	61 ± 8	31 ± 2
Ni	64 ± 47	240 ± 21
Cu	551 ± 432	24
Rb	7 ± 0.7	8 ± 5
Sr	392 ± 32	349 ± 10
Y	12 ± 2	20 ± 2
Zr	45 ± 6	127 ± 2
Ba	31 ± 9	136 ± 89
La	3 ± 0.1	23
Ce	7 ± 0.1	60
Nd	5 ± 0.3	30
Sm	2 ± 0.1	7
Eu	0.8 ± 0.1	1.5
Tb	0.3 ± 0.0	0.8
Yb	0.8 ± 0.1	1.5

Table 5.8 - Mean composition of JH1-US oxide-rich gabbros (A) and JH1-LS chilled margin (B). A was calculated from 9 samples; B was calculated from 2 samples, except for REE (1 sample only). Numbers in brackets indicate errors.

An alternative meaningful interpretation of the striking compositional divergence between troctolites and oxide-rich gabbros parental magmas is proposed by Bonnefoi *et al.* (1995): according to the authors, " at large undercooling, thermal feedback in a continuously fed and differentiating magma reservoirs promotes the existence of competing thermochemical steady states. Small variations in magma residence time and cooling rate indice a large thermal and chemical swing (magmatic bifurcation or catastrophe), which interrupts the liquid line of descent, leading to bimodal erupted products. [...] ". Petrological work on ODP leg 118 has revealed a quite spectacular and consistent magmatic gap between olivine gabbros and more differentiated oxide gabbros which are thought to be genetically related. Oxide gabbros are interpreted as late-stage differentiates injected into olivine gabbros at various level along shear zones. To make consistent this hypothesis it must be assumed the presence of a magma reservoir, at depth, in which primary magma evolved and was discontinuously expelled upwards.

About pneumatolytic gabbros

The hypothesis of late-magmatic pneumatolytic processes was postulated in Chapter 3 in order to explain « metagabbros » origin. The proposed model requires a still partially liquid basic magma (the solidification zone), overlying JH1 and JH2 and coming into contact with a volatile-rich evolved magma (Fig.3.6). Geochemical data confirm the presence of a volatile-rich evolved phase interacting with a dominant gabbroic melt.

In fact, bulk compositions of MG1 and MG2 are still gabbroic (SiO_2 < 52%), their isotopic composition is similar to that of troctolites and oxide-rich gabbros, and their REE patterns parallel those of olivine gabbros. Bulk compositions are characterized by random and large variations, are enriched in K_2O, P, Rb, Sr, Y, Zr, Ba and REE, and depleted in Cr, Co and Ni in comparison with most evolved ol-gabbros. The former group is typically comprised by those elements which concentrate in evolved liquids (incompatible elements), and the latter is comprised by elements which are almost absent in evolved liquids (compatible elements), because they are retained into early phases. Also, the low content of CO_2 in pneumatolytic gabbros and the lack of clear spatial relationships between the extent of secondary transformation and pendants exclude the possibility that secondary transformations were due to circulation of hydrothermal fluids from nearby carbonate sediments.

About syenites and monzonites

REE pattern parallelism and compositional trend continuity from gabbros to monzonites to syenites indicate that all magmatic rocks of JHM are likely to have been formed by differentiation of an initial basic magma. Then, a liquid line of descent could be costructed on the basis of liquid evolution

Assuming that the composition of JH1-LS chilled margin is the composition of the JHM parental magma and that monzonite and syenite compositions are liquid compositions, then a liquid line of descent can be constructed from the original primitive magma to the final differentiated liquid. The continuous depletion trend of MgO, CaO, Ni and Cr from the initial liquid to syenites indicates early fractionation of olivine, clinopyroxene and chromite,

which is perfectly consistent with the observed parageneses of olivine gabbros. The almost constant content of Sr in the parental magma and monzonites indicates that plagioclase did not fractionated in the early stage of differentiation, but only in the last stage from monzonites to syenites. Late plagioclase fractionation is also evidenced by the opposite Eu-anomaly in monzonites and syenites (Fig.5.7): the positive anomaly indicates that plagioclase was a fractionating phase at the time of monzonite formation while the negative anomaly in syenites indicates that the final differentiated liquid was depleted in the plagioclase component.

Finally, the isotopic composition of syenites is largely different from that of gabbros. In particular, the high value of Sr ratio indicates a long residence time and crustal contamination which is perfectly consistent with the late emplacement of syenites in JHM.

5.5 - Conclusions

Bulk compositions, REE signatures and isotopic ratios support the hypothesis that all JHM magmatic rocks belong to the same magmatic series, which is mildly alkaline and clearly bimodal. The cumulative feature of most olivine gabbros does not allow full reconstruction of the liquid line of descent for the magmatic association. However, the compositional change from the initial liquid, represented by the JH1-LS chilled margin, to the final one, represented by the syenites, indicates that liquid differentiation was essentially due to crystal settling and accumulation of olivine (crystal fractionation). Pneumatolytic gabbros have bulk compositions which are only mildly more evolved than those of ol-gabbros supporting the hypothesis of low-temperature interaction between basic and acidic melts at the origin of secondary transformations. Syenitic liquid was contaminated by crustal material and contamination is consequence of the longer residence time of the residual liquid prior to emplacement between gabbros.

- CHAPTER 6 -

Mineral Chemistry

As shown in Chapter 5, JHM olivine gabbros are cumulates and their bulk compositions are not representative of liquid compositions and cannot be used as markers of liquid evolution. Then, in order to investigate and discuss differentiation processes occurring during the formation of JHM magmatic rocks, the chemical compositions of mineral phases forming JH1 and JH2 olivine gabbros were investigated by a detailed electron microprobe and neutronic activation study. As well, feldspar, clinopyroxene, biotite and amphibole from pneumatolytic gabbros, monzonites and syenites were analysed by electron microprobe. Mineral data presentation and interpretation constitute the aim of Chapter 6.

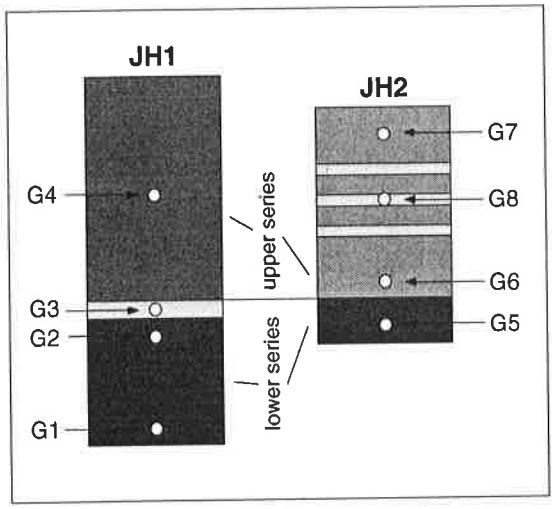

Fig.6.1 - Localisation of selected olivine gabbros which were the object of the electron microprobe and neutronic activation investigation. JH1-LS and JH2-US are layered series and two samples have been collected for each of them, one from the bottom and the other from the top of the series. G1 = 93.12 (TRC); G2 = 93.61 (TRC); G3 = 93.57 (LCG); G4 = 93.55 (OXG); G5 = 94.29 (TRC); G6 = 94.25 (OLG); G7 = 94.21 (OLG); G8 = 94.26 (ANR).

6.1. Mineral compositions

Olivine

Olivine is a major component of troctolites, olivine gabbros, oxide-rich gabbros and leucogabbros. In pneumatolytic gabbros it is replaced by Mg-chlorite and, rarely, talc.

Olivine from JH1 and JH2 (Table 6.1, Fig.6.2) is MgO-rich (Fo>50), weakly zoned and its composition in cores varies within JH1 and JH2, with the Fo content decreasing from the lower to the upper series of each complexes (Fo_{77} to Fo_{64} in JH1, and Fo_{75} to Fo_{63} in JH2) and from bottom to top in JH1-LS and JH2-US (Fo_{77} to Fo_{73} in JH1-LS troctolites, and Fo_{67} to Fo_{56} in JH2-US ol-gabbros). In JH1-LS leucogabbros, olivine composition is intermediate between that of olivine from JH1-LS troctolites and that of olivine from JH1-US oxide-rich gabbros (Fo_{70}). Compositional zoning (Figs.6.3) is not ubiquitous and, when present, it is characterized by very mild Fo depletion from core to rim (Δ_{Fo}<4%).

With regard to trace elements (Fig.6.4, Table 6.2), Ni parallels Fo while Co mildly decreases upwards in JH1-LS and in JH2-US, is slightly higher in leucogabbros and still higher in oxide-rich gabbros. Sc mildly increase upwards in JH1-LS troctolites, is higher in JH2-LS troctolites, and in leucogabbros, is still higher in oxide-rich gabbros and decreases from bottom to top in JH2-US. In JH1, Hf and Ta are higher in troctolites than in overlying leucogabbros and oxide-rich gabbros. In JH2, Ta is higher in troctolites than in overlying ol-gabbros, while Hf mildly increases from bottom to top in JH2-US.

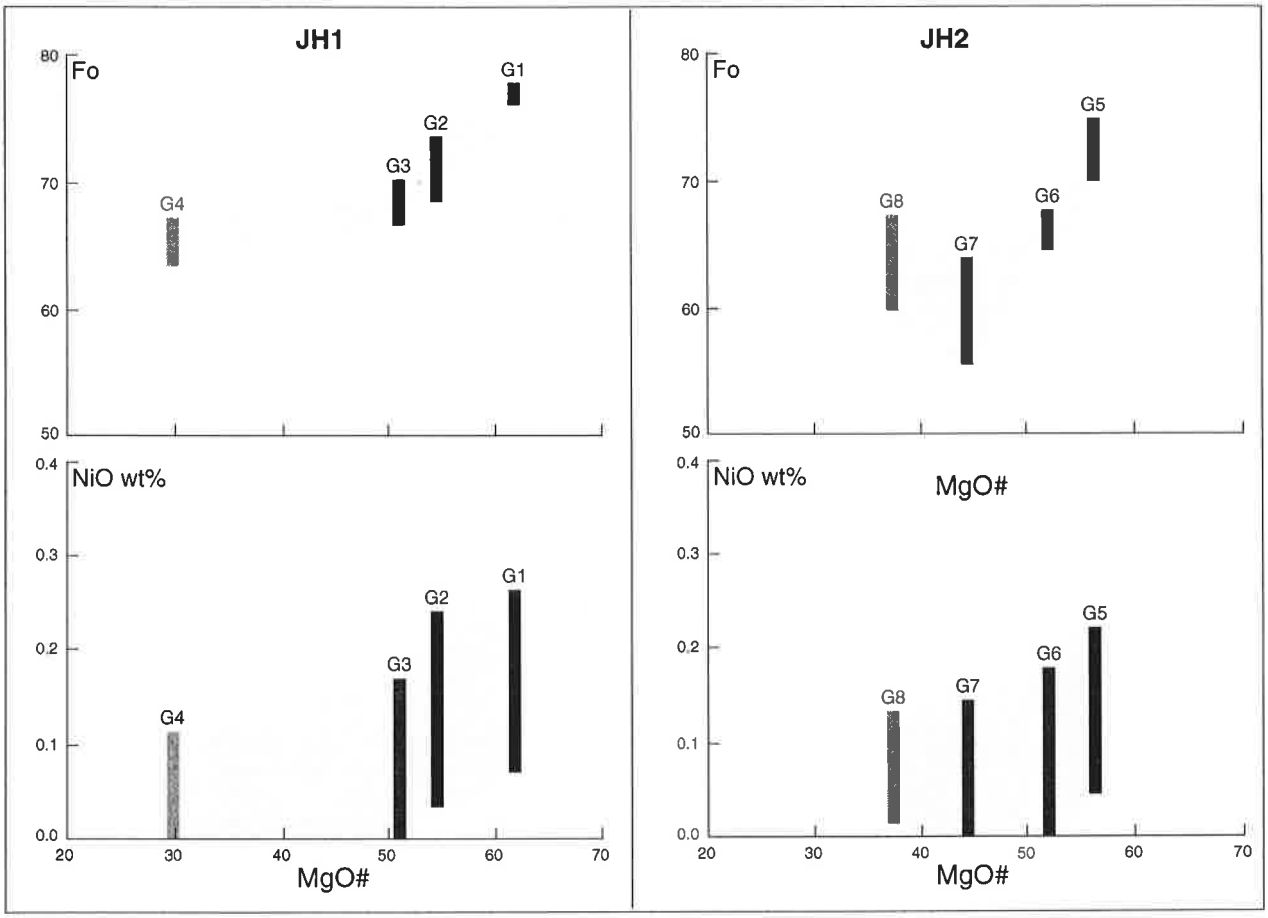

Fig.6.2 - Compositional variation in olivines from JH1 and JH2 olivine gabbros. Sample localisation in Fig.61. MgO# is the MgO number of the host rock (see Chapter 5). Fo = 100Mg/(Mg+Fe2+). Vertical bars are compositional ranges. G1 = 252 analysis points; G2 = 156; G3 = 175; G4 = 102; G5 = 209; G6 = 187; G7 = 122; G8 = 15.

Sample	G1	G2	G3	G4	G5	G6	G7	G8
Rock type	TRC	TRC	LCG	OXG	TRC	OLG	OLG	ANR
Series	JH1-LS	JH1-LS	JH1-LS	JH1-US	JH2-LS	JH2-US	JH2-US	JH2-US
SiO_2	38.30	37.77	37.29	36.48	37.67	36.71	35.63	36.75
TiO_2	0.01	0.04	0.04	0.03	0.00	0.04	0.06	0.01
Al_2O_3	0.00	0.04	0.01	0.02	0.00	0.02	0.03	0.03
Cr_2O_3	0.04	0.00	0.00	0.01	0.00	0.00	0.00	0.00
FeO	21.23	25.30	27.77	31.40	24.21	29.31	35.68	29.49
MnO	0.34	0.33	0.44	0.47	0.35	0.48	0.54	0.49
MgO	40.02	36.60	34.78	31.89	37.56	33.25	28.41	33.30
CaO	0.06	0.26	0.08	0.09	0.27	0.22	0.22	0.15
NiO	0.23	0.20	0.07	0.06	0.20	0.14	0.10	0.08
Total	100.23	100.54	100.47	100.45	100.26	100.17	100.67	100.31
Si^{4+}	0.991	0.993	0.993	0.990	0.989	0.990	0.987	0.990
Ti^{4+}	0.000	0.001	0.001	0.001	0.000	0.001	0.001	0.000
Al^{3+}	0.000	0.001	0.000	0.001	0.000	0.001	0.001	0.001
Cr^{3+}	0.001	0.000	0.000	0.000	0.000	0.000	0.000	0.000
Fe^{2+}	0.459	0.556	0.618	0.712	0.532	0.661	0.827	0.664
Mn^{2+}	0.007	0.007	0.010	0.011	0.008	0.011	0.013	0.011
Mg^{2+}	1.543	1.435	1.380	1.290	1.470	1.337	1.174	1.337
Ca^{2+}	0.002	0.007	0.002	0.003	0.008	0.006	0.007	0.004
Ni^{2+}	0.005	0.004	0.001	0.001	0.004	0.003	0.002	0.002
Fo	77.1	72.1	69.1	64.4	73.5	66.9	58.7	66.8

Table 6.1 - Representative analyses of olivine cores from JH1 and JH2. Structural formulae were calculated on the basis of 4 oxygens. Fo = 100Mg/(Mg+Fe).

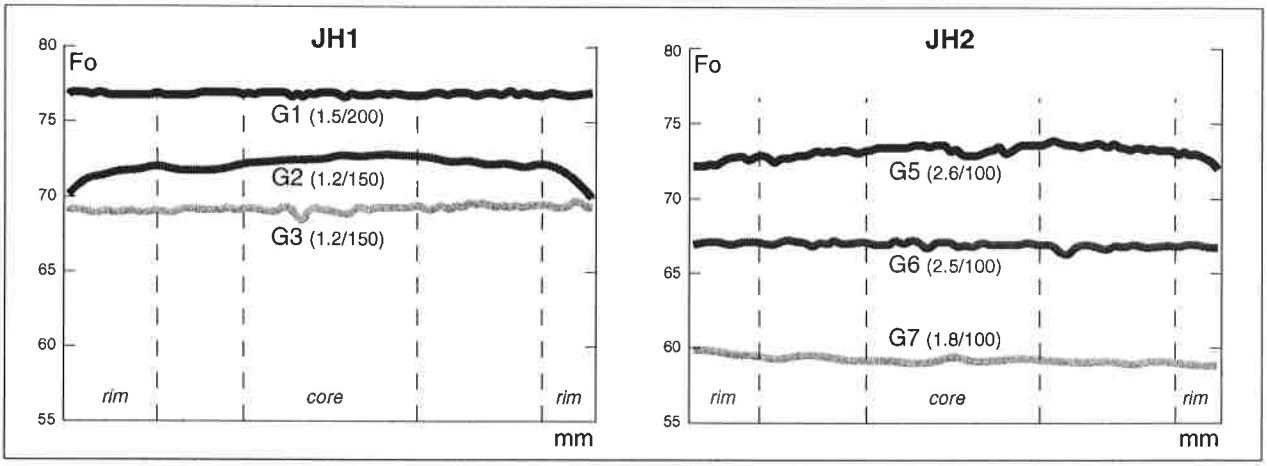

Fig.6.3 - Compositional profiles through olivines from JH1 and JH2 olivine gabbros. Fo = 100Mg/(Mg+Fe2+). Numbers in brackets are profile lenght (cm) and analysis points, respectively.

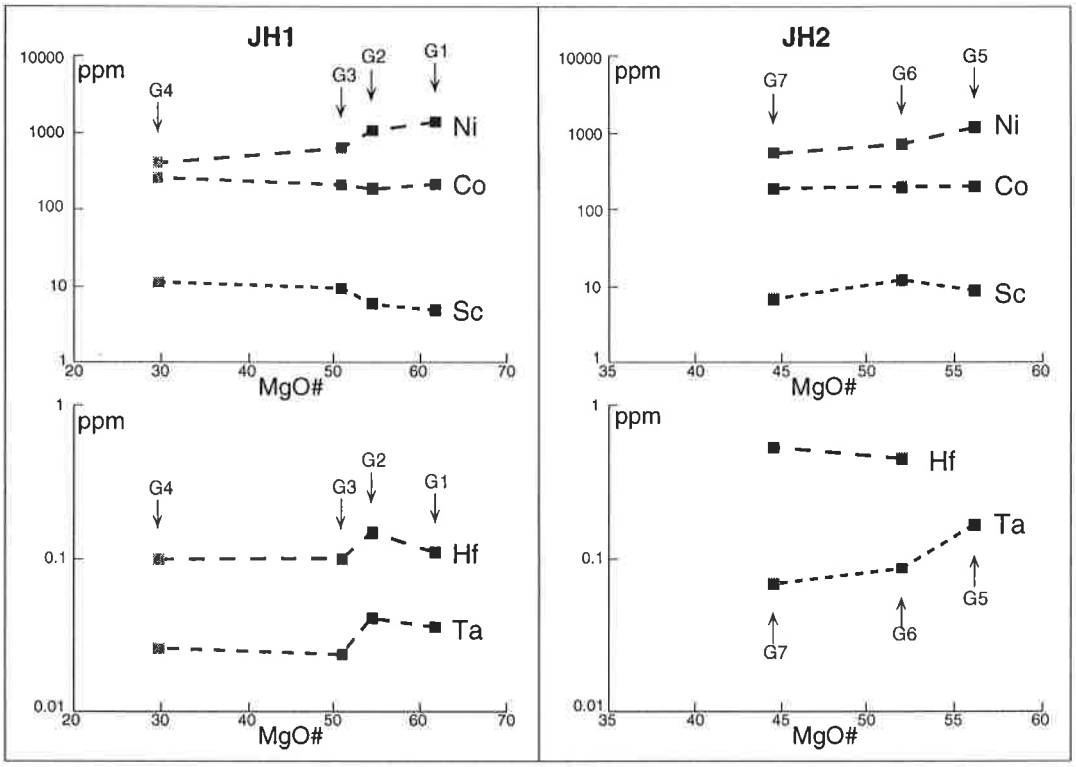

Fig.6.4 - Trace element concentrations in JH1 and JH2 olivines. MgO is the MgO number of the host rock.*

Sample	Sc	Co	Ni	Hf	Ta
G1	4.6 (0.0)	198 (0.07)	1376 (0.1)	0.11 (2.5)	0.036 (0.0)
G2	5.6 (0.0)	183 (0.0)	1022 (0.5)	0.15 (0.3)	0.040 (0.0)
G3	8.8 (0.0)	200 (0.0)	623 (0.5)	0.10 (2.8)	0.023 (/)
G4	11.2 (0.0)	255 (0.0)	385 (0.1)	0.10 (2.3)	0.026 (0.0)
G5	8.4 (3.7)	188 (1.1)	1177 (0.1)	n.d.	0.162 (0.0)
G6	11.5 (0.0)	189 (0.0)	684 (0.2)	0.45 (0.0)	0.084 (0.0)
G7	6.4 (0.2)	177 (0.0)	535 (0.2)	0.53 (0.0)	0.067 (0.0)

Table 6.2 - Trace element concentrations in olivines from JH1 and JH2. Numbers in brackets are standard deviations (1σ). n.d. = not detected.

Plagioclase and alkali-feldspar

Plagioclase is a major component of olivine gabbros and pneumatolytic gabbros, and alkali-feldspar is a major component of monzonites and syenites.

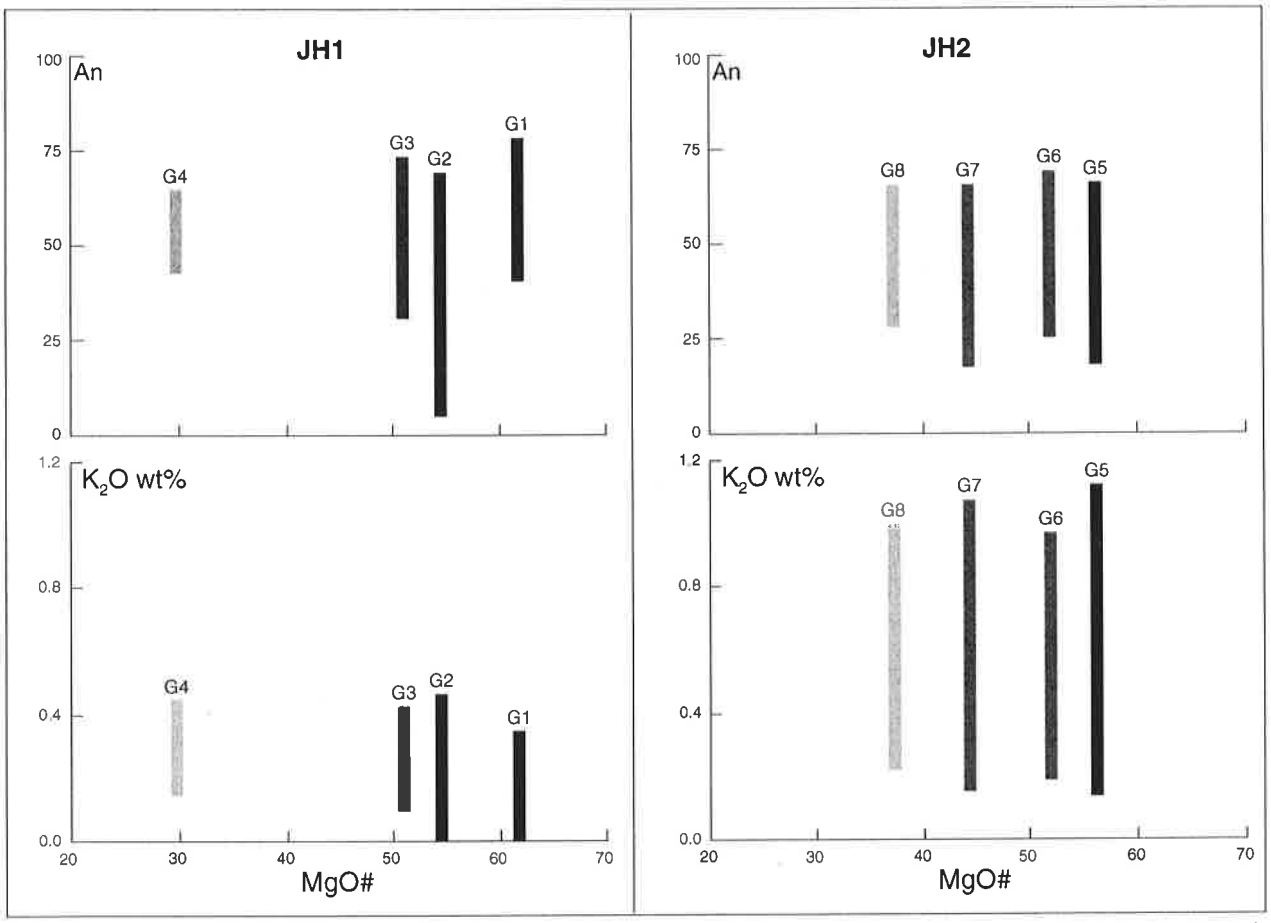

Fig.6.5 - Compositional variation in plagioclases from JH1 and JH2 olivine gabbros. Sample localisation in Fig.6.1. MgO# is the MgO number of the host rock (see Chapter 5). An = 100Ca/(Ca+Na+K). Vertical bars are compositional ranges. G1 = 464 analysis points; G2 = 158; G3 = 445; G4 = 276; G5 = 231; G6 = 488; G7 = 300; G8 = 509.

Plagioclase from JH1 and JH2 (Table 6.3, Fig.6.5) is labradorite to bytwonite, in cores, and albite to oligoclase in rims. Core composition mildly varies both from one series to another and within each series, with increasing An from bottom to top in JH1-LS troctolites (An_{60} to An_{68}) and decreasing in ol-gabbros (An_{68} to An_{64}). Plagioclase is, in cores, An_{65} in JH2-LS troctolites and An_{64} in oxide-rich gabbros. Plagioclase from leucogabbros is higher in An than plagioclase from underlying troctolites and from overlying oxide-rich gabbros (An_{72}). All plagioclases from JH2 olivine gabbros have higher contents of K_2O than those from JH1.

In plagioclases from ophitic troctolites, compositional zoning in the core of the large laths is the same as compositional zoning in the small laths enclosed by pyroxene megacrysts, and it is characterized by a sharp and abrupt increase of An content from the most internal portion to most external one (An_{60} to An_{77}, Fig.6.6). This reverse zoning reflects the beginning of augite crystallization (Morse, 1984) and, as a consequence, the earlier crystallization of plagioclase relative to clinopyroxene. Plagioclase from subhedral-granular troctolites and ol-gabbros commonly displays strong compositional zoning (Δ_{An}=40-50), with constant An in cores and stepwise decreasing An in rims. In plagioclase from oxide-rich gabbros (Fig. 6.6) compositional zoning is mild (Δ_{An}=20) and oscillatory. The lack of reverse zoning in the core reflects the simultaneous crystallization of plagioclase and clinopyroxene.

With regard to trace element (Table 6.4, Fig.6.7), Sr mildly increases upwards in JH1-LS troctolites and mildly decreases upwards in JH2-US; it is lower in leucogabbros, in JH2-LS and in oxide-rich gabbros. Sc is constant in JH1-LS troctolites, mildly upward decreasing in JH2-US ol-gabbros, higher in JH2-LS troctolites and lower in leucogabbros and in oxide-rich gabbros. Ni decreases from bottom to top in JH1 as well as in JH2. Hf, Ta, La, Eu, Tb and Th increase from bottom to top in JH1-LS troctolites, they are lower in overlying leucogabbros and still lower in oxide-rich gabbros. In JH2 plagioclase, the content of Hf, Ta, REE and Th is higher than in JH1, it is highest in JH2-LS troctolites and in JH2-US microgabbros, and it decreases upwards in JH2-US ol-gabbros.

Plagioclase from pneumatolytic gabbros (Table 6.5) has discontinuous compositional zoning, with large internal portions characterized by strong low-temperature transformation (saussuritization and/or prehnitization) and an external portion made up of untransformed albite (Ab_{91} to Ab_{99}).

Feldspar from monzonites (Table 6.5) is strongly heterogeneous anorthoclase with composition ranging from Ab_{99} to Or_{70} and locally rimmed by perthitic feldspar (Ab_2 to Ab_{99} and Or_0 to Or_{98}). Feldspar from syenites (Table 6.5) is homogeneous oligoclase to albite (Ab_{86} to Ab_{100}).

Sample	G1	G2	G3	G4	G5	G6	G7	G8
Rock type	TRC	TRC	LCG	OXG	TRC	OLG	OLG	ANR
Series	JH1-LS	JH1-LS	JH1-LS	JH1-US	JH2-LS	JH2-US	JH2-US	JH2-US
SiO_2	52.25	51.45	49.80	51.62	52.58	50.80	51.68	51.62
TiO_2	0.10	0.07	0.05	0.11	0.17	0.06	0.05	0.06
Al_2O_3	30.56	30.20	31.65	30.42	29.84	30.70	30.18	30.11
Fe_2O_3	0.27	0.77	0.51	0.55	0.35	0.50	0.48	0.37
MgO	0.04	0.05	0.02	0.06	0.01	0.01	0.01	0.01
CaO	12.54	12.92	14.10	12.72	12.37	13.47	13.24	12.98
Na_2O	4.32	3.95	3.31	4.05	4.44	3.62	3.99	3.90
K_2O	0.19	0.19	0.17	0.24	0.19	0.20	0.21	0.33
Total	100.27	99.61	99.63	99.76	99.95	99.37	99.85	99.38
Si^{4+}	9.458	9.395	9.120	9.401	9.541	9.304	9.417	9.441
Ti^{4+}	0.014	0.010	0.007	0.016	0.023	0.008	0.007	0.009
Al^{3+}	6.519	6.500	6.831	6.529	6.381	6.627	6.482	6.490
Fe^{3+}	0.037	0.106	0.071	0.075	0.048	0.069	0.066	0.051
Mg^{2+}	0.011	0.014	0.007	0.015	0.004	0.004	0.004	0.003
Ca^{2+}	2.431	2.528	2.766	2.481	2.405	2.644	2.586	2.542
Na^{1+}	1.516	1.397	1.174	1.430	1.562	1.286	1.410	1.383
K^{1+}	0.045	0.045	0.040	0.055	0.045	0.048	0.048	0.078
An	60.9	63.7	69.5	62.6	60.0	66.5	63.9	63.5
Ab	38.0	35.2	29.5	36.0	38.9	32.3	34.9	34.5
Or	1.1	1.1	1.0	1.4	1.1	1.2	1.2	1.9

Table 6.3 - Representative analyses of plagioclase cores from JH1 and JH2. Structural formulae were calculated on the basis of 32 oxygens. An = 100Ca/(Ca+Na+K). Ab = 100Na/(Ca+Na+K). Or = 100K/(Ca+Na+K).

Sample	Sc	Co	Ni	Sr	Hf	Ta	La	Eu	Tb	Th
G1	0.99 (0.4)	7.4 (0.3)	47 (0.4)	855 (0.2)	0.19 (1.6)	0.12 (0.0)	4.2 (0.2)	1.0 (0.0)	0.04 (4.5)	0.23 (0.0)
G2	0.94 (0.0)	5.8 (0.0)	38 (0.8)	923 (0.5)	0.67 (0.1)	0.16 (0.0)	4.9 (0.6)	1.1 (0.0)	0.07 (0.0)	0.68 (0.3)
G3	0.70 (1.1)	3.2 (0.0)	11 (1.4)	839 (0.6)	0.15 (0.0)	0.06 (0.0)	5.6 (0.0)	0.8 (2.5)	0.03 (0.0)	0.19 (0.0)
G4	0.81 (0.2)	2.0 (0.0)	6 (0.5)	522 (0.1)	0.04 (1.6)	0.03 (0.9)	2.2 (0.0)	0.5 (0.0)	0.01 (3.7)	0.06 (0.7)
G5	2.24 (3.7)	9.4 (1.1)	62 (0.6)	735 (2.7)	n.d.	0.35 (0.0)	8.5 (0.0)	1.4 (0.0)	0.22 (0.0)	1.03 (3.8)
G6	0.99 (0.0)	3.4 (0.0)	15 (0.9)	901 (0.3)	0.86 (0.0)	0.21 (0.0)	6.7 (0.0)	1.3 (0.0)	0.16 (0.0)	0.86 (0.0)
G7	0.78 (0.0)	4.1 (0.0)	13 (0.6)	856 (0.2)	1.52 (0.0)	0.21 (0.0)	7.3 (0.1)	1.5 (0.0)	0.12 (0.0)	0.79 (0.0)
G8	n.d.	1.9 (1.3)	5 (1.7)	824 (2.7)	n.d.	0.19 (0.0)	6.3 (0.5)	1.4 (0.0)	0.15 (0.0)	0.85 (0.0)

Table 6.4 - Trace element concentrations in plagioclases from JH1 and JH2. Numbers in brackets are standard deviations (1σ). n.d. = not detected.

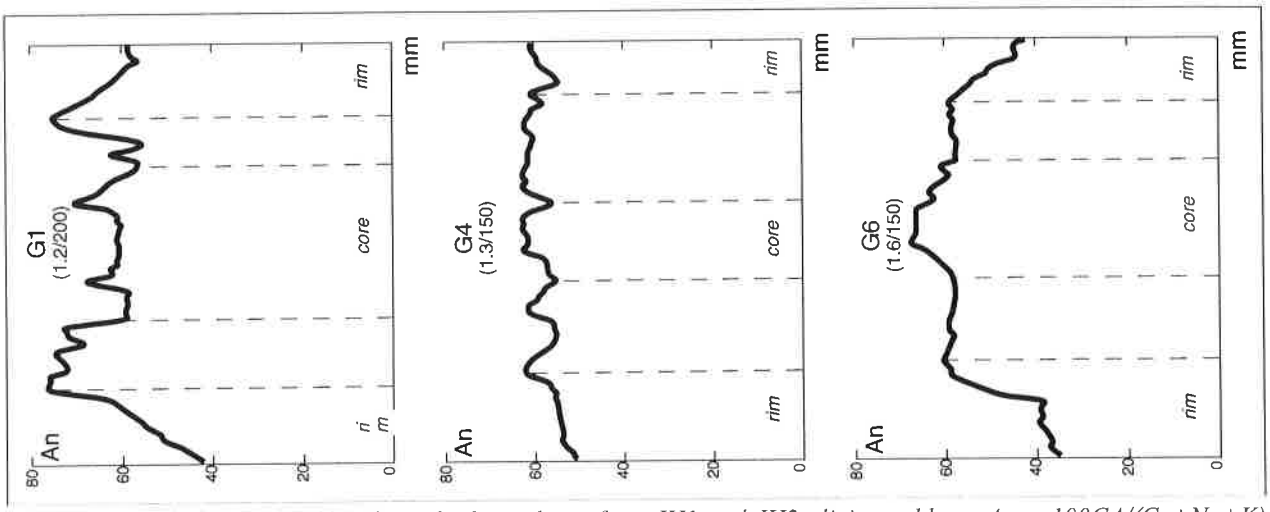

Fig.6.6 - Compositional profiles through plagioclases from JH1 and JH2 olivine gabbros. An = 100CA/(Ca+Na+K) Numbers in brackets are profile length (in cm) and numbers of analysis points, respectively.

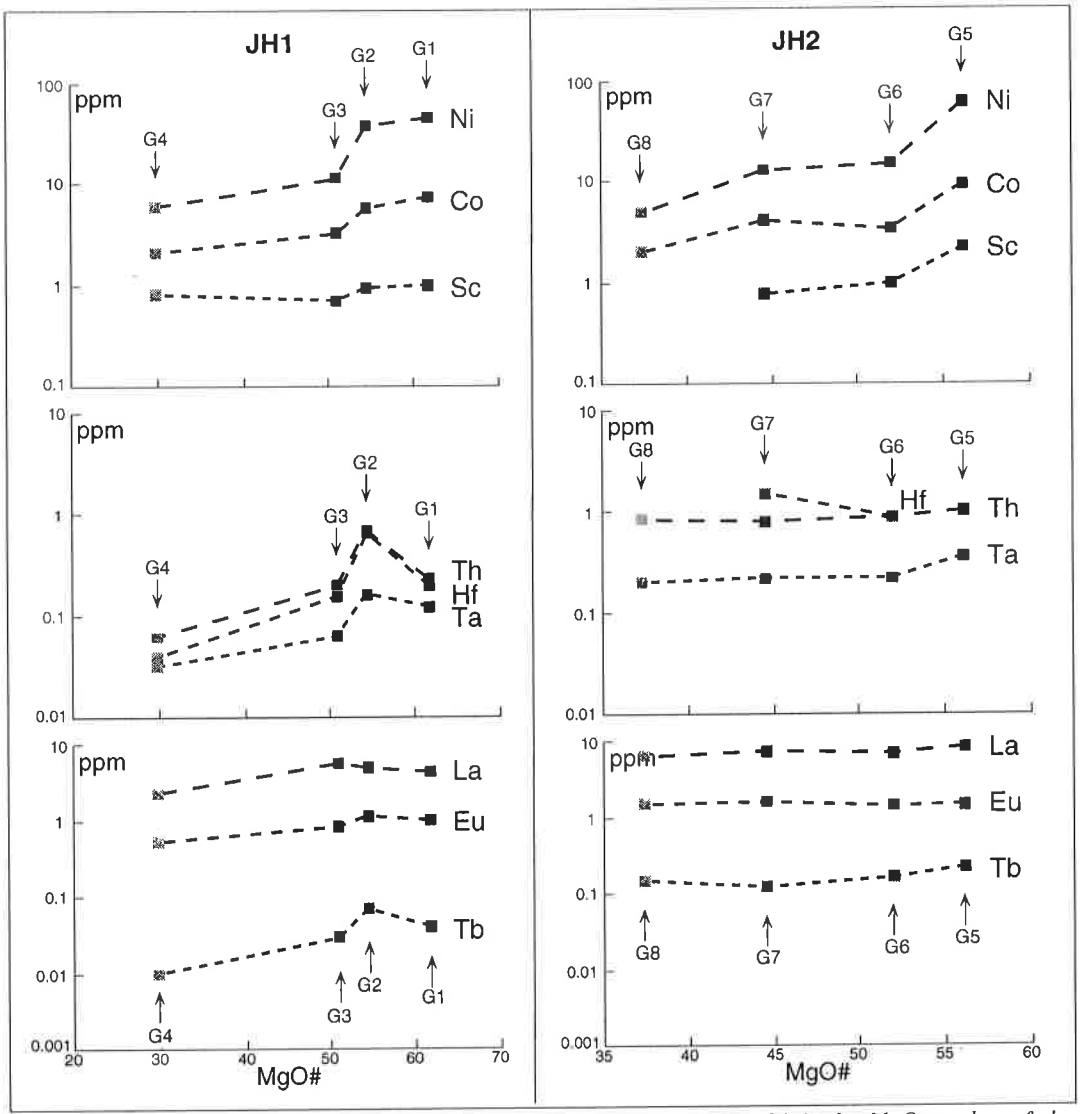

Fig.6.7 - Trace element concentrations in JH1 and JH2 plagioclases. MgO is the MgO number of the host rock.*

Sample	94.30	93.40	94.50	94.50	93.6	93.6
Rock type	PNG	PNG	MNZ	MNZ	SYE	SYE
SiO_2	67.83	67.71	67.85	64.54	68.95	68.44
TiO_2	0.02	0.04	0.04	0.00	0.00	0.00
Al_2O_3	19.74	19.87	19.16	17.93	19.40	19.33
Fe_2O_3	0.19	0.10	0.11	0.23	0.44	0.45
MgO	0.01	0.02	0.00	0.02	0.00	0.01
CaO	0.63	0.65	0.29	0.04	0.13	0.23
Na_2O	10.85	11.14	11.33	1.18	11.65	11.17
K_2O	1.04	0.07	0.83	15.20	0.31	0.79
Total	100.31	99.59	99.62	99.14	100.89	100.42
Si^{4+}	11.883	11.887	11.957	12.011	11.970	11.958
Ti^{4+}	0.002	0.006	0.005	0.000	0.000	0.000
Al^{3+}	4.076	4.110	3.980	3.933	3.969	3.981
Fe^{3+}	0.025	0.013	0.015	0.032	0.057	0.059
Mg^{2+}	0.002	0.005	0.000	0.005	0.001	0.002
Ca^{2+}	0.118	0.122	0.054	0.009	0.025	0.043
Na^{1+}	3.685	3.790	3.869	0.425	3.922	3.782
K^{1+}	0.233	0.016	0.187	3.608	0.068	0.176
An	2.9	3.1	1.3	0.2	0.6	1.1
Ab	91.3	96.5	94.1	10.5	97.7	94.5
Or	5.8	0.4	4.6	89.3	1.7	4.4

Table 6.5 - Representative analyses of feldspars from pneumatolytic gabbros (rim), monzonites and syenites. Structural formulae were calculated on the basis of 32 oxygens. An = 100Ca/(Ca+Na+K). Ab = 100Na/(Ca+Na+K). Or = 100K/(Ca+Na+K).

Clinopyroxene

Pyroxene from olivine gabbros and pneumatolytic gabbros is Mg-rich augite to diopside, while pyroxene from monzonites is hedenbergite to Mg-free augite (Fig.6.8). Wo content always exceed 40% in pyroxene from gabbros and 38% in pyroxene from monzonites.

Sample	G1	G2	G3	G4	G5	G6	G7	G8
Rock type	TRC	TRC	LCG	OXG	TRC	OLG	OLG	ANR
Series	JH1-LS	JH1-LS	JH1-LS	JH1-US	JH2-LS	JH2-US	JH2-US	JH2-US
SiO_2	49.55	50.07	50.36	51.49	50.64	50.66	51.47	50.40
TiO_2	1.49	1.18	1.31	0.66	1.63	0.97	1.00	1.71
Al_2O_3	3.98	3.68	3.06	2.06	2.90	2.72	2.07	2.72
Cr_2O_3	0.61	0.69	0.04	0.00	0.42	0.83	0.28	0.14
Fe_2O_3	2.74	2.04	2.88	2.50	2.15	2.52	1.45	2.01
FeO	3.91	5.29	4.99	5.95	5.07	4.26	6.12	6.05
MnO	0.13	0.13	0.18	0.19	0.20	0.11	0.18	0.18
MgO	14.81	14.55	14.86	14.73	14.70	15.39	15.14	14.34
CaO	21.74	21.55	21.60	21.53	21.33	21.55	21.24	21.32
Na_2O	0.49	0.41	0.43	0.47	0.70	0.44	0.42	0.58
K_2O	0.00	0.00	0.01	0.00	0.00	0.00	0.00	0.01
Total	99.50	99.67	99.78	99.59	99.73	99.46	99.36	99.44
Si^{4+}	1.841	1.862	1.871	1.918	1.880	1.882	1.917	1.883
$^{IV}Al^{3+}$	0.159	0.138	0.129	0.082	0.120	0.118	0.083	0.117
$^{VI}Al^{3+}$	0.016	0.024	0.005	0.009	0.007	0.001	0.008	0.003
Ti^{4+}	0.042	0.033	0.037	0.018	0.045	0.027	0.028	0.048
Cr^{3+}	0.018	0.020	0.001	0.000	0.012	0.024	0.008	0.004
$^{VI}Fe^{3+}$	0.077	0.057	0.080	0.070	0.060	0.070	0.041	0.056
Fe^{2+}	0.121	0.164	0.155	0.185	0.157	0.132	0.191	0.189
Mn^{2+}	0.004	0.004	0.006	0.006	0.006	0.003	0.006	0.006
Mg^{2+}	0.821	0.807	0.823	0.818	0.813	0.852	0.841	0.799
Ca^{2+}	0.865	0.859	0.860	0.859	0.848	0.858	0.848	0.853
Na^{1+}	0.035	0.030	0.031	0.034	0.050	0.032	0.030	0.042
K^{1+}	0.000	0.000	0.001	0.000	0.000	0.000	0.000	0.001
Wo	45.8	45.4	44.7	44.3	45.0	44.8	44.0	44.8
En	43.5	42.7	42.8	42.2	43.2	44.5	43.6	42.0
Fs	10.7	11.9	12.5	13.5	11.8	10.8	12.4	13.2

Table 6.6 - Representative analyses of clinopyroxene from JH1 and JH2. Structural formulae were calculated on the basis of 6 oxygens and 4 cations. Wo = 100Ca/(Ca+Mg+Fe^{tot}). En = 100Mg/(Ca+Mg+Fe^{tot}). Fs = 100 Fe^{tot}/(Ca+Mg+Fe^{tot}).

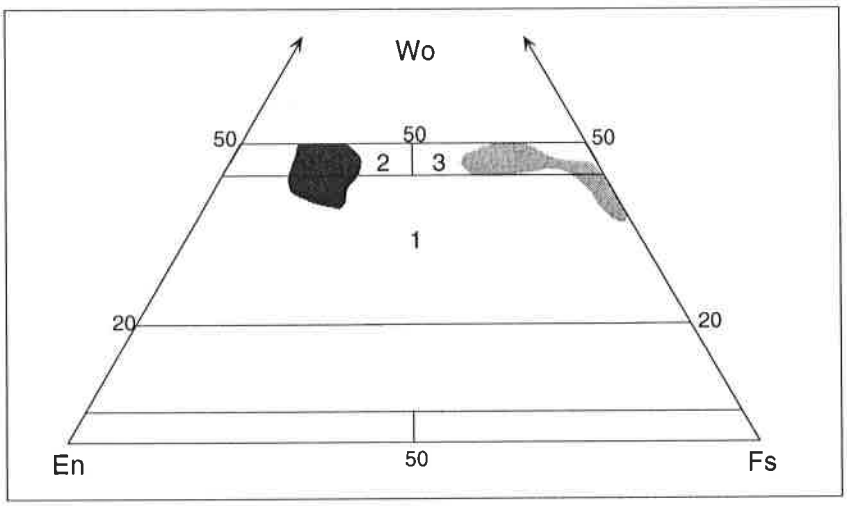

Fig.6.8 - Classification of JHM clinopyroxenes. 1 = augite; 2 = diopside; 3 = hedenbergite. Dark grey area is the compositional range of clinopyroxenes from olivine gabbros and pneumatolytic gabbros.

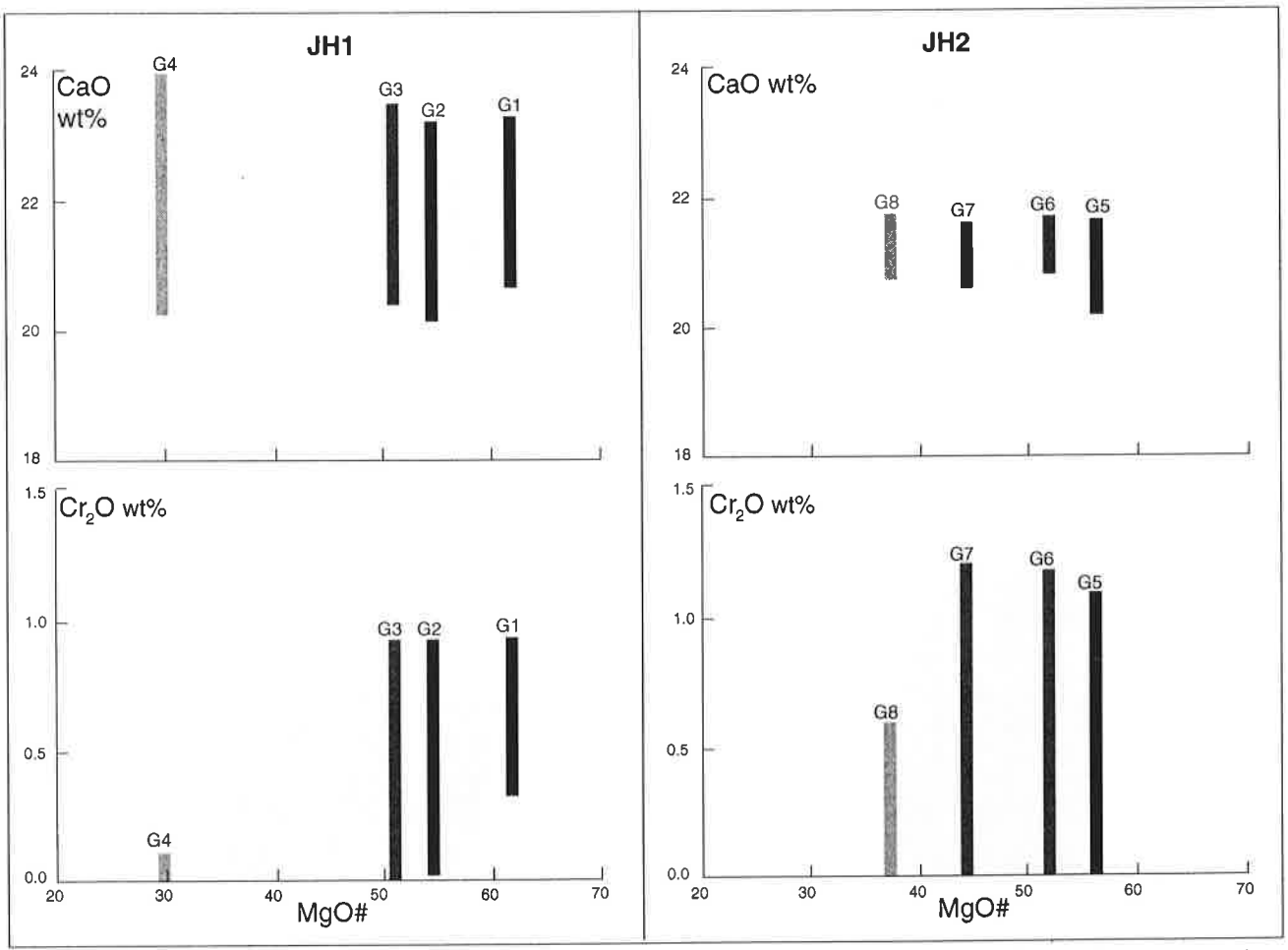

Fig.6.9 - Compositional variation in clinopyroxenes from JH1 and JH2 olivine gabbros. Sample localisation in Fig.6.1. MgO# is the MgO number of the host rock (see Chapter 5). Vertical bars are compositional ranges. G1 = 321 analysis points; G2 = 714; G3 = 269; G4 = 383; G5 = 179; G6 = 161; G7 = 376; G8 = 14.

In JH1 and JH2, pyroxene composition mildly varies from one series to another and within each series (Table 6.6, Fig.6.9), with increasing FeO from bottom to top in JH1 and in JH2-US, and constant CaO, Al_2O_3 and TiO_2. Cr_2O_3 does not exceed 1.5% in troctolites and ol-gabbros, and is almost absent in oxide-rich gabbros (<0.1%).

Compositional zoning in pyroxene from troctolites is rarely symmetrical, often oscillatory and discontinuous for all major elements. Except for few cases, variations are small and a strong Cr- and Ti-depletion is commonly present in the most external portion of rims; Al_2O_3 mirrors SiO_2 and parallels TiO_2. CaO content is constant, except for sudden sharp peaks, mirrored by TiO_2 and Al_2O_3. Compositional zoning in ol-gabbros and oxide-rich gabbros is commonly symmetrical and characterized by outward decreasing of MgO and Cr_2O_3, mirrored by FeO. Abrupt variations of Al_2O_3 have been observed in pyroxene from leucogabbros.

With regard to trace elements (Table 6.7, Fig.6.10), Sc and Co have roughly constant concentrations within JH1 and JH2 clinopyroxenes, and from one complex to the other, while Ni is higher in troctolites than in ol-gabbros. Hf, Ta, La, Eu, Tb and Th increase from JH1-LS troctolites to JH2-US ol-gabbros to JH2-LS troctolites. Because of the strong late-magmatic transformation of augite to amphibole and biotite, trace element concentrations from oxide-rich gabbros clinopyroxene were rejected.

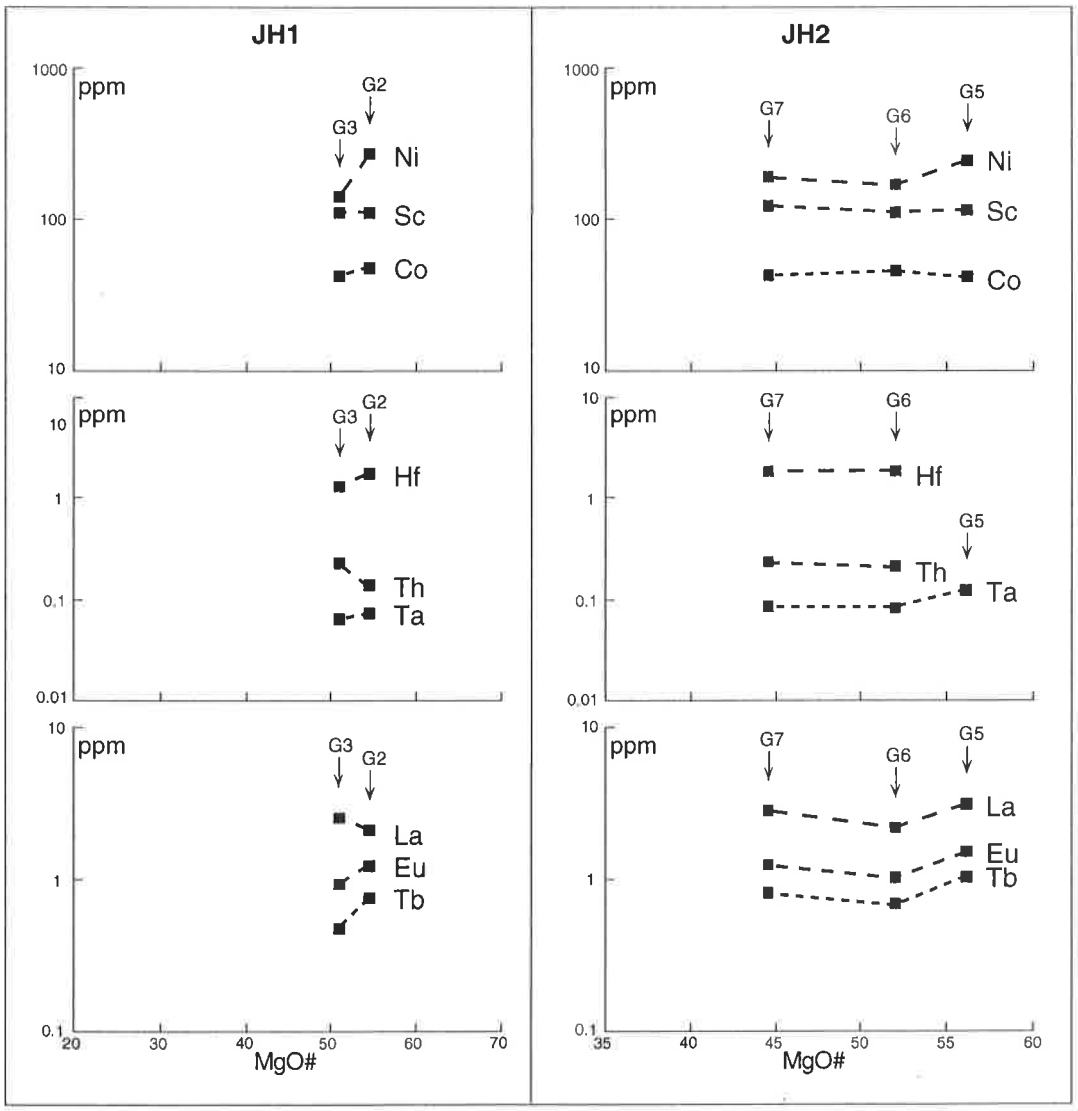

Fig.6.11 - Trace element concentrations in JH1 and JH2 clinopyroxenes. MgO is the MgO number of the host rock.*

Sample	Sc	Co	Ni	Hf	Ta	La	Eu	Tb	Th
G2	110 (0.7)	47 (0.0)	267 (0.5)	1.7 (0.0)	0.07 (2.2)	2.1 (0.0)	1.2 (1.4)	0.74 (2.0)	0.13 (0.0)
G3	109 (0.0)	42 (0.0)	138 (0.5)	1.3 (0.2)	0.06 (2.0)	2.6 (0.0)	0.9 (1.5)	0.48 (2.0)	0.22 (1.4)
G5	115 (3.7)	41 (1.1)	240 (0.3)	n.d.	0.12 (0.0)	3.1 (0.3)	1.5 (0.0)	1.03 (0.0)	n.d.
G6	111 (0.0)	45 (0.0)	166 (0.5)	1.8 (0.0)	0.08 (0.0)	2.2 (0.0)	1.0 (0.0)	0.67 (0.0)	0.20 (0.0)
G7	120 (0.1)	42 (0.0)	183 (0.4)	1.8 (0.0)	0.08 (0.0)	2.8 (0.1)	1.2 (0.1)	0.81 (0.0)	0.22 (0.0)

Table 6.7 - Trace element concentrations in clinopyroxenes from JH1 and JH2. Numbers in brackets are standard deviations (1σ). n.d. = not detected.

Clinopyroxene from pneumatolytic gabbros (Table 6.8, Fig.6.11) is still broadly the same as clinopyroxene from olivine gabbros (Mg-rich augite). Pyroxene from monzonites (Table 6.8, Fig.6.11) is, on the contrary, MgO-poor (<6%) and FeO-rich (up to 28%), and it is characterized by a strong irregular compositional zoning.

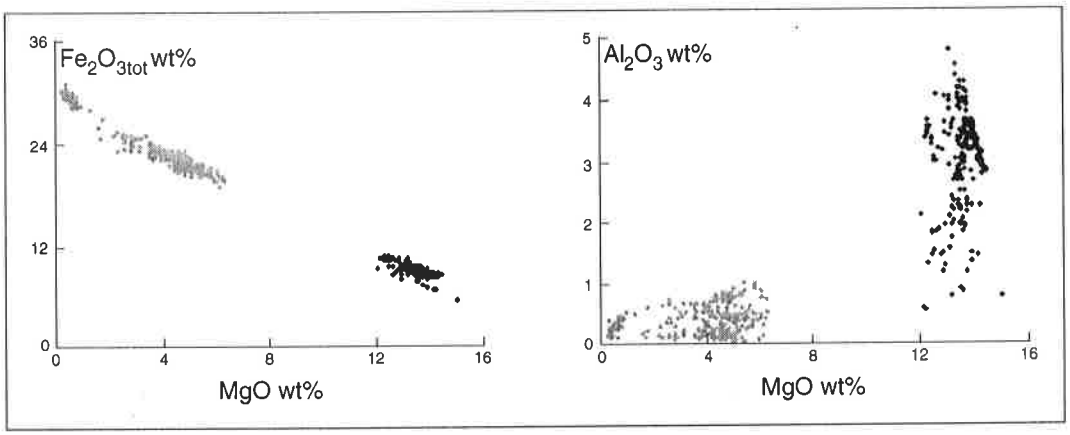

Fig.6.11 - Composition of clinopyroxenes from pneumatolytic gabbros (black symbols) and monzonites (grey symbols).

Sample	1B	3B	94.50	94.50	94.65
Rock type	PNG	PNG	MNZ	MNZ	MNZ
SiO_2	48.25	49.46	48.70	47.79	49.30
TiO_2	1.78	1.35	0.34	0.49	0.58
Al_2O_3	4.25	3.30	0.21	0.45	0.87
Cr_2O_3	0.22	0.04	0.01	0.02	0.00
Fe_2O_3	4.05	3.63	11.13	2.25	0.89
FeO	4.26	4.91	19.97	26.71	20.86
MnO	0.17	0.16	0.72	0.83	0.51
MgO	13.81	14.11	0.38	0.67	5.40
CaO	21.99	21.86	15.05	20.22	20.82
Na_2O	0.45	0.46	3.86	0.61	0.39
K_2O	0.00	0.00	0.00	0.03	0.00
Total	99.23	99.28	100.37	100.07	99.62
Si^{4+}	1.812	1.854	1.966	1.964	1.964
$^{IV}Al^{3+}$	0.188	0.146	0.010	0.022	0.036
$^{IV}Fe^{3+}$	0.000	0.000	0.024	0.014	0.000
$^{VI}Al^{3+}$	0.000	0.000	0.000	0.000	0.005
Ti^{4+}	0.050	0.038	0.010	0.015	0.017
Cr^{3+}	0.007	0.001	0.000	0.001	0.000
$^{VI}Fe^{3+}$	0.114	0.103	0.314	0.056	0.027
Fe^{2+}	0.134	0.154	0.674	0.918	0.695
Mn^{2+}	0.005	0.005	0.025	0.029	0.017
Mg^{2+}	0.773	0.788	0.023	0.041	0.321
Ca^{2+}	0.885	0.878	0.651	0.890	0.888
Na^{1+}	0.033	0.033	0.302	0.049	0.030
K^{1+}	0.000	0.000	0.000	0.002	0.000
Wo	46.3	45.5	38.0	45.7	45.6
En	40.5	40.9	1.4	2.1	16.5
Fs	13.2	13.6	60.6	52.2	37.9

Table 6.8 - Representative analyses of clinopyroxenes from pneumatolytic gabbros and monzonites. Structural formulae were calculated on the basis of 6 oxygens and 4 cations. Wo = $100Ca/(Ca+Mg+Fe^{tot})$. En = $100Mg/(Ca+Mg+Fe^{tot})$. Fs = $100\ Fe^{tot}/(Ca+Mg+Fe^{tot})$.

Magnetite

Magnetite is a major component in oxide-rich gabbros, where it constitutes, together with sulphides, up to 10% of the mode. It is interstitial and has exsolution lamellae of ilmenite, indicating post-magmatic low-temperature reequilibration. Magnetite is surrounded by rim of biotite and amphibole. It is TiO_2-rich and Cr_2O_3-free, and is characterized by large compositional variations related to low-temperature re-equilibration. Non-reequilibrated magnetite has the highest content of TiO_2, whereas reequilibrated magnetite has the highest content of Al_2O_3, FeO_{tot} and MgO.

Ilmenite

Primary ilmenite is a minor component (<2%) of all olivine gabbros, but oxide-rich gabbros; it is interstitial and rimmed by biotite and, if present, brown amphibole. Ilmenites from troctolites (Table 6.8, Fig.6.17) are Fe_2O_3-free and MgO-rich (up to 6%). In comparison with the MgO content which is commonly observed in ilmenites from mafic plutons (Cawthorn *et al.*, 1985; Frost & Lindsley, 1991), this is an exceptionally high value. In JH1-LS, from the bottom to the top, ilmenite displays decreasing TiO_2 and MgO, and increasing FeO_{tot}. Ilmenite from JH2-LS troctolite has a composition which is, if compared to the uppermost JH1-LS troctolite, mildly enriched in MgO and mildly depleted in FeO_{tot}. Ilmenite from leucogabbro is enriched in TiO_2 and depleted in FeO_{tot}, if compared with ilmenite from the uppermost JH1-LS troctolite. Ilmenite from JH2-US ol-gabbros (Table 6.9, Fig.6.12) displays decreasing FeO_{tot} and MgO from the bottom to the top of the series. In comparison with ilmenite from JH2-LS troctolite, they are mildly depleted in MgO and mildly enriched in TiO_2 and FeO_{tot}.

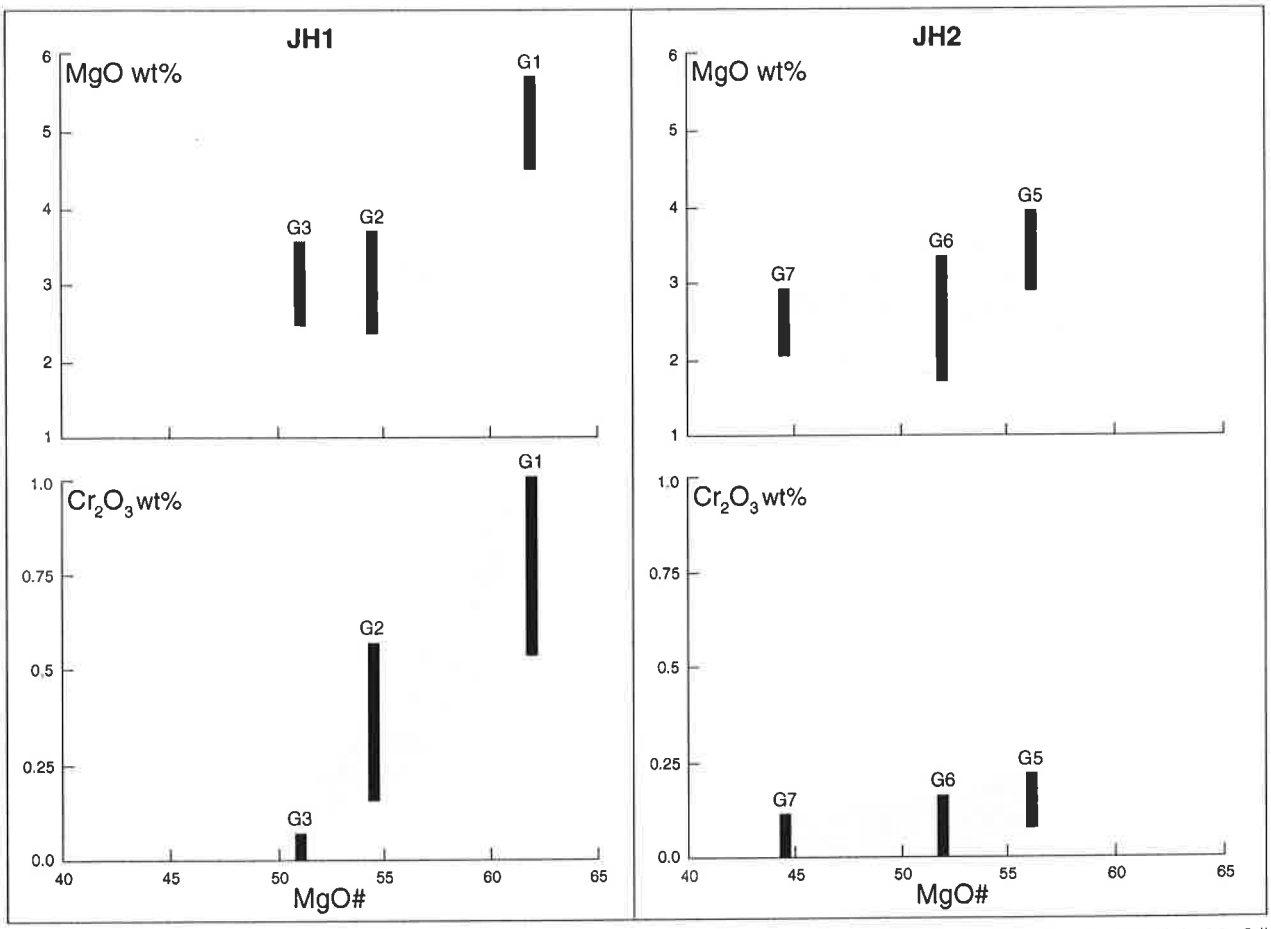

Fig.6.12 - Compositional variation in ilmenites from JH1 and JH2 olivine gabbros. Sample localisation in Fig.6.1. MgO# is the MgO number of the host rock (see Chapter 5). Vertical bars are compositional ranges. G1 = 28 analysis points; G2 = 83; G3 = 13; G5 = 12; G6 = 63; G7 = 43.

Sample	G1	G2	G4	G5	G6	G7
Rock type	TRC	TRC	OXG	TRC	OLG	OLG
Series	JH1-LS	JH1-LS	JH1-US	JH2-LS	JH2-US	JH2-US
SiO_2	0.03	0.03	0.07	0.03	0.00	0.03
TiO_2	49.90	48.60	12.20	50.12	49.67	51.37
Al_2O_3	0.11	0.13	3.07	0.06	0.05	0.07
Cr_2O_3	0.80	0.26	0.00	0.11	0.07	0.06
Fe_2O_3	0.00	0.00	39.93	0.00	0.00	0.00
FeO	42.39	47.01	42.06	45.68	46.38	45.05
MnO	0.43	0.65	0.44	0.44	0.52	0.65
MgO	5.39	3.15	1.07	2.96	2.81	2.48
CaO	0.00	0.00	0.04	0.03	0.01	0.00
NiO	0.13	0.08	0.17	0.08	0.00	0.00
CoO	0.16	0.08	0.23	0.08	0.02	0.05
V_2O_5	0.59	0.34	1.00	0.78	0.49	0.56
Total	99.94	100.32	100.30	100.37	100.01	100.32
Si^{4+}	0.000	0.000	0.000	0.002	0.000	0.001
Ti^{4+}	1.857	1.845	0.340	1.883	1.882	1.925
Al^{3+}	0.006	0.008	0.134	0.004	0.003	0.004
Cr^{3+}	0.031	0.010	0.000	0.004	0.003	0.003
Fe^{3+}	0.000	0.000	1.113	0.000	0.000	0.000
Fe^{2+}	1.754	1.984	1.302	1.908	1.953	1.877
Mn^{2+}	0.018	0.028	0.014	0.019	0.022	0.027
Mg^{2+}	0.398	0.237	0.059	0.220	0.211	0.184
Ca^{2+}	0.000	0.000	0.002	0.001	0.000	0.000
Ni^{2+}	0.005	0.003	0.005	0.003	0.000	0.000
Co^{2+}	0.007	0.003	0.007	0.003	0.001	0.002
V^{5+}	0.019	0.011	0.024	0.026	0.016	0.018

Table 6.9 - Representative analyses of Fe-Ti oxides from JH1 and JH2. Fe-Ti oxide from troctolites and ol-gabbros is ilmenite, Fe-Ti oxide from oxide-rich gabbros is magnetite. Structural formulae of ilmenite were calculated on the basis of 6 oxygens; structural formulae of magnetite were calculated on the basis of 3 oxygens and 4 cations.

Biotite

Biotite is a minor to major component in olivine gabbros and monzonites. It is always an interstitial phase, surrounding pyroxene and oxides.

Biotite from JH1 (Table 6.10, Fig.6.13) displays high and decreasing content of MgO from bottom to top, and increasing content of Fe_2O_{3tot} and TiO_2. K_2O is constant in JH1-LS troctolites and it is mildly higher in oxide-rich gabbros. Biotite from JH2 has constant MgO content and it differs from JH1 biotites mainly in their mildly higher K_2O content and in their mildly lower Na_2O and Al_2O_3 content.

Biotite from monzonites (Table 6.10) is MgO-poor and Fe_2O_{3tot}-rich; if compared with biotites from olivine gabbros, it is also mildly depleted in TiO_2, Al_2O_3, Na_2O and K_2O.

Amphibole

Amphibole is a minor to major component in JH1 olivine gabbros, pneumatolytic gabbros, monzonites and mesocratic syenites.

Amphibole from JH1 troctolites, leucogabbros and oxide-rich gabbros is brown and is kaersutite (Table 6.11, Figs.6.14 and 6.15). From the bottom to the top of the series it is characterized by small decrease of TiO_2, Al_2O_3 and MgO, and small increase of FeO and Na_2O. CaO is constant. Compositional zoning is weak or lacking. If compared with the uppermost JH1-LS troctolite, kaersutite from oxide-rich gabbros is enriched in Al_2O_3 and FeO, and depleted in MgO and Na_2O.

Amphibole from pneumatolytic gabbros is actinolite (Table 6.11, Figs.6.14 and 6.16), but compositional variations are large and zoning pronounced. According to the different content in SiO_2, two different families of actinolite can be distinguished: the first being SiO_2-richer ($SiO_2 \geq 51\%$), the other being SiO_2-poorer ($SiO_2 < 49\%$). SiO_2 is paralleled by MgO and CaO and mirrored by FeO and Na_2O.

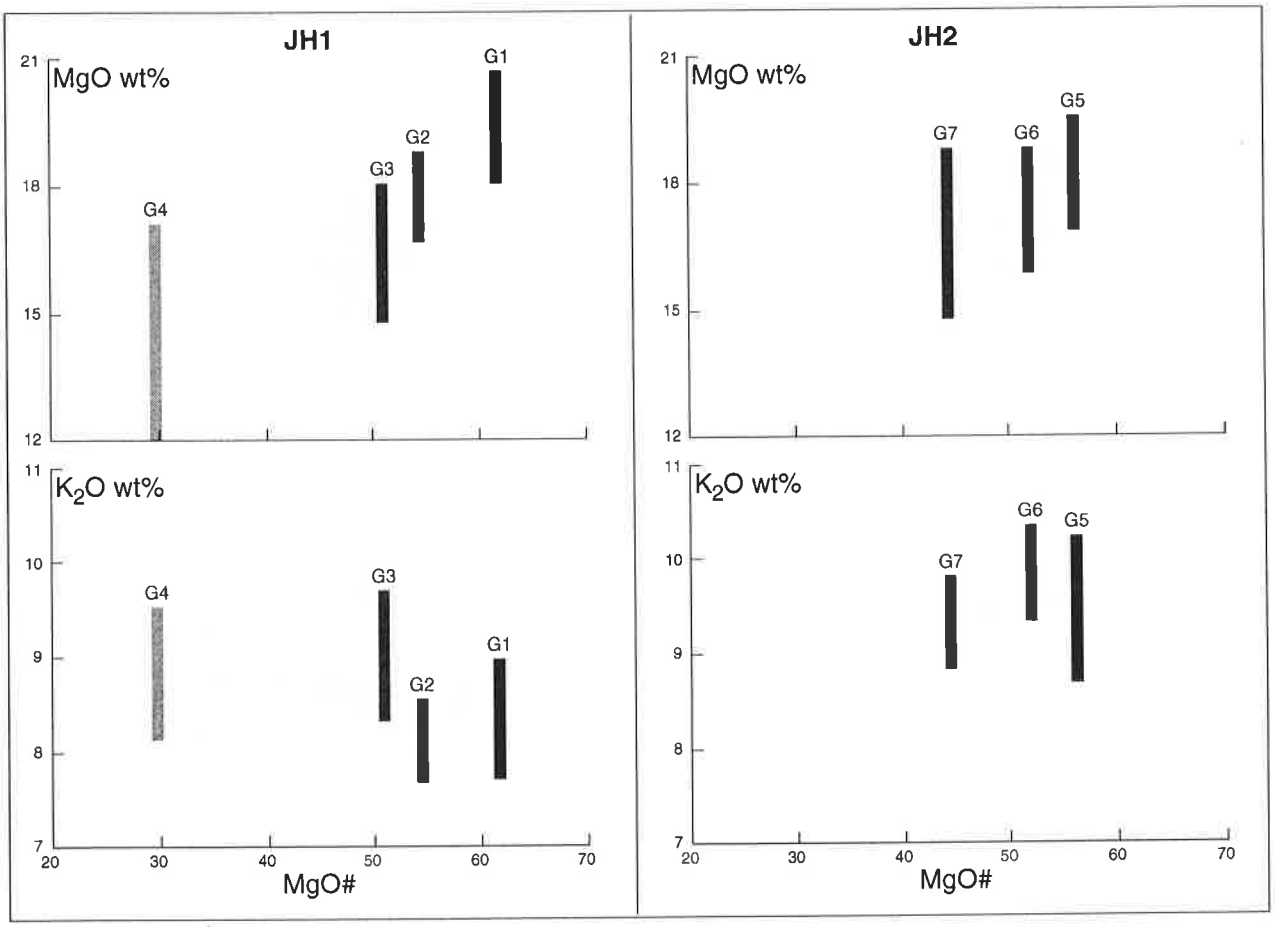

Fig.6.13 - Compositional variation in biotites from JH1 and JH2 olivine gabbros. Sample localisation in Fig.6.1. MgO# is the MgO number of the host rock (see Chapter 5). Vertical bars are compositional ranges. G1 = 20 analysis points; G2 = 35; G3 = 21; G4 = 9; G5 = 11; G6 = 35; G7 = 40.

Sample	G1	G2	G4	G5	G6	G7	94.65
Rock type	TRC	TRC	OXG	TRC	OLG	OLG	MNZ
Series	JH1-LS	JH1-LS	JH1-US	JH2-LS	JH2-US	JH2-US	
SiO_2	37.93	37.78	37.02	39.68	37.16	38.77	34.03
TiO_2	4.07	5.41	6.94	7.10	7.24	3.93	4.27
Al_2O_3	14.67	13.97	14.15	12.25	13.12	13.29	11.23
FeO	9.13	11.76	14.14	10.13	15.45	13.50	35.71
MnO	0.00	0.02	0.05	0.00	0.08	0.05	0.38
MgO	19.55	17.70	14.75	18.20	13.63	17.01	1.63
CaO	n.m.	0.03	0.05	0.02	0.02	0.05	0.16
Na_2O	1.05	1.33	0.72	0.91	0.42	0.46	0.24
K_2O	8.47	8.19	8.98	8.74	9.69	9.44	8.47
F	0.17	0.11	0.11	0.28	0.11	0.29	0.16
Total	95.04	96.30	96.93	97.32	96.92	96.78	96.29
Si^{4+}	2.761	2.749	2.718	2.839	2.756	2.840	2.820
Ti^{4+}	0.223	1.198	1.225	1.033	1.147	1.147	1.096
Al^{3+}	1.259	0.296	0.383	0.382	0.404	0.217	0.266
Fe^{2+}	0.556	0.715	0.868	0.606	0.958	0.827	2.474
Mn^{2+}	0.000	0.001	0.003	0.000	0.005	0.003	0.027
Mg^{2+}	2.121	1.920	1.614	1.941	1.507	1.857	0.201
Ca^{2+}	0.000	0.002	0.004	0.002	0.002	0.004	0.015
Na^{2+}	0.149	0.187	0.103	0.127	0.061	0.065	0.039
K^{1+}	0.787	0.761	0.841	0.798	0.917	0.883	0.895

Table 6.10 - Representative analyses of biotites from JH1, JH2 and monzonites. Structural formulae were calculated on the basis of 11 oxygens.

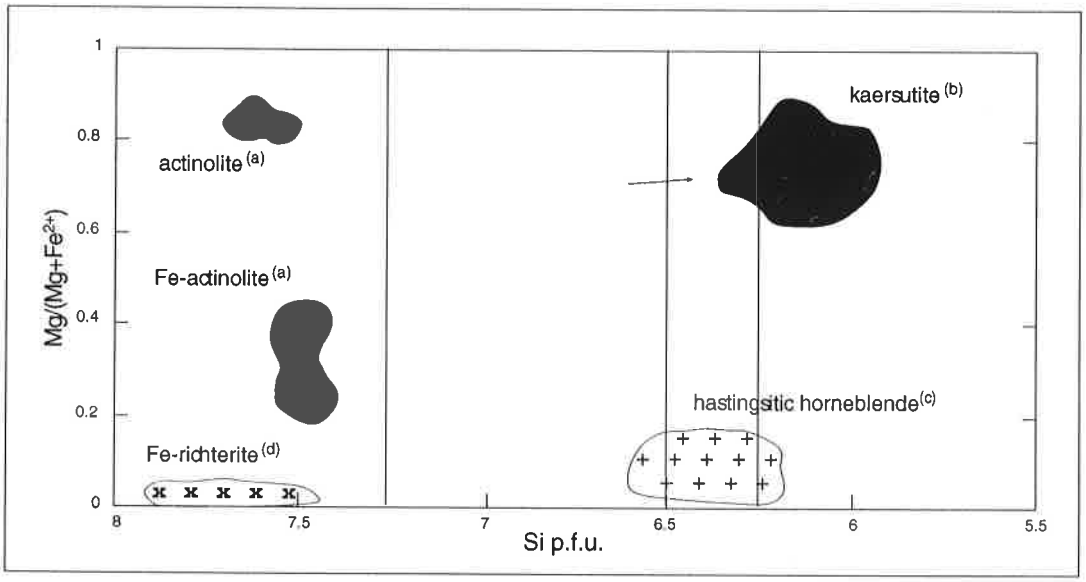

Fig.6.14 - Classification of JHM amphiboles (Leak, 1978). Dark area is olivine gabbro amphibole composition; grey area is secondary amphibole composition in pneumtolytic gabbros; ✖ is monzonite amphibole composition; + is syenite amphibole composition.

(a) = $(Ca+Na)_B \geq 1.34$; $Na_B < 0.67$; $(Na+K)_A < 0.5$; $Ti<0.5$

(b) = $(Ca+Na)_B \geq 1.34$; $Na_B < 0.67$; $(Na+K)_A < 0.5$; $Ti \geq 0.5$

(c) = $(Ca+Na)_B \geq 1.34$; $Na_B < 0.67$; $(Na+K)_A \geq 0.5$; $Ti <0.5$; $Fe^{3+} \geq {}^{VI}Al$

(d) = $(Ca+Na)_B \geq 1.34$; $0.67 < Na_B < 1.34$; $(Na+K)_A \geq 0.5$

Sample	G1	G2	G4	93.40	93.40	94.30	94.65	94.65	94.64	94.64
Rock type	TRC	TRC	OXG	PNG	PNG	PNG	MNZ	MNZ	SYE	SYE
SiO_2	41.28	42.06	41.12	48.21	51.93	53.21	47.59	48.26	38.81	37.10
TiO_2	5.18	4.06	4.72	0.88	0.01	0.55	0.11	0.51	2.92	0.09
Al_2O_3	12.21	10.07	11.58	0.69	0.26	0.79	1.24	0.92	8.41	9.63
Fe_2O_3	1.17	2.15	2.18	8.69	1.26	6.08	2.19	8.34	1.97	7.82
FeO	8.36	9.07	10.55	21.32	22.43	5.75	33.66	27.44	27.76	26.78
MnO	0.06	0.15	0.18	0.75	0.33	0.17	0.61	1.41	0.47	0.52
MgO	14.32	14.29	12.70	5.79	9.01	17.82	0.25	0.24	2.02	0.62
CaO	11.49	11.31	11.45	7.46	12.29	11.06	10.94	2.84	9.96	10.40
Na_2O	2.75	3.01	2.44	3.25	0.17	1.38	0.32	5.58	2.66	2.04
K_2O	0.88	0.79	1.02	0.65	0.00	0.28	0.21	1.79	1.32	1.91
Total	97.71	96.95	97.93	97.68	97.68	97.08	97.12	97.32	96.29	96.90
Si^{4+}	6.040	6.241	6.083	7.522	7.881	7.630	7.751	7.795	6.384	6.171
$^{IV}Al^{3+}$	1.960	1.759	1.917	0.127	0.046	0.133	0.238	0.175	1.616	1.829
$^{IV}Fe^{3+}$	0.000	0.000	0.000	0.351	0.073	0.236	0.011	0.030	0.000	0.000
$^{VI}Al^{3+}$	0.146	0.002	0.103	0.000	0.000	0.000	0.000	0.000	0.015	0.059
Ti^{4+}	0.570	0.453	0.525	0.103	0.001	0.059	0.013	0.062	0.361	0.011
$^{VI}Fe^{3+}$	0.129	0.240	0.243	0.669	0.071	0.420	0.257	0.983	0.244	0.979
Fe^{2+}	1.023	1.125	1.305	2.782	2.846	0.689	4.585	3.706	3.819	3.724
Mn^{2+}	0.008	0.018	0.022	0.099	0.043	0.021	0.084	0.193	0.066	0.073
Mg^{2+}	3.124	3.161	2.801	1.347	2.039	3.810	0.061	0.057	0.497	0.153
Ca^{2+}	1.801	1.797	1.814	1.246	1.998	1.699	1.910	0.492	1.755	1.853
Na^{1+}	0.780	0.865	0.700	0.982	0.050	0.383	0.102	1.747	0.850	0.658
K^{1+}	0.164	0.150	0.192	0.129	0.000	0.050	0.043	0.368	0.276	0.406

Table 6.11 - Representative analyses of amphiboles from JH1 olivine gabbros, pneumatolytic gabbros, monzonites and syenites. Structural formulae were calculated on the basis of 23 oxygens and (Si+Al+Ti+Fe+Mn+Mg)=13.

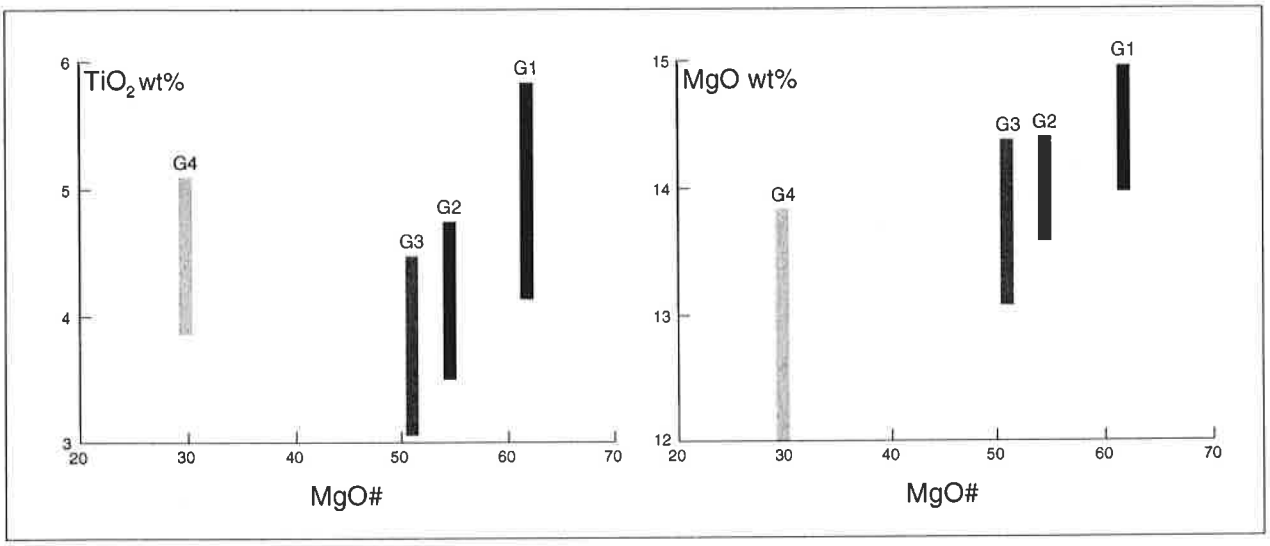

Fig.6.15 - Compositional variation in amphiboles from JH1 and JH2 olivine gabbros. Sample localisation in Fig.6.1. MgO# is the MgO number of the host rock (see Chapter 5). Vertical bars are compositional ranges. G1 = 114 analysis points; G2 = 66; G3 = 78; G4 = 186.

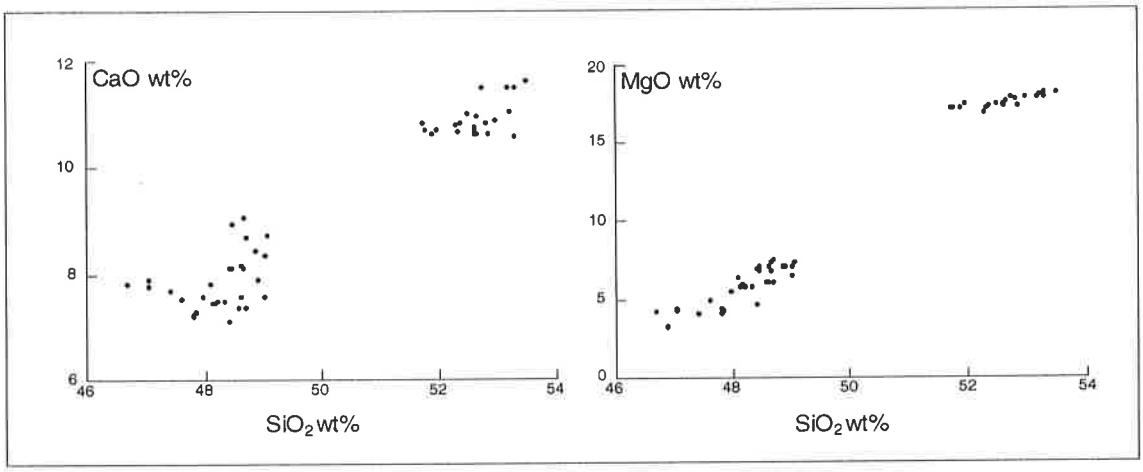

Fig.6.16 - Compositional variation in amphiboles from pneumatolytic gabbros.

Amphibole from monzonites is Fe-richterite (Table 6.11, Figs.6.14 and 6.17) and has marked compositional zoning (Fig.6.23), mostly evidenced by irregular variation of CaO and Na_2O. Na-rich portions correspond to the blue-greenish amphibole.

Amphibole from syenites is hastingsitic hornblende (Table 6.11, Figs.6.14 and 6.17) and, in comparison with amphibole from monzonites, is enriched in SiO_2, TiO_2, Al_2O_3, MgO, and CaO, and depleted in FeO and Na_2O.

Compositional zoning in amphiboles from syenites is strong, discontinuous and mostly characterized by abrupt and broadly parallel variations of TiO_2, MgO and Na_2O, which are mirrored by Al_2O_3, FeO_{tot} and K_2O. Ti-poor portions correspond to exsolution lamellae.

Compositional variations between lower and upper series in JH1 and JH2

All mineral phases constituting JH1-LS troctolites are characterized by decreasing MgO and increasing FeO_{tot} from bottom to top. CaO in plagioclase and pyroxene is almost constant, though compositional zoning in plagioclase is

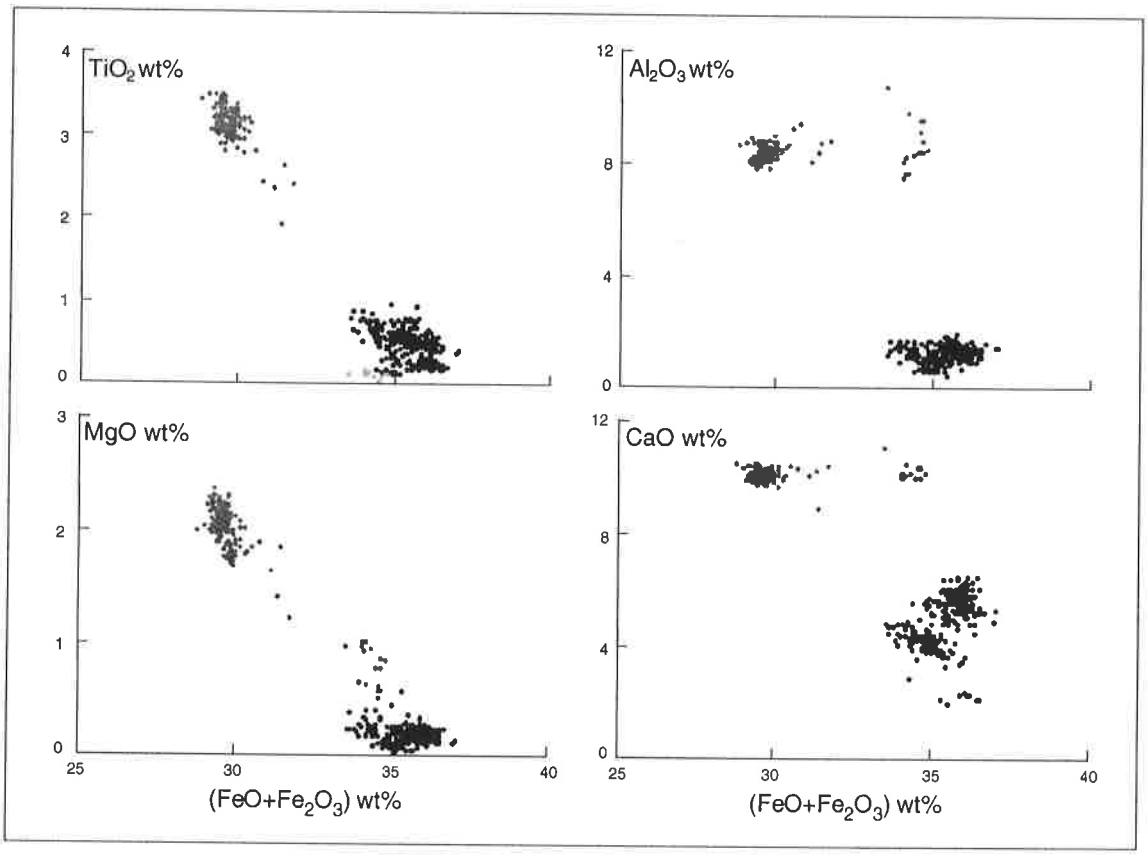

Fig.6.17 - Compositional variation in amphiboles from monzonites (black symbols) and syenites (grey symbols).

extremely pronounced. TiO_2 decreases in pyroxene, ilmenite and amphibole, but increases in biotite. Na_2O mildly increases and K_2O is constant in plagioclase, amphibole and biotite; Cr_2O_3 is constant in pyroxene. With regards to trace elements, Ni and Co contents vary in olivine, plagioclase and pyroxene, paralleling MgO. Sc mildly increases in olivine and it is constant in plagioclase. Sr increases in plagioclase; Hf, Ta, REE and Th increases in olivine and plagioclase (no INA data are available for pyroxene from the lowermost JH1-LS troctolite. Mineral composition of JH1-US oxide-rich gabbros differs for underlying troctolites their very low content of Ni and Cr, and for their high content of FeO_{tot}. Hf, Ta, REE and Th in olivine and plagioclase are roughly the same or mildly lower in oxide-rich gabbros than in the lowermost JH1-LS troctolites.

As in the case of JH1, JH2 mineral phases are not characterized by large compositional variations in major element abundances from the lower to the upper series. In JH2-US, MgO decreases upwards in olivine, pyroxene and ilmenite, and is constant in biotite. FeO_{tot} mirrors MgO; CaO and Na_2O are constant. Sr decreases in plagioclase, Sc increases in pyroxene, as well as Hf, Ta, REE and Th in plagioclase and pyroxene (only Tb decreases in plagioclase). If compared to JH2-LS troctolites, JH2-US ol-gabbros are poorer in incompatible elements.

Compositional variations between JH1 and JH2

Mineral compositions are characterized by significant variations from JH1 to JH2. In particular:

- plagioclase and biotite from JH1 are poorer in K_2O than plagioclase and biotite from JH2 (Fig.6.4), and this is independent on the An content of plagioclase. In particular, K_2O in plagioclase and biotite from JH2-LS troctolite is higher than K_2O in plagioclase and biotite from JH1-US oxide-rich gabbros, which are considered, according to the MgO and Ni content of olivine, as being the more evolved olivine gabbros in JHM;

- olivine, plagioclase and pyroxene from JH2 are all enriched in Ta, Hf, REE and Th, if compared to olivine, plagioclase and pyroxene from JH1.

6.2. Discussion

About crystal fractionation in JH1 and JH2

The presence and the style of modal and cryptic layering in JH1-LS troctolites (decrease in olivine modal content and in MgO content in all mineral phases from bottom to top) indicates the presence of a fractional crystallization process in JH1-LS, controlled by olivine precipitation. Similarly, fractional crystallization through olivine settling is also considered as the main differentiation process controlling liquid evolution in JH2-US. However, Sr decrease in plagioclases from ol-gabbros indicates, unlike in JH1-LS troctolites, a major role played by plagioclase in JH2-US differentiation.

The lack of the enrichment trend for incompatible elements (Hf, Ta, REE and Th) from troctolites to oxide-rich gabbros in JH1 and from troctolites to ol-gabbros in JH2 reflects the lack of fractional crystallization controlling the transition from one series to another. Also, the high trace element content in JH2-LS phases, relative to JH1-LS, excludes a fractional crystallization process relating JH1 troctolites to JH2 troctolites. Modeling of these liquids evolution is the aim of Chapter 7.

About residual liquid expulsion

In a cooling magma chamber, if the residual liquid is trapped between cumulus phases, then volatile-rich, MgO-poor interstitial phases are expected to be formed in the late-magmatic stage as well as normal zoning in the early precipitated phases (orthocumulates). The hypothesis of coexisting liquid expulsion (§ 4.4 and 5.3) is supported by the lack of normal zoning in olivines and it is perfectly consistent with the presence of pneumatolytic processes. In fact, if residual liquid was expelled upwards, then a stratified magma chamber consisting of a lower basic portion and of a still liquid upper portion filled with water-rich liquid originated. However, ilmenite, amphibole and biotite from JHM olivine gabbros, which are interstitial phases, are all MgO-rich and this not consistent with an origin from a evolved liquid. Consequently, they cannot represent the product of the solidification of the residual liquid, but rather of the solidification of a still primitive liquid in contact with a evolved liquid. In fact, the presence of amphibole and biotite, which are hydrous phases replacing in the last crystallization stage cumulus phases, reflects the presence of a certain amount of water- and K-rich liquid in the empty spaces. It follows that the residual liquid was probably partially retained within cumulates during gabbros solidification and that its presence together with a still MgO-rich liquid favoured the crystallization of hydrous and «primitive» phases.

About pneumatolysis

The composition of pyroxene relics in pneumatolytic gabbros (Mg-rich augite) indicates that these rocks originated from olivine gabbros belonging to the same family than JH1 and JH2 olivine gabbros, confirming the origin of these rocks by secondary transformation of their underlying series. The alkaline composition of MG2 feldspars rim supports the presence of an evolved liquid interacting with solidifying gabbros (Hibbard, 1981). The lack of hornblende and the presence of actinolite in pneumatolytic gabbros supports the low-temperature "metamorphic " grade (greenschist facies) which olivine gabbros underwent during pneumatolysis (Spear, 1993). Also, the bimodal distribution of actinolite compositions reflects a double crystallization stage, the first characterized by the presence of a MgO-, CaO-rich liquid (the primitive liquid), the other by the presence of a MgO-, Ca-poor liquid (the hybrid one).

About evolution and contamination of monzonites and syenites

The presence of hedenbergite, Fe-richterite and Fe-rich biotite reflects an alkaline Fe-rich liquid at the origin of monzonites. As olivine gabbros are characterized by a Fe-enrichment trend in all mineral phases, the high Fe content of mineral phases in monzonites is consistent with an origin by fractional crystallization. Amphibole from syenites is richer in MgO, TiO_2, and CaO, and depleted in SiO_2 and Na_2O, if compared to amphibole from monzonites, and this is not consistent with a differentiation process by fractional crystallization relating monzonites to syenites. Rather, it is argued that amphibole-bearing syenites (mesocratic syenites) formed through late-magmatic contamination of the syenitic liquid by a more basic liquid, and this is in good accordance with the postulated coexistence of acidic and basic liquids during the last stage of JHM magmatic evolution.

- CHAPTER 7 -

Modeling of Liquid Compositions and Evolution

The presence of layering in igneous complexes implies that the constituent rock compositions do not represent original liquids, but rather mixtures between crystals and melts whose relative proportions depend on layer-forming mechanisms (for review, see Naslund & McBirney, 1996). These mechanisms operate during magma emplacement and crystallisation in response to convection and mechanical processes (gravity settling, magma currents, magmatic deformation, compaction, tectonic deformation), and as a result of variations in intensive parameters (nucleation rate, oxygen fugacity and pressure fluctuations) which induce, for example, liquid immiscibility, diffusion-controlled nucleation and growth, and crystal growth in thermal gradients. Among the proposed mechanisms, compositional convection seems to play a basic role in the formation of cumulates (Tait *et al.*, 1984; Sparks & Huppert, 1984; Sparks *et al.*, 1985; Brandeis & Jaupart, 1986; Tait & Jaupart, 1992; Campbell, 1996; Tait & Jaupart, 1996).

Given that bulk composition trends in layered intrusions cannot be considered as liquid lines of descent, liquid compositions must be calculated through mathematical and graphical methods (Albarede, 1976; Duchesne, 1978; Nielsen, 1988; Chalokwu *et al.*, 1993; Bedard, 1994, Loferski *et al.*, 1996), or approximated by the assumption that chilled margins and associated dike compositions are representative of parental magma compositions (Longhi *et al.*, 1983; Upton *et al.*, 1985; Mathison & Hamlyn, 1987, Hoover, 1989; Wiebe & Snyder, 1993; Bevins *et al.*, 1994, Turner, 1996).

In this chapter, physical conditions of crystallization in JHM are discussed and liquid compositions are calculated through the concentrations of selected trace elements in a constant three-phase cotectic assemblage (olivine + plagioclase + clinopyroxene) and a selection of mineral-liquid partition coefficients. Estimated liquid compositions allow calculation of partial melting and crystal fractionation degrees affecting magma formation and evolution.

7.1. Physical conditions of crystallization in JH1 and JH2

Pressure

As indicated by geological setting and field relationships, JHM magma chamber was originally located at shallow depth. Low pressure crystallization in JH1 and JH2 (<0.5 Gpa) is supported by crystallisation order (olivine, plagioclase and clinopyroxene), low Al_2O_3 content and low $^{VI}Al/^{IV}Al$ ratio in augite (LeBas, 1962; Presnall *et al.*, 1978; Wass, 1979).

Temperature

No geothermometer is available in JHM olivine gabbros and crystallization temperatures are deduced by comparison with similar basaltic synthetic systems. Experimental studies (Hill & Roeder, 1974; French & Cameron, 1981; Thy & Lofgren, 1994) of the low-pressure evolution of transitional to mildly alkalic basaltic liquids indicate that a liquidus temperature of 1200°C is consistent with the observed paragenesis and crystallization order. The crystallization temperature of Fe-Ti oxides in gabbros from transitional and mildly alkalic basalts is 1110°C (Thy & Lofgren, 1994). The temperature of crystallization of amphibole estimated on its Ti content (Otten, 1984) is close to 1000°C in ilmenite-saturated basaltic liquids.

Oxygen fugacity

The lack of magnetite-ilmenite couples prevent quantitative estimates of oxygen fugacity (f_{O_2}) in JHM gabbros. However, the late crystallization of Fe-Ti oxides in all JHM gabbros and the comparison with synthetic systems

(Hill & Roeder, 1974; Thy & Lofgren, 1994) allows $\log(f_{O_2})$ to be estimated close to -12, i.e. in the vicinity of MW buffer.

Cooling rate

Ophitic texture in troctolites and microgabbros reflects high cooling rates (Coish & Taylor, 1979; Hort & Spohn, 1991; Cashman, 1993; Mathison, 1987), which are consistent with the shallow emplacement of JHM magma chambers and the widespread occurrence of cold bodies (roof pendants) within the magma chamber. A decreasing cooling rate from the bottom to the top of the magma chamber and from the walls to the inner zones is indicated by the transition from ophitic to subhedral-granular texture in troctolites and ol-gabbros.

7.2. Liquid evolution from trace element mineral composition

Given that melt structure, crystallization pressure, temperature and oxygen fugacity did not significantly change from troctolites to oxide-rich gabbros to ol-gabbros (§ 6.1), the mineral/liquid partition coefficients ($D=C^{min}/C^{liq}$) can be considered as roughly constant in all gabbros. Then, variations of trace element abundances in minerals from JH1 to JH2 and from lower to upper series are attributable to variations of original liquid compositions. In other words, despite the cumulative nature and the relatively small variation of major element compositions, our new trace element data permit: 1) discrimination between JH1 and JH2; 2) discrimination between lower and upper series in JH1 and JH2; and 3) modeling of liquid compositions and evolution.

As shown in Chapter 6, the abundances of incompatible elements (REE, Ta, Hf and Th) in olivine, plagioclase and clinopyroxene vary in parallel to each other from JH1 to JH2, from the lower to the upper series in the two complexes, and within the two layered series (JH1-LS and JH2-US). In particular:

- mineral phases from JH2 are, to different extent, richer in incompatible elements than mineral phases from JH1;

- mineral phases from JH1-US oxide-rich gabbros and from JH2-US ol-gabbros are poorer in incompatible elements than mineral phases from underlying troctolites;

- mineral phases from JH1-LS and JH2-US are characterized by a mild enrichment trend for most incompatible elements;

- mineral phases from oxide-rich gabbros are the poorest ones in Ni, Cr, Sr and incompatible elements.

Then, on the basis of the variation trend of incompatible elements we can argue that:

- JHM gabbros did not originate from a unique parental magma;

- the upper series of each complex did not originate by crystal fractionation of the respective lower series;

- JH1-LS and JH2-US evolved by crystal fractionation.

In fact, if JH1 and JH2 gabbros originated from a unique parental magma, the abundances of incompatible elements in olivine, plagioclase and clinopyroxene should be approximatively the same in all series, since the incompatible element contents of basaltic melts do not vary much in the first stages of differentiation. Also, when crystal fractionation is the main differentiation process, the less differentiated the liquid is, the poorest in incompatible elements it is. According to the Ni content of olivines (Ni^{Ol}), it can be affirmed that in JHM the less differentiated rocks are JH1-LS troctolites (Ni^{Ol}>1000 ppm) and the more differentiated rocks are ol-gabbros and oxide-rich gabbros (Ni^{Ol}<700 ppm) and this is in contrast with the incompatible element contents which are higher in JH1-LS troctolites than in JH1-US oxide-rich gabbros, and higher in JH2-LS troctolites than in JH2-US ol-gabbros. From the preceding observations we propose that the four series forming JH1 and JH2 (JH1-LS, JH1-US, JH2-LS and JH2-US) originated from the injection and the crystallization of four distinct batches of melt: two of them were involved in the formation of JH1, and the other two in JH2.

If different parental magmas were involved in the genesis of the JHM series, we must attribute the different contents of compatible elements (Ni, Cr and Sr) to a earlier stage of crystal fractionation. In particular, since a decreasing content of Ni reflects olivine fractionation, it can be argued that the parental liquid of the JH1-US oxide-rich gabbros was affected by early olivine fractionation more than the parental liquids of the ol-gabbros and troctolites. As well, since a decreasing content of Cr reflects chromite fractionation and a decreasing content of Sr reflects plagioclase fractionation, it can be argued that the parental liquid of the JH1-US oxide-rich gabbros was affected by early chromite and plagioclase fractionation more than the parental liquids of the ol-gabbros and troctolites.

7.3. Calculation of liquid compositions

MgO

If the MgO content of the olivine (C^{Ol}) is known, then the MgO content of the coexisting basaltic liquid (C^{Liq}) is given by the equation:

$\log C^{Liq} = \log C^{Ol} + 1.87 - {}^{3740}/_{T°(K)}$ (Roeder & Emslie, 1970).

Assuming a temperature of 1200°C for olivine crystallization and using a representative value of the MgO content in olivine cores (C^{Ol}), the ranges of the MgO content in JH1 and JH2 coexisting liquids are 8.1 to 8.8 wt% from G2 to G1 in JH1-LS, 8.4 wt% for JH2-LS troctolites (G5), 7.3 wt% for JH1-US oxide-rich gabbros (G4), and 6.6 to 7.3 wt% from G7 to G6 in JH2-US (Table 7.1). In JH1-LS and JH2-US the most MgO-rich liquids correspond to the most Ni-rich olivines and are considered as the parental liquids of the respective series (G1 and G6, respectively).

Series	JH1-LS	JH1-LS	JH1-LS	JH1-US	JH2-LS	JH2-US	JH2-US	JH2-US
Rock type	TRC	TRC	LCG	OXG	TRC	OLG	OLG	ANR
Sample no.	G1	G2	G3	G4	G5	G6	G7	G8
MgO in olivine (wt%)	41.1	37.9	36.1	33.7	38.8	34.1	31.3	32.9
MgO in the liquid (wt%)	8.8	8.1	7.7	7.3	8.4	7.3	6.6	7.1

Table 7.1: Calculated MgO contents of JH1 and JH2 liquids. MgO in olivine was measured by electron microprobe in olivine cores. MgO in the liquid is calculated according to Roeder & Emslie (1970).

Trace elements

As shown by textural relationships, olivine, plagioclase and augite from troctolites, ol-gabbros and oxide-rich gabbros are likely to be cotectic phases during JH1 and JH2 crystallisation. Thus, the knowledge of mineral/liquid partition coefficients allows estimation of the composition of coexisting liquids through three independent calculations using olivine, clinopyroxene and plagioclase compositions. Complications due to differential crystal settling are ignored for simplification.

A range of liquid compositions was obtained for each mineral phase of each sample using the mineral trace element content and two different values of partition coefficients. These two values are the largest and the smallest one among all selected partition coefficients (Table 7.2) and they define a range within whom all selected partition coefficients fall. Partition coefficient selection was made according to the following criteria: 1) synthetic and natural basic systems (SiO_2<52%); 2) physical and chemical conditions comparable to those which occurred during JHM olivine gabbros crystallisation (i.e. high temperature, low pressure, low f_{O_2}).

Three compositional ranges were then obtained for each sample (one from olivine, one from plagioclase and one from pyroxene), and the common range was considered as representative of the coexisting liquid (Fig.7.1). Table 7.3

gives the composition of all calculated liquids. N-MORB normalization (Fig.7.2) shows that the JHM liquid pattern fits well with alkali-basalt patterns (except for positive anomalies of Th and Ta), indicating the soundness of calculations.

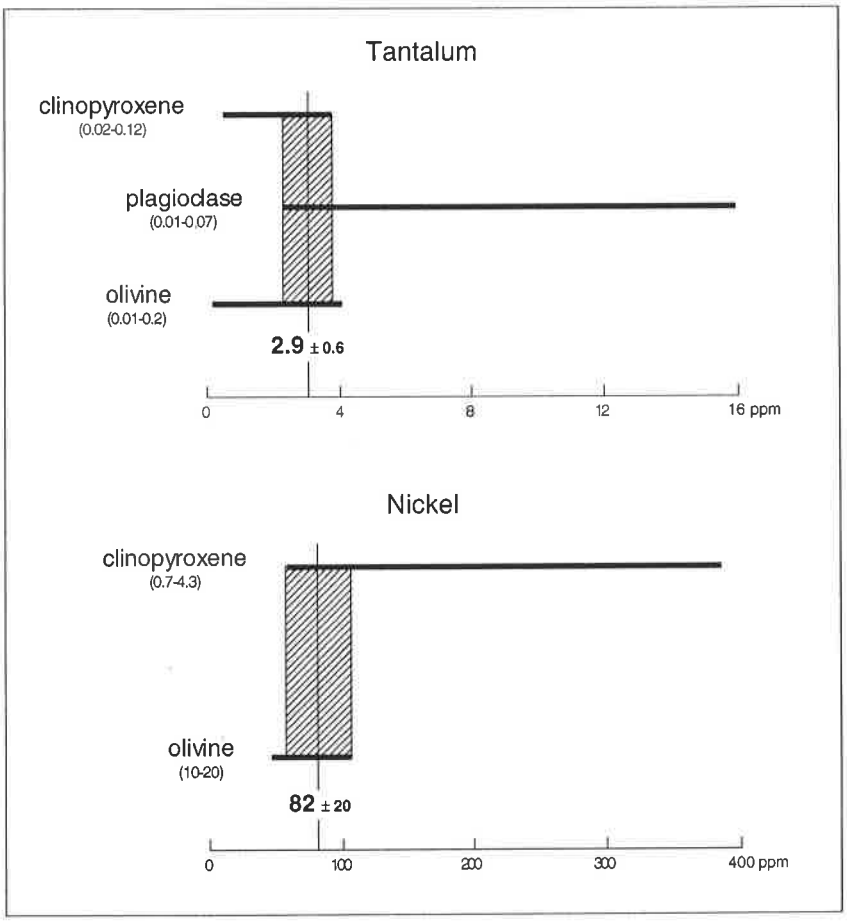

Fig.7.1 - Graphical representation of liquid calculation method. Dashed areas are the common compositional ranges (see the texts for explanation). Numbers in bold are the calculated values; numbers in brackets are the mineral/liquid partition coefficient ranges.

	olivine	plagioclase	clinopyroxene
Sc	0.1 - 0.9	0.01 - 0.07	1.3 - 4.5
Co	3.6 - 6.6	0.01 - 0.1	0.5 - 2.0
Ni	6 - 35	0.03 - 0.05	0.7 - 4.3
Sr	n.f.	1.2 - 2.9	0.07 - 0.27
Hf	< 0.07	0.01 - 0.08	0.2 - 0.9
Ta	0.01 - 0.2	0.01 - 0.07	0.02 - 0.12
La	< 0.05	0.06 - 0.3	0.05 - 0.17
Eu	< 0.05	0.11 - 1.0	0.4 - 0.8
Tb	< 0.05	0.02 - 0.19	0.5 - 1.0
Th	< 0.05	0.01 - 0.13	< 0.1

Table 7.2: Selected partition coefficients. Data from: Onuma et al. (1968); Higuchi & Nagasawa (1969); Philpotts & Schnetzler (1970); Sun et al. (1974); Drake & Weill (1975); Weill & McKay (1975); McKay & Weill (1976); Lindstrom & Weill (1978); Leeman & Lindstrom (1978); Hart & Davis (1978); Villemant et al. (1981); Ray et al. (1983); Dostal et al. (1983); Green & Pearson (1985); Dunn (1987); Lemarchand et al. (1987); Colson et al. (1988); Liotard et al. (1988); Kuehner et al. (1989); Kinzler et al. (1990); Blundy & Wood (1991); Nielsen et al. (1992); Gallahan & Nielsen (1992); LaTourrette & Burnett (1992); Hart & Dunn (1993); Kennedy et al. (1993); Dunn & Sen (1994); Jenner et al. (1994); Lundstrom et al. (1994). n.f. = not found.

Series	JH1-LS	JH1-LS	JH1-LS	JH1-US	JH2-LS	JH2-US	JH2-US
Rock type	TRC	TRC	LCG	OXG	TRC	OLG	OLG
Sample	G1	G2	G3	G4	G5	G6	G7
MgO (wt%)	8.8	8.1	7.7	7.3	8.4	7.3	6.6
Sc	25 (±20)	40 (±16)	54 (±30)	62 (±50)	55 (±29)	55 (±31)	45 (±19)
Co	43 (13)	39 (12)	43 (13)	55 (16)	40 (12)	41 (12)	38 (11)
Ni	103 (±34)	82 (±20)	47 (±15)	29 (±10)	88 (±29)	53 (±15)	48 (±5)
Sr	504 (±209)	544 (±225)	457 (±168)	307 (±128)	433 (±180)	531 (±220)	504 (±209)
Hf	n.m.	4.4 (±2.6)	3.5 (±2.0)	n.m.	6.5 (±3.7)	4.7 (±2.7)	4.6 (±2.7)
Ta	2.5 (±0.8)	2.9 (±0.6)	1.5 (±0.7)	1.5 (±1.2)	5.5 (±0.4)	3.6 (±0.6)	3.6 (±0.6)
La	n.m.	29 (±13)	29 (±14)	22 (±15)	45 (±17)	33 (±11)	37 (±13)
Eu	n.m.	2.0 (±0.6)	1.5 (±0.4)	2.4 (±1.9)	2.6 (±0.8)	1.9 (0.6)	2.2 (±0.6)
Tb	n.m.	1.1 (±0.3)	0.7 (±0.2)	0.3 (±0.3)	1.5 (±0.4)	1.0 (±0.2)	1.2 (±0.3)
Th	n.m.	8.9 (±3.6)	11 (±8)	3.0 (±2.6)	42 (±34)	13 (±7)	14 (±8)

Table 7.3 - Calculated trace element compositions of JH1 and JH2 liquids. Trace elements are expressed as ppm (see the text and Fig.7.1 for calculation method). Numbers in brackets indicate error limits. The liquid composition of anorthosite G8 was not calculated because of the lack of olivine and pyroxene data. n.m. = not measured, as well as the liquid composition of troctolite G1 for Hf, La, Eu, Tb and Th.

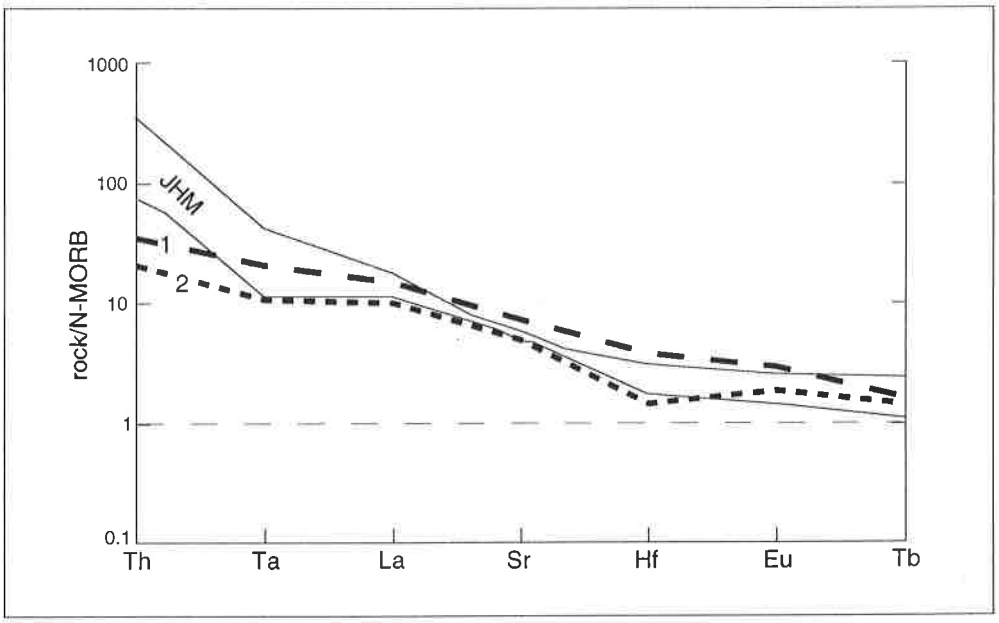

Fig. 7.2. Incompatible elements patterns for OIB (1), alkali-basalts (2) and JHM calculated liquids (grey area). Normalizing values and OIB data from Sun & McDonough (1989); alkali-basalt data from Baker et al. (1977).

7.4. The liquid lines of descent in JH1 and JH2

Liquids calculated from Sc, Sr, Hf, REE and Th are characterized by large compositional uncertainties, due to the large uncertainty of their mineral-liquid partition coefficients, and cannot be used in modeling; on the contrary, liquids calculated from Ni and Ta are better constrained, and they allow us to draw liquid lines of descent in JH1 and JH2 (Fig.13), and to model liquids evolution. In particular, the high incompatibility of Ta in olivine, plagioclase and clinopyroxene allows us to evaluate the degree of partial melting of the mantle source producing the JHM parental magmas. The high compatibility of Ni in basaltic systems, in turn, allows us to calculate the amount of early olivine fractionation in these primary magmas to give JHM olivine gabbros composition.

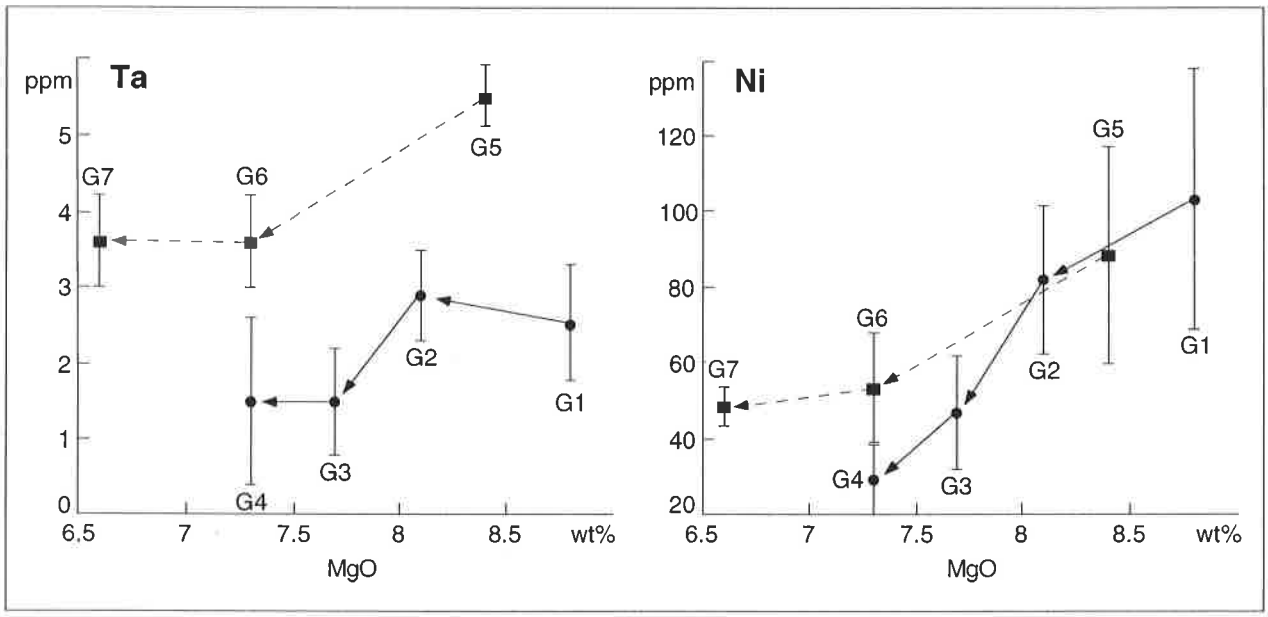

Fig. 7.3. Liquid lines of descent in JH1 and JH2 for Tantalum and Nickel. Vertical bars indicate uncertainties. Black circles and unbroken lines = JH1 samples; black squares and broken lines = JH2 samples. For sample localisation see Fig.6.1.

Partial Melting

In JH1, the calculated Ta content (Table 7.3) slightly increases from the most primitive troctolite to the most differentiated one (2.5 to 2.9 ppm), and it is lower in JH1-US oxide-rich gabbros (1.5 ppm). In JH2-LS, the calculated Ta content is high (5.5 ppm), and it is lower and constant in JH2-US (3.6 ppm). The higher content of Ta in JH2-LS troctolites relative to JH1-LS troctolites indicates that the two lower series cannot be related by a common differentiation process. As well, the Ta-depletion trend from lower to upper series in both complexes is not attributable to a continuous crystal fractionation process linking troctolites to ol-gabbros to oxide-rich gabbros. As already argued on the basis of variations of the mineral trace element composition, four different parental magmas must be supposed at the origin of the four series.

The presence of different parental magmas can be attributed either to different magma sources or to different degrees of partial melting of a same magma source. Similar ages, similar isotopic composition and field relationships make the hypothesis of different magma sources strongly unrealistic. If the presence of different parental magmas generated by different degrees of partial melting is accepted, then it follows that JH2-LS parental magma originated from the smallest degree of partial melting (highest Ta content), and JH1-US parental magma originated from the largest degree of partial melting (lowest Ta content).

Assuming the same primitive source for JH1 and JH2 parental liquids, a concentration of Ta in the magma source of 0.1 ppm and a bulk partition coefficient of 0.01 (Villemant *et al.*, 1981; Lemarchand *et al.*, 1987), and according to the batch melting equation $C_L/C_0=1/F+D-FD$, where C_L is the trace element concentration in the liquid, C_0 is the trace element concentration in the source, and F is the melt fraction, the JH2-LS parental magma

originated from 0.8% of melting, the JH2-US on from 1.8%, the JH1-LS one from 3 % and the JH1-US one from 5.7%. Because of the large uncertainty in partition coefficients, these absolute values are strongly questionable, but they are robust in terms of demonstrating a gradual increase in degree of partial melting from JH2-LS to JH1-US parental magma.

Crystal Fractionation

During partial melting processes the content of a highly compatible element in the liquid portion is broadly constant and low for small melt fractions (F<0.5) independently of its content in the source. On the basis of the calculated degrees of partial melting, assuming a Ni content in the primitive source of 2100 ppm (Jagoutz *et al.*, 1979) and a mineral-liquid partition coefficient of 15 for Ni (Jones, 1984; Beattie *et al.*, 1991), the Ni content in the produced melts (primary magmas) is approximatively constant and close to 150 ppm. Then, solving the Rayleigh equation for crystal fractionation $C_L/C_0=F^{(D-1)}$, we can evaluate the degree of olivine fractionation that gabbros underwent before their emplacement within the Mesozoic cover. Calculation gives 2.4% of crystal fractionation for JH1-LS troctolites, 3.3% for JH2-LS troctolites, 6.8% for JH2-US ol-gabbros and 11.0% for JH1-US oxide-rich gabbros.

Comparing calculated values of JH1-LS liquids and measured compositions of JH1-LS chilled margin (Table 5.8), it can be observed that the calculated Ni and the MgO contents are higher in the chilled margin (240 ppm and 10.4%, respectively) than in the calculated liquids. This could mean that the supposed early stage of olivine fractionation did not occured at depth before magma emplacement within the Mesozoic cover, but at the base of JH1-LS and that, today, the lower portion of the series is not exposed. In other words, the troctolite G1 does not represent the most primitive gabbros of the series, but a already differentiated one.

7.5. Conclusions

The Jebel Hayim Massif in the Moroccan High Atlas comprises two alkaline gabbroic layered complexes formed by distinct batches of magma evolving in shallow magma chambers. On the basis of the content of compatible and incompatible elements in three-phase mineral assemblages, parental magma compositions have been calculated and interpreted in terms of partial melting and crystal fractionation prior to magma emplacement (Fig.7.5).

The oxide-rich gabbro parental magma formed through the largest degree of partial melting (5.7%) and the largest degree of early crystal fractionation (11%). The occurence of an early differentiation stage is supported by the low content of Ni in olivine, of Cr in clinopyroxene and Sr in plagioclase, and it was characterized by olivine, chromite and plagioclase precipitation. The JH1-LS troctolite parental magma formed through a smaller degree of partial melting (3%) and a small degree of early olivine fractionation (2.4%), as shown by its low incompatible element abundances and its high compatible element abundances. The presence of Cr-spinel inclusions in olivine and the Cr-rich composition of pyroxene indicate that early chromite fractionation was very limited, if compared to oxide-rich gabbros. The JH2-LS troctolites parental magma formed through the smallest degree of partial melting (0.8%) and a small degree of early olivine fractionation (3.3%). Finally, the JH2-US ol-gabbros parental magma formed through a small degree of partial melting (1.8%) and an intermediate degree of early olivine fractionation (6.8%).

In conclusion, the layered structure of JHM is the result of successive injections of cogenetic, but differently formed and evolved primary magmas. Magma emplacement occurred during the Upper Jurassic (Oxfordian) at the bottom of the Mesozoic cover of the Central High Atlas and was favoured by a sinistral strike-slip regime and by the reactivation of pre-existing vertical fault systems. According to radiometric data, JH1-LS troctolites are younger than JH2-US ol-gabbros and this is consistent with a multi-stage magma emplacement and the partial melting sequence. If our propositions are valid, small batches of primary liquids could evolve rapidly at a mantle or lower crustal level before their emplacement at higher crustal level. Each series originated from small batches of basaltic magmas (MgO comprised between 6.5 and 9%) which formed by small degrees (<6%) of partial melting of an uncontaminated source, without creation of large magma reservoirs: this kind of magma formation and evolution is a meaningful explanation for the absence of geophysical signature at a low or infracrustal level, despite the wideness of the basic magmatism in the High Atlas.

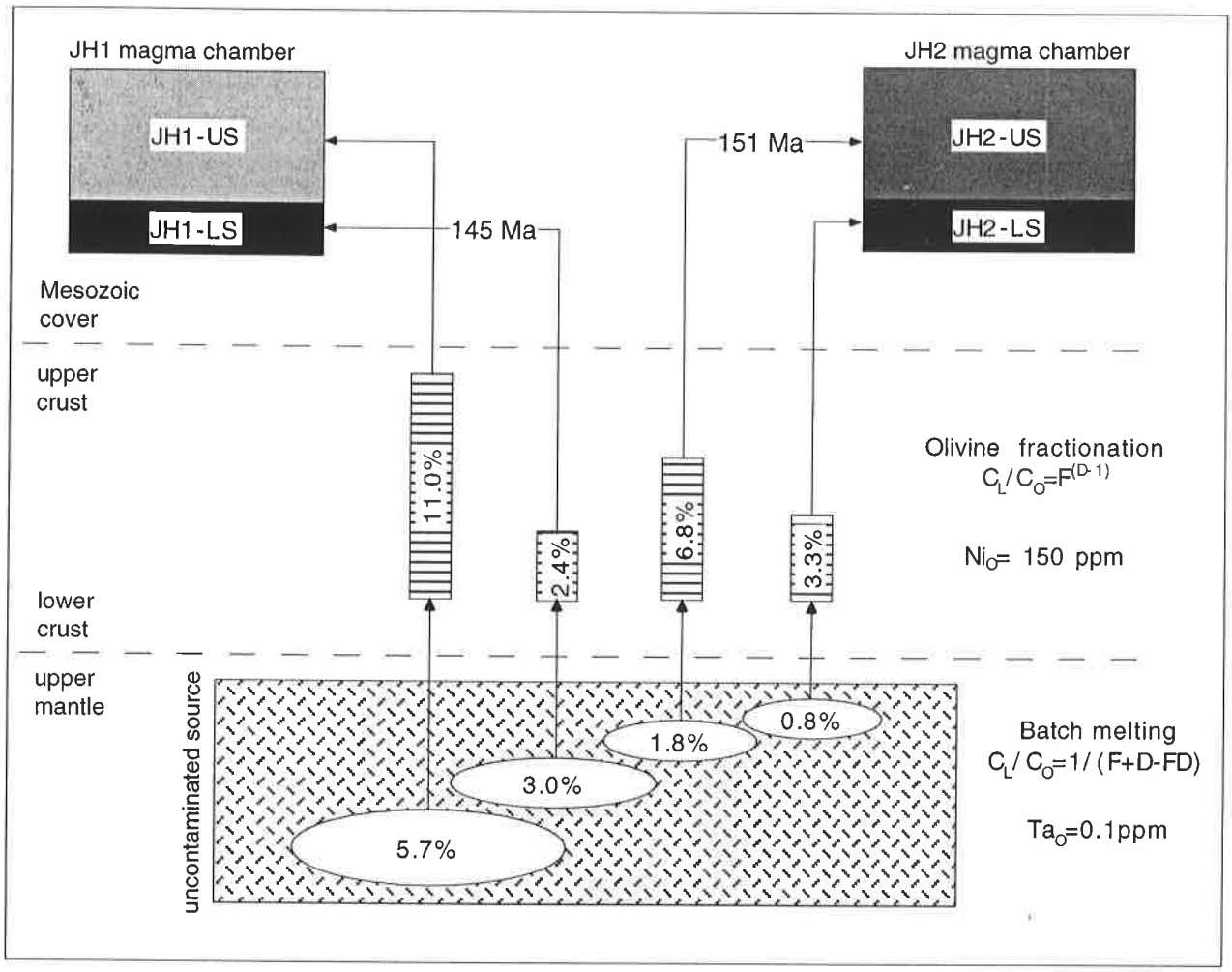

Fig. 7.4. Mantle partial melting (below), early olivine fractionation (middle) and JHM magmas emplacement at the bottom of the Mesozoic cover (above). Percentages indicate the increasing degree of partial melting (below) and the different degree of early olivine fractionation (middle).

- CHAPTER 8 -

A Global Model for JHM Evolution

In Chapter 3, 4, 5 and 6 new data from field, petrographic, geochemical and mineralogical investigations of the Jebel Hayim Massif were presented and discussed. In Chapter 7 liquid evolution in the two main complexes was modeled allowing quantitative estimation of the degrees of partial melting and fractional crystallization which are at the origin of the magmatic series. Now, a global evolutive model for the investigated area during the Middle to Upper Jurassic can be presented on the basis of the large amount of petrographic, mineralogical, geochemical and structural informations (Fig.8.1). Three main episodes have been distinguished.

Anticline Formation

This is the oldest episode recorded in the investigated area. It occurred during the Middle Jurassic and culminated in the Bajocian, with the deposition of a coral-reef horizon, indicating the presence of topographic highs (anticlinal ridges). Anticlines formed following a pre-existing "en echelon" fault system and were separated by large and flat syncline, disappearing close to the convergence point of anticlines.

Magma Emplacement

During the Early Malm two major events occurred simultaneously: 1) the first one was the beginning of a transtensional phase, and 2) the second one was the partial melting of the underlying continental mantle.

The transtensional phase was sinistral and directly related to the eastward drift of Africa. The same fault system which controlled anticline formation continued to be active, and new shear fractures appeared affecting the pre-existing anticline structures and fragmenting into blocks the mid-Jurassic cover. The horizontal movement of blocks along major and shear fractures caused extension or compression at the intersection of faults.

At the same time partial melting occurred in the underlying mantle and new magma was created (Fig.7.1); after a partial melting which did not not exceed 6% of the source, a basic magma periodically and intermittently ascended to the continental crust and finally solidified at the bottom of the Mesozoic cover. One or more differentiation stages characterized by olivine ± chromite fractionation preceded the final magma emplacement which occurred in the Oxfordian and was favoured by the presence of vertical faults and by blocks movement, which was able to create suitable space. Measured cooling ages (151 Ma for JH2-US ol-gabbros and 145 Ma for JH1-LS troctolites) are in agreement with calculated degree of partial melting: partial melting increases with time and, as a consequence, the largest degree of partial melting, the youngest gabbros. Also, estimated volumes of JH1 and JH2 lower and upper series (§ 2.2.1) are in agreement with calculated degrees of partial melting: volume increases with partial melting and, as a consequence, the thickest series (JH1-US), the largest degree of partial melting (6%).

Magma cooling was characterized by roof pendants collapse into the magma chamber, by intermittent magma chamber replenishments, originating the composite and layered structure of the intrusion, by fractional crystallisation in single batches of magma, by locally vigorous convection and by pneumatolysis. This last occurred in a sub-volcanic environment during the last stage of magma chamber solidification and it was triggered by the presence of a volatile-rich evolved liquid, originated by differentiation of the basic magma. Magmatic activity concluded with the emplacement of monzonites and syenites and monzonites which are interpreted as the last products of basic magma differentiation. This last episode was characterized by the coexistence and mixing of basic and acidic melts, originating hybrid rocks (mesocratic syenites).

Magma Chamber Extrusion

The present position of the Jebel Hayim Massif is not the original one. Vertical movements affected the whole intrusion during and after magma cooling, moving it up from the bottom of the Mesozoic cover (its original place)

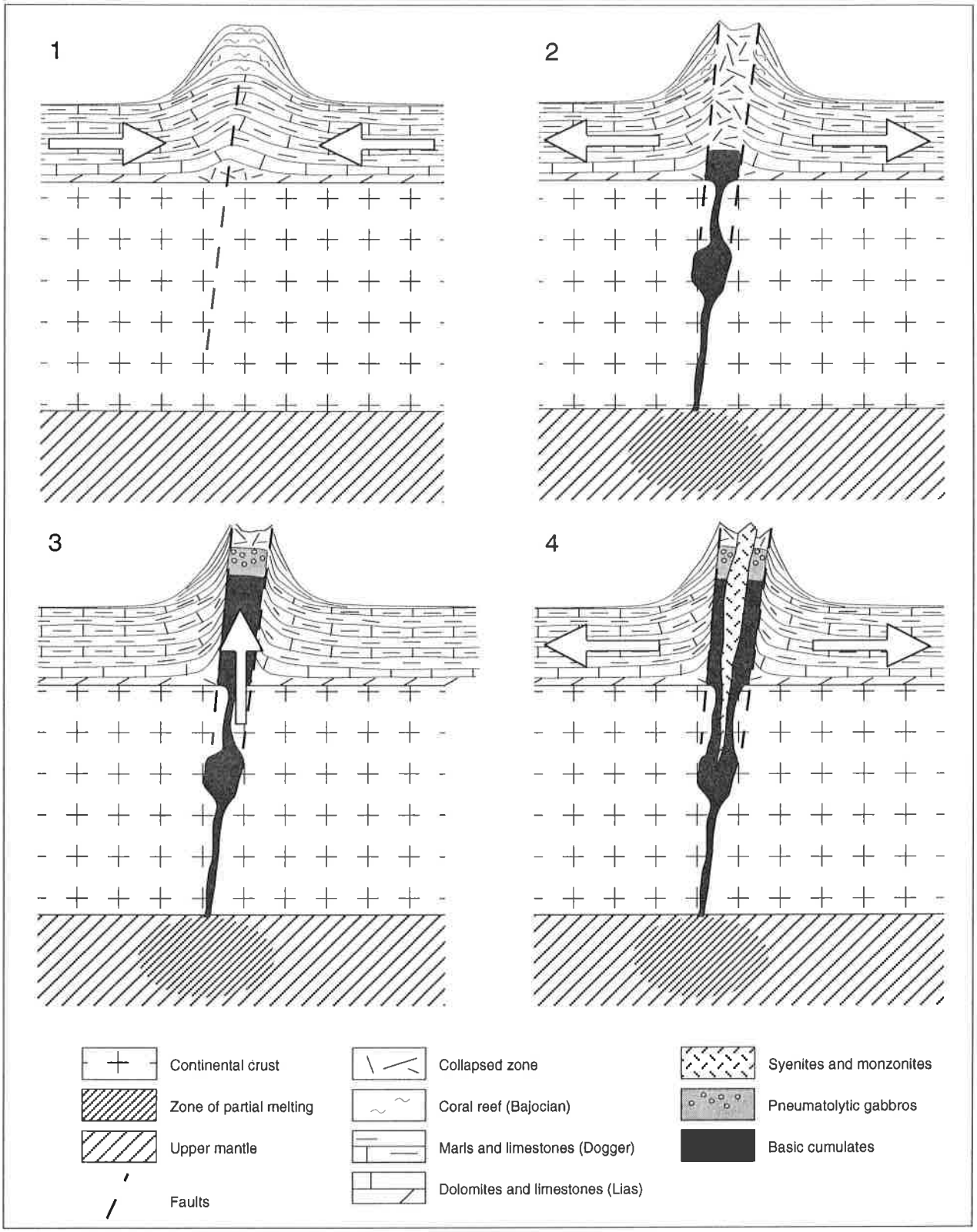

Fig.8.1 - Simplified reconstruction of JHM history during the Middle to Upper Jurassic (sedimentary formations overlying the coral reef horizon are not represented). 1) Anticline and coral reef formation (Bajocian); 2) Anticline break and magma emplacement at the bottom of the Mesozoic cover (Oxfordian); 3) Magma chambers uplift and pneumatolysis (Oxfordian); 4) Syenite and monzonite intrusion. Figure is dimensionless.

to the mid-Jurassic sequences and fragmenting it into several disconnected blocks. Magma chamber extrusion was driven by pre-existing vertical faults, the same which favoured magma ascent and emplacement.

Implications for the Central High Atlas history

The similarity of magmatic associations and geological setting between JHM and the other intrusive massifs in the Central High Atlas (Chèvremont, 1975; Monbaron, 1980; Brechbühler, 1984; Studer, 1987; Lhachmi, 1992; Zayane, 1992; Beraâouz & Bonin, 1993) allows us to suppose a similar origin for all intrusive massifs. Partial melting occurred discontinuously in time and space below the axial zone of the belt, magma ascended intermittently to the upper crust and it solidified at the base of the Mesozoic cover. Different degrees of partial melting and early differentiation stages occurring before magma emplacement generated distinct compositions of parental magmas. Later, magma chambers were tectonically extruded from the bottom of the Mesozoic cover to the mid-Jurassic sequences. With regards to the Central High history, the most important consequences of this kind of magma emplacement mechanism are:

- magma emplacement was not synsedimentary with mid-Jurassic sedimentation and anticline formation (age of magma cooling is younger than Dogger);

- magma emplacement was favoured by a sinistral transtensive régime;

- the presence of an unique large magma reservoir can be excluded. As a consequence, we can explain the lack of gravimetric anomaly below the Central High Atlas.

Finally, a few words must be spent about the cause of the thermal gradient increase which was at the origin of the partial melting of the mantle below the continenatl crust of the Atlas. In particular, two different but probably interactive causes are here suggested as starting points of discussion:

- the decrease of the thermal conductivity in the continental crust. This could be due to the presence of an overlying 7-8 km thick pile of water-rich sediments which deposed during the Early and Middle Jurassic in the Central High Atlas basin. Calculations are needed to prove this hypothesis.

- the proximity of an active mid-ocean ridge. During the Oxfordian, the Atlantic Ocean was already opened between North Africa and North America (Steiner *et al.*, in press), but a new mid-ocean ridge and new hot oceanic crust were forming between Africa and Iberia (Favre *et al.*, 1991; Favre & Stampfli, 1992). The High Atlas trench was a large fault system related to the mid-ocean ridge of the Alpine Neotethys.

References

Albarede F. (1976) - *Some trace element relationships among liquid and solid phases in the course of the fractional crystallization of magmas.* Geochimica et Cosmochimica Acta, 40, 667-673.

Allègre C.J. & Minster J.F. (1978) - *Quantitative models of trace elements behaviour in magmatic processes.* Earth and Planetary Science Letters, 38, 1-25.

Arth J.G. (1976) - *Behavior of trace elements during magmatic processes - A summary of theoretical models and their applications.* Journ.Research U.S. Geol.Survey, 4, 41-47.

Beattie P., Ford C. and Russell D. (1991) - *Partition coefficients for olivine-melt and orthopyroxene-melt systems.* Contrib.Mineral.Petrol., 109, 212-224.

Beattie P., Drake M., Jones J., Leeman W., Longhi J., McKay G., Nielsen R., Palme H., Shaw D., Takahashi E. and Watson B. (1993) - *Terminology for trace-element partitioning.* Geochimica et Cosmochimica Acta, 57, 1605-1606.

Bedard J.H. (1994) - *A procedure for calculating the equilibrium distribution of trace elements among the minerals of cumulate rocks, and the concentration of trace elements in the coexisting liquids.* Chemical Geology, 118, 143-153.

Beraâouz E.H. & Bonin B. (1993) - *Magmatisme alcalin intra-continental en contexte de décrochement: le massif plutonique de Tirrhist, Haut-Atlas (Maroc).* C.R. Acad.Sci.Paris, 317, 647-653.

Beraâouz E.H., Platevoet B. and Bonin B. (1994) - *Le magmatisme mésozoïque du Haut-Atlas (Maroc) et l'ouverture de l'Atlantique central.* C.R. Acad.Sci.Paris, 318, 1079-1085.

Bertrand H., Dostal J. and Dupuy C. (1982) - *Geochemistry of Early Mesozoic tholeiites from Morocco.* Earth and Planetary Science Letters, 58, 225-239.

Bevins R.E., Lees G.J., Roach R.A., Rowbotham G. and Floyd P.A. (1994) - *Petrogenesis of the St David's Head Layered Intrusion, Wales: a complex history of multiple magma injection and in situ crystallization.* Transactions of the Royal Society of Edinburgh: Earth Sciences, 85, 91-121.

Black R., Lameyre J. and Bonin B. (1985) - *The structural setting of alkaline complexes.* Journal of African Earth Sciences, 3, 5-16.

Blundy J.D. & Wood B.J. (1991) - *Crystal-chemical controls on the partitioning of Sr and Ba between plagioclase feldspar, silicate melts, and hydrothermal solutions.* Geochimica et Cosmochimica Acta, 55, 193-209.

Bonnefoi C.C., Provost A. and Albarède F. (1995) - *The "Daly gap" as a magmatic catastrophe.* Nature, 378, 270-272.

Brandeis G. & Jaupart C. (1986) - *On the interaction between convection and crystallization in cooling magma chambers.* Earth and Planetary Sciences Letters, 77, 345-361.

Brechbühler Y.-A. (1985) - *Etude structurale et géologique du Haut Atlas calcaire entre le Jebel Ayachi et Rich (Maroc).* Unpublished Thesis, Université de Neuchâtel (CH), 128 pp.

Brede R., Hauptmann M. and Herbig H.-G. (1992) - *Plate tectonics and intracratonic mountain ranges in Morocco - The Mesozoic-Cenozoic development of the Central High Atlas and the Middle Atlas.* Geologische Rundschau, 81/1, 127-141.

Brede R. (1992) - *Structural aspects of the Middle and the High Atlas (Morocco) - phenomena and causalities.* Geologische Rundschau, 81, 171-184.

Brown W.L. (1993) - *Fractional crystallization and zoning in igneous feldspars: ideal water-buffered liquid fractionation lines and feldpsar zoning paths.* Contrib.Mineral.Petrol., 113, 115-125.

Burgess C.J. & Lee C.W. (1978) - *The development of a lower Jurassic carbonate tidal flat, Central High Atlas, Morocco. 1: Sedimentary history.* Journal of Sedimentary Petrology, 48, 777-794.

Caïa J. (1968) - *Roches éruptives basiques et minéralosations en plomb, zinc et strontium de la région de Tirrhist (Haut Atlas de Midelt).* Notes et Mémoires du Service Géologique du Maroc, 206, 7-36.

Cameron M. & Papike J.J. (1981) - *Structural and chemical variations in pyroxenes.* American Mineralogist, 66, 1-50.

Campbell I.H. (1996) - Fluid dynamic processes in basaltic magma chambers. From "Layered Intrusions", Developments in Patrology, 15, 45 - 76.

Carman Jr M.F. (1994) - *Mechanisms of differentiation in shallow mafic alkaline intrusions, as illustrated in the Big Bend area, western Texas.* Journal of Volcanology and Geothermal Research, 61, 1-44.

Cashman K.V. (1993) - *Relationship between plagioclase crystallization and cooling in basaltic melts.* Contrib.Mineral.Petrol., 113, 126-142.

Cawthorn R.G., Groves D.I. and Marchant T. (1985) - *Magnesina ilmenite: clue to high-Mg parental magma of the Insizwa Complex, Transkei.* Canadian Mineralogist, 23, 609-618.

Chalokwu C.I., Grant N.K., Ariskin A.A. and Barmina G.S. (1993) - *Simulation of primary phase relations and mineral compositions in the Partridge River intrusion, Duluth Complex, Minnesota: implications for the parent magma composition.* Contrib.Mineral.Petrol., 114, 539-549.

Chayla B., H. J. and Joron J.L. (1973) - *Analyse par activation dans les neutrons épithermiques. Application à la détermination d'éléments en trace dans les roches.* C.R. Acad.Sci. Paris, 277 (série D), 273-275.

Chèvremont P. (1975) - *Ler roches éruptives basiques des boutonnières de Tassent et Tasraft et leurs indices métallifères dans leur cadre géologique (Haut-Atlas Centrale, Maroc).* Unpublished Thesis, Université Claude Bernard (Lyon I, F), 148 pp.

Choubert G. & Faure-Muret A. (1962) - *Evolution du domain atlasique marocain depuis les temps paléozoïques.* From "L'évolution paléogéographique et structurale des domaines méditerranéens et alpins d'Europe. Livre à la mémoire du Professeur P.Fallot", 1, 447-527.

Coish R.A. & Taylor L.A. (1979) - *The effect of cooling rate on texture and pyroxene chemistry in DSDP LEG 34 basalt: a microprobe study.* Earth and Planetary Science Letters, 42, 389-398.

Colson R.O., McKay G.A. and Taylor L.A. (1988) - *Temperature and composition dependencies of trace element partitioning: olivine/melt and low-Ca pyroxene/melt.* Geochimica et Cosmochimica Acta, 52, 539-553.

Cosca M., Sutter J.F. and Essene E.J. (1991) - *Cooling and inferred uplift/erosion history of the Grenville Orogen, Ontarion; constraints from 40Ar/39Ar thermochronology.* Tectonics, 10, 959-977.

Dostal J., Dupuy C., Carron J.P., Le Guen de Kerneizon M. and Maury R.C. (1983) - *Partition coefficients of trace elements: application to volcanic rocks of St.Vincent, West Indies.* Geochimica et Cosmochimica Acta, 47, 525-533.

Drake M.J. & Weill D.F. (1975) - *Partition of Sr, Ba, Ca, Y, Eu2+, Eu3+, and other REE between plagioclase feldspar and magmatic liquid: an experimental study.* Geochimica et Cosmochimica Acta, 39, 689-712.

Duchesne J.-C. (1978) - *Quantitative modeling of Sr, Ca, Rb, and K in the Bjerkrem layered lopolith (S.W. Norway).* Contrib.Mineral.Petrol., 66, 175-184.

Duda A. & Schmincke H.-U. (1985) - *Polybaric differentiation of alkali basaltic magmas: evidence from gree-core clinopyroxenes (Eifel, FRG).* Contrib.Mineral.Petrol., 91, 340-353.

Dunn T. (1987) - *Partitioning of Hf, Lu, Ti, and Mn between olivine, clinopyroxene and basaltic liquid.* Contrib.Mineral.Petrol., 96, 476-484.

Dunn T. & Sen C. (1994) - *Mineral/matrix partition coefficients for orthopyroxene, plagioclase, and olivine in basaltic to andesitic systems: a combined analytical and experimental study.* Geochimica et Cosmochimica Acta, 58, 717-733.

Elsdon R. (1982) - *Autometasomatic alteration of gabbro, Kap Edvard Holm intrusive complex, East Greenland.* Mineralogical Magazine, 45, 219-225.

Evans I., Kendall C.G.St.C. and Butler J.C. (1997) - *Genesis of Liassic shallow and deep water rhythms, Central High Atlas mountains, Morocco.* Journal of Sedimentary Petrology, 47, 120-128.

Evensen N.M., Hamilton P.J. and O'Nions R.K. (1978) - *Rare-earth abundances in chondrite meteorites.* Geochimica et Cosmochimica Acta, 42, 1199-1212.

Fadile A. (1987) - *Structure et évolution alpine du Haut Atlas Central sur la transversale Aghbala-Imilchil (Maroc).* Thése de Docteur Ingénieur, Univ. P.Sabatier, Toulouse (F), 968.

Favre P., Stampfli G.M. and Wildi, W. (1991) - *Jurassic sedimentary record and tectonic evolution of the northwestern corner of Africa.* Paleogeography, Paleoecology, Paleoclimatology, 87, 53-73.

Favre P. & Stampfli G.M. (1992) - *From rifting to passive margin: the example of the Red Sea, Central Atlantic and Alpine Tethys.* Tectonophysics, 215, 69-97.

Fedan B. et al. (1986) - *Données préliminaires sur la découverte d'intrusions jurassiques moyen atlasiques.* Bull.Inst.Sc.Rabat., 10, 53.

French W.J. & Cameron E.P. (1981) - *Calculation of the temperature of crystallization of silicates from basaltic melts.* Mineralogical Magazine, 44, 19-26.

Froitzheim N., Stets J. and Wurster P. (1988) - *Aspects of Western High Atlas tectonics.* From "The Atlas system of Morocco", 15, 219-244.

Frost B.R. & Lindsley D.H. (1991) - *Occurence of iron-titanium oxides in igneous rocks.* From "Oxide Minerals: Petrologic and Magnetic Significance", Reviews in Mineralogy, 25, 433-468.

Gallahan W.E. & Nielsen R.L. (1992) - *The partitioning of Sc, Y, and the rare earth elements between high-Ca pyroxene and natural mafic to intermediate lavas at 1 atmosphere.* Geochimica et Cosmochimica Acta, 56, 2387-2404.

Gamble R.P. & Taylor L.A. (1980) - *Crystal/liquid partitioning in augite: effects of cooling rate.* Earth and Planetary Science Letters, 47, 21-33.

Gast P.W. (1968) - *Trace element fractionation and the origin of tholeiitic and alkaline magma types.* Geochimica et Cosmochimica Acta, 32, 1057-1086.

Giese P. & Jacobshagen V. (1992) - *Inversion tectonics of intracontinental ranges: High and Middle Atlas, Morocco.* Geologische Rundschau, 81/1, 249-259.

Grant N.K. & Chalokwu C.I. (1992) - *Petrology of the Partridge River Intrusion, Duluth Complex, Minnesota: II. Geochemistry and strontium isotope systematics in Drill Core DDH-221.* Journal of Petrology, 33, 1007-1038.

Green T.H. (1980) - *Island arc and continent-building magmatism: a review of petrogenetic models based on experimental petrology and geochemistry.* Tectonophysics, 63, 367-385.

Green T.H. & Pearson N.J. (1985) - *Rare earth element partitioning between clinopyroxene and silicate liquid at moderate to high pressure.* Contrib.Mineral.Petrol., 91, 24-36.

Hailwood E.A. & Mitchell J.C. (1971) - *Paleomagnetic and radiometric dating results from Jurassic intrusions in South Morocco.* Geophys.J.R.Astron.Society, 24, 351-364.

Hart S.R. & Davis K.E. (1978) - *Nickel partitioning between olivine and silicate melt.* Earth and Planetary Science Letters, 40, 203-219.

Hart S.R. & Dunn T. (1993) - *Experimental cpx/melt partitioning of 24 trace elements.* Contrib.Mineral.Petrology, 113, 1-8.

Heitzmann P. (1987) - *Le Trias dans le Haut Atlas central de Midelt-Imilchil (Maroc) - lithostratigraphie et signification tectonique.* Eclogae geol.Helvetiae, 80, 669-684.

Hermann K. (1995) - Les ajouts: la chaux hydraulique. Bulletin du Ciment, 5, 3-7.

Hibbard M.J. (1981) - *The magma mixing of mantled feldspars.* Contrib.Mineral.Petrol., 76, 158-170.

Higuchi H. & Nagasawa H. (1969) - *Partition of trace elements between rock-forming minerals and the host volcanic rocks.* Earth and Planetary Science Letters, 7, 281-287.

Hill R. & Roeder P. (1974) - *The crystallization of spinel from basaltic liquid as a function of oxygen fugacity.* Journal of Geology, 82, 709-729.

Hoover J.D. (1989) - *The chilled marginal gabbro and other contact rocks of the Skaergaard intrusion.* Journal of Petrology, 30, 441-476.

Hort M. & Spohn T. (1991) - *Crystallization calculations for a binary melt cooling at constant rates of heat removal: implications for the crystallization of magma bodies.* Earth and Planetary Science Letters, 107, 463-474.

Housh T.B. & Luhr J.F. (1991) - *Plagioclase-melt equilibria in hydrous systems.* American Mineralogist, 76, 477-492.

Ibouh H., Bouabdelli M. and F. Z. (1996) - *Indices de tectonique synsédimentaire dans les dépôts aaléno-bajociens de la région d'Imilchil (Haut Atlas central, Maroc).* Miscellanea del Servizio Geologico Nazionale, 5, 305-310.

Irvine T.N. (1975) - *Crystallization sequences in the Muskox intrusion and other layered intrusions-II. Origin of chromite layers and similar deposits of other magmatic ores.* Geochimica et Cosmochimica Acta, 39, 991-1020.

Irvine T.N. (1980) - *Magmatic density currents and cumulus processes.* American Journal of Science, 280-A, 1-58.

Jacobshagen V., Brede R., Hauptmann M., Heinitz W. and Zylka R. (1988) - *Structure and post-Paleozoic evolution of the Central High Atlas.* From "The Atlas system of Morocco", Lecture Notes in Earth Sciences, 15,

Jacobshagen V. (1992) - *Major fracture zones of Morocco: the South Atlas and the Transalboran fault system.* Geologische Rundschau, 81, 185-197.

Jagoutz E., Palme H., Baddenhausen H., Blum K., Cendales M., Dreibus G., Spettel B., Lorenz V. and Wänke H. (1979) - *The abundances of major, minor and trace elements in the earth's mantle as derived from primitive ultramafic nodules.* Proc.Lunar Planet.Sci.Conf., 10th, 2031-2050.

Jenner G.A., Longerich H.P., Jackson S.E. and Fryer B.J. (1990) - *ICP-MS - A powerful tool for high-precision trace-element analysis in Earth Sciences: evidence from analysis of selected U.S.G.S. references samples.* Chemical Geology, 83, 133-148.

Jenner G.A., Foley S.F., Jackson S.E., Green T.H., Fryer B.J. and Longerich H.P. (1994) - *Determination of partition coefficients for trace elements in high pressure-temperature experimental run products by laser ablation microprobe-inductively coupled plasma-mass spectometry (LAM-ICP-MS).* Geochimica et Cosmochimica Acta, 58, 5099-5103.

Jenny J. (1983) - *Les décrochements de l'Atlas de Demnat (Haut Atlas central, Maroc): prolongation orientale de la Zone de décrochement du Tizi-n-Test et clef de la compréhension de la tectonique atlasique.* Eclogae geol.Helv., 76/1, 243-251.

Jenny J. (1984) - *Dynamique de la phase tectonique synsédimentaire du Jurassique moyen dans le Haut Atlas central (Maroc).* Eclogae geol.Helvetiae, 77, 143-152.

Jones J.H. (1984) - *Temperature- and pressure-indipendent correlations of olivine/liquid partition coefficients and their application to trace element partitioning.* Contrib.Mineral.Petrol, 88, 126-132.

Kennedy A.K., Lofgren G.E. and Wasserburg G.J. (1993) - *An experimental study of trace element partitioning between olivine, orthopyroxene and melt in chondrules: equilibrium values and kinetic effects.* Earth and Planetary Science Letters, 115, 177-195.

Kinzler R.J., Grove T.L. and Recca S.I. (1990) - *An experimental study on the effect of temperature and melt composition on the partitioning of nickel between olivine and silicate melt.* Geochimica et Cosmochimica Acta, 54, 1255-1265.

Kohn S.C., Henderson C.M.B. and Mason R.A. (1989) - *Element zoning trends in olivine phenocrysts from a supposed primary high-Mg andesite: an electron- and ion-microprobe study.* Contrib.Mineral.Petrol., 103, 242-252.

Kuehner S.M., Laughlin J.R., Grossman L., Johnson M.L. and Burnett D.S. (1989) - *Determination of trace element mineral/liquid partition coefficients in melilite and diopside by ion and electron microprobe techniques.* Geochimica et Cosmochimica Acta, 53, 3115-3130.

Kushiro I. (1960) - *Si-Al relation in clinopyroxene from igneous rocks.* American Journal of Science, 258, 548-554.

Larsen R.B. & Brooks C.K. (1994) - *Origin and evolution of gabbroic pegmatites in the Skaergaard Intrusion, East Greenland.* Journal of Petrology, 35, 1651-1679.

LaTourrette T.Z. & Burnett D.S. (1992) - *Experimental determination of U and Th partitioning between clinopyroxene and natural and synthetic basaltic liquid.* Earth and Planetary Science Letters, 110, 227-244.

Laville E., Lesage J.-L. and Seguret M. (1977) - *Géométrie, cinématique (dynamique) de la tectonique atlasique sur le versant sud du Haut Atlas marocain. Aperçu sur les tectoniques hercyniennes et tardi-hercyniennes.* Bull.Soc.géol.France, 19, 527-539.

Laville E. (1978) - *Incidence des jeux successifs d'un accident synsédimentaire sur les structures plicatives du versant nord du Haut Atlas central (Maroc).* Bull.Soc.géol.France, 20, 329-337.

Laville E. (1981) - *Rôle de décrochements dans le mécanisme de formation des bassins d'effondrement du Haut Atlas marocain au cours des temps triasique et liasique.* Bull.Soc.géol.France, 23, 303-312.

Laville E. & Harmand C. (1982) - *Evolution magmatique et tectonique du bassin intracontinental mésozoïque du Haut Atlas (Maroc): un modèle de mise en place synsédimentaire de massifs "anorogéniques" liés à des décrochements.* Bulletin de la Société géologique de France, XXIV,

Laville E. & Petit J.-P. (1984) - *Role of synsedimentary strike-slip faults in the formation of Moroccon Triassic basins.* Geology, 12, 424-427.

Laville E. & Piqué A. (1992) - *Jurassic penetrative deformation and Cenozoic uplift in the Central High Atlas (Morocco): a tectonic model. Structural and orogenic inversions.* Geologische Rundschau, 81, 157-170.

Leake B.E. (1978) - *Nomenclature of amphiboles.* American Mineralogist, 63, 1023-1052.

LeBas M.J. (1962) - *The role of aluminum in igneous clinopyroxenes with relation to their parentage.* American Journal of Science, 260, 267-288.

Leeman W.P. & Lindstrom D.J. (1978) - *Partitioning of Ni^{2+} between basaltic and synthetic melts and olivines - an experimental study.* Geochimica et Cosmochimica Acta, 42, 801-816.

Lemarchand F., Villemant B. and Calas G. (1987) - *Trace element distribution coefficients in alkaline series.* Geochimica et Cosmochimica Acta, 51, 1071-1081.

Lhachmi A. (1992) - *Pétrologie de l'intrusion alcaline et des roches magmatiques associées de la région d'Anemzi (Haut Atlas Central-Maroc).* Unpublished Thesis, Museum National d'Histoire Naturelle (Paris, F), 153 pp.

Lindstrom D.J. & Weil D.F. (1978) - *Partitioning of transition metals between diopside and coexisting silicate liquids. I. Nickel, cobalt, and manganese.* Geochimica et Cosmochimica Acta, 42, 817-831.

Liotard J.M., Briot D. and Boivin P. (1988) - *Petrological and geochemical relationships between pyroxene megacrysts and associated alkali-basalts from Massif Central (France).* Contrib.Mineral.Petrol, 98, 81-90.

Liou J.C. (1971) - *Synthesis and stability relations of prehnite, $Ca_2Al_2Si_3O_{10}(OH)_2$.* The American Mineralogist, 56, 507-531.

Liou J.C. (1973) - *Synthesis and stability relations of epidote, $Ca_2Al_2FeSi_3O_{12}(OH)$.* Journal of Petrology, 14, 381-413.

Liou J.C., Kuniyoshi S. and Ito K. (1974) - *Experimental studies of the phase relations between greenschist and amphibolite in a basaltic system.* American Journal of Science, 274, 613-632.

Longhi J., Wooden J.L. and Coppinger K.D. (1983) - *The petrology of high-Mg dikes from the Beartooth Mountains, Montana: a search for the parent magma of the Stillwater Complex.* Journal of Geophysical Research, B, Solid Earth and Planets, 88, 53-69.

Lundstrom C.C., Shaw H.F., Ryerson F.J., Phinney D.L., Gill J.B. and Williams Q. (1994) - *Compositional controls on the partitioning of U, Th, Ba, Pb, Sr and Zr between clinopyroxene and haplobasaltic melts: implications for uranium series disequilibria in basalts.* Earth and Planetary Science Letters, 128, 407-423.

Makris J., Demnati A. and Klussman J. (1985) - *Deep seismic soundings in Morocco and a crust and upper mantle model deduced from seismic and gravity data.* Annales Geophysicae, 3, 369-380.

Manspeizer W., Puffer J.H. and Cousminer H.L. (1978) - *Separation of Morocco and eastern North America: a Triassic-Liassic stratigraphic record.* Geol.Soc.Amer.Bull., 89, 901-920.

Mathison C.I. (1987) - *Pyroxene oikocrysts in troctolitic cumulates - evidence for supercooled crystallisation and postcumulus modification.* Contrib.Mineral.Petrol, 97, 228-236.

Mathison C.I. & Hamlyn P.R. (1987) - *The McIntosh layered troctolite-olivine gabbri intrusion, East Kimberly, Western Australia.* Journal of Petrology, 28, 211-234.

Mattauer M., Tapponier P. and Proust F. (1977) - *Sur les mécanismes de formation des chaînes intracontinentales. L'exemple des chaînes atlasiques du Maroc.* Bull.Soc.géol.France, 19, 521-526.

Mattis A.F. (1977) - *Nonmarine triassic sedimentation, Central High Atlas mountains, Morocco.* Journal of Sedimentary Petrology, 47, 107-119.

McKay G.A. & Weill D.F. (1976) - *Petrogenesis of KREEP.* Proc.Lunar Sci.Conference, 7th, 2427-244.

Mevel C. & Velde D. (1976) - *Clinopyroxenes in Mesozoic pillow lavas from the French Alps: influence of cooling rate on compositional trends.* Earth and Planetary Science Letters, 32, 158-164.

Michard A., Westphal M., Bossert A. and Hamzeh R. (1975) - *Tectonique de blocs dans le socle atlaso-mésetien du Maroc; une nouvelle interpretation des données géologiques et paléomagnetiques.* Earth and Planetary Science Letters, 24, 363-368.

Michard A. (1976) - *Eléments de géologie marocaine.* Notes et Mémoires du Service Géologique du Maroc, 407 pp.

Minster J.F., Minster J.B., Treuil M. and Allègre C.J. (1977) - *Systematics use of trace elements in igneous processes- Part II. Inverse problem of the fractional crystallization process in volcanic series.* Contrib.Mineral.Petrol., 61, 49-77.

Monbaron M. (1980) - *Le magmatisme basique de la région de Tagalft, dans son contexte géologique régional (Haut-Atlas central, Maroc).* C.R. Acad.Sci.Paris, 290 (série D), 1337-1340.

Monbaron M. (1981) - *Sédimentation, tectonique synsédimentaire et magmatisme basique: l'évolution paléogéographique et structurale de l'Atlas de Beni Mellal (Maroc) au cours du Mésozoïque; ses incidences sur la tectonique tertiaire.* Eclogae geol.Helvetiae, 74/3, 625-638.

Monbaron M. (1988) - *Un relief anté-Bathonien enfoui sur l'emplacement de la ride du Jbel La'bbadine (Haut Atlas central, Maroc); conséquences pour la chronologie de l'orogenèse atlasique.* Notes et Mémoires du Service géologique du Maroc, 44, 87-98.

Moody J.B., Meyer D. and Jenkins J.E. (1983) - *Experimental characterization of the greenschist/amphibolite boundary in mafic systems.* American Journal of Science, 283, 48-92.

Morimoto N., Fabries J., Ferguson A.K., Ginzburg I.V., Ross M., Seifert F.A. and Zussman J. (1988) - *Nomenclature of pyroxenes.* Mineralogical Magazine, 52, 535-550.

Morse S.A. (1981) - *Kigplait geochemistry IV: the major elements.* Geochimica et Cosmochimica Acta, 45, 461-479.

Nakamura Y. (1973) - *Origin of sector-zoning of igneous clinopyroxenes.* American MIneralogist, 58, 986-990.

Naslund H.R. (1989) - *Petrology of the Basistoppen Sill, East Greenland: a calculated magma differentiation trend.* Journal of Petrology, 30, 299-319.

Naslund H.R. & McBirney A.R. (1996) - Mechanisms of formation of igneous layering. From "Layered Intrusions", Developments in Petrology, 15, 1-43.

Nielsen R.L. (1988) - *A model for the simulation of combined major and trace element liquid lines of descent.* Geochimica et Cosmochimica Acta, 52, 27-38.

Nielsen R.L., Gallahan W.E. and Newberger F. (1992) - *Experimental determined mineral-melt partition coefficients for Sc, Y and REE for olivine, orthopyroxene, pigeonite, magnetite and ilmenite.* Contrib.Mineral.Petrol, 110, 488-499.

O'Hara M.J. & Fry N. (1996) - *The highly compatible trace element paradox - Fractional crystallization revisited.* Journal of Petrology, 37, 859-890.

Onuma N., Higuchi H., Wakita H. and Nagasawa H. (1968) - *Trace element partition between two pyroxenes and the host lava.* Earth and Planetary Science Letters, 5, 47-51.

Otten M.T. (1984) - *The origin of brown horneblende in the Artfjället gabbro and dolerites.* Contrib.Mineral.Petrol, 86, 189-199.

Panjasawatwong Y., Danyushevsky L.V., Crawford A.J. and Harris K.L. (1995) - *An experimental study of the effects of melt composition on plagioclase-melt equilibria at 5 and 10 kbar: implications for the origin of magmatic high-An plagioclase.* Contrib.Mineral.Petrol., 118, 420-432.

Philpotts J.A. & Schnetzler C.C. (1970) - *Phenocrysts-matrix partition coefficients for K, Rb, Sr and Ba, with applications to anorthosite and basalt genesis.* Geochimica et Cosmochimica Acta, 34, 307-322.

Presnall D.C., Dixon S.A., Dixon J.R., O'Donnell T.H., Brenner N.L., Schrock R.L. and Dycus D.W. (1978) - *Liquidus phase relations on the join diopside-forsterite-anorthite from 1 atm to 20 kbar: their bearing on the generation and crystallization of basaltic magma.* Contrib.Mineral.Petrol, 66, 203-220.

Proust F., Petit J.-P. and Tapponier P. (1977) - *Lâccident du Tizi n'Test et le rôle des décrochements dans la tectonique du Haut Atlas occidental (Maroc).* Bull.Soc.géol.France, 19, 541-551.

Ray G.L., Shimizu N. and Hart S.R. (1983) - *An ion microprobe study of the partitioning of trace elements between clinopyroxene and liquid in the system diopside-albite-anorthite.* Geochimica et Cosmochimica Acta, 47, 2131-2140.

Rock N.M.S., Gwalani L.G. and Griffin B.J. (1994) - *Alkaline rocks and carbonatites of Amba Dongar and adjacent areas, Deccan Alkaline Province, Gujarat, India. 2. Complexly zoned clinopyroxene phenocrysts.* Mineralogy and Petrology, 51, 113-135.

Roeder P.L. & Emslie R.F. (1970) - *Olivine-liquid equilibrium.* Contrib.Mineral.Petrol, 29, 275-289.

Roelandts I. (1988) - *Comparison of Inductively Coupled Plasma and Neutronic Activation analysis for precise and accurate determination of nine rare-earth elements in geological materials.* Chemical Geology, 67, 171-180.

Sadki D. (1992) - *Les variations de faciés et les discontinuités de sédimentation dans le Lias-Dogger du Hau Atlas central (Maroc): chronologie, caractérisation, corrélations.* Bull.Soc.géol.France, 163, 179-186.

Sebai A., Feraud G., Bertrand H. and Hanes J. (1991) - *40Ar/39Ar dating and geochemistry of tholeiitic magmatism related to the early opening of the Central Atlantic rift.* Earth and Planetary Science Letters, 104, 455-472.

Seufert G. (1988) - *Jurassic sediments and synsedimentary tectonics in the Central High Atlas, Morocco.* Bull.Soc.géol.France, 4, 375-390.

Singer B.S., Pearce T.H., Kolinsnik A.M. and Myers J.D. (1993) - *Plagioclase zoning in mid-Pleistocene lavas from the Seguam volcanic center, central Aleutian arc, Alaska.* American Mineralogist, 78, 143-157.

Snyder D., Carmichael I.S.E. and Wiebe R.A. (1993) - *Experimental study of liquid evolution in an Fe-rich, layered mafic intrusion: constraints of Fe-Ti oxide precipitation on the T-f_{O2} and T-r paths of tholeiitic magmas.* Contrib.Mineral.Petrol, 113, 73-86.

Sparks R.S.J. & Huppert H.E. (1984) - *Density changes during the fractional crystallization of basaltic magmas: fluid dynamic implications.* Contrib.Mineral.Petrol, 85, 300-309.

Sparks R.S.J., Huppert H.E., Kerr R.C., McKenzie D.P. and Tait S.R. (1985) - *Postcumulus processes in layered intrusions.* Geological Magazine, 122, 555-568.

Sparks R.S., Huppert H.E., Koyaguchi T. and Hallworth M.A. (1993) - *Origin of modal and rhythmic igneous layering by sedimentation in a convecting magma chamber.* Nature, 361, 246-249.

Spear F.S. (1993) - *Metamorphic phase equilibria and pressure-temperature-time paths.* Mineral.Soc.America, 799 pp.

Stanley R.G. (1981) - *Middle Jurassic shoaling of the Central High Atlas sea near Rich, Morocco.* Journ.Sedim. Petrol., 51, 895-907.

Steiner C., Hobson A., Favre, P., Stampfli G.M. and Hernandez J. (in press) - *Early Jurassic sea-floor spreading in the Central Atlantic - The Jurassic sequence of Fuerteventura (Canary Islands).* GSA Bulletin.

Studer M. & du Dresnay R. (1980) - *Déformations synsédimentaires en compression pendant le Lias supérieur et le Dogger, au Tizi n'Irhil (Haut Atlas central de Midelt, Maroc).* Bull.Soc.géol.France, XXII, 391-397.

Studer M. (1987) - *Tectonique et pétrographie des roches sédimentaires, éruptives et métamorphiques de la région de Tounfite-Tirrhist (Haut Atlas central mésozoïque, Maroc).* Notes et Mémoires du Service Géologique du Maroc, 43, 65-197.

Sun C.-O., Williams R.J. and Sun S.-S. (1974) - *Distribution coefficients of Eu and Sr for plagioclase-liquid and clinopyroxene-liquid equilibria in oceanic ridge basalt: an experimental study.* Geochimica et Cosmochimica Acta, 38, 1415-1433.

Tait S.R., Huppert H.E. and Sparks R.S.J. (1984) - *The role of compositional convection in the formation of adcumulate rocks.* Lithos, 17, 139-146.

Tait S.R. & Jaupart C. (1992) - *Compositional convection in a reactive crystalline mush and melt differentiation.* Journal of Geophysical Research, B, Solid Earth and Planets, 97, 6735-6756.

Tait S.R. & Jaupart C. (1996) - *The production of chemically stratified and adcumulate plutonic igneous rocks.* Mineralogical Magazine, 60, 99-114.

Thy P. & Lofgren G.E. (1994) - *Experimental constraints on the low-pressure evolution of transitional and mildly alkalic basalts: the effect of Fe-Ti oxide minerals and the origin of basaltic andesites.* Contrib.Mineral.Petrol, 116, 340-351.

Treuil M. & Varet J. (1973) - *Critères volcanologiques, pétrologiques et géochimiques de la gènese et de la differentiation des magmas basiques: exemple de l'Afar.* Bull.Soc.géol.France, 15, 506-540.

Treuil M., Joron J.-L., Jaffrezic H., Villemant B. and Calas G. (1979) - *Géochimie des éléments hygromagmatophiles, coefficients de partage minéraux/liquides et propriétés structurales de ces éléments dans les liquides magmatiques.* Bull.Minéral., 102, 402-409.

Tsuchiyama A. (1985) - *Crystallization kinetics in the system CaMgSi2O6-CaAl2Si2O8: development of zoning and kinetics effects on element partitioning.* American Mineralogist, 70, 474-486.

Turner S.P. (1996) - *Petrogenesis of the late-Delamerian gabbroic complex at Black Hill, South Australia: implications for convective thinning of the lithospheric mantle.* Mineralogy and Petrology, 56, 51-89.

Upton B.G.J., Stephenson D. and Martin A.R. (1985) - *The Tugtutôq older giant dyke complex: mineralogy and geochemistry of an alkali gabbro-augite syenite-foyaite association in the Gardar Province of South Greenland.* Mineralogical Magazine, 49, 623-643.

Villemant B., Jaffrezic H., Joron J.-L. and Treuil M. (1981) - *Distribution coefficients of major and trace elements; fractional crystallization in the alkali basalt series of Chaîne des Puys (Massif Central, France).* Geochimica et Cosmochimica Acta, 45, 1997-2016.

Villemant B. (1988) - *Trace element evolution in the Phlegrean Fields (Central Italy): fractional crystallization and selective enrichment.* Contrib.Mineral.Petrol., 98, 169-183.

Wager L.R., Brown G.M. and Wadsworth W.J. (1969) - *Types of igneous cumulates.* Journal of Petrology, 1, 73-85.

Wass S.Y. (1979) - *Multiple origin of clinopyroxenes in alkalic basaltic rocks.* Lithos, 12, 115-132.

Weill D.F. & McKay G.A. (1975) - *The partitioning of Mg, Fe, Sr, Ce, Sm, Eu, and Yb in lunar igneous systems and a possible origin of KREEP by equilibrium partial melting.* Proc.Lunar Sci.Conference, 6th, 1143-1158.

Westphal M., Montigny R., Thuizat R., Bardon C., Bossert A., Hamzeh R. and Rolley J.P. (1979) - *Paléomagnetisme et datation du volcanisme permien, triasique et crétacé du Maroc.* Canadian Journal of Earth Sciences, 16, 2150-2164.

Wiebe R.A, & Snyder D. (1993) - *Slow, dense replenishments of a basic magma chamber: the layered series of the Newark Island layered intrusion, Nain, Labrador.* Contrib.Mineral.Petrol., 113, 59-72.

Wigger P., Asch G., Giese P., Heinsohn W.D., El Alami S.O. and Ramdani F. (1992) - *Crustal structure along a traverse across the Middle and High Atlas mountains derived from seismic reflexion studies.* Geologische Rundschau, 81, 237-248.

Zayane R. (1992) - *La série plutonique jurassique du Haut Atlas Central marocain (région d'Imilchil): pétrographie et géochimie; aspects structuraux de sa mise en place.* Unpublished Thesis, Université de Brest (F), 201 pp.

Appendixes

Appendix 1 - Parageneses of JHM magmatic rocks

Appendix 2 - Analytical conditions and detection limits

Appendix 3 - X-Ray fluorescence analyses

Appendix 4 - ICP-MS analyses

Appendix 5 - Photos

Appendix 6 - Outcrop map of the Jebel Hayim Massif

Appendix 1 - Parageneses of JHM magmatic rocks.

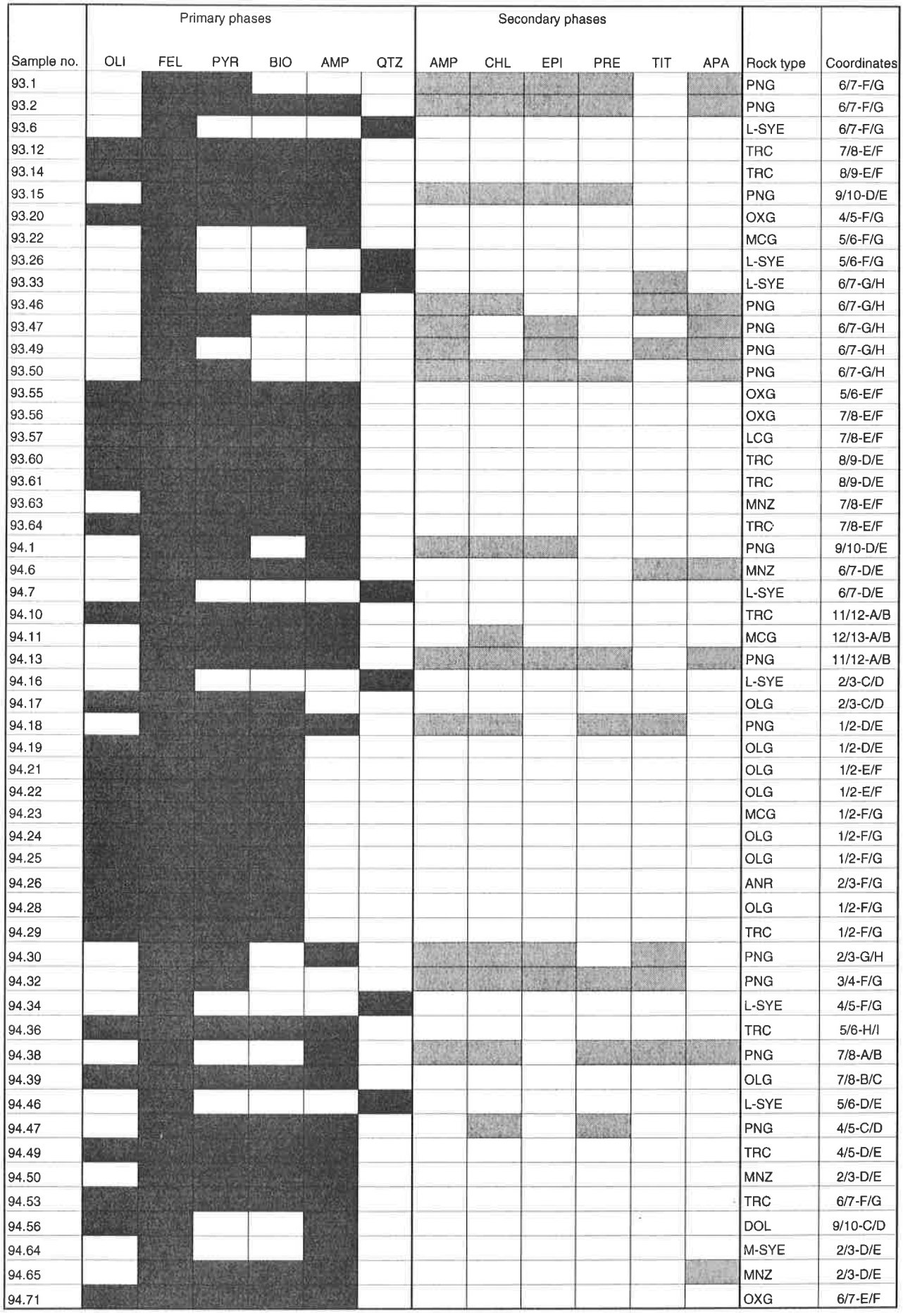

	Primary phases						Secondary phases							
Sample no.	OLI	FEL	PYR	BIO	AMP	QTZ	AMP	CHL	EPI	PRE	TIT	APA	Rock type	Coordinates
93.1													PNG	6/7-F/G
93.2													PNG	6/7-F/G
93.6													L-SYE	6/7-F/G
93.12													TRC	7/8-E/F
93.14													TRC	8/9-E/F
93.15													PNG	9/10-D/E
93.20													OXG	4/5-F/G
93.22													MCG	5/6-F/G
93.26													L-SYE	5/6-F/G
93.33													L-SYE	6/7-G/H
93.46													PNG	6/7-G/H
93.47													PNG	6/7-G/H
93.49													PNG	6/7-G/H
93.50													PNG	6/7-G/H
93.55													OXG	5/6-E/F
93.56													OXG	7/8-E/F
93.57													LCG	7/8-E/F
93.60													TRC	8/9-D/E
93.61													TRC	8/9-D/E
93.63													MNZ	7/8-E/F
93.64													TRC	7/8-E/F
94.1													PNG	9/10-D/E
94.6													MNZ	6/7-D/E
94.7													L-SYE	6/7-D/E
94.10													TRC	11/12-A/B
94.11													MCG	12/13-A/B
94.13													PNG	11/12-A/B
94.16													L-SYE	2/3-C/D
94.17													OLG	2/3-C/D
94.18													PNG	1/2-D/E
94.19													OLG	1/2-D/E
94.21													OLG	1/2-E/F
94.22													OLG	1/2-E/F
94.23													MCG	1/2-F/G
94.24													OLG	1/2-F/G
94.25													OLG	1/2-F/G
94.26													ANR	2/3-F/G
94.28													OLG	1/2-F/G
94.29													TRC	1/2-F/G
94.30													PNG	2/3-G/H
94.32													PNG	3/4-F/G
94.34													L-SYE	4/5-F/G
94.36													TRC	5/6-H/I
94.38													PNG	7/8-A/B
94.39													OLG	7/8-B/C
94.46													L-SYE	5/6-D/E
94.47													PNG	4/5-C/D
94.49													TRC	4/5-D/E
94.50													MNZ	2/3-D/E
94.53													TRC	6/7-F/G
94.56													DOL	9/10-C/D
94.64													M-SYE	2/3-D/E
94.65													MNZ	2/3-D/E
94.71													OXG	6/7-E/F

Sample no.	Primary phases						Secondary phases						Rock type	Coordinates
	OLI	FEL	PYR	BIO	AMP	QTZ	AMP	CHL	EPI	PRE	TIT	APA		
94.73													OXG	6/7-E/F
94.76													TRC	5/6-F/G
94.77													OXG	5/6-F/G
94.77b													OXG	6/7-E/F
94.78													OXG	7/8-E/F
94.80													OXG	7/8-E/F
94.81													OXG	7/8-E/F
94.96													MCG	8/9-A/B
94.97													TRC	8/9-A/B
94.104													OLG	2/3-E/F
94.110													MCG	7/8-F/G
94.118B													TRC	10/11-B/C
94.121													TRC	10/11-B/C
94.124													L-SYE	10/11-B/C
94.125													PNG	11/12-B/C
95.1													PNG	4/5-I/J
95.9													L-SYE	6/7-D/E
95.11													L-SYE	6/7-D/E
95.15													PNG	2/3-H/I
95.17													PNG	2/3-G/H
95.18													PNG	1/2-G/H
95.19													TRC	1/2-F/G
95.21													PNG	6/7-J/K
95.25													PNG	6/7-I/J
95.30													TRC	11/12-C/D
95.31													MCG	11/12-C/D
95.33													PNG	2/3-F/G
95.35													M-SYE	3/4-C/D
A													PNG	6/7-G/H
B													TRC	7/8-E/F
C													TRC	8/9-E/F
E													L-SYE	6/7-F/G
F													PNG	6/7-F/G
G													PNG	6/7-F/G
H													L-SYE	6/7-F/G
1A													MCG	2/3-H/I
2A													TRC	2/3-G/H
3A													PNG	2/3-G/H
4A													PNG	3/4-G/H
11A													PNG	4/5-G/H
12A													DOL	5/6-G/H
14A													L-SYE	5/6-G/H
1B													PNG	6/7-C/D
3B													PNG	6/7-C/D
6B													PNG	7/8-C/D
9B													PNG	8/9-C/D

Feldspar from TRC, OXG, OLG, LCG, ANR, MCG, DOL, PNG and MNZ is plagioclase. Feldspar from MNZ and SYE is alkali-feldpspar.

Pyroxene from TRC, OXG, OLG, LCG, ANR, MCG, DOL and PNG is augite. Pyroxene from MNZ is hedenbergite.

Amphibole from TRC, OXG, OLG and LCG is kaersutite. Amphibole from PNG is actinolite. Amphibole from MNZ is Fe-richterite.

Amphibole from SYE is hastingsitic hornblende. Fe-Ti oxide is ilmenite in all samples, but OXG (magnetite).

OLI = olivine; FEL = feldspar; PYR = pyroxene; BIO = biotite; AMP = amphibole; QTZ = quartz; CHL = chlorite; EPI = epidote; PRE = prehnite; TIT = titanite; APA = apatite. For rock abbreviations see Chapter 1.

Appendix 2 - Analytical conditions and detection limits.

Part A - Analytical conditions for Electron Microprobe analysis

Mineral	Element	1	2	3	4	standard	Mineral	Element	1	2	3	4	standard
Amphibole	Si^{4+}	35	15	15	0.1	diopside	Olivine	Si^{4+}	25	15	20	0.1	forsterite
	Ti^{4+}	20	15	15	0.1	$MnTiO_3$		Ti^{4+}	25	15	20	0.1	$MnTiO_3$
	Al^{3+}	35	15	15	0.1	hornblende		Al^{3+}	25	15	20	0.1	jadeite
	Cr^{3+}	20	15	15	0.1	Cr_2O_3		Fe^{2+}	25	15	20	0.1	fayalite
	Fe^{+2}	20	15	15	0.1	hedenbergite		Mn^{2+}	25	15	20	0.1	$MnTiO_3$
	Mn^{2+}	20	15	15	0.1	$MnTiO_3$		Mg^{2+}	25	15	20	0.1	forsterite
	Mg^{2+}	35	15	15	0.1	diopside		Ca^{2+}	25	15	20	0.1	wollastonite
	Ca^{2+}	20	15	15	0.1	wollastonite		Ni^{2+}	60	15	20	0.1	NiO
	Na^{1+}	35	15	15	0.1	jadeite							
							Plagioclase	Si^{4+}	15	15	15	0.1	anorthite
Biotite	Si^{4+}	25	15	15	0.1	phlogopite		Ti^{4+}	15	15	15	0.1	$MnTiO_3$
	Ti^{4+}	20	15	15	0.1	$MnTiO_3$		Al^{3+}	15	15	15	0.1	anorthite
	Al^{3+}	25	15	15	0.1	biotite		Fe^{+3}	15	15	15	0.1	hedenbergite
	Fe^{2+}	25	15	15	0.1	biotite		Mg^{2+}	15	15	15	0.1	diopside
	Mn^{2+}	25	15	15	0.1	$MnTiO_3$		Ca^{2+}	15	15	15	0.1	anorthite
	Mg^{2+}	25	15	15	0.1	phlogopite		Na^{1+}	15	15	15	0.1	albite
	Ca^{2+}	15	15	15	0.1	wollastonite		K^{1+}	20	15	15	0.1	orthoclase
	Na^{1+}	25	15	15	0.1	jadeite							
	K^{1+}	20	15	15	0.1	phlogopite	Pyroxene	Si^{4+}	20	15	20	0.1	diopside
	F	60	15	15	0.1	phlogopite		Ti^{4+}	30	15	20	0.1	$MnTiO_3$
								Al^{3+}	30	15	20	0.1	andalusite
Fe-Ti oxide	Si^{4+}	30	15	20	0.1	wollastonite		Cr^{3+}	30	15	20	0.1	Cr_2O_3
	Ti^{4+}	30	15	20	0.1	$MnTiO_3$		Fe^{2+}	20	15	20	0.1	hedenbergite
	Al^{3+}	30	15	20	0.1	spinel		Mn^{2+}	20	15	20	0.1	$MnTiO_3$
	Cr^{3+}	20	15	20	0.1	Cr_2O_3		Mg^{2+}	20	15	20	0.1	diopside
	Fe^{2+}	20	15	20	0.1	hematite		Ca^{2+}	20	15	20	0.1	wollastonite
	Mn^{2+}	20	15	20	0.1	$MnTiO_3$		Na^{1+}	30	15	20	0.1	jadeite
	Mg^{2+}	60	15	20	0.1	spinel							
	Ca^{2+}	30	15	20	0.1	wollastonite							
	Ni^{2+}	20	15	20	0.1	NiO							
	Co^{2+}	20	15	20	0.1	CoO							
	V^{5+}	20	15	20	0.1	V_2O_5							

Column 1 = counting time (s); Column 2 = voltage (hv); Column 3 = current (na); Column 4 = required precision (%).

Part B - Detection limits for trace element analysis

Elemer	1	2
Nb	3	
Zr	2	
Y	1	1.0
Sr	1	
Rb	1	
Ga	1	
Zn	3	
Cu	4	
Ni	2	
Co	2	
Cr	3	
V	3	
Ba	3	
S	10	
La		0.1
Ce		0.1
Pr		0.1
Nd		0.1
Sm		0.1
Eu		0.05
Gd		0.1
Tb		0.1
Dy		0.1
Ho		0.05
Er		0.1
Tm		0.1
Yb		0.1
Lu		0.05
Th		0.1
U		0.1

Column 1 = X-ray fluoresence (ppm); Column 2 = ICP-MS (ppm)

Rock type	TRC	TRC	TRC	OXG	OXG	TRC	TRC	OXG	OXG	TRC	OXG	OXG	TRC	TRC	OXG	TRC	OXG	TRC	OXG	TRC	TRC	TRC	TRC	TRC
Sample no.	93/14	C	93/12	93/20	94/71	B	94/10	94/77B	93/55	94/53	94/73	94/78	94/76	94/49	94/77	94/29	94/80	93/64	93/56	93/61	94/36	94/118B	93/60	95/30
Analysis	1	2	3	4	5	6	7	8	9	10	11	12	13	14	15	16	17	18	19	20	21	22	23	24
SiO_2	40.76	40.98	41.58	42.08	42.22	42.29	42.31	42.36	42.43	42.49	42.52	42.78	42.79	42.91	43.35	43.37	43.45	43.45	43.62	44.08	44.16	44.35	44.68	44.82
TiO_2	0.56	0.56	0.60	3.48	2.65	0.57	0.92	2.78	2.65	0.68	2.85	2.59	0.76	1.01	2.98	0.79	2.43	0.67	2.50	0.88	1.47	1.09	1.06	1.74
Al_2O_3	8.49	8.74	8.71	13.37	13.84	11.10	9.94	14.08	13.69	10.80	13.44	13.52	11.97	11.24	13.90	9.88	13.07	13.11	14.20	11.50	12.35	11.55	12.07	13.76
Fe_2O_3	3.75	7.13	4.48	9.12	11.26	4.45	n.m.	9.32	8.78	n.m.	9.46	10.46	6.06	n.m.	9.11	2.99	8.65	3.20	9.28	4.86	n.m.	6.75	2.29	n.m.
FeO	11.29	7.95	10.40	8.68	5.80	8.95	n.m.	7.86	8.06	n.m.	7.56	6.10	6.90	n.m.	7.67	12.01	7.06	10.32	6.38	9.53	n.m.	6.68	11.16	n.m.
Fe_2O_{3tot}	16.30	15.96	16.04	18.77	17.71	14.40	15.34	18.05	17.74	15.02	17.86	17.24	13.73	14.34	17.63	16.33	16.50	14.67	16.37	15.45	14.36	14.17	14.69	13.30
MnO	0.17	0.18	0.17	0.14	0.12	0.16	0.17	0.13	0.12	0.17	0.13	0.11	0.16	0.17	0.13	0.19	0.12	0.17	0.12	0.18	0.16	0.17	0.16	0.18
MgO	25.67	26.15	25.94	6.63	7.32	22.26	20.66	7.04	7.49	21.11	7.06	7.29	18.57	18.51	7.14	20.87	7.83	16.92	7.15	18.41	14.97	16.85	16.34	10.73
CaO	4.75	4.86	5.12	11.46	13.02	5.33	5.58	12.23	12.54	6.07	12.94	13.51	6.68	7.55	12.65	5.61	13.80	7.65	13.20	6.48	6.71	7.86	6.85	8.57
Na_2O	1.46	1.30	1.35	2.76	1.96	1.81	1.81	2.42	2.25	1.75	2.11	1.91	1.87	1.97	2.17	2.12	1.84	2.04	2.26	2.09	2.72	1.91	2.32	2.18
K_2O	0.28	0.28	0.24	0.40	0.23	0.28	0.61	0.35	0.28	0.32	0.23	0.22	0.36	0.64	0.23	0.49	0.23	0.26	0.24	0.51	1.15	0.74	0.64	1.47
P_2O_5	0.12	0.07	0.10	0.08	0.05	0.09	0.14	0.07	0.06	0.11	0.05	0.05	0.12	0.14	0.05	0.10	0.05	0.06	0.05	0.12	0.24	0.16	0.13	0.22
H_2O	1.63	0.48	0.61	0.70	n.m.	2.36	n.m.	n.m.	0.65	n.m.	n.m.	n.m.	n.m.	n.m.	n.m.	0.53	n.m.	0.82	0.43	1.10	n.m.	n.m.	1.74	n.m.
CO_2	0.27	0.55	0.63	0.29	n.m.	0.35	n.m.	n.m.	0.10	n.m.	n.m.	n.m.	n.m.	n.m.	n.m.	0.09	n.m.	0.25	0.18	0.21	n.m.	n.m.	0.22	n.m.
LOI	n.m.	n.m.	n.m.	n.m.	0.56	n.m.	1.45	0.71	n.m.	0.69	0.70	0.56	2.68	0.56	0.70	n.m.	0.66	n.m.	n.m.	n.m.	1.93	1.01	n.m.	2.43
Total	99.20	99.23	99.93	99.19	99.03	100.00	98.93	99.35	99.10	99.21	99.05	99.10	98.92	99.04	100.08	99.04	99.19	98.92	99.61	99.95	100.22	99.12	99.66	99.40
S	168	196	199	147	406	189	252	1051	57	202	1183	297	196	240	1051	71	286	219	384	242	308	288	236	372
V	102	101	110	881	865	94	136	1018	807	111	1084	857	117	157	1018	129	802	146	815	140	185	175	146	244
Cr	1133	1152	1250	17	19	1007	988	21	19	909	19	19	775	746	21	732	34	694	16	671	488	648	596	342
Co	109	112	123	57	58	105	97	66	51	99	64	54	85	89	66	96	58	86	78	89	83	83	86	66
Ni	806	851	878	65	91	706	689	3	84	640	9	81	580	490	3	547	149	471	94	545	488	441	481	287
Cu	66	89	98	232	1055	79	123	36	683	90	37	989	57	107	36	15	1000	80	891	97	97	93	91	58
Zn	113	110	115	92	85	102	112	91	76	123	83	82	121	104	91	114	81	110	79	115	115	104	108	108
Ga	13	12	13	28	20	13	17	20	28	15	19	20	10	17	20	16	19	17	25	18	21	13	18	12
Rb	4	4	4	7	6	5	11	7	7	5	7	7	6	9	7	9	6	5	5	9	19	12	10	27
Sr	340	233	231	410	370	304	432	436	410	289	401	364	343	376	436	263	339	388	365	352	408	383	374	470
Y	6	3	5	14	n.d.	3	11	n.d.	12	7	n.d.	n.d.	n.d.	11	n.d.	8	n.d.	6	10	11	16	7	11	7
Zr	31	29	31	58	45	29	58	45	42	37	42	45	45	68	45	51	45	26	35	57	109	81	65	111
Nb	n.d.	n.d.	n.d.	n.d.	n.d.	n.d.	n.d.	n.d.	n.d.	n.d.	n.d.	n.d.	n.d.	n.d.	n.d.	n.d.	n.d.	n.d.	n.d.	n.d.	12	2	2	16
Ba	n.d.	n.d.	n.d.	47	26	n.d.	101	38	n.d.	53	29	21	17	103	38	n.d.	22	n.d.	23	n.d.	179	57	49	215

Oxide concentrations are expressed as wt%; trace element concentrations are expressed as ppm. n.m. = not measured; n.d. = not detected. For trace element detection limits see Annex 3. For rock abbreviations see Chapter 1.

Rock type	PNG	TRC	PNG	PNG	PNG	MCG	OLG	PNG	PNG	MCG	PNG	OLG	PNG	PNG	MCG	OLG	PNG	OLG	OLG	PNG	LCG	OLG	OLG	PNG
Sample no.	3B	94/121	9B	95/1	94/96	95/31	2A	94/1	G	1A	94/38	94/28	93/50	93/47	94/11	94/39	6B	94/24	94/25	1B	93/57	94/97	94/17	95/18
Analysis	25	26	27	28	29	30	31	32	33	34	35	36	37	38	39	40	41	42	43	44	45	46	47	48
SiO_2	44.90	44.92	45.00	45.09	45.49	45.51	45.59	45.87	46.12	46.24	46.26	46.46	46.49	46.68	46.76	46.81	46.81	46.87	47.09	47.26	47.32	47.45	47.59	47.71
TiO_2	2.91	1.25	2.81	3.27	3.91	1.82	1.31	1.03	2.78	1.52	3.26	0.86	2.15	3.05	1.75	1.10	1.90	1.11	1.06	1.71	0.67	1.46	1.58	1.91
Al_2O_3	16.19	11.87	17.67	15.70	14.19	14.59	14.76	16.02	16.35	14.03	16.47	12.41	14.37	13.24	15.23	15.47	16.34	11.84	12.80	17.67	18.94	14.13	14.38	15.44
Fe_2O_3	n.m.	6.43	n.m.	n.m.	n.m.	n.m.	5.25	n.m.	11.78	n.m.	n.m.	3.99	n.m.	n.m.	n.m.	n.m.	n.m.	3.92	2.51	n.m.	2.70	n.m.	2.54	n.m.
FeO	n.m.	7.06	n.m.	n.m.	n.m.	n.m.	8.02	n.m.	1.54	n.m.	n.m.	7.66	n.m.	n.m.	n.m.	n.m.	n.m.	8.57	8.10	n.m.	5.06	n.m.	8.84	n.m.
Fe_2O_{3tot}	12.89	14.28	12.40	13.53	15.18	12.74	14.16	11.15	13.49	12.89	8.23	12.50	13.38	17.11	12.91	10.73	10.23	13.44	11.51	8.90	8.32	11.49	12.36	12.76
MnO	0.14	0.17	0.12	0.16	0.21	0.19	0.16	0.12	0.15	0.15	0.06	0.15	0.14	0.20	0.16	0.15	0.12	0.17	0.14	0.11	0.10	0.15	0.15	0.23
MgO	4.71	16.13	4.66	4.66	5.26	8.42	11.29	9.91	4.30	9.98	4.16	15.26	6.47	4.19	8.66	10.57	6.62	13.46	12.42	5.66	8.65	10.48	9.88	5.88
CaO	9.37	6.22	11.07	9.87	7.96	7.27	7.89	6.57	8.64	8.11	12.12	8.67	10.11	7.55	6.44	9.86	11.52	9.78	10.73	11.06	11.09	9.11	8.01	7.05
Na_2O	4.13	2.21	3.13	2.93	3.42	3.19	2.70	3.35	3.51	2.87	3.94	2.46	2.77	4.04	3.16	2.94	2.98	2.57	2.66	3.67	3.00	2.90	3.63	3.16
K_2O	1.22	0.71	1.35	1.37	1.37	1.20	0.72	1.33	1.78	0.64	0.43	0.51	1.33	1.04	1.63	0.70	1.17	0.60	0.56	1.18	0.33	0.89	1.05	1.97
P_2O_5	0.27	0.16	0.14	0.17	0.31	0.26	0.17	0.14	0.25	0.20	1.25	0.11	0.14	0.79	0.26	0.14	0.23	0.14	0.11	0.25	0.10	0.19	0.23	0.20
H_2O	n.m.	n.m.	n.m.	n.m.	n.m.	n.m.	1.13	n.m.	1.99	n.m.	n.m.	0.38	n.m.	n.m.	n.m.	n.m.	n.m.	0.55	0.52	n.m.	0.94	n.m.	1.02	n.m.
CO_2	n.m.	n.m.	n.m.	n.m.	n.m.	n.m.	0.21	n.m.	0.35	n.m.	n.m.	0.10	n.m.	n.m.	n.m.	n.m.	n.m.	0.08	0.24	n.m.	0.14	n.m.	0.10	n.m.
LOI	2.48	2.87	1.94	2.34	1.88	3.31	n.m.	3.54	n.m.	2.57	3.26	n.m.	1.82	1.19	2.79	1.18	1.91	n.m.	n.m.	1.93	n.m.	1.29	n.m.	2.78
Total	99.21	100.00	100.29	99.09	99.18	98.50	99.20	99.03	99.54	99.20	99.44	99.02	99.17	99.08	99.75	99.65	99.83	99.66	98.94	99.40	99.04	99.54	99.00	99.09
S	350	292	392	118	458	174	252	144	408	198	55	80	188	49	54	343	292	89	88	54	202	289	131	46
V	431	162	488	473	433	229	193	139	443	191	121	145	365	139	220	161	272	193	189	105	91	182	179	244
Cr	15	527	17	23	18	292	406	297	20	319	12	785	211	20	361	491	302	678	710	85	289	479	344	162
Co	48	78	51	46	45	56	68	60	50	64	48	74	60	49	66	60	50	70	65	27	51	53	63	49
Ni	15	583	16	n.d.	n.d.	228	255	184	5	325	3	301	26	n.d.	198	263	91	236	192	31	134	285	198	25
Cu	20	76	37	n.d.	n.d.	67	58	28	14	101	n.d.	n.d.	n.d.	30	53	74	49	18	15	46	86	56	37	55
Zn	98	121	93	79	96	161	104	72	87	114	30	85	64	156	84	125	88	92	81	70	54	87	95	107
Ga	27	13	27	18	22	13	22	19	27	22	24	18	26	30	23	20	23	20	19	30	20	13	23	16
Rb	23	14	27	31	20	24	15	27	46	13	7	8	34	16	32	12	18	9	9	27	5	16	15	49
Sr	908	366	1674	786	699	661	421	698	372	257	284	332	356	440	1054	534	785	330	359	712	526	446	417	370
Y	21	8	19	7	17	10	12	12	15	18	38	10	17	34	20	13	18	14	13	18	7	8	19	11
Zr	104	86	69	88	152	135	65	64	68	88	109	51	68	124	105	65	90	66	60	83	35	101	107	93
Nb	9	1	2	5	20	13	1	n.d.	4	0	8	n.d.	1	9	8	n.d.	6	1		3	n.d.	5	5	6
Ba	264	73	170	188	186	163	71	234	218	81	31	38	182	206	370	108	193	53	37	256	n.d.	114	90	383

Oxide concentrations are expressed as wt%; trace element concentrations are expressed as ppm. n.m. = not measured; n.d. = not detected. For trace element detection limits see Annex 3. For rock abbreviations see Chapter 1.

Rock type	DOL	PNG	PNG	PNG	DOL	OLG	PNG	OLG	PNG	OLG	OLG	PNG	PNG	PNG	PNG	PNG	PNG	PNG	MCG	PNG	PNG	PNG	MCG	PNG
Sample no.	94/56	93/2	94/47	95/21	12A	94/19	93/1	94/104	4A	94/22	94/21	F	94/81	94/32	95/25	95/33	95/15	95/19	93/22	11A	94/18	A	94/23	3A
Analysis	49	50	51	52	53	54	55	56	57	58	59	60	61	62	63	64	65	66	67	68	69	70	71	72
SiO_2	47.74	47.77	47.83	48.00	48.02	48.13	48.15	48.24	48.28	48.53	48.79	48.82	48.87	48.87	48.96	49.13	49.14	49.29	49.45	49.66	49.68	49.72	49.73	49.76
TiO_2	1.55	1.93	1.53	1.68	1.64	1.53	1.81	1.44	2.88	1.52	1.36	4.84	0.93	1.22	2.70	1.65	2.78	1.55	1.85	1.52	1.71	1.53	1.66	1.19
Al_2O_3	14.74	16.43	18.87	16.63	15.69	14.19	17.27	14.60	19.03	14.96	13.99	13.68	15.59	17.06	15.85	15.81	14.42	15.07	15.09	15.85	17.49	15.68	14.93	21.29
Fe_2O_3	n.m.	n.m.	n.m.	n.m.	n.m.	3.28	n.m.	5.10	n.m.	3.94	2.64	5.42	4.24	n.m.	n.m.	n.m.	n.m.	n.m.	n.m.	n.m.	4.61	3.79	3.29	n.m.
FeO	n.m.	n.m.	n.m.	n.m.	n.m.	7.78	n.m.	6.54	n.m.	7.39	7.98	5.57	3.75	n.m.	n.m.	n.m.	n.m.	n.m.	n.m.	n.m.	5.03	5.99	8.35	n.m.
Fe_2O_{3tot}	12.47	11.88	8.83	11.05	12.31	11.93	10.49	12.37	10.07	12.15	11.51	11.61	8.41	9.22	11.75	11.18	14.23	12.40	6.65	10.29	10.20	10.45	12.57	6.54
MnO	0.12	0.15	0.11	0.11	0.14	0.15	0.13	0.15	0.11	0.14	0.14	0.16	0.09	0.15	0.16	0.15	0.15	0.14	0.13	0.13	0.13	0.14	0.15	0.09
MgO	8.58	6.06	4.66	5.06	6.83	9.27	4.60	10.73	3.03	9.17	9.22	4.13	8.47	6.26	4.32	5.73	3.64	9.32	10.34	5.46	3.76	5.87	8.64	3.26
CaO	7.61	9.43	11.48	8.37	7.06	9.37	9.06	7.46	9.19	7.80	10.17	9.68	13.93	9.93	6.92	9.09	7.69	7.85	9.89	10.68	8.68	9.86	8.00	10.50
Na_2O	3.94	2.98	3.39	3.65	4.47	3.35	3.32	3.16	3.84	3.59	3.22	4.70	2.34	3.10	4.39	3.10	4.30	3.24	3.95	3.26	4.30	3.52	3.51	3.61
K_2O	0.69	1.16	1.14	1.26	1.03	0.86	1.57	1.00	1.17	1.04	0.78	0.77	0.28	1.22	1.45	1.03	0.97	1.02	0.32	1.10	1.33	1.03	1.07	1.05
P_2O_5	0.17	0.21	0.19	0.20	0.20	0.18	0.24	0.20	0.18	0.21	0.15	0.48	0.06	0.13	0.34	0.20	0.39	0.19	0.25	0.18	0.27	0.19	0.22	0.17
H_2O	n.m.	n.m.	n.m.	n.m.	n.m.	0.85	n.m.	n.m.	n.m.	0.86	0.85	1.51	n.m.	n.m.	n.m.	n.m.	n.m.	n.m.	n.m.	n.m.	1.74	1.49	0.44	n.m.
CO_2	n.m.	n.m.	n.m.	n.m.	n.m.	0.07	n.m.	n.m.	n.m.	0.09	0.09	0.36	n.m.	n.m.	n.m.	n.m.	n.m.	n.m.	n.m.	n.m.	0.50	0.36	0.07	n.m.
LOI	2.44	1.43	1.11	3.08	2.48	n.m.	2.52	0.43	1.30	n.m.	n.m.	n.m.	0.52	1.82	2.54	2.06	1.79	0.08	1.79	1.53	n.m.	n.m.	n.m.	1.67
Total	100.05	99.43	99.14	99.09	99.87	99.01	99.16	99.05	99.08	99.24	99.38	100.12	99.07	98.98	99.38	99.13	99.50	100.15	99.71	99.66	99.23	99.17	100.06	99.13
S	1091	116	89	51	225	124	231	139	109	131	136	322	155	47	50	68	138	446	56	61	56	220	115	209
V	186	256	192	177	207	192	233	160	296	174	201	265	197	156	244	221	263	172	197	227	207	203	176	248
Cr	317	190	47	115	231	376	119	317	13	295	495	11	36	460	64	59	58	278	270	552	49	193	261	118
Co	63	53	39	46	51	57	49	60	55	61	56	54	53	48	42	47	47	59	33	49	48	66	59	45
Ni	248	72	39	47	112	143	30	259	n.d.	233	136	4	76	43	36	12	n.d.	251	220	26	28	29	206	57
Cu	30	47	59	n.d.	n.d.	34	29	40	28	53	26	13	93	94	n.d.	n.d.	44	52	24	120	43	52	61	26
Zn	70	99	78	46	165	97	65	112	99	104	97	50	52	147	126	75	63	98	14	88	73	184	106	49
Ga	22	25	24	15	24	23	24	18	27	24	22	26	16	23	19	15	19	16	20	23	26	21	24	18
Rb	16	21	15	28	25	14	32	16	23	20	13	19	6	30	28	22	22	19	4	20	18	19	19	14
Sr	616	450	704	611	311	467	471	403	567	396	434	300	431	534	1021	396	438	380	339	433	648	367	379	675
Y	21	19	17	11	20	17	20	11	16	18	16	48	n.d.	15	19	11	22	9	19	20	21	17	20	11
Zr	96	92	89	106	113	84	111	99	88	98	82	166	40	68	158	97	151	111	129	84	109	92	109	76
Nb	3	2	4	5	3	3	3	4	3	5	2	32	n.d.	n.d.	13	6	16	6	8	1	6	5	6	0
Ba	209	139	146	155	450	65	163	96	172	111	79	88	2	221	306	178	195	165	48	158	153	84	115	117

Oxide concentrations are expressed as wt%; trace element concentrations are expressed as ppm. n.m. = not measured; n.d. = not detected. For trace element detection limits see Annex 3. For rock abbreviations see Chapter 1.

Rock type	MCG	PNG	PNG	PNG	PNG	PNG	ANR	MNZ	MNZ	MNZ	SYE	SYE	SYE	SYE	SYE	SYE	SYE	SYE	SYE	SYE	SYE	SYE	SYE
Sample no.	94/110	93/49	93/46	94/13	94/30	94/125	94/26	94/50	94/65	94/6	95/9	95/11	95/35	94/64	94/124	E	H	94/34	93/6	93/33	14A	94/46	94/7	94/16
Analysis	73	74	75	76	77	78	79	80	81	82	83	84	85	86	87	88	89	90	91	92	93	94	95	96
SiO_2	49.80	50.00	50.20	50.41	50.50	50.65	52.37	55.44	56.50	57.68	62.47	62.71	62.92	63.61	64.66	64.91	65.55	66.00	66.24	66.55	66.80	68.33	69.30	70.27
TiO_2	1.82	2.39	1.41	1.25	2.26	2.85	1.03	1.17	0.99	0.88	0.12	0.58	0.31	0.42	0.39	0.44	0.34	0.39	0.36	0.29	0.45	0.24	0.48	0.25
Al_2O_3	14.89	14.76	16.10	18.07	16.13	14.00	24.02	16.37	16.54	17.28	15.58	16.36	16.23	15.99	15.82	16.27	16.57	16.47	16.62	16.57	18.11	18.51	19.06	17.21
Fe_2O_3	n.m.	9.74	n.m.	n.m.	n.m.	5.49	0.99	n.m.	8.34	n.m.	n.m.	n.m.	n.m.	3.24	5.60	5.03	n.m.	n.m.	0.98	n.m.	n.m.	n.m.	n.m.	n.m.
FeO	n.m.	4.21	n.m.	n.m.	n.m.	9.42	1.85	n.m.	2.27	n.m.	n.m.	n.m.	n.m.	3.11	1.81	1.92	n.m.	n.m.	0.36	n.m.	n.m.	n.m.	n.m.	n.m.
Fe_2O_{3tot}	7.05	14.42	9.95	8.48	11.94	15.96	3.05	11.01	10.86	9.33	5.66	5.49	5.93	6.70	7.61	7.16	5.67	6.64	1.38	5.29	1.42	1.69	0.48	1.05
MnO	0.07	0.11	0.14	0.12	0.10	0.23	0.03	0.24	0.20	0.12	0.06	0.11	0.11	0.20	0.02	0.02	0.02	0.00	0.00	0.01	0.02	0.03	0.01	0.01
MgO	10.35	3.03	5.52	4.60	3.16	2.77	1.82	1.00	0.65	0.51	0.13	0.27	0.05	0.03	0.20	0.22	0.02	0.00	0.16	0.00	0.11	0.03	0.00	0.17
CaO	9.27	6.19	10.70	7.77	7.22	5.00	10.17	4.33	4.16	3.99	2.81	1.53	1.00	1.14	0.83	0.90	0.95	0.53	2.82	0.84	1.72	0.15	0.15	1.38
Na_2O	3.73	6.17	3.37	3.42	4.72	4.90	4.92	6.46	6.45	7.14	8.04	6.66	6.88	5.92	8.23	9.04	7.06	8.47	9.88	9.56	10.19	9.63	10.23	8.70
K_2O	0.82	0.60	1.02	2.69	1.66	1.72	1.03	2.03	2.49	1.54	1.17	4.62	4.85	5.77	1.11	0.70	3.42	0.72	0.09	0.65	0.49	0.53	0.29	0.31
P_2O_5	0.23	0.95	0.19	0.15	0.57	0.57	0.16	0.34	0.23	0.25	0.01	0.03	0.04	0.03	0.06	0.06	0.04	0.05	0.05	0.03	0.06	0.01	0.01	0.04
H_2O	n.m.	1.47	n.m.	n.m.	n.m.	n.m.	0.59	n.m.	n.m.	n.m.	n.m.	n.m.	n.m.	n.m.	n.m.	0.40	n.m.	n.m.	0.20	n.m.	n.m.	n.m.	n.m.	n.m.
CO_2	n.m.	0.18	n.m.	n.m.	n.m.	n.m.	0.08	n.m.	n.m.	n.m.	n.m.	n.m.	n.m.	n.m.	n.m.	0.16	n.m.	n.m.	1.88	n.m.	n.m.	n.m.	n.m.	n.m.
LOI	1.15	n.m.	0.95	2.26	1.53	1.96	n.m.	0.72	1.05	1.21	3.07	1.18	0.80	0.64	0.40	n.m.	0.42	0.76	n.m.	0.17	0.93	0.84	0.36	0.69
Total	99.18	99.80	99.55	99.22	99.79	99.56	99.06	99.11	99.87	99.93	99.12	99.54	99.12	100.10	99.13	100.07	100.06	100.03	99.64	99.96	100.30	99.99	100.37	100.08
S	387	1576	177	76	67	50	66	47	53	79	n.d.	56	36	228	26	n.d.	n.d.	n.d.	n.d.	n.d.	60	n.d.	n.d.	n.d.
V	231	106	220	190	170	96	78	6	19	12	1	5	9	13	15	12	6	6	n.d.	4	3	4	6	3
Cr	283	14	249	81	45	23	80	n.d.	18	7	1	n.d.	1	7	6	7	2	3	2	3	n.d.	1	n.d.	n.d.
Co	29	51	50	39	36	48	18	28	23	18	16	12	13	21	28	36	21	22	32	23	16	12	11	20
Ni	261	1	23	20	11	n.d.	19	n.d.	n.d.	n.d.	n.d.	n.d.	n.d.	n.d.	4	3	n.d.	3	3	n.d.	n.d.	n.d.	n.d.	1
Cu	n.d.	29	74	109	19	n.d.	12	17	n.d.	n.d.	n.d.	n.d.	n.d.	n.d.	28	35	n.d.	n.d.	n.d.	14	n.d.	n.d.	n.d.	30
Zn	20	63	98	79	68	98	10	193	174	65	18	72	594	115	8	21	15	5	3	11	5	8	n.d.	8
Ga	15	29	24	23	31	24	26	30	28	29	45	30	34	40	35	37	36	36	30	39	29	48	31	26
Rb	13	10	19	55	29	27	12	21	31	16	9	26	56	62	15	9	36	12	n.d.	8	7	11	3	5
Sr	359	373	418	1672	460	411	709	422	354	424	51	55	71	55	178	103	118	75	64	67	151	38	54	286
Y	22	46	20	17	38	32	12	35	39	24	35	24	40	49	53	60	45	40	58	48	30	9	12	50
Zr	126	163	90	59	156	184	71	244	311	117	336	178	522	450	427	412	352	379	403	437	224	317	122	508
Nb	12	19	n.d.	n.d.	18	26		29	21	5	2	6	63	45	25	56	33	39	44	38	9	12	17	25
Ba	225	140	137	601	228	243	1	355	381	601	3	215	305	86	146	11	441	55	n.d.	53	32	n.d.	n.d.	n.d.

Oxide concentrations are expressed as wt%; trace element concentrations are expressed as ppm. n.m. = not measured; n.d. = not detected. For trace element detection limits see Annex 3. For rock abbreviations see Chapter 1.

Appendix 4 - ICP-MS analyses.

Rock type	TRC	OXG	TRC	OXG	TRC	OXG	TRC	TRC	TRC	PNG	OLG	MCG	PNG	MCG	OLG	PNG	LCG	DOL	PNG	DOL	OLG	MCG	MCG	PNG
Sample no.	93.12	94.71	94.10	93.55	94.76	94.77	94.29	93.61	94.118B	3B	2A	1A	93.47	94.11	94.25	1B	93.57	94.56	93.20	12A	94.21	93.22	94.23	93.49
Analysis	1	2	3	4	5	6	7	8	9	10	11	12	13	14	15	16	17	18	19	20	21	22	23	24
Y	6	10	11	9	10	10	n.d.	9	13	21	13	19	34	20	n.d.	18	7	19	18	21	n.d.	19	n.d.	47
La	3.5	3.1	7.3	3.3	5.2	3.0	n.d.	5.1	8.9	13.5	9.1	9.9	18.9	15.6	n.d.	12.4	3.8	10.0	11.3	14.5	n.d.	23.4	n.d.	34.2
Ce	7.4	7.3	15.1	7.4	11.5	7.2	5.4	10.8	18.4	29.5	19.0	21.5	41.7	32.7	6.1	26.2	8.3	21.4	23.8	30.6	8.8	59.9	13.4	71.5
Pr	1.1	1.1	1.9	1.0	1.5	1.1	11.5	1.4	2.3	4.0	2.4	2.8	5.7	4.1	13.1	3.3	1.1	2.8	3.1	3.9	19.1	7.7	27.4	9.0
Nd	4.7	5.1	8.2	5.0	7.0	5.7	1.4	6.4	10.4	17.7	10.4	12.3	26.3	17.6	1.7	15.1	4.7	12.7	13.6	16.7	2.5	30.4	3.5	40.5
Sm	2.3	2.1	2.5	2.0	2.5	2.3	6.2	2.2	3.3	5.5	3.2	4.4	8.3	5.3	7.8	4.7	1.6	4.4	4.4	5.3	11.2	7.1	15.8	12.2
Eu	0.69	0.74	0.81	0.74	0.77	0.88	2.0	0.76	1.01	1.68	1.09	1.22	2.48	1.53	2.7	1.45	0.78	1.38	1.22	1.40	3.7	1.48	4.8	3.01
Gd	1.6	2.0	2.5	1.9	2.3	2.3	0.74	1.9	2.8	4.9	3.0	4.0	7.9	4.5	0.94	4.1	1.5	4.1	4.1	4.6	1.28	5.6	1.51	10.9
Tb	0.4	0.3	0.4	0.3	0.3	0.4	1.9	0.3	0.4	0.7	0.5	0.6	1.2	0.7	2.3	0.7	0.3	0.6	0.6	0.7	3.6	0.8	4.5	1.6
Dy	1.5	2.0	2.0	1.8	2.0	2.1	0.3	1.9	2.5	4.5	2.6	3.8	6.5	4.0	0.4	3.5	1.5	3.7	3.6	4.3	0.5	4.2	0.7	9.1
Ho	0.44	0.38	0.38	0.36	0.36	0.41	1.7	0.38	0.48	0.81	0.50	0.72	1.17	0.75	2.3	0.65	0.30	0.71	0.69	0.76	3.2	0.71	4.2	1.61
Er	0.8	0.9	1.0	0.9	1.1	1.0	0.32	1.0	1.3	2.1	1.2	1.9	3.2	1.9	0.43	1.8	0.7	2.0	1.8	2.1	0.60	1.9	0.77	4.3
Tm	0.3	0.1	0.2	0.1	0.1	0.1	0.8	0.2	0.2	0.3	0.2	0.3	0.4	0.3	1.1	0.2	0.1	0.3	0.2	0.3	1.5	0.3	2.0	0.5
Yb	0.8	0.8	0.9	0.7	0.9	0.9	0.1	0.9	1.0	1.8	1.1	1.6	2.3	1.6	0.1	1.5	0.6	1.6	1.5	1.9	0.2	1.5	0.3	3.3
Lu	0.30	0.13	0.14	0.10	0.13	0.11	0.8	0.14	0.15	0.24	0.16	0.24	0.32	0.22	1.0	0.20	0.12	0.22	0.20	0.26	1.3	0.19	1.6	0.45
Th	0.6	0.3	1.0	0.3	0.4	0.3	0.7	0.7	1.0	1.5	1.2	1.3	2.1	2.1	0.7	1.3	0.3	1.5	1.4	2.1	0.9	1.6	2.0	3.2
U	0.3	n.d.	0.3	0.1	0.2	n.d.	0.2	0.3	0.3	0.6	0.3	0.4	0.5	0.6	0.2	0.4	0.2	0.4	0.5	0.6	0.3	0.5	0.6	0.8

Rock type	PNG	PNG	PNG	ANR	MNZ	MNZ	SYE	SYE	SYE	SYE	SYE
Sample no.	93.46	94.30	94.13	94.26	94.65	94.60	94.64	94.12	E	94.34	93.60
Analysis	25	26	27	28	29	30	31	32	33	34	35
Y	20	37	36	n.d.	43	23	53	58	64	38	59
La	11.0	30.7	21.7	n.d.	28.7	17.5	43.9	40.8	33.9	25.2	32.3
Ce	23.5	61.9	45.6	9.5	59.2	37.1	90.5	87.6	81.2	52.3	83.7
Pr	3.0	7.7	5.9	19.3	7.4	4.7	10.5	10.7	10.5	7.3	10.5
Nd	13.3	32.5	26.6	2.4	31.9	20.5	42.2	42.5	43.8	31.1	41.2
Sm	4.4	9.6	8.5	10.4	9.7	6.2	11.9	12.3	13.4	9.1	13.3
Eu	1.40	2.24	2.04	3.3	3.60	4.01	1.66	2.12	1.94	1.58	1.17
Gd	4.3	8.7	7.9	1.35	8.7	5.5	9.8	10.7	11.7	7.7	11.3
Tb	0.7	1.3	1.2	2.9	1.5	0.8	1.6	1.8	2.0	1.2	1.9
Dy	3.8	7.4	6.9	0.4	8.5	4.7	9.7	10.5	12.0	7.0	11.5
Ho	0.72	1.36	1.28	2.5	1.62	0.88	1.87	2.01	2.27	1.37	2.15
Er	1.9	3.5	3.4	0.45	4.6	2.3	5.4	6.0	6.5	4.1	5.9
Tm	0.2	0.5	0.5	1.2	0.6	0.3	0.8	0.8	0.9	0.6	0.8
Yb	1.6	2.8	3.0	0.2	3.8	2.0	5.6	5.3	5.7	4.3	5.2
Lu	0.22	0.40	0.44	1.0	0.57	0.34	0.81	0.75	0.87	0.64	0.77
Th	1.5	2.8	2.8	1.3	4.1	1.5	7.3	8.1	9.4	7.1	8.2
U	0.5	1.0	0.9	0.4	1.4	0.5	2.2	2.3	2.7	2.4	2.6

Concentrations are expressed as ppm. n.d. = not detected. For detection limits see Annex 3. For rock abbreviations see Chapter 1.

Appendix 5 - Photos.

Photo 1 - Jebel Hayim and the Tradagal Valley.

Photo 2 - Anefgou and Jebel Sloul.

Photo 3 - Jebel Tameskourt. This mountain is the northern limb of the E-W trending Anefgou anticline. (see Chapter 3)

Photo 4 - The Islane Plateau. This valley is the syncline between the Anefgou anticline and the Tirrhist anticline. (see Chapter 3)

Photo 5 - Assamer n'Inouzana and Tizi Islane. It is the most deformed area between JHM and the Tirrhist Massif. (see Chapter 3)

Photo 6 - Jebel Fazaz. This mountain is a drag fold formed by a vertical E-W trending limb. (see Chapter 3)

Photo 7 - A sedimentary body within JHM. It comprises strongly deformed limestones and dolomites. (see Chapter 3)

Photo 8 - A sedimentary body at the contact between JHM and country rock. It comprises red pelites and dolomites. (see Chapter 3)

Photo 9 - A ten metres thick level of «white breccias» at the contact between JHM and country rock (6/7-J). (see Chapter 3)

Photo 10 - Tectonic contact between JHM gabbros and country rock marls in the Tardagal valley (9/10-E/F). (see Chapter 3)

Photo 11 - Troctolite outcrop (7/8-E/F).
(see Chapter 3)

Photo 12 - Leucocratic ocelli within pneumatolytic gabbros (6/7-G/H).
(see Chapter 3)

Photo 13 - Magmatic contact between syenites and monzonites at Jebel Hayim (6/7-D/E).
(see Chapter 4)

Photo 14 - Basic dikes intruding syenites (9/10-C/D).
(see Chapter 4)

Photo 15 - Ophitic texture of troctolites (10x).
(see Chapter 4)

Photo 16 - Flow texture of oxide-rich gabbros (10x).
(see Chapter 4)

Appendix 6 - Outcrop map of the Jebel Hayim Massif.

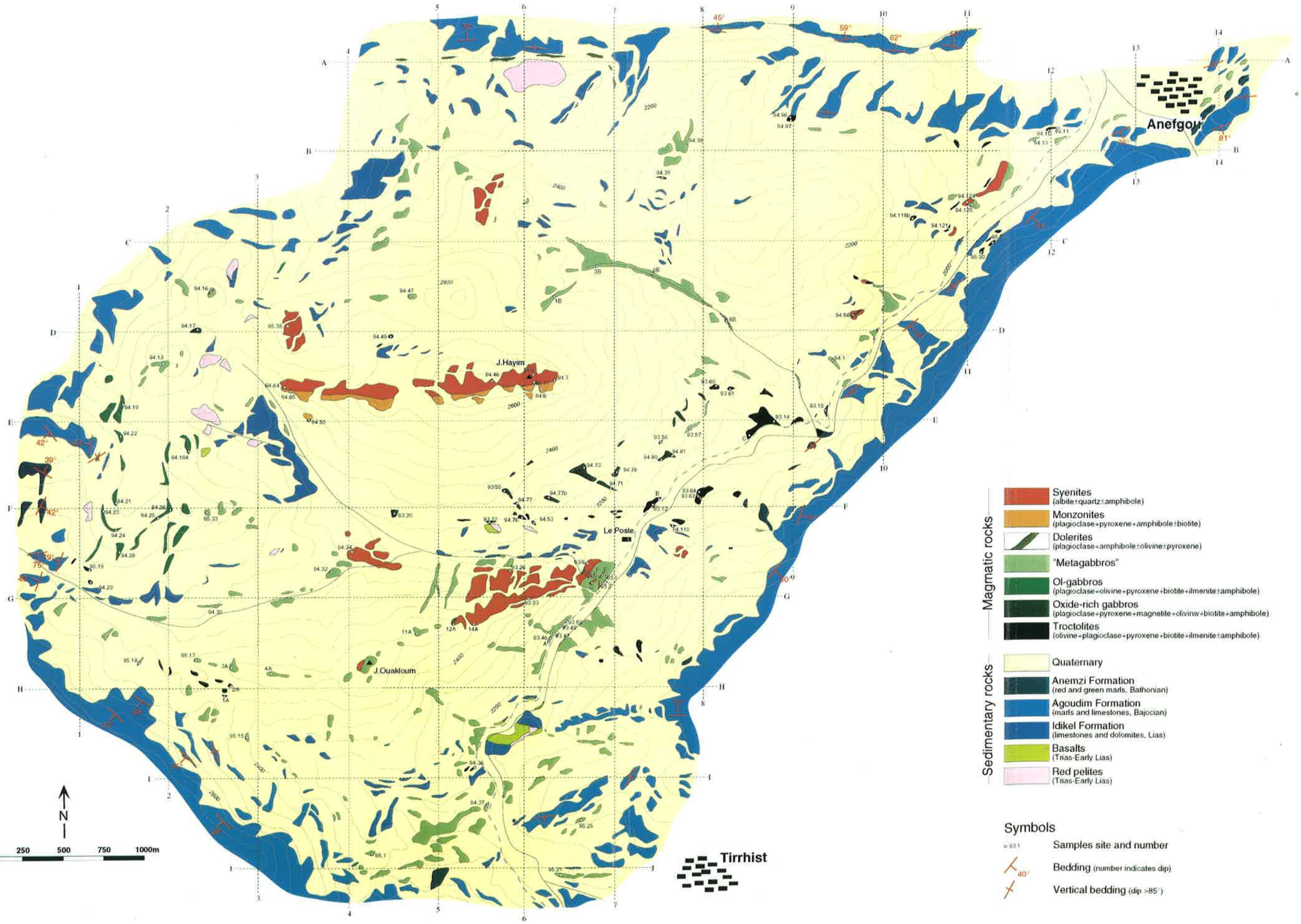

No. 30 BAUD A., POPOVA I., DICKINS J.M., LUCAS S. and ZACHAROV Y. (eds.) 1997. Late Paleozoic and Early Mesozoic Circum-Pacific Events: Biostratigraphy, Tectonic and Ore Deposits of Primoryie (Far East Russia). IGCP Project 272, 202 pp., 71 text-figs., 17 tables, 48 pls.

No. 31 ARMANDO G. 1999. Intracontinental alkaline magmatism: Geology, Petrography, Mineralogy and Geochemistry of the Jebel Hayim Massif (Central High Atlas - Morocco). 106 pp., 51 figs., 23 tables, 1 map.

Mémoires de Géologie (Lausanne)

No. 1 BAUD A. 1987. Stratigraphie et sédimentologie des calcaires de Saint-Triphon (Trias, Préalpes, Suisse et France). 202 pp., 53 text-figs., 29 pls.

No. 2 ESCHER A., MASSON H. and STECK A. 1988. Coupes géologiques des Alpes occidentales suisses. 11 pp., 1 text-figs., 1 map.

No. 3 STUTZ E. 1988. Géologie de la chaîne de Nyimaling aux confins du Ladakh et du Rupshu (NW-Himalaya, Inde) - évolution paléogéographique et tectonique d'un segment de la marge nord-indienne. 149 pp., 42 text-figs., 11 pls.

No. 4 COLOMBI A. 1989. Métamorphisme et géochimie des roches mafiques des Alpes ouest-centrales (géoprofil Viège-Domodossola-Locarno). 216 pp., 147 text-figs., 2 pls.

No. 5 STECK A., EPARD J.-L., ESCHER A., MARCHANT R., MASSON H. and SPRING L. 1989. Coupe tectonique horizontale des Alpes centrales. 8 pp., 1 map.

No. 6 SARTORI M. 1990. L'unité du Barrhorn (Zone Pennique, Valais, Suisse). 140 pp., 56 text-figs., 3 pls.

No. 7 BUSSY F. 1990. Pétrogenese des enclaves microgrenues associées aux granitoïdes calco-alcalins: exemple des massifs varisque du Mont-Blanc (Alpes occidentales) et miocène du Monte Capanne (Ile d'Elbe, Italie). 309 pp., 177 text-figs.

No. 8 EPARD J.-L. 1990. La nappe de Morcles au sud-ouest du Mont-Blanc. 165 pp., 59 text-figs.

No. 9 PILLOUD C. 1991. Structures de déformation alpines dans le synclinal de Permo-Carbonifère de Salvan-Dorénaz (massif des Aiguilles Rouges, Valais). 98 pp., 59 text-figs.

No. 10 BAUD A., THELIN P. and STAMPFLI G. (Eds) 1991. Paleozoic geodynamic domains and their alpidic evolution in the Tethys. IGCP Project No. 276. Newsletter No 2., 155 pp.

No. 11 CARTER E. 1993. Biochronology and Paleontology of uppermost Triassic (Rhaetian) radiolarians, Queen Charlotte Island, British Columbia, Canada. 132 pp., 15 text-figs., 21 pls.

No. 12 GOUFFON Y. 1993. Géologie de la « nappe » du Grand St-Bernard entre la Doire Baltée et la frontière suisse (Vallée d'Aoste - Italie). 147 pp., 56 text-figs., 3 pls.

No. 13 HUNZIKER J.C., DESMONS J. and HURFORD A.J. 1992.Thirty-two years of geochronological work in the Central and Western Alps: a review on seven maps. 59 pp., 18 text-figs., 7 pls.

No. 14 SPRING L. 1993. Structures gondwaniennes et himalayennes dans la zone tibétaine du Haut Lahul-Zanskar oriental (Himalaya indien). 148 pp., 66 text-figs., 1 pl.

No. 15 MARCHANT R. 1993. The Underground of the Western Alps. 137 pp., 104 text-figs.

No. 16 VANNAY J.C. 1993. Géologie des chaînes du Haut-Himalaya et du Pir Panjal au Haut-Lahul (NW Himalaya, Inde). 148 pp., 44 text-figs., 6 pls.

No. 17 PILLEVUIT A. 1993. Les Blocs Exotiques du Sultanat d'Oman: Evolution paléogéographique d'une marge passive flexurale. 249 pp., 138 text-figs., 7 pls.

No. 18 GORICAN S. 1994. Jurassic and Cretaceous radiolarian biostratigraphy and sedimentary evolution of the Budva Zone (Dinarides, Montenegro). 120 pp., 20 text-figs., 28 pls.

No. 19 JUD R. 1994. Biochronology and systematics of Early Cretaceous radiolaria of the Western Tethys. 147 pp., 29 text-figs., 24 pls.

No. 20 DI MARCO G. 1994. Les terrains accretés du sud du Costa Rica. Evolution tectonostratigraphique de la marge occidentale de la plaque Caraïbe. 166 pp., 89 text-figs., 6 pls.

No. 21 O'DOGHERTY L. 1994. Biochronology and paleontology of middle Cretaceous radiolarians from Umbria-Marche Appenines (Italy) and Betic Cordillera (Spain). 415 pp., 35 text-figs., 73 pls.

No. 22 GUEX J. and BAUD A. (Eds.) 1994. Recent Developments on Triassic Stratigraphy. 184 pp.

No. 23 BAUMGARTNER P.O., O'DOGHERTY L., GORICAN S., URQUHART E., PILLEVUIT A. and DE WEVER P. (Eds.) 1995. Middle Jurassic to Lower Cretaceous Radiolaria of Tethys: Occurrence, Systematics, Biochronology. 1162 pp.

No. 24 REYMOND B. 1994. Three-dimensional sequence stratigraphy offshore Louisiana, Gulf of Mexico (West Cameron 3D seismic data). 215 pp., 169 text-figs., 49 pls.

No. 25 VENTURINI G. 1995. Geology, Geochronology and Geochemistry of the Inner Central Sesia Zone (Western Alps - Italy). 183 pp., 57 text-figs., 12 pls.

No. 26 SEPTFONTAINE M., BERGER J.P., GEYER M., HEUMANN C., PERRET-GENTIL G. et SAVARY J. 1995. Catalogue des types paléontologiques déposés au Musée Cantonal de Géologie, Lausanne. 76 pp.

No. 27 GUEX J. 1995. Ammonites hettangiennes de la Gabbs Valley Range (Nevada, USA). 130 pp., 22 text-figs., 32 pls.

No. 28 HÜRLIMANN A., BESSON-HÜRLIMANN A. and MASSON H. 1995. Stratigraphie et tectonique de la partie orientale de l'écaille de la Gummfluh (Domaine Briançonnais des Préalpes). 132 pp., 62 text-figs., 39 pls., 6 maps.

No. 29 DOBMEIER C. 1996. Die variskische Entwicklung des südwestlichen Aiguilles-Rouges-Massives (Westalpen, Frankreich). 191 pp., 70 text-figs., 18 tables, 1 map.

Order from **Institut de Géologie et Paléontolgie,**
Université de Lausanne, BFSH-2. CH-1015, SWITZERLAND.
http://wwww-sst.unil.ch/publidep.htm Fax: (41) 21-692.43.05
Bank Transfer: Banque Cantonale Vaudoise 1002 Lausanne
Account Number: **C.323.52.56** Institut de Géologie, rubrique: Mémoires

Price 30 CHF per volume except volume 23 (100 CHF). The price doesn't include postage and handling

- Please do not send check -